PHD THESIS

SUPERCAPACITOR ELECTRODE MATERIALS BASED ON SURFACE TUNED BINARY, TERNARY METAL OXIDES AND CARBON NANOSTRUCTURES

Aswini R
Dept of Nanoscience
and Technology
University of Calicut

2024

SUPERCAPACITOR ELECTRODE MATERIALS BASED ON SURFACE TUNED BINARY, TERNARY METAL OXIDES AND CARBON NANOSTRUCTURES

Thesis

Submitted to the Faculty of Science

University of Calicut in Partial Fulfilment of the

Requirement for the Degree

Doctor of Philosophy

By

Aswini R

Under the Guidance of

Dr. Sindhu S

Department of Nanoscience and Technology
University of Calicut
Kerala-673635

April-2024

UNIVERSITY OF CALICUT
Department of Nanoscience & Technology

Calicut University P.O.,
Kerala, 673635, INDIA
0494 2407373, 2407374
Email: sindhus@uoc.ac.in
Website: https://nanotechnology.uoc.ac.in

Dr. Sindhu S
Professor & Head

CERTIFICATE

This is to certify that the thesis entitled "***Supercapacitor Electrode Materials Based on Surface Tuned Binary, Ternary Metal Oxides and Carbon Nanostructures"*** is a bona-fide record of research work carried out by **Smt. Aswini. R.** under my supervision in partial fulfillment of the requirements for the award of the degree of Doctor of Philosophy in Nanoscience and Technology of the University of Calicut. The plagiarism check is carried out and this work or part thereof has not been presented before for the award of any other degree. Also, the corrections/suggestions recommended by the adjudicators have been incorporated in the thesis and that the contents in the thesis and the soft copy are one and the same.

Dr. Sindhu S.

(Supervising Guide)
Professor and Head
Department of Nanoscience and Technology
University of Calicut

DECLARATION

I hereby declare that the work presented in the thesis entitled *"**Supercapacitor Electrode Materials Based on Surface Tuned Binary, Ternary Metal Oxides and Carbon Nanostructures**"* is based on the original work done by me under the guidance of Dr. Sindhu S, Professor and Head, Department of Nanoscience and Technology, University of Calicut and has not been included in any other thesis submitted previously for the award of any degree. The contents of the thesis are undergone plagiarism check using ithenticate software at C.H.M.K. Library, University of Calicut, and the similarity index found within the permissible limit. I also declare that the thesis is free from AI generated contents.

University of Calicut Aswini R

12/04/2024

Dr. Sindhu S

This Thesis is Dedicated to All Who Gave Constant Love, Support, Peace and Inspiration

ACKNOWLEDGEMENT

My PhD journey comes to an end with my thesis, and as I reflect back with a sense of accomplishment, I gratefully acknowledge so many people including teachers, mentors, family members, lab mates, and friends, significantly contributed to finishing this enormous job. It is my pleasure to express my gratitude for their great assistance and notable guidance during the research period.

I would like to express my deepest thanks to my supervisor, **Dr. Sindhu S**, Professor, Dept of Nanoscience and Technology, University of Calicut, for accepting me as a student and to finish my PhD work under her guidance. I appreciate all of her encouragement and helpful advice during my doctoral studies.

I would like to convey my sincere thanks to University of Calicut for the PhD grant. The grant helped me at the time of financial struggles while conducting my research, specifically when it comes to analyzing my samples. I would like to thank Central Sophisticated Instrumentation Facility (CSIF), University of Calicut for doing the sample analysis. I would want to express my gratitude to all teaching and non-teaching staffs of Dept. of nanoscience and technology, especially **Dr. Kishore Sridharan, Dr. Shibu E. S, Dr. Vijisha K. Rajan, Smt. Dhanya K** for the help during the research period.

I would also like to express my gratitude to the teachers and students from other Departments and Institutes especially **Dr. Jeyanthinath M** (Assistant Professor, Madurai Kamaraj University), **Dr. Deepa K G** (Assistant Professor, Dept of Physics, Kerala University) and their students for their assistance for doing electrochemical studies. I also want to express my heartfelt thanks to teachers and research scholars in Department of Physics and Chemistry, CSIF instrumentation facility ,University of Calicut for their help in completing several material characterizations.

I want to express my gratefulness to my seniors, **Dr Jyothilakshmi V P, Dr. Nijisha P, Dr.**

Niveditha C V, Dr. Dharsana M V, Dr. Bhabina N M, Dr. Jabeen Fatima and Dr. Rajitha R, for lending helping hands during numerous key moments. I would like to express my gratitude towards lab peoples specially **Amritha Raveendran, Swetha P, Neethumol, Deepa, Nishanth**. In addition, I want to express my heartfelt gratitude to my dear friends **Rival Jose V, Sreeraj P, Sainul Abid K A, Akshay P, Elza Johnson V, Anjitha, Athira E, Athul Krishna M, Safa Leen, Fida Lulu, Shamjith Khan KC, Dijuraj, Ajisha P C, Athira Vijayan, Nikhil Santhosh and Sravan Das P** for their unwavering support and encouragement.

My sincere gratitude goes to my parents and brother for the love, care and sacrifices they made to nurture my life and provide me the freedom to pursue my desires. I thank each and every person who has supported me while I pursue my PhD and keep them in my thoughts.

Aswini R.

CONTENTS

6.2 Saw Dust (Ailanthus Triphysa) Derived Hierarchical Porous Carbon

6.3 Leaf Derived Microporous Carbon from Palmyra Palm Leaves

List of Figures

List of Tables

List of Abbreviations

1. ARGO-Autoclaved Reduced Graphene Oxide
2. ASC - Asymmetric Supercapacitor
3. BET - Brauner Emmet Teller
4. BJH -Barret Joyner Halenda
5. CFs - Carbon Fibers
6. CNFs - Carbon Nanofibers
7. CV - Cyclic Voltammetry
8. DMF - Dimethyl Formamide
9. EDLCs - Electrical Double Layer Capacitors
10. EES - Electrochemical Energy Storage Systems
11. EIS - Electrochemical Impedance Analysis
12. FE-SEM - Field Emission Scanning Electron Microscopy
13. FTIR - Fourier Transform InfraRed spectrometer
14. GCD - Galvanostatic Charge-Discharge Analysis
15. KI - Potassium Iodide
16. PAN - Poly Acrylo Nitrile
17. PEA - Porosity Enhancing Agents
18. PEDOT - Poly-(3,4-Ethylene Dioxythiophene)
19. PVDF-Polyvinylidene Fluoride
20. SSA - Specific Surface Area
21. TGA- Thermogravimetric Analysis
22. TPV - Total Pore Volume
23. XPS - X-ray Photoelectron Spectroscopy
24. XRD - X-ray Diffraction

List of Publications

1. **Aswini, R**.; Swaminathan, S.; Mayandi, J. Phase-Selective Synthesis of Monoclinic VO_2(B) Nanosheets and its Self-Assembled Nanoflower Binary Hybrids for Energy Storage, (Accepted-JES)
2. **Aswini, R**.; Swaminathan, S. Boosting Specific Capacitance: Harnessing Redox-Additive Electrolytes for Enhanced Performance in Porous Carbon Derived from Leaves- Chemical Physics Letters, 2024, 843, 141238
3. **Aswini R**, Swaminathan, S, Mayandi, J., Deepa K. G. Template Free Synthesis of Vacancy Tailored, Highly Mesoporous One-Dimensional δ-MnO_2 for Energy Storage Applications, Nanoexpress, 2024, 5,015024
4. **Aswini, R**.; Swaminathan, S.; Mayandi, J. Simple and Scalable Green Approach for Synthesizing Hierarchically Porous Hexagonal Shaped 3D Carbon Structure for Sodium-ion Storage. Chemistry Select 2023, 8,45.
5. **Aswini, R**.; Niveditha, C. V.; Swaminathan, S. Flexible Graphene Electrodes from Potentiodynamic Reduction in Neutral Medium for Enhanced Specific Capacitance and Cyclic Stability. Materials Today: Proceedings 2022, 56, 587–593.
6. Niveditha, C. V.; **Aswini, R**.; Jabeen Fatima, M. J.; Ramanarayan, R.; Pullanjiyot, N.; Swaminathan, S. Feather like Highly Active Co_3O_4 Electrode for Supercapacitor Application: A Potentiodynamic Approach. Material Research Express 2018, 5,065501
7. Swetha, P.; **Aswini,R**; Bineesh,M; Muhammed Shahin.,T.H.; Sridharan, K.; Swaminathan, S. Cost Efficient Fabrication of Flexible Polymer Meta composites: Impact of Carbon in Achieving Tunable Negative Permittivity at Low Radio Frequency Range. Materials Today Communications 2023, 34, 105287.

Conference Presentations

1. **International Conference on Advances in Functional Materials and Coatings, ICAMFC-2024**, Aswini, R.; Swaminathan, S- Optimizing Supercapacitor Electrode Performance Through Potentiodynamically Synthesized Binder-Free Nickel Oxide Thin Film with One-Dimensional Morphology- **Oral presentation**

2. **International Conference on Advanced Materials, ICAM-2024**, Aswini, R.; Swaminathan, S- Development of Scalable Mesoporous Zinc Tellurium oxide – Graphene Hybrid Material for Energy Storage- **Oral presentation**

3. **International Conference on Advanced Materials for Sustainability, ICAMS-2023**- Aswini, R.; Swaminathan, S; Jeyanthinath, M, Crafting Highly Porous Hexagonal 3D Carbon Structures for Energy Storage Applications- **Oral presentation**

4. **National Conference on Emerging Frontiers in Chemical Science, EFCS-2022**- Aswini, R.; Swaminathan, S; Jeyanthinath, M, Biomass Derived Activated Carbon with Improved Porosity for Energy Storage- **Poster presentation**

5. **International Conference on Material, Machines and Information Technology, ICMMIT 2022-** Aswini, R.; Niveditha, C. V.; Swaminathan, S, Flexible Graphene Electrodes from Potentiodynamic Reduction in Neutral Medium for Enhanced Specific Capacitance and Cyclic Stability- **Oral presentation**

6. **International Conference on Science and Engineering of Materials, ICSEM 2021-** Aswini, R.; Niveditha, C. V.; Swaminathan, S, Potentiodynamically Synthesized Nanoworm like Nickel oxide thin film as Supercapacitor electrode - **Oral presentation**

PREFACE

In modern world, energy storage devices play a crucial role due to the growing demand for reliable and sustainable energy sources. These devices are essential for controlling the intermittency of renewable energy sources like solar and wind and allowing for the storage of surplus energy generated during peak times for use during periods of low output. This capability is crucial for balancing supply and demand on the grid, reducing dependency on fossil fuels, and eventually, addressing climate change. Furthermore, energy storage devices are essential for improving grid stability, allowing for the integration of electric vehicles, and providing backup power during outages, making them necessary components of modern energy systems. Due to these facts the energy storage systems such as battery, supercapacitor, fuel cell etc got more importance.

Supercapacitors are essential in today's environment because of their quick energy delivery and storage capabilities, which addressing the growing demand for high-power applications. Unlike traditional batteries, supercapacitors can be charged and discharged quickly, making them ideal for use in gadgets that require frequent energy usage, such as in electric vehicles, renewable energy systems, and portable electronics. Additionally, supercapacitors also have a longer lifespan and higher efficiency than batteries, which makes them as an essential component in the transition towards more sustainable and efficient energy storage solutions, ultimately leading to a greener and more advanced society.

Chapter 1. Introduction

The first chapter provides an introduction to energy storage and its importance. The detailed discussion of supercapacitor, how it is working and the components and its peculiarities are descripted. This chapter discusses the potential of electrochemical energy storage methods and their advantages. The details of different materials, mechanism are discussed. The components of the electrochemical capacitor and its peculiarities are also discussed. The advantages of

using VO_2, MnO_2 and Biomass derived carbons, CNF as electrode material is also described in this chapter. Through this chapter, the effectiveness of sol gel method, hydro-solvothermal and electrospinning techniques in producing nanostructures, activation during biomass carbon preparation that can be employed for synthesizing electrode material is explained.

Chapter 2. Synthesis and Characterization Techniques

The second chapter goes into details on the theory underlying the hydrothermal, sol gel and electrospinning processes. The detailed theory behind the different techniques used to characterize the synthesized materials is also covered. Various techniques are used to investigate the structural, morphological and surface aspects of the synthesized materials. The structural analysis was carried out using XRD, Raman spectroscopy, and XPS spectroscopy. SEM imaging was used to determine the size and morphology of the synthesized samples. BET surface area analyser was used to assess the porosity and surface area of synthesized metal oxides, porous carbon and CNFs. Electrochemical methods used to determine the capacity of material is detailed in this chapter.

Chapter 3. Temperature Tuned Phase Selective Synthesis of VO_2 (B) Nanosheet and Self-Assembled Flower like Binary Hybrid

The third chapter explores the hydrothermal synthesis of mesoporous VO_2 (B) nanoparticles. The detailed analysis of synthesized samples utilising various techniques is also presented. This chapter explains how to tune the porosity and morphology of VO_2 (B) nanoparticles by altering the hydrothermal temperatures. We observed an interesting nanosheets morphologies of VO_2 (B) during different hydrothermal temperature. These findings lead to control nanosheet transformation, porosity, specific surface area. which can enhance its applicability in electrochemical storage. Further enhancement in the energy storage can be improved by introducing reduced graphene oxide. This develops a flower like morphology with better storage property.

Chapter 4. Porosity and Defect Tuned δ-MnO_2 Polymorph for Enhanced Electrical Conductivity

This chapter explains the preparation of phase selective synthesis of δ-MnO_2 by simple chemical method. The synthesis carried out by adding reducing agents like citric acid and ammonium oxalate in the manganese precursor. By annealing samples under different conditions and changing reducing agent produce various morphology, specific surface area and point defects of selective samples is discussed. as well as their electrochemical analysis were described in this chapter.

Chapter 5. Solvothermal Synthesis of Ternary Mesoporous Zincospiroffite ($Zn_2Te_3O_8$) - RGO Hybrid

This chapter outlined the $Zn_2Te_3O_8$, a ternary metal oxide synthesized through a solvothermal method. The enhancement of its electrical conductivity is achieved by making hybrid with graphene by the addition of graphene oxide during synthesis. Thus, produced hybrid material improves all energy storage parameter including specific capacitance, energy density and power density.

Chapter 6. Synthetic and Biomass Derived Porous Carbon with Redox Additive Electrolyte for Supercapacitor Application

In Chapter 6, it is examined how carbon-based material act with redox additive electrolyte as energy storage and three carbon materials are detailed here. The first material discuss how carbonization in temperature affects the final characteristics of CNFs. In this study, PAN nanofibers are carbonized at temperatures of 500 °C, 700 °C and 900 °C, and the characteristics of the resultant CNFs are compared to find the ideal carbonization temperature, which is provided in this chapter. The second and third materials are biomass derived carbon. These are synthesized from saw dust and palm leaf sources. Initially the precarbonized samples are subjected to activation using $ZnCl_2$ and followed by pyrolysis at high temperature yield highly

porous carbon.

Chapter 7. Conclusion and Scope of Future Work

The present research study is summarized in chapter 7, along with potential areas for future application. The improved nanomaterials exhibit good storage property even though its storge capacities can improvise by changing electrolyte and its ionic contents. So, its application extended to other fields like K-ion storage, batteries etc.

ആമുഖം

ആധുനിക ലോകത്ത്, വിശ്വസനീയവും സുസ്ഥിരവുമായ ഊർജ്ജ സ്രോതസ്സുകളുടെ വർദ്ധിച്ചുവരുന്ന ആവശ്യം കാരണം ഊർജ്ജ സംഭരണ ഉപകരണങ്ങൾ നിർണായക പങ്ക് വഹിക്കുന്നു. സൗരോർജ്ജം, കാറ്റ് തുടങ്ങിയ പുനരുപയോഗ ഊർജ്ജ സ്രോതസ്സുകളെ ഇടയ്ക്കിടെ നിയന്ത്രിക്കുന്നതിന് ഈ ഉപകരണങ്ങൾ അത്യന്താപേക്ഷിതമാണ്. പീക്ക് സമയങ്ങളിൽ ഉൽപാദിപ്പിക്കുന്ന മിച്ച ഊർജ്ജം സംഭരിച്ച് കുറഞ്ഞ ഉൽപ്പാദനം ഉള്ള കാലഘട്ടങ്ങളിൽ ഉപയോഗിക്കുന്നതിന് അനുവദിക്കുന്നു. ഗ്രിഡിലെ വിതരണവും ഡിമാൻഡും സന്തുലിതമാക്കുന്നതിനും ഫോസിൽ ഇന്ധനങ്ങളുടെ ആശ്രിതത്വം കുറയ്ക്കുന്നതിനും ഒടുവിൽ കാലാവസ്ഥാ വ്യതിയാനത്തെ അഭിസംബോധന ചെയ്യുന്നതിനും ഈ കഴിവ് നിർണായകമാണ്. കൂടാതെ, ഗ്രിഡ് സ്ഥിരത മെച്ചപ്പെടുത്തുന്നതിനും വൈദ്യുത വാഹനങ്ങളുടെ സംയോജനം അനുവദിക്കുന്നതിനും തടസ്സസമയത്ത് ബാക്കപ്പ് പവർ നൽകുന്നതിനും അവ ആധുനിക ഊർജ്ജ സംവിധാനങ്ങളുടെ ആവശ്യമായ ഘടകങ്ങളാക്കി മാറ്റുന്നതിനും ഊർജ്ജ സംഭരണ ഉപകരണങ്ങൾ അത്യന്താപേക്ഷിതമാണ്. ഈ വസ്തുതകൾ കാരണം ഊർജ്ജ സംഭരണ സംവിധാനങ്ങളായ ബാറ്ററി, സൂപ്പർ കപ്പാസിറ്റർ, ഇന്ധന സെൽ തുടങ്ങിയവയ്ക്ക് കൂടുതൽ പ്രാധാന്യം ലഭിച്ചു.

ഇന്നത്തെ പരിതസ്ഥിതിയിൽ സൂപ്പർ കപ്പാസിറ്ററുകൾ അത്യന്താപേക്ഷിതമാണ്, കാരണം അവയുടെ ദ്രുത ഊർജ്ജ വിതരണവും സംഭരണ ശേഷിയും ഉയർന്ന പവർ ആപ്ലിക്കേഷനുകളുടെ വർദ്ധിച്ചുവരുന്ന ആവശ്യകതയെ അഭിസംബോധന ചെയ്യുന്നു.പരമ്പരാഗത ബാറ്ററികളിൽ നിന്ന് വ്യത്യസ്തമായി, സൂപ്പർകപ്പാസിറ്ററുകൾ വേഗത്തിൽ ചാർജ് ചെയ്യാനും ഡിസ്ചാർജ് ചെയ്യാനും കഴിയും, വൈദ്യുത വാഹനങ്ങൾ, പുനരുൽപ്പാദിപ്പിക്കാവുന്ന ഊർജ്ജ സംവിധാനങ്ങൾ, പോർട്ടബിൾ ഇലക്ട്രോണിക്സ് തുടങ്ങിയ ഇടയ്ക്കിടെ ഊർജ്ജ ഉപയോഗം ആവശ്യമായി വരുന്ന ഗാഡ്ജെറ്റുകളിൽ ഉപയോഗിക്കാൻ അവയെ അനുയോജ്യമാക്കുന്നു. കൂടാതെ, സൂപ്പർകപ്പാസിറ്ററുകൾക്ക് ബാറ്ററികളേക്കാൾ ദൈർഘ്യമേറിയ ആയുസ്സും ഉയർന്ന ക്ഷമതയുമുണ്ട്, ഇത് കൂടുതൽ സുസ്ഥിരവും കാര്യക്ഷമവുമായ ഊർജ്ജ സംഭരണ പരിഹാരങ്ങളിലേക്കുള്ള പരിവർത്തനത്തിലെ ഒരു പ്രധാന ഘടകമായി മാറുന്നു. ഇത് ആത്യന്തികമായി ഹരിതവും കൂടുതൽ വികസിതവുമായ ഒരു സമൂഹത്തിലേക്ക് നയിക്കുന്നു.

1. Introduction

One of the most pressing issues confronting the world's population is the energy crisis. Climate anomalies affect or have an impact on natural resources, which lessens reliance on them. The increasing cost of energy and the restriction of ongoing uses hasten the extraction of natural resources. Over the last few decades, fossil fuels have been a popular source of energy.[1] These fall under the category of non-renewable energy sources, their accessibility, and availability are declining these days. Frequent natural disasters that happened recently around the Globe throws an alarming treat on the aftermath of climate change. The contribution of academics or a researcher towards the reduction of the impact of these kinds of natural disasters on humanity values a lot. Major implication of the climate change is due to the global warming contributed by the amplified CO_2 level in the atmosphere. Efficient energy management is very much important to handle the climate change due to global warming. This is why many research groups focuses on the tapping of energy from renewable energy resources using efficient materials or devices. Thousands of literatures can be seen published by the research groups on the harvesting of energy from renewable resources. Analogous to this, the materials or devices for the efficient storage of this energy is also most important. The development of a sustainable society should place more emphasis on maximizing energy extraction from renewable energy sources and implementing efficient energy storage systems [2,3].

One of the major goals of maximizing the use of renewable energy on the grid is its capacity to store electricity for later use. Energy storage is simply the act of capturing energy once and storing it for later. The main methods of storing energy in various forms, such as thermal, kinetic, chemical, etc., and then converting it back to electricity when the need arose. In the current situation, it is necessary to transform energy coming from various sources or forms into electricity. This energy conversion primarily involves three processes; generation, transmission, and distribution. Another important factor is the ability to store energy and deliver it as needed.

1.1 Electrochemical Energy Storage

Electrochemical energy storage systems (EES) have gained popularity in recent years. As a result, EES systems, which include electrochemical capacitors, batteries, and fuel cells are more important. The EES must make a significant contribution to the implementation of sustainable energy systems. Flow cells, fuel cells, rechargeable batteries, and supercapacitors are attention-seeking EES systems (figure 1.1). Supercapacitors and batteries are used for both

transportation and electrification[2,3].

Figure 1.1 Major electrochemical energy storage systems in our economy*

Energy storage has traditionally relied on rechargeable batteries all over the world. The main focus of these studies is the lithium-ion battery. This type of battery is commonly used for recharging purposes and appropriate choice for the electrical vehicle market. Despite its high-power density, this system has a low memory effect, which prevented overcharging, reducing its use in hybrid vehicles. In this situation, supercapacitors are the ideal capacitors to use for these applications. Supercapacitors are used in electrical circuits that allow fast charging and discharging [4,5]. Introducing supercapacitors meets the demand for large amounts of energy in the shortest time possible for hybrid vehicles.

1.2 Supercapacitors

The capacitors contain mainly two conductive electrodes. An insulated dielectric material is sandwiched between the two conducting electrodes. When voltage is applied, opposite charges are accumulated on the surface of the electrode material. The charge is separated by the dielectric medium and an electric field is produced. That allows the storage of energy in the capacitor. The capacitance C is defined as equation (1),

$$C = \frac{Q}{V} \qquad (1)$$

Where 'Q' is, the charge and 'V' is the voltage applied.

The capacitance of a conventional parallel plate capacitor is defined as equation (2),

$$C = \frac{\varepsilon_o \, \varepsilon_r A}{D} \qquad (2)$$

Where 'ε_o' is the dielectric constant of the free space; 'ε_r' is the dielectric constant of the

material, ‘A’ is the area of the electrode material and ‘D’ is the distance between the two electrodes. Capacitors are classified mainly into three; they are electrolytic, non-electrolytic, and supercapacitors[2].

Supercapacitors are generally known as ultra-capacitors which behave extremely differently from the existing conventional capacitors. Whereas conventional capacitors are made up of two metallic plates separated by a thick ceramic coating or plastic film. There is no dielectric region of this type in supercapacitors, instead a paper or other thin material soaked in an electrolyte act as a separator. Also, these are storing more energy per mass release and store more energy quickly. Supercapacitors have several advantages over traditional energy storage systems. The supercapacitor consists of a thin dielectric layer with high surface area and the porous nature enhances the storage ability[6]. These characteristics make supercapacitors highly applicable in variety of fields such as aviation, electronics, the medical sector and transportation and figure 1.2 illustrates the diverse applications of supercapacitors.

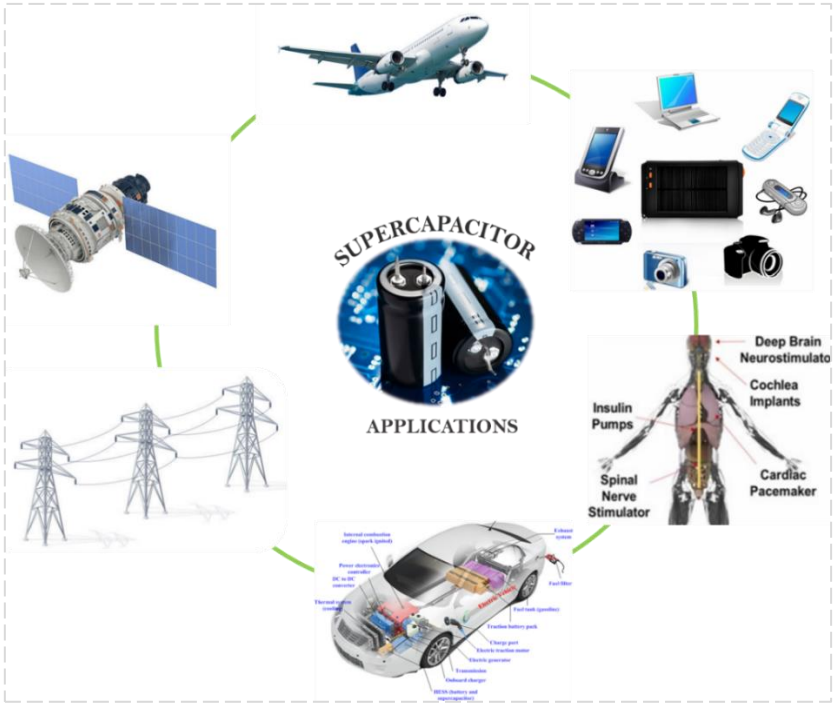

Figure 1.2 Illustration of various applications of supercapacitor*

Supercapacitors can be broadly classified into mainly three categories based on the mechanism of charge storage. These are electrical double layer, pseudocapacitive and hybrid capacitor. In electrical double layer capacitors (EDLCs), storage occurs non-faradically or statically. In pseudocapacitive systems, the energy is stored by faradic process, where redox reactions in the system responsible for the charge storage. The hybrid combines both EDLCs and pseudocapacitive mechanisms, depending on their specific arrangements.

The electrical double-layer mechanism belongs to the carbonaceous materials. It is possible to

achieve the goal of having an energy system that can store high energy and generate high output power by combining advanced materials possessing multifunctional properties with smart designs. Supercapacitor turns out to be one of the near-best alternatives compared to batteries. Supercapacitors are distinguishable from batteries due to their high-power density, and the ability to charge and discharge rapidly. So, this related application requires a high-power intake supply and delivery and pulsed energy[1,7 ,8]. The structure of a supercapacitor involves a cathode (positive electrode), anode (negative electrode), separator, and electrolyte mainly and available in different types based on various purpose and uses shown in figure 1.3. The separator between the electrodes is used to prevent an electric short circuit. The electrolyte inside the supercapacitor acts as an ion reservoir and is mainly classified into three. Which includes aqueous, organic, and ionic electrolytes. Applying an external bias, the electrons migrate from the negative electrode to the positive electrode. At the same time, the cations and anions move to positive and negative electrodes respectively due to generated driving force from the electric field between the two electrodes. The electrons move from the positive terminal through the external load to the negative terminal.

Figure 1.3 Supercapacitor arranged in different types based on their application and usage*

1.3 Classification of Supercapacitors

Electrochemical capacitors or supercapacitors or ultracapacitors are very attractive power sources for portable electronic systems. Supercapacitors are also used in automotive system. Due to its high specific power, surface area, stability, and long durability, it serves as a power source by itself or in combination with other systems or devices.

The energy density of the supercapacitor is several times higher than that of the conventional capacitors. The energy density and power density are related to the embedded charge storage mechanism in each system. Mainly two mechanisms, electric double layer and pseudocapacitive, were responsible for the storage capacity of the supercapacitor [6]. The main

classification based on the charge storage is shown in figure 1.4.

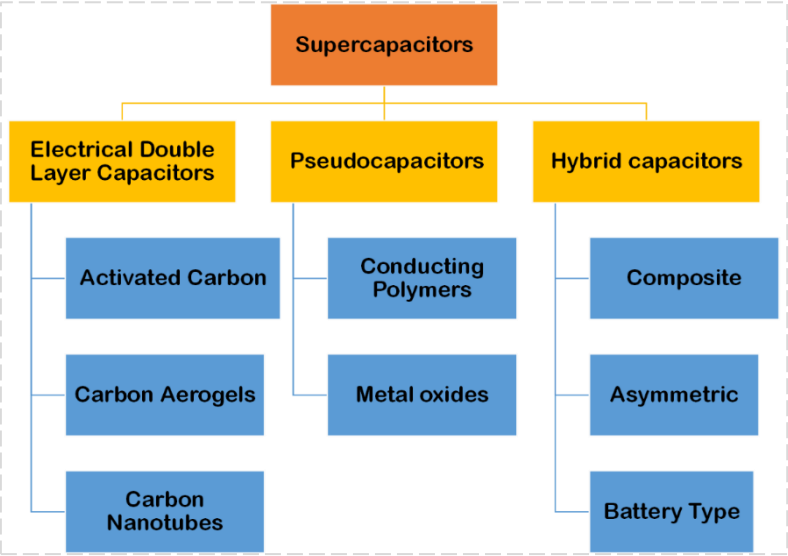

Figure 1.4. The main classification of supercapacitors based on the energy storage mechanism

1.3.1 Electric Double Layer Capacitance Mechanism

The basic principle underlying in this mechanism is the adsorption of ions at the electrode surface. Which is similar to the working mechanism of the dielectric capacitor. The basic concept in theoretical electrochemistry like the Gouy-Chapman-Stern theory explains the formation of double layers by the polarization at the electrode-electrolyte interface. The electrostatic potential and the decay of the ionic charge distribution occur at the Debye length of 1-10 nm range. The double layer of the electrode material stores the charge by a true capacitance effect i.e., without any charge transfer at the electrode-electrolyte interface. The surface charge generation takes place by the dissociation of the surface atoms and adsorbed-ions from the electrolyte and crystal defects of the electrode material used. The excess or deficiency of charge generation leads to electroneutrality at the electrode-electrolyte interface. The thickness of the double layer is affected by the concentration and ionic size and is approximately 5-10 A^{o} for highly concentrated electrolytes[7].

There are different double-layer models introduced. Among these Helmholtz's model of charge storage states that two layers of opposite charges are simultaneously formed at the electrode-electrolyte interface and their separation is equal to atomic distance. Further modification done in the Helmholtz model done by Gouy and Chapman, introduces the diffusion layer concept that a continuous charge distribution layer is formed along the electrolyte layer. In this concept, the electric double-layer, capacitance formed is inversely proportional to the separation distances. So, there is a probability to get high specific capacitance at the electrode's outer surface. A further modification was put forward by Stern who combine the Helmholtz model

and the Gouy-Chapman model. The stern layer is introduced in this concept, and the ions sturdily adhered to the electrode. The factor determining the EDLC is the binary layer formed at the electrode-electrolyte interface, which is smaller compared to the thickness of the separator between the two electrodes[1].

The structure of the EDLC contains two electrodes differentiated with a separator and a suitable electrolyte given in Figure 1.5. The separator should be an ion-permeable membrane. The principle behind the EDLC is the formation of the electrical double layer to store energy. When voltage is applied, charges get accumulated on the surface of the two electrodes. The ions of the electrolyte diffuse through the membrane and reach the electrode surface. This will create a double-layer charge on the electrode surface. The EDLC consists of two capacitors, but each electrode will be a single capacitor. If these are connected in a series fashion, the total capacitance C can be calculated by using the equation (3).

$$C = \frac{C_1 \times C_2}{C_1 + C_2} \qquad (3)$$

C_1 and C_2 are the capacitance of individual capacitors. The capacitance measured is using equation (4)

$$C = \frac{A \times \varepsilon_o}{d} \qquad (4)$$

Where 'C' is capacitance in Farad, 'A' is surface area, 'd' is the Debye length, and 'ε_o' is the permittivity of the free space. The electrostatic attraction between the ions at the electrode and electrolyte is responsible for energy storage[7,8].

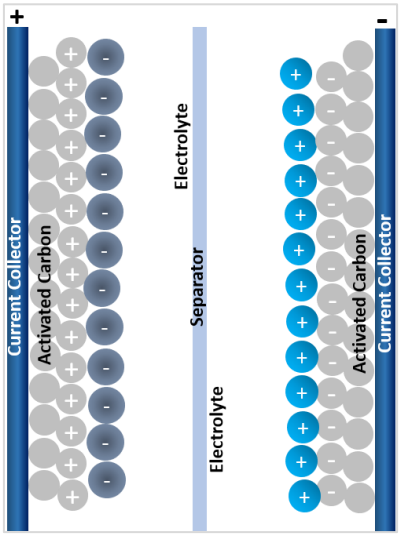

Figure 1.5. Structure of EDLC supercapacitor

1.3.2 Faradic or Pseudocapacitive Storage Mechanism

It is completely non-electrostatic and capacitance is contributed by faradic reactions at the

electrode-electrolyte interface. The charge transfer between the electrode and electrolyte leads to higher energy density than EDLC. By applying a suitable potential, the faradic current is generated from electro-sorption or redox reactions from the pseudocapacitive materials like metal oxide or conducting polymers. Due to the occurrence of redox reactions, the pseudocapacitor has a shorter life cycle and power density and the schematic representation is given in figure 1.6.

The voltammetric response of active material peak current at varying sweep rates is given by equation (5)

$$i = av^b \qquad (5)$$

'i' is the current at a fixed potential of sweep rate (*v*), where $i = nFAC * D^{0.5} v^{0.5} (\alpha nF/RT)^{0.5} \pi^{0.5} \chi(bt)$. The a and b are adjustable parameters, if b value is 1 denote the capacitive process whereas b value is 0.5 denotes the current is controlled by diffusion limited process.

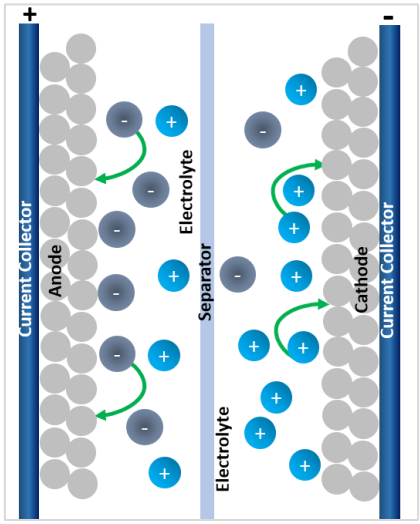

Figure 1.6. Structure of pseudocapacitor

In case of pseudo capacitance, the capacitance is due to reversible faradic reduction and charge separation. Along with the reversible redox reaction the intercalation and electro-sorption on the electrode surface are responsible for the pseudo capacitance. The energy densities of devices based on pseudo-capacitance are greater than those on electrical double-layer capacitance. The phase changes in the pseudo-capacitance materials limit their lifetime and power densities due to the faradic reaction. In EDLC phase changes are not observed and have a long lifetime. There are two electrode materials to store charge in pseudocapacitors. One is conducting polymer and the other is a metal oxide. The common conducting polymers used are polyaniline, polythiophene, polypyrrole, poly (3,4-ethylene dioxythiophene) (PEDOT), and other π-conjugated conducting polymers. Sometimes these materials exhibit specific

capacitance greater than that of the metal oxides[9].

Metal oxides like manganese oxide, ruthenium oxide, iron oxide, nickel oxide, etc. are used as electrode materials. Conducting polymer shows high capacity and conductivity but low cost compared to carbon-based electrode materials. Metal oxides are also conductive so it will improve the performance of the capacitor. Ruthenium oxide is the most explored metal oxide and gives a good result. In some cases, its performance is greater than that of EDLC and conductive polymers. The performance of the supercapacitor can be increased by combining the mechanism of the EDLC and pseudocapacitors; this will generate the third class of the supercapacitor known as the hybrid supercapacitor[5].

1.3.3 Hybrid Supercapacitors

Hybrid supercapacitors consist of the mechanism of both EDLC and pseudocapacitors. It is also known as the asymmetric capacitor. It contains asymmetric electrodes, one electrode contains EDLC and the second one will follow pseudocapacitance. Hybrid supercapacitors exploit the faradic and non–faradic processes. Here the faradic electrode is responsible for energy storage and non–faradic or capacitive electrodes enable power storage and depicted in figure 1.7. According to the electrode configuration hybrid supercapacitors are classified into three[8] and these are (a) composite, (b) asymmetric, and (c) battery types given in figure 1.8.

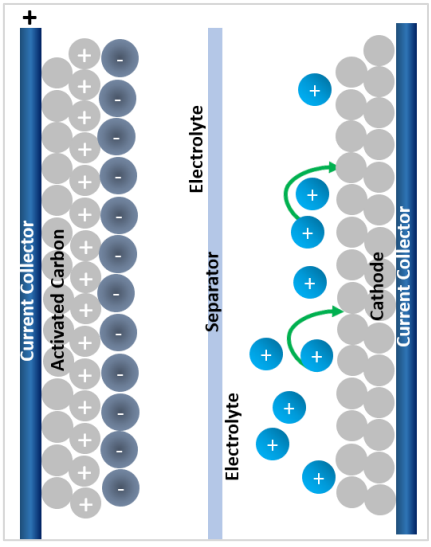

Figure 1.7 Schematic Representation of hybrid supercapacitor

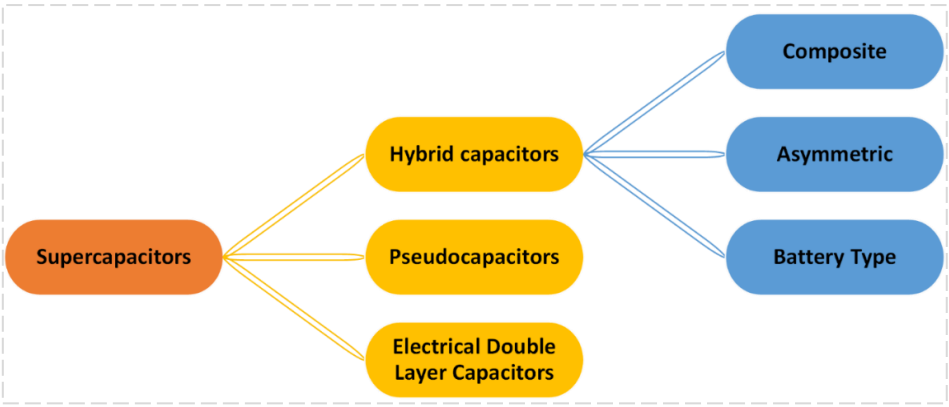

Figure 1.8 Classification of hybrid supercapacitor based on electrode configuration

1.3.3.1 Composite Electrodes

Composite hybrid electrode contains both carbon-based material and metal oxide or a conductive polymer. It incorporates both EDLC and pseudocapacitance in a single electrode for charge storage. The carbon-based material provides an electrical double-layer charge, a non–faradic mechanism workout in this type. Also, it provides a high surface area, which is an important factor in charge storage it increases the capacitance. Whereas the metal oxide component contributes the faradic mechanism of the pseudocapacitance that facilitates enhancement in total specific capacitance.

1.3.3.2 Asymmetric Electrodes

An asymmetric hybrid capacitor is formed by the coupling of the two types of electrodes such as EDLC and pseudocapacitance. The coupling of the carbon-based negative electrode and conducting polymer-based positive electrode. Generally, the conducting polymer-based electrode has lower resistance than carbon-based electrodes. Asymmetric hybrid supercapacitors can achieve high energy and power density with comparable electrical double-layer capacitors. It shows high cyclic stability compared with normal pseudocapacitors.

1.3.3.3 Battery Type Electrodes

The structure of battery-type supercapacitors is also similar to that of asymmetric hybrid capacitors. Two different electrodes are coupled with each other in these types of supercapacitors. That is a supercapacitor electrode combined with a battery-type electrode. It is the combination of the high-energy batteries, high power, and cyclic stability of supercapacitors. Carbon-based materials are widely used for supercapacitor applications[10]. In the present work, the carbon-based material to be selected is graphene. This is derived from graphite; it is one of the allotropes of carbon.

1.4 Designing of Supercapacitor

The components of supercapacitors are similar to conventional systems it contains (a) current

collector, (b) active electrode material, (c) electrolyte, (d) separator, and (e) sealants as shown in figure 1.9. The basic form of the supercapacitor consists of two identical electrodes, which are sandwiched using the electrolytes and separator.

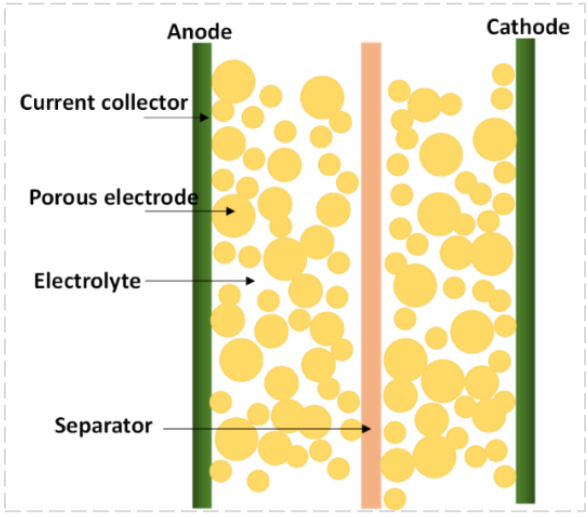

Figure 1.9 Schematic representation of supercapacitor components

1.4.1 Current Collectors

It's a transporting medium of current from an external source to electrode material. It is capable to charge and discharge and withstand the heat generated inside the cell. The material should resist chemical corrosion due to electrolytes and commonly available current collectors are shown in figure 1.10. The active material makes better contact with the current collector and minimizes the resistance while experimenting. The current collectors withstand long-term charge-discharge cycling tests. The common current collectors used are aluminum sheets, iron, stainless steel sheets, nickel foam, nickel mesh, carbon cloth, etc. To tackle the adhesion problem of active material, polymer binders like Nafion, polytetrafluoroethylene, polyvinylidene fluoride, carboxy methyl cellulose, etc are used.

Figure 1.10 Images of various commercially available current collectors for supercapacitor fabrication like nickel foam, copper sheet, carbon cloth, graphitic plate, stainless steel and glassy carbon electrode*

1.4.2 Electrolyte

Electrolytes play an inevitable role in supercapacitor applications. The operating potential window varies with the nature of the electrolyte. The electrolyte is classified mainly into aqueous, organic, and ionic liquids and depicted in figure 1.11. The square nature of the voltage window depends on the ionic resistivity and has an inverse correlation. Also, the energy density and power density are directly proportional to voltage window and electrolyte conductivity. The electrolyte functions as a conductive medium and acts as a route for dissociation. The factors which affect the performance of the electrolyte are the adsorption rate of the anion and cation, formation of a double layer, equivalent series resistance, and conductivity of the electrolyte. To perform in a better way the extent of the contact between electrode and electrolyte is to attain maximum surface. The concentration of the electrolyte is depending upon the degree of dissociation 'α'.

The aqueous electrolyte belongs the different pHs like acid, neutral, and alkaline. HCl, H_2SO_4, NaCl, Na_2SO_4, KNO_3, KCl, KOH, NaOH, etc belongs to these categories. The enhancement in specific capacitance probability is high in aqueous electrolytes. The ionic conductivity is very high compared to other types and is low cost and abundance. The restriction arises due to the 0 V-1.2 V of voltage window and further increment leads to the decomposition of the water and thus collapses the working of the cell.

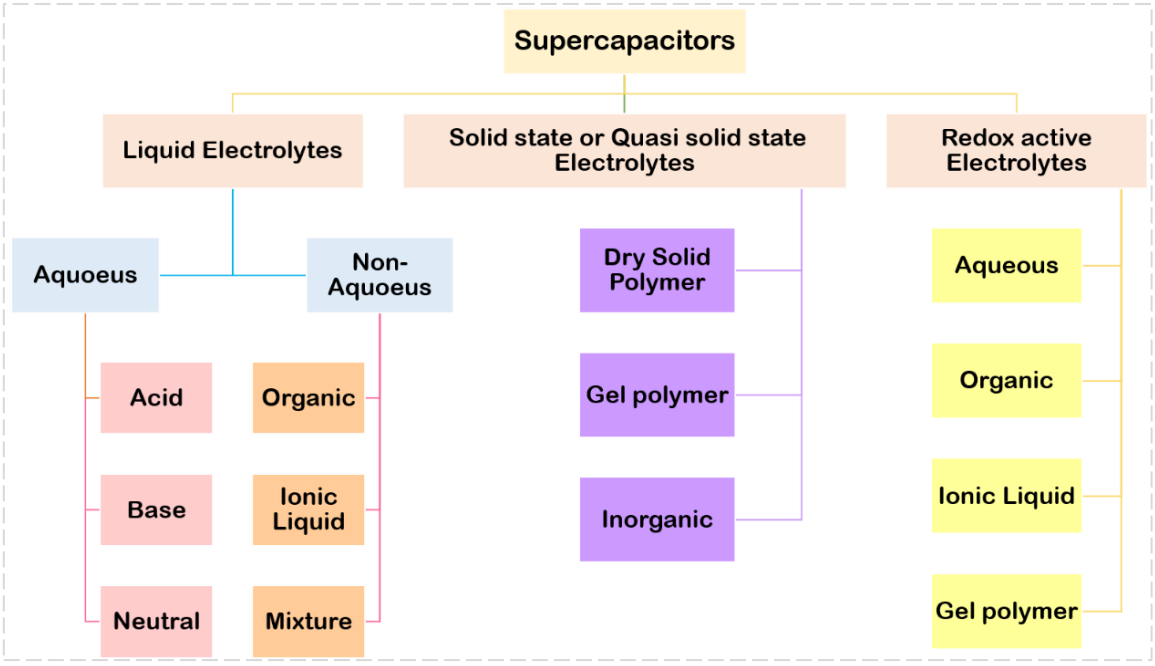

Figure 1.11. Classification of electrolytes in supercapacitor application

The higher potential window of 0 V- 2.7 V suggests organic electrolyte is better than aqueous one. A higher operating potential window enhances the specific capacitance of the cell. The

energy density considerably lifts due to the wider operating voltage window than that of an aqueous one. The most commonly used organic electrolyte are acetonitrile and propylene carbonate. However, the toxicity and highly flammable nature resists its use though it has lower ionic resistivity.

In the case of ionic liquids, they are inflammable and non-toxic. The operating voltage window of ionic liquids is 0 V- 5 V. It is a liquid form of solvent-free molten salts, the insufficient ionic conductivity, compared to the organic and aqueous electrolyte, is due to the presence of large ions in ionic liquids[1].

1.4.3 Separator

It is an inevitable part and functions as a barrier between two electrodes and also avoids short circuits. The material should be non-conductive, easily wettable, induce minimum ionic resistance, less intrinsic resistance due to the chemicals used, and resist the volume and pressure change. The commonly used separators are paper, glass ceramics, polymers like polyethylene, propylene carbonate, polyamide, polyvinylidene fluoride polypropylene, etc, and a few of them are shown in figure 1.12. The other required features are it should be low cost, abundant, have mechanical strength, and chemical resistance. These have a role in determining the specific capacitance.

Figure 1.12 Commercially available separators for the fabrication of supercapacitors*

1.4.4 Sealants

It is a material used to prevent the escape of a substance from inside the cell. In a supercapacitor, it acts as a protective shield for the electrodes and prevents the leakage of electrolytes. These block from the outside contaminants like water, chemicals air, etc, and other factors which causes the degradation of electrolyte. The proper sealing condition is always a hemetic seal which prevents water and gas in the cell. There are various types of sealants can be used. Silicone, epoxy, and polyurethane[2]. The choice of sealants depends on the factors such as the type of electrolyte used, the operating conditions of the supercapacitor, and the desired level of protection.

1.5. Active Electrode Materials

Active materials exist in numerous numbers so it is broadly classified into three EDLCs, pseudo and hybrid. The EDLC materials are generally carbon-based materials with high surface area. pseudocapacitive material belongs to metal oxide and conducting polymer[11]. Other materials like metal nitride, sulfides, chalcogenides, and carbides are also belonging to this class and are categorized in figure 1.13. The hybrid materials are the combination of the above two which include carbon-metal oxide-composite, redox asymmetric and battery-capacitor combination, etc.

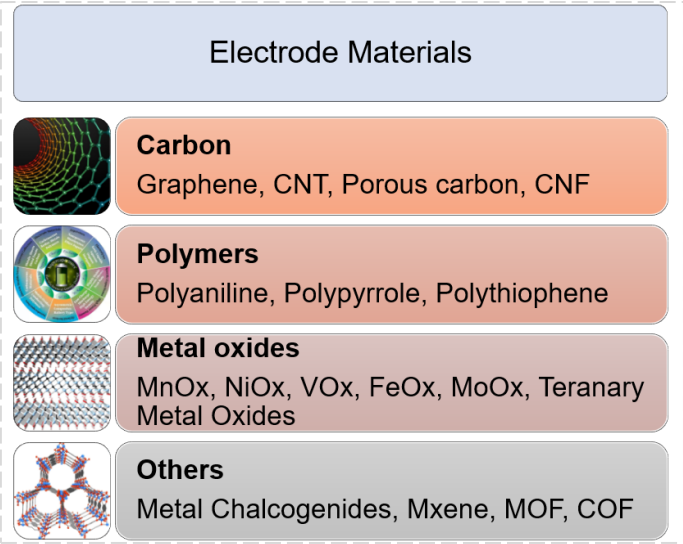

Figure 1.13 Different types of electrode material used in supercapacitor*

1.5.1 Metal oxides

Metal oxides act as an alternative in supercapacitor electrode material, due to the high specific capacitance and specific power transition. Considering transition metal oxides, Ruthenium oxide (RuO_2) exhibit high theoretical specific capacitance in the range of ~1300 F/g. Even though RuO_2 has high theoretical capacitance its use is reduced due to the high cost and toxicity as well as its limited availability. Searching for low-cost, conducting material ended up with other transition materials like Fe_2O_3, TiO_2, MnO_2, Co_3O_4, SnO_2, VO_2, V_2O_5, etc. Considering these materials MnO_2 has a theoretical specific capacitance close to the RuO_2 and fulfilling the conditions like low cost, conductivity, and ease of availability. Other transition metal oxides show supercapacitive properties and can be enhanced by making composites with other metal oxide or carbonaceous materials[7].

1.5.1.1 Manganese Oxide (MnO_2)

Manganese oxide has enough natural abundance without any toxic effects. The satisfactory specific capacitance of MnO_2 made it as a promising candidate. The charge storage mechanism

in MnO_2 has mainly based on redox reaction-based pseudocapacitive nature and the charge storage mechanism is represented in an equation (6) below.

$$MnO_2 + xA^+ + yH^+ + (x+y)e^- \leftrightarrow MnOOA_xH_y \qquad (6)$$

MnO_2 is regarded as a viable candidate for electrode material in electrochemical capacitors due to its low cost, non-toxicity, abundance, straightforward and simple synthesis, environmental friendliness, and strong theoretical specific capacitance, i.e between 1100 F/g to 1300 F/g [12,13]. Goodenough and Lee[14] did extensive research on this and published the first report on the MnO_2 pseudocapacitor behavior in 1999. They assess MnO_2's pseudo-capacitive behavior in a 2M KCl aqueous electrolyte solution. MnO_2 micro-powders and micrometer-thick films exhibit 150 F/g in neutral aqueous electrolyte solutions with a voltage window of 1V, taking into account its energy storage properties. In comparison with other metal oxides, RuO_2 [15] exhibits higher theoretical specific capacitance. Even though crystalline MnO_2 exists in various crystal structures, like α, β, γ, and δ depicted in figure 1.14, based on their preparation methods [16,17]. Depending on the method of preparation, different phase formations lead to variations in specific capacitances. The specific capacitance of the electrode material is determined by factors such as specific surface area, morphology, thickness, mass of the electrode coating, and type and nature of the electrolyte.

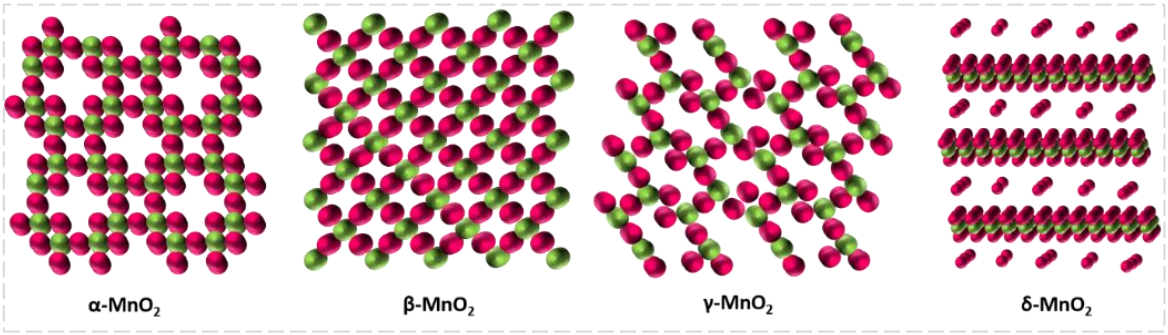

Figure 1.14 Different crystalline phases of Manganese dioxide

Considering a few results of MnO_2, in an aqueous neutral electrolyte solution, α-MnO_2 shows specific capacitance ranging from 265 F/g to 320 F/g [18]. When compared to the other crystalline phases of MnO_2 like β, γ, and δ [17], the δ-MnO_2 has higher capacitive nature due to its layered structure, which is similar to graphene[19]. One of the most important elements in determining the specific capacitance of a synthesized material is its morphology. For MnO_2, different morphologies, such as nanosheets, nanoflowers, nanowires, nanobelts, nanoneedles, nanowhiskers, and nanospheres[13] are possible. Its unique surface area, which is between 20 m^2/g and 150 m^2/g, also influences the performance. The large specific surface area of MnO_2 shortens the transport or diffusion path lengths [20,21] for both ions and electrons, resulting in

faster kinetics and thus higher charge-discharge capacities. As a result, nanowires on smaller diameter electrodes have a higher specific capacitance (350 F/g) than nanorods (243 F/g) [21]. To improve and promote electrical conductivities, create a carbon composite or dope it with another suitable material or create some anionic and cationic vacancies. When it comes to carbon composites with MnO_2, pure MnO_2 in composites with activated carbon, graphene, CNTs, and other materials provides better results. With the aqueous neutral electrolyte, MnO_2 composites with CNT gives 700 F/g in a total potential window of 1V [22]. Similarly, doping some transition metal oxides such as Ni, Co, and Fe makes them better. For instance, the Co-doped MnO_2 exhibits a specific capacitance of 377 F/g [23]. Making some vacancies in the action, such as oxygen or metal ion vacancies, is another method of enhancing the performance of MnO_2. The presence of vacancies or defects improves the activity of oxide systems. Chen et al. note this improvement in α-MnO_2, which after chemical preparation has a high capacitance of 736.60 F/g and a specific surface area of 119.50 m^2/g [24]. Yang et al. chemically prepared doped MnO_2 with various cations, such as Cu^{2+}, Co^{2+}, and Ni^{2+} ions [23]. The induced defect in the crystalline systems causes the doping with metal ions to alter the intrinsic conducting properties. When compared to the other two metal cations, the Ni^{2+} doped MnO_2 measured with a high specific capacitance of 234 F/g at 8 A/g. In δ-MnO_2 prepared by electrostatic self-assembly, Gao et al. introduce surface Frenkel defects involving metal ion vacancy, which result in nanosheets with porous morphology and specific surface areas of 150 m^2/g with specific capacitances of 306 F/g at 0.2 A/g [25]. The defect-induced MnO_2 materials are used for optical and catalytic studies in addition to supercapacitor research. Reenu et al. investigated the optical properties of coprecipitated and hydrothermally synthesized α-MnO_2 that contained Mn vacancies. The effect of surface defects on the system is well-studied using photoluminescence spectroscopy [26]. In another case, MnO_2 with a surface oxygen vacancy that is active toward the catalytic combustion activity of o-xylene was created by Wu et al. using a wet chemical method [27].

1.5.1.2 Vanadium Oxide (VO_x)

Vanadium exists as a partially filled 3d orbital in electronic configuration, which leads to different oxides such as VO, V_2O_5, V_2O_3, VO_2, V_4O_7, V_6O_{13}, etc. These variety of vanadium oxides are classifieds into different series like Magneli ($V_n O_{2n-1}$) and Wadsley ($V_{2n} O_{5n-2}$). It is a well-studied system because of its first-order reversible phase transition from the semiconductor to the metallic state at its critical points of 68 ^oC. This transformation alters the electronic structure as well as the optical properties of vanadium oxide.

VO_2 exists in a rutile hexagonal structure above the transition temperature and below its

transition temperature exist as the monoclinic system. This is where the metal-to-semiconductor conversion is taking place and is in an invertible transition state. Vanadium dioxide is a significant binary compound, it exists in five crystalline phases, the most stable of which are rutile type VO_2(R), as well as monoclinic VO_2(M), metastable VO_2(B), tetragonal VO_2(A) and VO_2(C) and few of them are shown in figure 1.15.

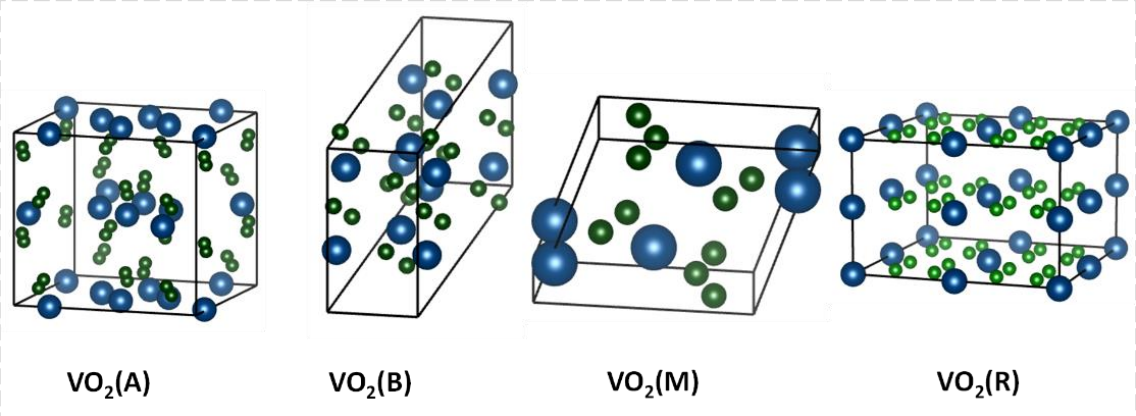

Figure 1.15 Crystalline structures of different polymorphic phases of vanadium dioxides

From the previous literature it is known that, the VO_2(R) and VO_2(M) exhibit fully reversible metal-semiconductor phase transitions (MST) at the critical temperature of 68 ^oC. Meantime, there is a clear transformation in the electrical resistivity and optical transmittance of magnitude around 10^4-10^5. Among previously mentioned phases, VO_2(A) is a meta-stable phase and possess a three-dimensional network of VO_6 octahedron. The VO_2(B) is a metallic phase consisting of distorted octahedrons which share corners and edges. VO_2(B) is one of the promising cathode materials in Li-ion batteries as well as supercapacitors due to its reversible structural switch between crystalline and amorphous phases under high pressure[28]. Among other metal oxides vanadium oxides shows theoretical capacitance of 1000 F/g -2000 F/g. The few literature reports of vanadium oxides as supercapacitor application are given. Chen et al studied VO_2@CC give 78.8 at 10 A/g at 1.65V in aqueous electrolyte system. Lv et al prepared VO_2 nanobelt/reduced graphene oxide composite for flexible supercapacitor gives 353 F/g at 1A/g. Zhang et al prepared VO_2 (B) hollow spheres and solid spheres provide specific capacitance of 336 F/g and 272 F/g at 2 mA/cm^2 respectively. Ren et al prepared VO_2 nanoparticle on edge-oriented graphene foam. The areal capacitance of 119 mF/cm^2 obtained for VO_2/EOGF (edge-oriented graphene foam) in supercapacitor application and 144 mAhg^{-1} at 20 A/g for Li-ion battery studies.

Numerous synthesis methods, including Pulsed Laser Ablation, Magnetron Sputtering, Chemical Vapour Deposition, Sol-Gel synthesis, Wet Chemical methods, Thermolysis, and Hydrothermal synthesis, are used to produce VO_2(B). Hydrothermal synthesis is one of the

better options because of its lower temperature, green reaction conditions, simplicity of operation, and low cost. Furthermore, morphology and porosity tuning can be accomplished by varying surfactants, templates, and solvents[28].

The monoclinic VO_2(B) was first explored for the Li^+ intercalation in the reversible electrochemical reaction. The VO_2(B) of various nanostructures, such as 0D, 1D nanobelts, nanorods, nanotubes and nanobelts, 2D nanosheets, nanowires, nanobelts, and 3D nanoflowers, is achievable with different synthesis selection and reaction circumstances[28,29].

1.5.2 Ternary Metal Oxide

Recently, there has been extensive exploration of advanced functional materials to meet the urgent need for faster and more efficient energy storage systems. Among the various electrode materials, ternary metal oxides have garnered significant attention due to their low cost, environmental benignity, multiple oxidation states, and high theoretical specific capacitance. Ternary metal oxides exist in different forms such as AB_2O_4, $ABO_{2/3/4}$, and $A_3B_2O_8$, with a general formula of $A_xB_yO_2$. The ternary or metal oxide systems ($A_xB_yO_x$) are generated by the addition of an extra metal ion to the binary metal oxide system. The combination of these metals enhances the conductivity of all systems. In a ternary metal oxide, both metal elements have lower and higher oxidation states. One of the cations in the binary metal oxide was replaced/ doped/substituted/ exchanged to form ternary systems. For example, combinations of metal ions like Zn, Ni, Cu, Co, Mn, Fe etc. Ternary metal oxides can exhibit various morphologies, including 0D, 1D, 2D and 3D nanostructures. These materials can be synthesized using a variety of methods, such as chemical precipitation, sol gel synthesis, electrodeposition, molten salt, hot injection, electrospinning, hydrothermal and solvothermal techniques. The properties like surface area, ionic conductivity, electronic conductivity, mechanical conductivity and chemical stability make ternary oxide as a good candidate for energy storage application.

Ternary metal oxide-based supercapacitor studies are seen in the literature, Perera et al reported Co_3 Mn_x O_4 material, exhibit 173.6 F/g. Wang et al reported a simple ion-adsorption-annealing method for porous $ZnCo_2O_4$ shows exhibit remarkable specific capacitance. Li et al reported multi-shelled hollow microspheres $NiCo_xO_x$ shows high specific capacitance of 1884 F/g at 3 A/g with excellent rate capability. Ishaq et al studied the $MeFe_2O_4$/RGO with polypyrrole shows specific capacitance of 232 F/g. These studies demonstrate that the ternary metal composites exhibiting superior energy storage properties.

1.5.3 Carbon-Based Materials

Carbon-based materials are the most commonly used electrode material for electric double

layer capacitors (EDLCs) due to their electrical conductivity, chemical stability, high specific surface area. These materials are existed in a variety of shapes and sizes. The commonly used carbon electrodes include carbon nanofiber[30], carbon spheres[31], carbon nano-onions[32], carbon hydrogel[33], carbon nanotubes[34], graphene[34], activated carbons[35], graphite and highly porous carbon, details given in figure 1.16. This thesis focuses on studying the electrochemical activity of porous carbon (or activated carbon derived from biomass sources), graphene and carbon nanofiber in a supercapacitor structure.

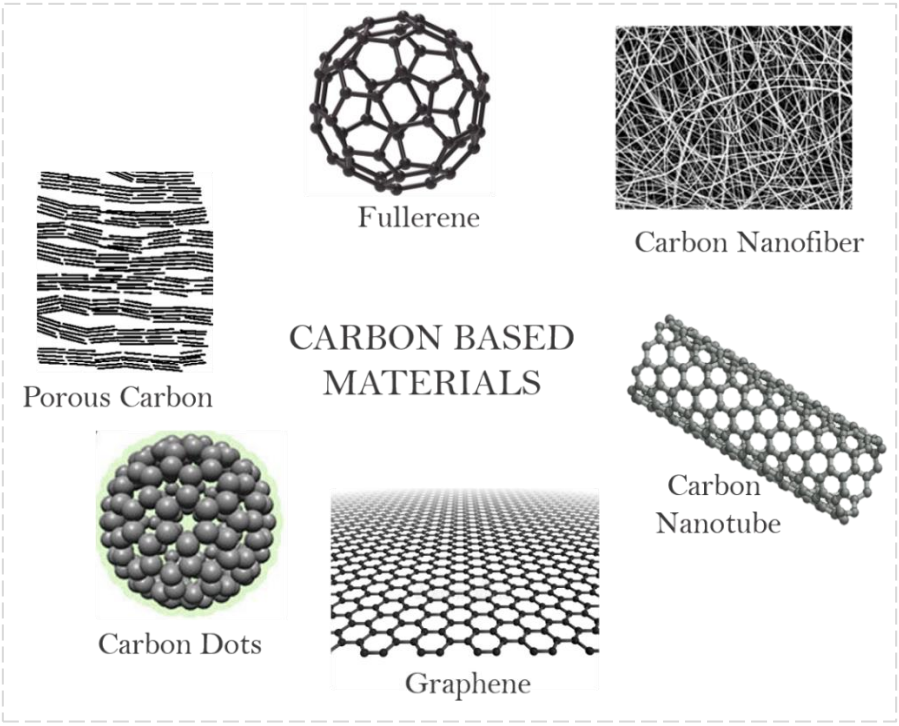

Figure 1.16 Various carbon-based materials in energy storage applications*

Porous carbon has properties such as high specific surface area, conductivity, tunable porosity, chemical stability, and long shelf life, making it an attractive choice to be an electrode material in supercapacitors and other energy storage systems. There are various sources from which activated carbon can be produced using a variety of techniques[36–39]. Porous carbon can be synthesized from agricultural waste materials like different parts of the plants like, leaf, root, stem, flower, husk, bark, peel, shell, etc and such formed carbon is known as biomass derived carbon. These biowastes include or are composed of compounds like starch, protein, sugar, hydrocarbons, cellulose, hemicellulose, water, lipids, lignin, and several other functional groups. The advantages of biomass-derived carbon are depicted in figure 1.17. The porous carbon preparation from biomass mainly carried out through activation and pyrolysis step, where the activation method includes chemical as well as physical methods.

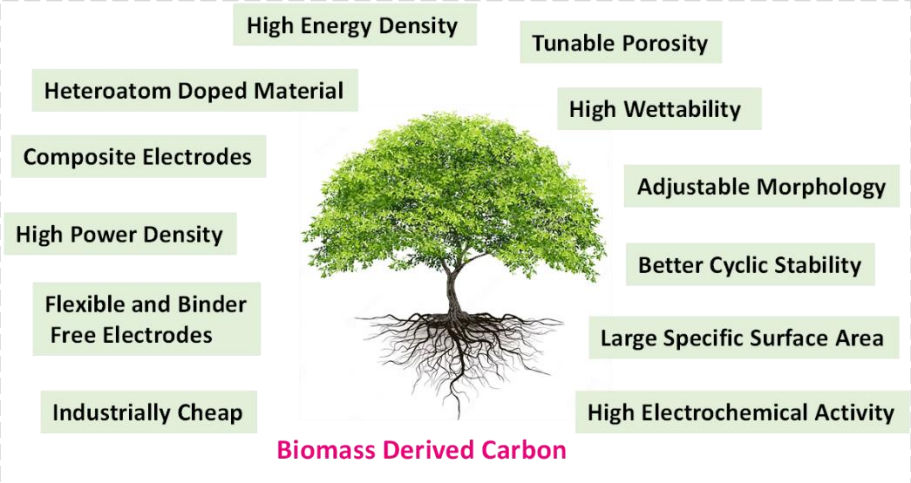

Figure 1.17 Advantages of biomass-derived carbon in energy storage*

In the physical activation method, the activating gas causes the formation of pores. The gases used are steam, carbon dioxide, hydrogen, nitrogen, air, or a combination of these[40]. In chemical activation, the raw material impregnated with activating a strong oxidizing agent or strong dehydrating agent under an inert atmosphere generated porous nature to the material. These activating components are also known as porosity-enhancing agents (PEA), which fall into the categories of acid, base, and neutral. The classification of the porosity-enhancing activating agents is listed in Table 1.1. This allows the raw material to be penetrated, subjected to additional thermal processing, and produce high specific surface area. The porosity will aid in the rapid passage of electrolyte ions into the pores.

Reagents	**Examples**
Acidic	H_3PO_4, H_2SO_4
Basic	KOH, $NaOH$, K_2CO_3, Na_2CO_3
Metal salt	$ZnCl_2$, $AlCl_3$

Table 1.1 Porosity enhancing activating agents with examples

Graphene is two-dimensional material of a single layer of carbon hexagons consisting of sp^2 hybridized carbon bonds including π-bonding or electron clouds. They have interesting physical and chemical properties with promising applications. The unique properties like high mechanical strength, fast electron transport, good biocompatibility and high surface area make graphene more application-oriented. It consists of honeycomb lattice and it possesses van der Waals interactions, which may lead to wrinkling and restacking. The importance of graphene in supercapacitors is to have optimum porosity and pore size distribution that give access to

the electrolyte more easily[41]. Various methods exist for the synthesis of graphene like, thermal exfoliation, Hummer's method, green synthesis, etc. According to the synthesis technique the properties are varied.

The carbon nanofiber is a promising electrode material in supercapacitor application due to their unique properties. It exhibits high electrical conductivity, mechanical stability, surface area and chemical stability. The carbon nanofibers are easily formed by electrospinning technique. Based on the precursors used, experimental conditions, viscosity, applied voltage etc, the carbon nanofibers show various properties and morphologies. Also, its high aspect ratio, interconnected network structure, better ion transport and high specific surface area make it a better candidate for energy storage. In addition to that, controlled synthesis process with tunable porosities and surface functionalities enhances its electrochemical properties. The carbon-based materials mentioned above exhibit exciting conducting properties, making them a suitable candidate for energy storage applications.

1.6 Objective and Scope of the Work

This research focuses on various electrode materials used for supercapacitor applications, specifically investigating surface-tuned binary and ternary metal oxides, as well as carbon nanostructures, which exhibit pseudocapacitive and electric double-layer mechanisms respectively. Binary metal oxide like Vanadium oxide-VO_2(B) and Manganese oxide- δ-MnO_2 will be used because they are readily available and exhibit excellent electrochemical characteristics. A novel ternary metal oxide, Zinc tellurium oxide -$Zn_2Te_3O_8$, as electrode material will be checked for the performance efficiency. The carbon nanostructures like carbon nanofibers and highly porous carbon derived from natural sources also will be investigated.

Chemical approaches like sol-gel and hydrothermal methods are adopting for the synthesis of binary (VO_2(B) and δ-MnO_2) and ternary metal oxide ($Zn_2Te_3O_8$). Optimization of morphology of VO_2(B) will be controlled hydrothermally at different temperatures and by adding graphene oxide during synthesis, its graphene hybrids can be prepared, to increase the electrochemical activity. Morphological variations, surface area, porosity, and electrochemical characteristics will also be investigated. Vacancy tailoring can be achieved in δ-MnO_2 by sol-gel method to improve electrochemical characteristics. Two reducing agents like citric acid and ammonium oxalate are chosen to tailor the defect density in δ-MnO_2. Properties like surface area, porosity and conductivity can be further controlled by changing the heating environment and annealing rate. The solvothermal approach will be used to synthesize ternary metal oxide $Zn_2Te_3O_8$ and its reduced graphene oxide hybrids. Three different hybrids, prepared by altering the volume

of graphene oxide will be used as electrode material for super capacitor application. The changes in surface area, porosity, and electrochemical characteristics are correlated.

This work proposes to prepare various carbon-based materials by adopting different synthetic approaches. Carbon nanofibers can be prepared by electrospinning of Poly Acrylo Nitrile (PAN). Carbon nanofibers with different diameters are planned to be prepared by altering the annealing temperature to 500 °C, 700 °C, and 900 °C. In addition, highly porous carbon materials can be prepared readily from available biomass sources (Saw dust-*Ailanthus Triphysa* and leaf-*Palmyra Palm*) followed by $ZnCl_2$ activation and carbonization. Physical property tuning of the carbon nanostructures can be achieved by changing carbon: $ZnCl_2$ mass ratio as 1:0, 1:2, 1:4, and 1:6.

The physicochemical properties of the prepared electrode materials are planned to be studied using various methods. X-ray Diffraction (XRD), Raman spectroscopy, and X-ray photoelectron spectroscopy (XPS) will be used to characterize the structure and chemical composition. Fourier Transform Infrared spectrometer (FTIR) will be used analyse Chemical structure and functional groups. Morphology can be obtained from field emission scanning electron microscopy (FE-SEM) analysis. BET (Brunauer Emmet Teller) analysis is used to determine surface area and porosity. Wettability analysis will be carried out by contact angle measurement. Electrochemical analysis, such as cyclic voltammetry (CV), galvanostatic charge-discharge analysis (GCD), electrochemical impedance analysis (EIS), and cyclic stability tests, are used to investigate supercapacitor applications. Symmetric and asymmetric supercapacitors will be prepared with synthesized materials with an aqueous neutral electrolyte (Sodium Sluphate-Na_2SO_4). The carbon materials are also examined with a redox additive electrolyte, which is made by adding potassium iodide (KI) into the sodium sulphate.

*****

Reference

[1] C. Zhao, W. Zheng, *Front. Energy Res.* 2015, *3*, DOI 10.3389/fenrg.2015.00023.
[2] A. Muzaffar, M. B. Ahamed, K. Deshmukh, J. Thirumalai, *Renewable and Sustainable Energy Reviews* 2019, *101*, 123–145.
[3] N. A. Elessawy, J. El Nady, W. Wazeer, A. B. Kashyout, *Sci Rep* 2019, *9*, 1129.
[4] N. G.J., P. S.R, M. A.M., B. S.M., D. T.D., *ES Energy Environ.* 2022, DOI 10.30919/esee8c739.
[5] A. González, E. Goikolea, J. A. Barrena, R. Mysyk, *Renewable and Sustainable Energy Reviews* 2016, *58*, 1189–1206.
[6] S.E. Chun, B. Evanko, X. Wang, D. Vonlanthen, X. Ji, G. D. Stucky, S. W. Boettcher, *Nat Commun* 2015, *6*, 7818.
[7] N. I. Jalal, R. I. Ibrahim, M. K. Oudah, *J. Phys.: Conf. Ser.* 2021, *1973*, 012015.
[8] N. Kumar, S.B. Kim, S.Y. Lee, S.J. Park, *Nanomaterials* 2022, *12*, 3708.
[9] M. Graczyk-Zajac, G. Trykowski, M. Wilamowska-Zawłocka, *Electrochimica Acta* 2021, *383*, 138356.
[10] A. Eftekhari, *J. Mater. Chem. A* 2018, *6*, 2866–2876.
[11] P. K. Panda, A. Grigoriev, Y. K. Mishra, R. Ahuja, *Nanoscale Adv.* 2020, *2*, 70–108.
[12] H. Peng, H. Fan, J. Sui, C. Wang, W. Zhang, W. Wang, *ChemistrySelect* 2020, *5*, 869–874.
[13] M. Huang, F. Li, F. Dong, Y. X. Zhang, L. L. Zhang, *Journal of Materials Chemistry A* 2015, *3*, 21380–21423.
[14] H. Y. Lee, J. B. Goodenough, *Journal of Solid State Chemistry* 1999, *223*, 220–223.
[15] Y. Yang, Y. Liang, Y. Zhang, Z. Zhang, Z. Li, Z. Hu, *New Journal of Chemistry* 2015, *39*, 4035–4040.
[16] N. Shimamura, R. Kanda, Y. Matsukubo, Y. Hirai, H. Abe, Y. Hirai, T. Yoshida, H. Yabu, A. Masuhara, *ACS Omega* 2019, *4*, 3827–3831.
[17] J. Shin, J. K. Seo, R. Yaylian, A. Huang, Y. S. Meng, *International Materials Reviews* 2020, *65*, 356–387.
[18] C.C. Hu, T.W. Tsou, *Electrochimica Acta* 2002, *47*, 3523–3532.
[19] S. Devaraj, N. Munichandraiah, *Journal of Physical Chemistry C* 2008, *112*, 4406–4417.
[20] L. Zhang, L. Kang, H. Lv, Z. Su, K. Ooi, Z.H. Liu, *Journal of Materials Research* 2008, *23*, 780–789.
[21] M.S. Wu, *Applied Physics Letters* 2005, *87*, 153102.
[22] J. Yan, Z. Fan, T. Wei, J. Cheng, B. Shao, K. Wang, L. Song, M. Zhang, *Journal of Power Sources* 2009, *194*, 1202–1207.
[23] K. Rajendra Prasad, N. Miura, *Electrochemistry Communications* 2004, *6*, 1004–1008.
[24] Y. Chen, C. Zhou, G. Liu, C. Kang, L. Ma, Q. Liu, *Journal of Materials Chemistry A* 2021, *9*, 2872–2887.
[25] P. Gao, P. Metz, T. Hey, Y. Gong, D. Liu, D. D. Edwards, J. Y. Howe, R. Huang, S. T. Misture, *Nature Communications* 2017, *8*, 14559.
[26] R. E. John, A. Chandran, M. Thomas, J. Jose, K. C. George, *Applied Surface Science* 2016, *367*, 43–51.
[27] Y. Wu, R. Feng, C. Song, S. Xing, Y. Gao, Z. Ma, *Catalysis Today* 2017, *281*, 500–506.
[28] Ch. Leroux, G. Nihoul, G. Van Tendeloo, *Phys. Rev. B* 1998, *57*, 5111–5121.
[29] B. Hong, J. Zhao, K. Hu, Y. Yang, Z. Luo, X. Li, C. Gao, *RSC Adv.* 2017, *7*, 22341–22346.
[30] J. Sodtipinta, T. Amornsakchai, P. Pakawatpanurut, *Advances in Natural Sciences: Nanoscience and Nanotechnology* 2017, *8*, 035017.
[31] A. G. Pandolfo, A. F. Hollenkamp, *Journal of Power Sources* 2006, *157*, 11–27.
[32] M. A. Yahya, M. H. Mansor, W. A. A. W. Zolkarnaini, N. S. Rusli, A. Aminuddin, K. Mohamad, F. A. M. Sabhan, A. A. A. Atik, L. N. Ozair, Melaka, Malaysia, 2018, p. 030023.
[33] H. Yang, S. Ye, J. Zhou, T. Liang, *Frontiers in Chemistry* 2019, *7*, 1–17.
[34] C. Wang, H. Li, J. Zhao, Y. Zhu, W. Z. Yuan, Y. Zhang, *International Journal of Hydrogen Energy* 2013, *38*, 13230–13237.
[35] Z. Liu, X. Zhou, F. Wu, Z. Liu, *ACS Omega* 2020, *5*, 10106–10114.
[36] Z. Zhu, H. Jiang, S. Guo, Q. Cheng, Y. Hu, C. Li, *Scientific Reports* 2015, *5*, 15936.
[37] D. Qu, H. Shi, *Journal of Power Sources* 1998, *74*, 99–107.
[38] J. L. Goldfarb, G. Dou, M. Salari, M. W. Grinstaff, *ACS Sustainable Chemistry & Engineering* 2017, *5*, 3046–3054.
[39] B. Liu, L. Liu, Y. Yu, Y. Zhang, A. Chen, *New Journal of Chemistry* 2020, *44*, 1036–1044.
[40] W. Tian, H. Zhang, X. Duan, H. Sun, G. Shao, S. Wang, *Adv. Funct. Mater.* 2020, *30*, 1909265.
[41] H. Zhang, D. Yang, A. Lau, T. Ma, H. Lin, B. Jia, *Small* 2021, *17*, 2007311.

*(The individual images used in figures 1.1,1.2,1.3,1.10,1.12,1.13,1.16 and 1.17 are taken from internet sources)

2. Synthesis and Characterization Techniques

2.1 Synthesis Methods

The particle dimension goes smaller and smaller and reaches the nanometer scale, its properties changed drastically and will influence both physical and chemical properties. In nanotechnology, synthesis methods of materials got much attention due to the dependence on various properties like morphology, crystallinity, electronic states, shape, phase, structure, etc. The mode of synthesis and its reaction condition affect the properties of the nanomaterial. Several techniques are available for the synthesis and a few of them are sol-gel, hydrothermal, solvothermal, electrochemical, sonochemical, physical vapour deposition and chemical vapor deposition[1,2].

The synthesis of the nanomaterials depends on the mode and its reaction parameters such as molarity, dilution, the ratio of the reactants, temperature, pressure, etc. The sol-gel method is one of the easy and simple and low-cost experimental methods from which the morphology and properties of the nanomaterial could be easily tuned by maintaining a proper reaction atmosphere. Likewise, solvothermal or hydrothermal methods offer a simple and green method that needs a very lower crystallization temperature, sometimes with no need for further calcination or sintering step. In addition to that one- dimensional nanofibers can easily be prepared by electrospinning technique. It is the simplest method of fabricating nanofiber with the assistance of polymer matrix.

2.1.1 Sol-gel Synthesis

Sol-gel synthesis is a simple, low-cost experiment at a mild or low temperature. It is possible to generate different structures of nanomaterials with the same precursor by varying the experimental conditions. Another advantage of this method is repeatability, simplicity, and reliability during the liquid phase synthesis. The properties of the nanomaterial can be easily changed by doping, where precise control can be done over this method. The formation of the sol is caused by the metal oxide present in the system by hydrolysis and condensation[3], represented by following equations (1-3).

$$\boldsymbol{Metal\ precursor + Reducing\ agents \xrightarrow[Temperature]{} colloids\ of\ metal\ oxide\ or\ hydroxide}$$

$$\xrightarrow[Temperature]{} \boldsymbol{Colloids\ of\ metal\ oxide\ or\ hydroxides} \qquad (1)$$

$$\equiv M - X + OH\ or\ H_2O \xrightarrow{Hydrolysis} \equiv M - OH\ +\ X^- \qquad (2)$$

$$\equiv M - OH + OH - M \equiv \xrightarrow{Condensation} \equiv M - O - M \equiv\ + H_2O \qquad (3)$$

These chemical transformations make some gel formation. The evaporation rate and

evaporation methods make xerogel, aerogel, etc (figure 2.1). Sol-gel is a technique that dissolves a compound in liquid and resolidifies it in a controlled manner. The compounds of multi-components can easily be prepared with controlled stoichiometry by mixing the sols of different compounds. Also, it prevents the inhomogeneity, that generates in coprecipitation reaction. In addition to that it enables atomic-level mixing, which results in small particles which are easily sinterable. This technique is used to prepare a variety of materials with various shapes including thin fibers, porous structures, and dense powders[3,4]. Among different methods, the sol-gel method got much attention due to the aforementioned reasons.

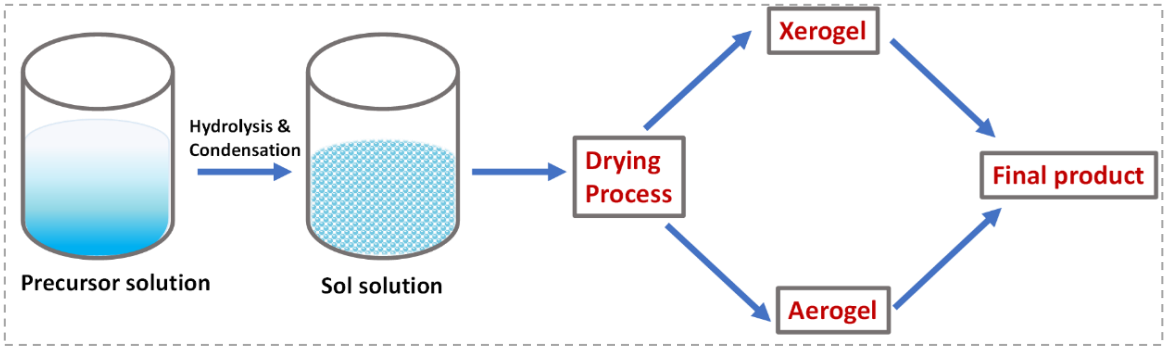

Figure 2.1 Representation of sol-gel technique

2.1.2 Hydrothermal or Solvothermal Technique

The hydrothermal technique is an established niche in nanomaterial synthesis. This technique is one of the lower-temperature synthesis methods also used to generate highly homogeneous and monodispersed nanomaterials. The heterogeneous chemical reaction is carried out in the presence of an aqueous or non-aqueous medium by maintaining the temperature above ambient condition and pressure > 1 atm in a closed system. The reactions are carried out in a particular experimental setup called an autoclave (figure 2.2). Care should be taken that the aqueous or non-aqueous solvents are maintained near supercritical or supercritical conditions.

Figure 2.2 (a) A photograph of stainless-steel autoclave with teflon liner used for the hydro/ solvothermal process and (b) representation of metal oxide synthesis using hydrothermal method

Based on the solvents used, it can be represented as hydrothermal (water), alcothermal (alcohol), glycothermal (glycol), ammonothermal (ammonia), etc. The precursor used is commonly metal salts (inorganic materials) with suitable solvents. The other changing parameters that affect the property of the product are temperature, pressure, volume, the concentration of the reactants, reaction time, etc[2]. These conditions affect the crystal structure, size, shape, composition of the samples, etc. The advantages of these are cost-effectiveness, environmentally safe closed system conditions, expects higher purity products, metastable products are formation etc.

2.1.3 Electrospinning Technique

Electrospinning is a versatile method used for making ultrafine fibers with sizes ranging from nanometers to micrometers. In this process high voltage is applied to a polymer solution or melt, causing a charged jet to be ejected from a spinneret. Once the electrostatic repulsion overcomes the surface tension of the polymeric solution, it is ejected from the tip of the needle[5]. Electrostatic repulsion causes the jet to whip, resulting in quick evaporation of the solvent or cooling of the polymer melt [5–7]. The fibers are solidifying and meantime it gets deposited over the grounded metallic collector. The grounded collector is kept at a particular distance from the metallic capillary needle[8]. The final product will be a very thin, uniform, and mechanically stable fiber mat. The basic electrospinning technique scheme is given in Figure 2.3.

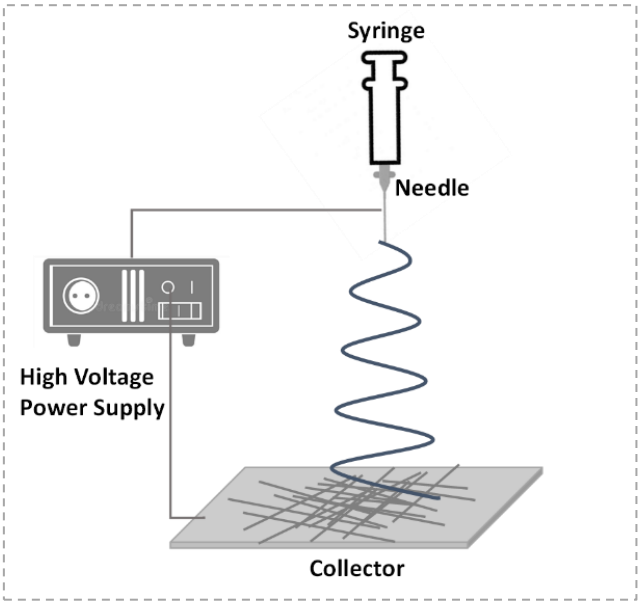

Figure 2.3 Representation of basic electrospinning setup

This technique is widely used for the preparation of nanofibers for applications such as tissue engineering, filtration, and energy storage because of its ability to produce high surface area

fibers with precise morphology and composition. Modification of the parameters like polymer concentration, applied voltage, spinneret to collector distance to adjust the properties of electrospun fibers for specific applications.

2.2 Characterization Techniques

The structure, morphology, optical, electrical, and thermal properties of the synthesized material are investigated with different characterization techniques. For the current studies, the following characterization techniques are used.

- ✓ X-Ray diffraction analysis
- ✓ Raman spectroscopy
- ✓ Field emission scanning electron microscopy
- ✓ Fourier transform infrared spectroscopy
- ✓ X-ray photoelectron spectroscopy
- ✓ Brunauer Emmet Teller analysis
- ✓ Contact angle measurements
- ✓ Cyclic voltammetry
- ✓ Galvanostatic charge-discharge
- ✓ Electrochemical Impedance spectroscopy

2.2.1 Structural and Phase Analysis

2.2.1.1 X-Ray Diffraction (XRD)

X-ray diffraction analysis is used for the structural aspects of a material such as crystal structure and atomic spacing. The X-ray beam with a wavelength range from 0.7 to 2 A^{o}, incident on the sample, and it gets diffracted. The electromagnetic waves interacting with an object produce constructive interference by satisfying Bragg's law of X-ray diffraction shown in figure 2.4.

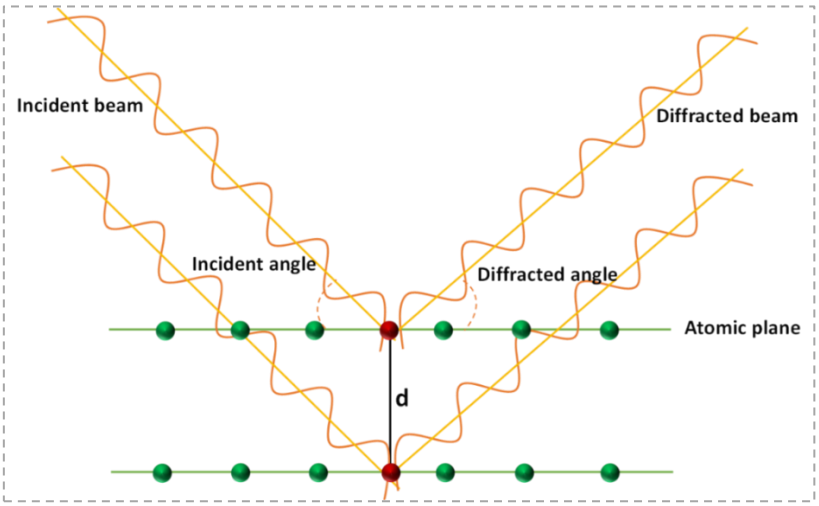

Figure 2.4 Schematic representation of X-ray scattering in atomic planes

These diffracted rays are responsible for the intense peaks obtained during analysis. This is used for the identification of the crystal structure, and to measure the average distance between the planes, lattice parameters and geometry, etc. This is based on Bragg's law of X-ray diffraction[9,10]. According to this law (4),

$$n\lambda = 2d\sin\theta \qquad (4)$$

Where 'n' is the order, 'λ' is the wavelength of incident radiation, 'd' is interplanar distance, and 'θ' is the incident angle.

XRD analysis is done by using a Rigaku Miniplex X-Ray diffractometer with CuKα radiation (λ= 0.1544nm). The data acquired from XRD analysis are;

- Determination of crystal structure
- Phase determination like amorphous or crystalline
- Crystallite size measurement and degree of crystallinity
- Orientation of single crystals
- Measures residual stress
- Quantitative analysis of phases

2.2.1.2 Raman Spectroscopy

Raman spectroscopy is an effective technique used for investigating vibrational, rotational, and other low-frequency modes in a system. It is based on the inelastic scattering of monochromatic light. Usually a laser source is used, where photons interact with the molecular vibrations or phonons in the sample. The scattered light is then collected and analyzed to provide valuable information about the molecular structure, crystallinity, and chemical bonding within the material. The fundamental principle underlying Raman spectroscopy is based on inelastic collisions. When light interacts with a sample, the majority of photons undergo elastic scattering, known as Rayleigh scattering, while a small fraction undergoes inelastic scattering, known as Raman scattering. In Raman scattering, the frequency of the scattered light will be smaller than that of incident photon. The Raman shift is represented by equation (5).

$$Raman\ shift = \Delta\nu = \nu_{Raman} - \nu_{incident} \qquad (5)$$

This discrepancy arises from changes in the vibrational, rotational, and electronic energy levels of the molecules in the sample. The frequency of the incident radiation exceeds that of the scattered radiation, results the formation of the Stokes line in the Raman spectrum. When the frequency of the incident radiation is lower than the frequency of the scattered radiation, the scattered light appears as anti-Stokes lines in the Raman spectra, as shown in figure 2.5. As a result, the Stokes bands in the Raman spectrum typically appear more intense than anti-Stokes

bands. This phenomenon occurs because the population of molecules in the higher energy state (related with anti-Stokes scattering) is generally lower than in the lower energy state (related with Stokes scattering), leading to weaker anti-Stokes signals compared to the Stokes signals[11].

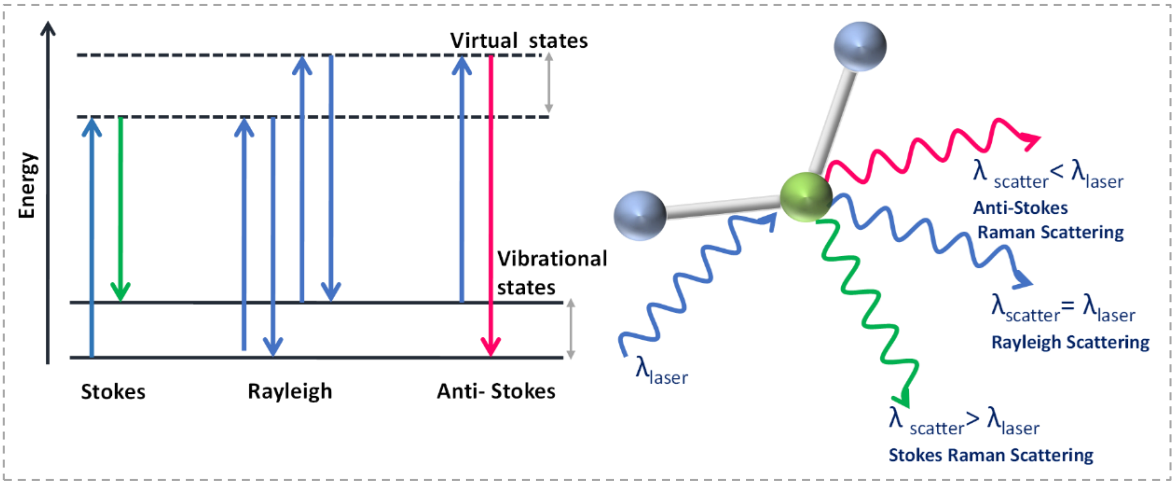

Figure 2.5 Generation of Raman scattering during analysis

The intensity of scattered light in Raman spectroscopy is compared with the incident light's energy or frequency, resulting a unique "fingerprint" for each molecule. Analyzing the obtained bands and their intensity enables the identification of specific molecules. Changes in band frequency, peak intensity, and peak broadening can reveal the amount of stress in the material and its crystallinity[12]. By collecting data from several sample areas, the sample's homogeneity can be assessed. Raman spectra provide information on the material's composition, crystallinity, surface bond vibrations, as well as the detection of IR inactive molecular vibrations and impurity detection[13].

2.2.1.3 X-Ray Photoelectron Spectroscopy (XPS)

X-ray photoelectron spectroscopy (XPS), also known as electron spectroscopy for chemical analysis (ESCA), is a powerful tool used to determine the elemental composition, chemical states, and electronic states of materials. X-ray photoelectron spectroscopy (XPS), also known as electron spectroscopy for chemical analysis (ESCA), operates based on the photoelectric effect. When the sample surface is irradiated with X-rays, the X-rays interact with the core electrons of the atoms in the material. These core electrons can be excited to higher energy levels and then relax back to their original energy levels, emitting characteristic X-ray photoelectron peaks. By analyzing the binding energies and intensities of these peaks able to understand the elemental composition and its chemical environment. The depth of penetration of X-rays is in the range of micrometers, normally gives the signal from a depth of 10 nm. XPS is performed under ultra-high vacuum conditions to prevent interference from air and ensure

accurate measurements. The excited photoelectrons lose some energy as they travel through the material, and only those that escape without being scattered are detected. This technique is valuable for studying surfaces, thin films, and interfaces in various fields, including materials science, surface science, and nanotechnology[14,15]. The photoelectric effect is represented in equation (6).

$$E_{KE} = hv - \phi - E_v \qquad (6)$$

E_{KE} is the kinetic energy of the ejected electron, hv is the energy of photons, ϕ is the work function and E_v is the binding energy.

The XPS instrumentation includes a monochromatic X-ray source that generates X-rays directed to the sample being analyzed. The emitted photoelectrons are then accelerated towards a hemispherical analyzer, where their kinetic energies are analyzed. By measuring the kinetic energies of the photoelectrons, the binding energies of core electrons from which they were emitted can be determined. This information provides valuable insights into the chemical environment and electronic structure of the sample. The detector in the analyzer records the intensity of the emitted photoelectrons as a function of their kinetic energy and generating a spectrum. The entire system operates under ultra-high vacuum conditions, typically around 10^{-9} torr, to minimize electron scattering and ensure accurate measurements. The signal generation and instrumentation setup shown in figure 2.6. The analysis provides the information for identifying the elements based on their peak binding energy, quantifying elements based on the peak area or intensity, spin-orbit splitting, kinetic energy effects, and chemical composition except for H and He[12,16].

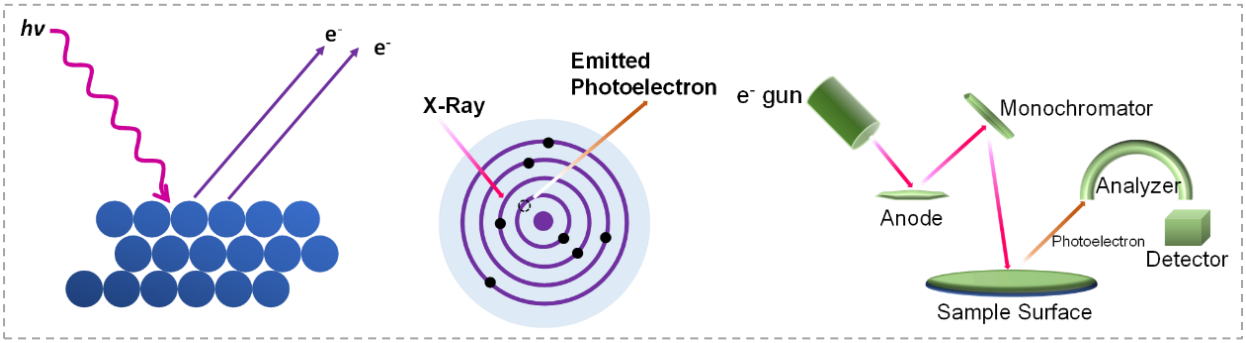

Figure 2.6 Schematics of signal generation and XPS instrumentation setup

2.2.1.4 Fourier Transform- Infrared (FT-IR) spectroscopy

Fourier Transform Infrared Spectroscopic analysis is an important tool which gives sufficient information about the chemical structure of a compound. The absorption of infrared causes various bonds in a molecule that tend to stretch or bend. When the photon's energy and the molecule's vibrational energy level coincide, the photon's energy is absorbed. The molecule is

excited from the lower vibrational level to the higher vibrational level when the IR radiation couples with the sample's molecular vibration. Figure 2.7 (a and b) shows infrared region on electromagnetic spectrum and the instrumentation setup.

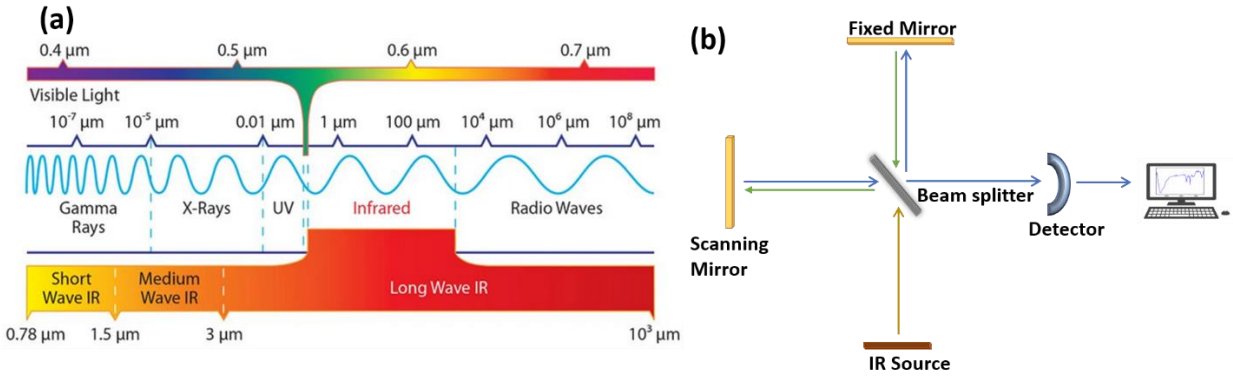

Figure 2.7 (a) Infrared region on the electromagnetic spectrum* and (b) instrumental setup of FTIR interferometer unit

The absorbed energy serves to raise the amplitude of the vibrational motion of a bond in a molecule. Not all bonds in the IR spectrum can absorb IR energy. Bonds with a shift in dipole moment are capable of absorbing infrared radiation. To confirm functional groups, greater IR absorption (4000 cm^{-1}-1400 cm^{-1}) is used. The fingerprint region corresponds to the distinctive IR absorption at the lower region (1400 cm^{-1}-600 cm^{-1}). When a sample is exposed to infrared radiation, it can absorb some radiation and transmit the rest. Some radiations get reflected back to the source itself. Basically, the IR spectra are a plot of transmitted frequencies Vs the intensity of the transmission. The samples are analyzed using PerkinElmer FTIR spectrometer-spectrum two analyzer. From FTIR, following details are obtained (i) inorganic and organic nature of the samples, (ii) the presence of impurities (iii) quantitative analysis by evaluating the area under the spectrum and (iv) molecular structure.

2.2.2 Morphology Analysis

2.2.2.1 Field Emission Scanning Electron Microscopy (FE-SEM)

FE-SEM is a widely using imaging technique in material science and nanotechnology. It is a non-destructive method with high spatial resolution and high magnification. When electrons from the high-energy electron beam strike on the sample and interact in different ways. The electron penetrated into the sample and emits back in the form of photons or electrons. The emitted signals are generated a two-dimension image of the surface of the sample[14,15]. The representation of electron beam generation and instrumental setup is shown in figure 2.8.

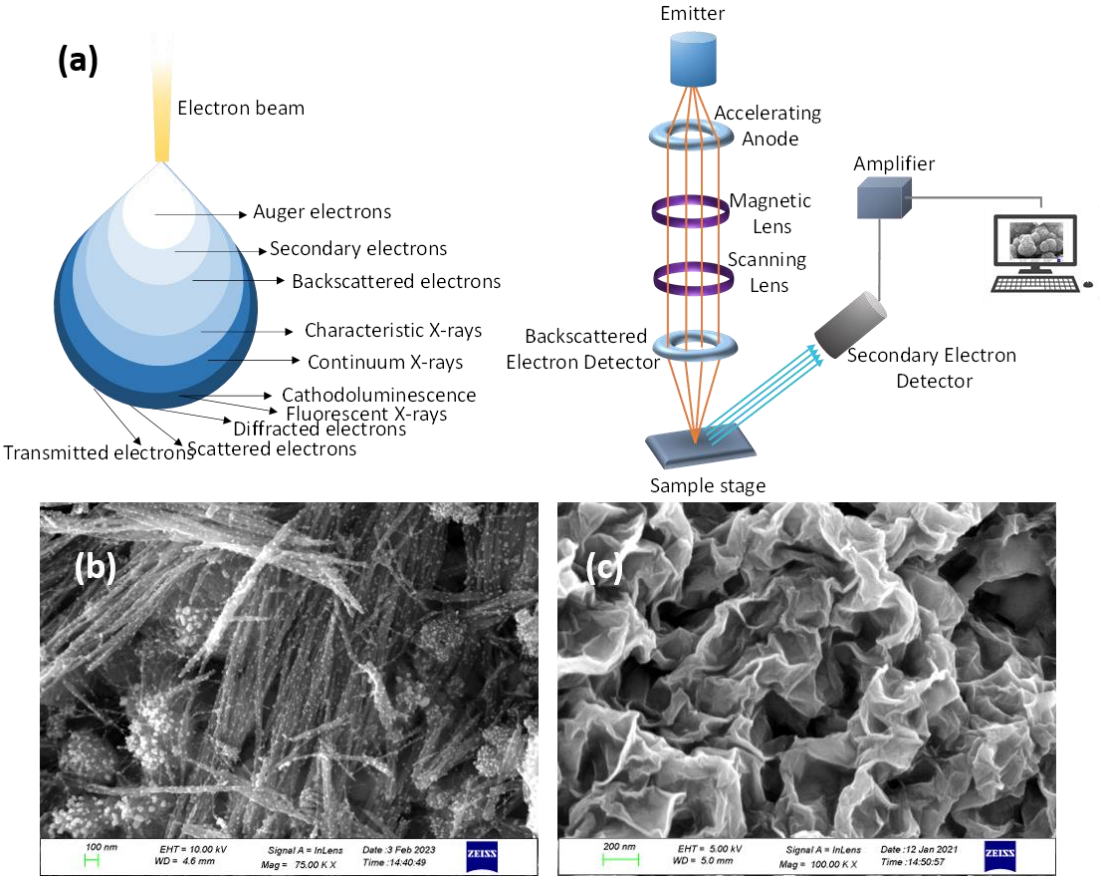

Figure 2.8 (a) Representation of electron beam generation and instrumental setup, (b) and (c) FESEM images of nanowire and nanosheets

The instrumentation contains an electron gun, lenses, a high vacuum chamber, a sample holder, and a detector. The electron beam of high energy range 0.5 KeV to 40 KeV is used with a condenser lens that can focus a spot of diameter range 0.40 nm to 5 nm. Then allows to raster scan in the x and y direction on the sample over a rectangular area. FE-SEM operates by generating an electron beam using a field emission source, typically a tungsten filament or a field emission gun. The electron beam is accelerated towards the sample surface using an electromagnetic lens with a fine probe size (typically less than 1 nm in diameter). The sample should be kept in a vacuum chamber to prevent electron scattering. When a focused electron beam interacts with the sample, various signals are generated, including auger electrons, secondary electrons, fluorescence, backscattered electrons, X-rays etc. The image formation in SEM is based mainly on backscattering electrons, secondary electrons, and X-rays (for elemental mapping). These signals are collected by detectors, and convert them into high resolution images. FE-SEM provides information about morphology and microstructure additionally it gives information about the chemical composition and distribution of the system and the amount of doping[12].

2.2.3 Surface Area and Porosity Analysis

2.2.3.1 Brunauer- Emmet Teller (BET) Analysis

BET is a standard method used to determine the surface area and porosity of materials based on N_2 adsorption-desorption. It relies on the assumption of multilayer adsorption of gas on a flat surface. However, this assumption becomes invalid when monolayers overlap. Materials are classified based on their pore size into microporous, mesoporous, and macroporous categories. Pores with diameters up to 2 nm are considered microporous, those between 2 nm and 50 nm are mesoporous, and those larger than 50 nm are macroporous. In theory, the monolayer adsorption of gas molecules on a solid surface occurs up to a certain gas pressure above the solid surface at a fixed temperature[17] and represented by equation (7).

$$\theta = \frac{\alpha P}{1 + \alpha P} \qquad (7)$$

Where *'θ'* is the fractional of the sample surface, *'α'* is a constant, and *'P'* is the gas pressure. The amount of gas adsorbed depends on the exposed surface area and the sample surface was cooled by using liquid N_2 to get the adsorption. There is no more adsorption occurs after attaining a saturated pressure. After forming the adsorption layers sample was subjected to heating for releasing the adsorbed nitrogen and quantified. The obtained data is known as the BET isotherm and is the plot of total adsorbed gas Vs relative pressure[18,19]. The adsorption isotherm varies with the porous nature of the material and the typical graph shown in figure 2.9.

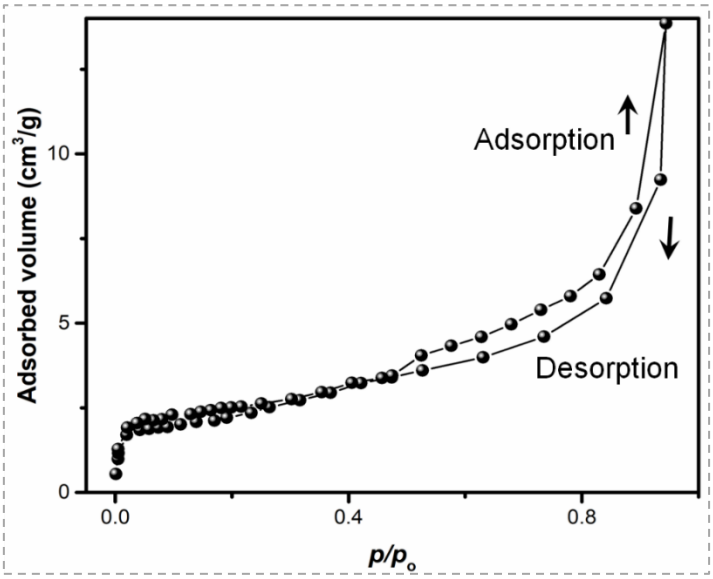

Figure 2.9 Representation of a N_2 adsorption and desorption isotherms plot during BET analysis

2.2.4 Wettability Characteristics

2.2.4.1 Contact Angle Measurement

This technique is one of the useful techniques to know the interaction between the surface of the electrode with the electrolyte as well as the chemical nature of the surface by means of qualitatively and quantitatively. The surface wettability measurement is used as the primary evaluation technique for the solid-liquid interface. The surface science of the prepared material is important for its storage application and its efficiency[20].

This is one of the easiest and most dependable methods to correlate surface wettability and hydrophilic or hydrophobic nature. The advantages of this with respect to other techniques are environmentally friendly, minimum time, reduced chemical cost, and less labour for the measurement. Here measures the shape of the liquid droplets formed due to the pressure difference created between air and the liquid interface[21]. It is one of the handy techniques which reduces the use, money, and time of other sophisticated instruments related to measurements[22]. The behavior of the solid-liquid interface at various surfaces is shown in figure 2.10.

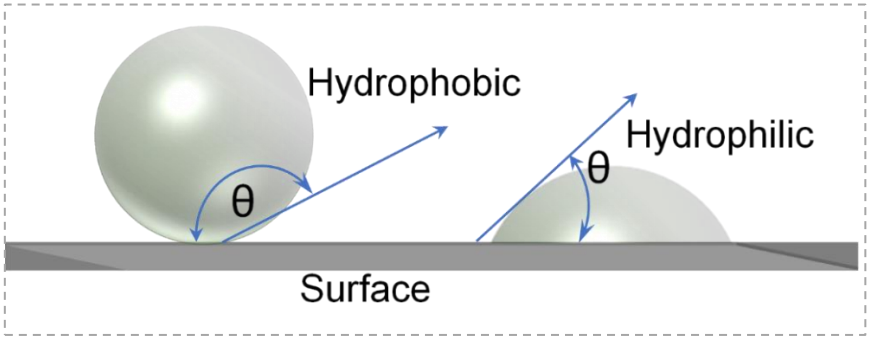

Figure 2.10 Contact angle measuring hydrophobic and hydrophilic surface

2.2.5. Supercapacitor Application

2.2.5. 1 Cyclic voltammetry (CV)

It is a widely used technique for knowing qualitative information about an electrochemical reaction like the redox process, adsorption process, heterogeneous electron transfer reactions, etc. It offers information regarding rapid locations of the redox potential of a particular electroactive species. It consists of linear scanning of the potential with respect to a stationary working electrode by a triangular potential waveform. The potentiostat measures the current generated from the electrochemical reaction consecutive to the applied potential and a straight analog ramp is required for the performance. The applied ramp consists of a series of small potential steps which approximate the desired linear ramp. In short, the potential of the working electrode was scanned linearly and measured the current generated from oxidoreduction

reactions[22]. The representation of the electrochemical setup and parameters are shown in figure 2.11.

The CV is obtained by measuring the current between a working electrode and a counter electrode, which directly measures as the function of potential. The potential is applied across the reference electrode and working electrode. The current flow inside the system is from the working electrode to the counter electrode or vice versa. The potential of the working electrode is controlled with respect to the reference electrode and it does not pass any current. The specific capacitance of each electrode is calculated by the equation[23,24] (8),

$$C_s\left(\frac{F}{g}\right) = \frac{2I/\frac{dv}{dt}}{m * V} \qquad (8)$$

Where 'I' is the average current, 'dv/dt' is the scan rate, 'm' is the mass of the electrode, and 'V' is the potential window. The energy density, E, and power density P are calculated using the following equations[23,24], (9), and (10).

$$E\left(\frac{Wh}{kg}\right) = \frac{C_s\ (\Delta V^2)}{28.8} \qquad (9)$$

$$P\left(\frac{kW}{kg}\right) = \frac{E}{t} * 3.6 \qquad (10)$$

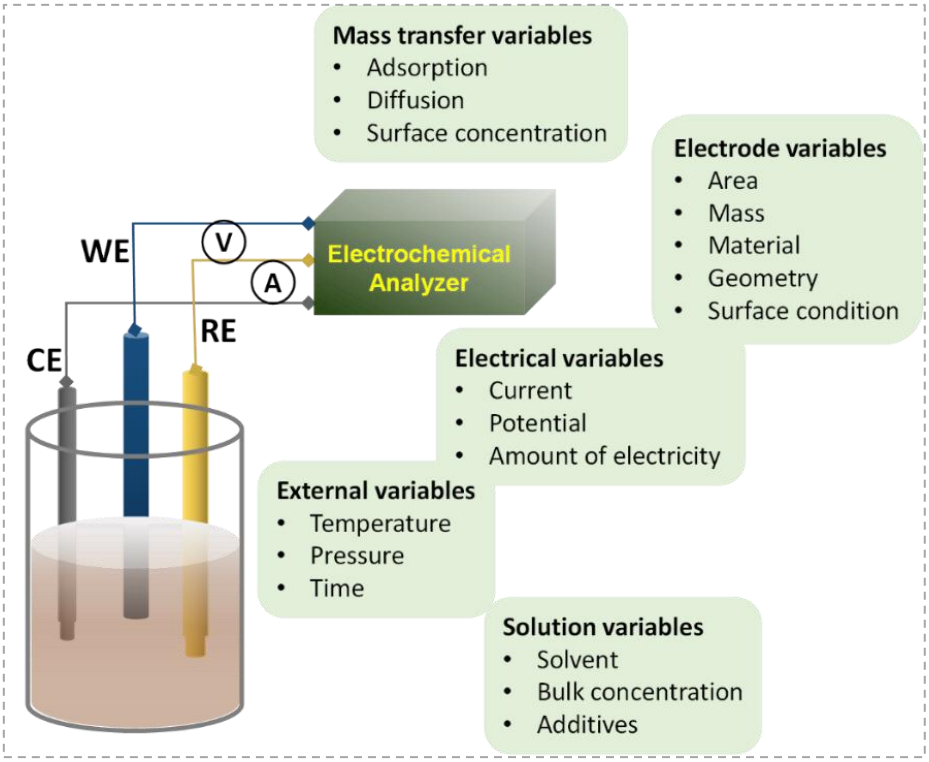

Figure 2.11 Representation of three-electrode setup and depending variables

2.2.5.2 Galvanostatic Charge –Discharge (GCD)

Characterization via the galvanostatic charge-discharge (GCD) is one of the major tools for

supercapacitors to measure their charging and discharging criterion. It is a reliable analysis to determine the energy density, power density, and other parameters like equivalent series resistance and cyclic stability of the supercapacitor[23,25].

The GCD measurement of metal oxide system is shown in figure 2.12. In this method, the experiment is run by applying a constant current, and the potential is measured as a function of time. Various modes were available for the measurements, PCGA-potentiodynamic cycling with galvanostatic acceleration-electrode cycling under potentiodynamic mode. GCPL-galvanostatic cycling with potential limitation, cycling under galvanostatic mode with an imposed current. APGC- alternate pulse galvano cycling, perform fast galvano steps between two values. GCPL method is used for the supercapacitor analysis.

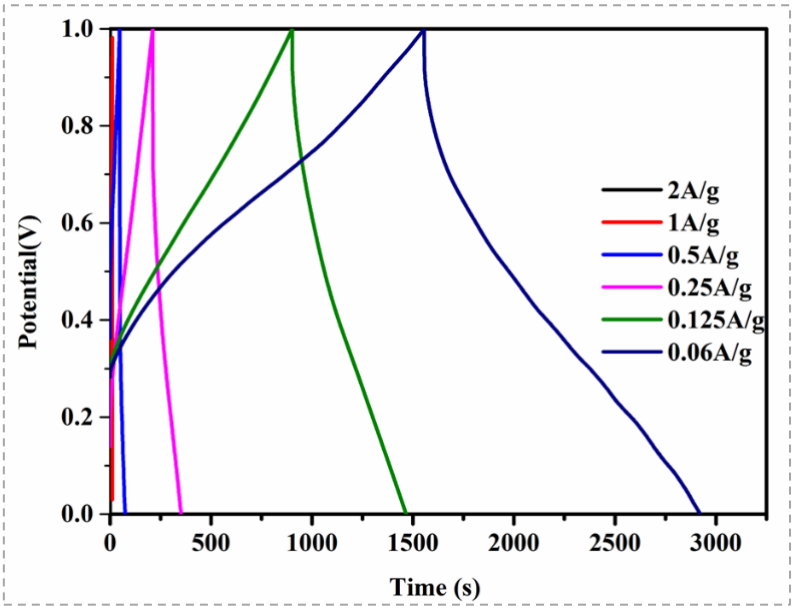

Figure 2.12 A representative GCD graph of metal oxide

2.2.5.3 Electrochemical Impedance Spectroscopy (EIS)

EIS is a powerful computational technique for analyzing physical as well as chemical processes in a solution and solids. In terms of electrochemistry, a sinusoidal signal is employed for measuring the rate constant of a fast electron transfer reaction in a very short time interval with an electrochemical cell. Also acquiring information related to complicated reactions involving electrode-electrolyte interface or surface and solution reactions.

This technique has been used in the valuation of batteries, supercapacitors, solar cells, fuel cell development, corrosion, sensors, etc. Classified into different based on the applied input; PEIS-potentiostatic impedance, performs in a potentiostatic mode by applying sinusoidal impulse around a fixed potential of E or relative to the cell equilibrium potential. GEIS-Galvanostatic impedance, current is controlled in this situation. In SGEIS- staircase galvano electrochemical impedance, applying sinus around a current ‘I’ sweep in galvanostatic mode. SPEIS-staircase

potentio electrochemical impedance, measured by applying staircase potential sweep. It is an excellent technique used for the characterization of electrochemical systems. Impedance is a measure of the ability of the circuit to resist the flow of electrical current. Simply the principle behind the EIS is applying a small amplitude sinusoidal signal and measuring the response, a representative EIS graph is shown in figure 2.13.

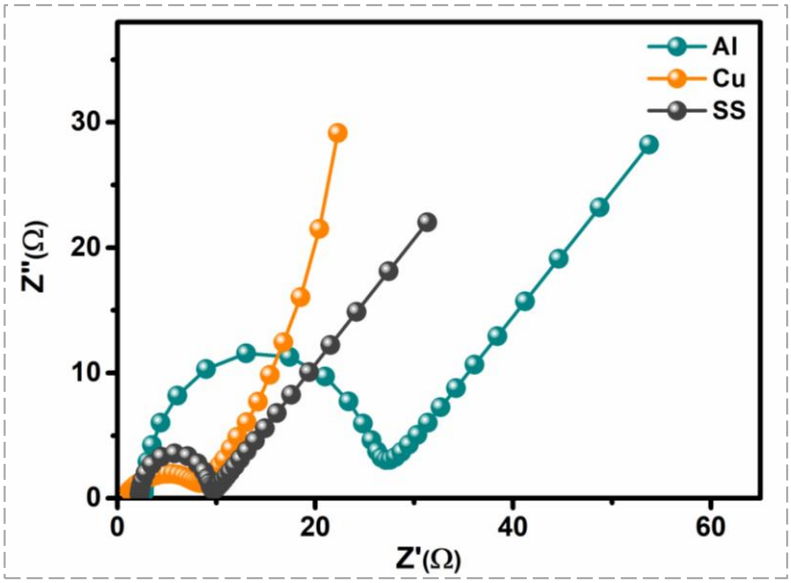

Figure 2.13 A representative EIS graph of different current collectors

Ohm's Law-based mathematical approach is used for the analysis of the impedance spectra.[26] According to this law, impedance Z(ω) is represented by equation (11),

$$Z(\omega) = \frac{E(\omega)}{i(\omega)} \qquad (11)$$

Where E (ω) is the frequency-dependent–potential, i (ω) is the frequency-dependent current. The Nyquist plot is a typical diagram used for analyzing electrochemical terms like electrolyte solution resistance (R_s), electrode polarization resistance (R_p), double layer capacitance (C_{dl}), etc by using a corresponding equivalent circuit (figure 2.14). In the equivalent circuit, R_1 is the series resistance, R_2 is the resistance at the interface[22]. Where C is the capacitor and W is the Warburg diffusion resistance. By plotting Z' (Ω) Vs Z''(Ω) get a plot depicted in figure 2.13. Analyzing the Nyquist plot for getting different parameters described earlier.

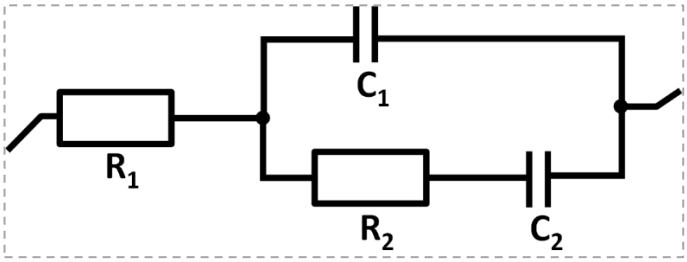

Figure 2.14 Randle's circuit for a two-electrode setup

2.2.6 Quantifying Capacitive Properties

2.2.6.1 Current Response Vs Sweep Rate

The rate of insertion-extraction of the cations and anions in an electrolyte depends upon the redox reaction. The high specific capacitance was observed at the slowest scan rate due to the slow charging-discharging process. That is the solvated anions and cations diffused very slowly and access all possible pores in it. With the fast scan rate, the anions and cations didn't get enough time to access the pores or active sites resulting in low specific capacitance[27].

The total charge stored in a particular material is represented by the area under the curve. Which is the combination of the faradic and non-faradic process. The faradic process arises from the redox reaction whereas the non-faradic process originates from the electric double-layer formation. The capacitive effect was characterized by analyzing the CV data at various scan or sweep rates (υ). The measured current and scan rate are related and is expressed by a power law, I= a υ^b, where 'I' is the current, 'a' and 'b' are variable parameters. The parameter 'b' calculated from the slope of the log I vs log υ plot and give the quantitative information about reaction kinetics. If b=0.5 which satisfies Cottrell's equation, I= $\upsilon^{1/2}$, and exhibits an ideal diffusion-controlled process. If b=1 the process is capacitive (surface controlled) and the parameter b is lie between 0.5 and 1, the process is the combination of both diffusion controlled and capacitive process [22].

2.2.6.2 Trassati's Method of Analysis

To determine capacitive effects, Trassati's method was used. For that, we assuming semi-infinite diffusion condition in which ions are unrestrictedly diffuse to the interface of electrode-electrolyte with respect to the bulk electrolyte. There exists a linear correlation between the reciprocal of the areal capacitance (C^{-1}),[27] (calculated from CV data) and the square root of the scan rate ($\nu^{1/2}$). Evaluation of total specific capacitance (C_T) calculated using equation (12) given below,

$$C^{-1} = k\nu^{1/2} + C_T^{-1} \qquad (12)$$

Where C, ν, and C_T denote the areal capacitance, scan rate, and total or maximum capacitance. C_T corresponds to the y-intercept of the linear plot of C^{-1} vs $\nu^{1/2}$. The total capacitance is the combination of electrical double layer and pseudo capacitance. The areal capacitance (C) plotting against the inverse of the square root of the scan rate ($\nu^{-1/2}$) and y-intercept of the linear plot gives the maximum electric double layer capacitance (C_{EDL}) given in equation (13).

$$C = k\nu^{-1/2} + C_{EDL} \qquad (13)$$

Where C, ν, and C_{EDL} are the calculated maximum areal capacitance, scan rate, and maximum

electrical double layer respectively. The maximum pseudocapacitance (C_{PS}) is derived by subtracting C_{EDL} from C_T [25,28,29]. The contribution of each type of mechanism is analyzed by the given equations (14) and (15).

$$C_{EDL}\% = \frac{C_{EDL}}{C_T} \times 100\ \% \qquad (14)$$

$$C_{PS}\% = \frac{C_{PS}}{C_T} \times 100\ \% \qquad (15)$$

The percentage of electric double layer and pseudo-capacitance[29] is denoted by C_{EDL}% and C_{PS}%.

2.2.7 Electrode Preparation for Supercapacitor

In general, supercapacitor electrodes are prepared from a mixture containing an active material, polymeric binder, and a suitable solvent. In addition to that some conducting additives are added into it for compensating the loss during preparation. The active material or sample, additive, and polymeric binder were taken in the ratio (75:10:15 for metal oxides or 80:10:10 for carbon), then mixed with a suitable solvent such as N-methyl pyrrolidone (NMP). The prepared paste or slurry is coated over the pre-weighed substrate[30]. The coating is carried out by several methods like blade coating, spray coating, spin coating, drop casting, etc. The electrode preparation is schematically represented in figure 2.15.

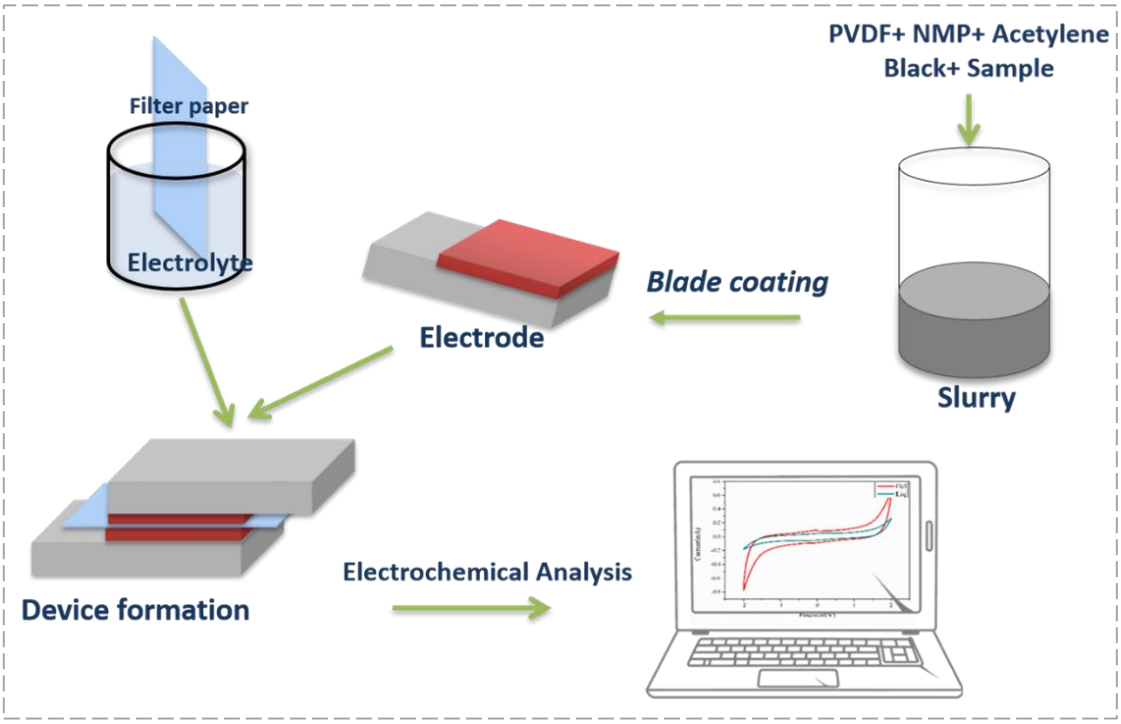

Figure 2.15 Schematic representation of electrode preparation for the supercapacitor analysis

The coated electrode dried to evaporate the solvent. Then dried electrodes are weighed to know the amount coated over a specific area (1*1 cm^2, 1.5 * 1.5 cm^2, etc). In this work, all the

electrodes are prepared by the doctor blade method by mixing active material with carbon black as conducting additive and polyvinylidene fluoride (PVDF) in (NMP) as the solvent on the stainless-steel substrate. The electrode material weight was kept in the range of 1-2 mg/cm^2 all over the studies.

The synthesized materials are characterized by different instruments. Field emission scanning electron microscopy (ZEISS-GEMINISEM 300) was used to examine the surface topography, morphology, and microstructure development over the adsorbents. The crystal structure and crystalline nature were assessed using a PANalytical-Xpert3 powder X-Ray diffractometer. A 532 nm DPSS laser, the Alpha 300RA from WiTec in Germany instrumentation was used to conduct the Raman analysis. The crystal Fourier transform infrared spectroscopy (FTIR) was recorded with Perkin Elmer spectrum two FTIR spectrophotometer using the KBr pellet method. The XPS analysis were carried out by Thermo Scientific ESCALAB Xi+and x-ray photoelectron spectroscopy (XPS) from 0 eV to 1300 eV. After degassing at 200 ^oC for 18 hours, the specific surface area (SSA) was measured using $N_{2,}$ and the Brunner-Emmet-Teller (BET) model was used to analyze the adsorption-desorption isotherm. Using the Barrett-Joyner-Halenda (BJH) and *t*-plot methods, the porosity was assessed. Thermogravimetric analysis (TGA) is carried out with Perkin-Elmer STA 8000 instrument. The Kyowa drop master DMs 401 was used to test the wettability characteristics. Biologic SP-150 and SP-300 were used for the electrochemical response measurements.

*****

References

[1] J. A. Darr, J. Zhang, N. M. Makwana, X. Weng, *Chem. Rev.* 2017, *117*, 11125–11238.
[2] Y. X. Gan, A. H. Jayatissa, Z. Yu, X. Chen, M. Li, *Journal of Nanomaterials* 2020, *2020*, 1–3.
[3] M. Parashar, V. K. Shukla, R. Singh, *J Mater Sci: Mater Electron* 2020, *31*, 3729–3749.
[4] M. Niederberger, *Acc. Chem. Res.* 2007, *40*, 793–800.
[5] J. Xue, T. Wu, Y. Dai, Y. Xia, *Chem. Rev.* 2019, *119*, 5298–5415.
[6] I. N. Strain, Q. Wu, A. M. Pourrahimi, M. S. Hedenqvist, R. T. Olsson, R. L. Andersson, *J. Mater. Chem. A* 2015, *3*, 1632–1640.
[7] J.Y. Chen, H.C. Hsieh, Y.C. Chiu, W.-Y. Lee, C.C. Hung, C.C. Chueh, W.C. Chen, *J. Mater. Chem. C* 2020, *8*, 873–882.
[8] I. S. Chronakis, in *Micro-Manufacturing Engineering and Technology*, Elsevier, 2010, pp. 264–286.
[9] E. M. Moroz, *Russ. Chem. Rev.* 2011, *80*, 293–312.
[10] C. Giannini, M. Ladisa, D. Altamura, D. Siliqi, T. Sibillano, L. De Caro, *Crystals* 2016, *6*, 87.
[11] H. Da Silva, A. Porto, C. Caliman, R. De Freitas Filho, A. Cotta, W. Macedo, A. P. Teixeira, *J. Braz. Chem. Soc.* 2018, DOI 10.21577/0103-5053.20180066.
[12] T. Mudalige, H. Qu, D. Van Haute, S. M. Ansar, A. Paredes, T. Ingle, in *Nanomaterials for Food Applications*, Elsevier, 2019, pp. 313–353.
[13] N. Sahoo, G. Tatrari, C. Tewari, M. Karakoti, B. S. Bohra, A. Danadapat, *RSC Adv.* 2022, *12*, 5118–5134.
[14] P. S. Kumar, K. G. Pavithra, Mu. Naushad, in *Nanomaterials for Solar Cell Applications*, Elsevier, 2019, pp. 97–124.
[15] P. H. Salame, V. B. Pawade, B. A. Bhanvase, in *Nanomaterials for Green Energy*, Elsevier, 2018, pp. 83–111.
[16] J. Miao, C. Zhou, X. Yan, H. Jiang, M. You, Y. Zhu, Y. Li, W. Zhou, X. Cheng, *Energy Fuels* 2021, *35*, 2766–2774.
[17] N. Hwang, A. R. Barron, BET surface area analysis of nanoparticles.
[18] M. Thommes, K. Kaneko, A. V. Neimark, J. P. Olivier, F. Rodriguez-Reinoso, J. Rouquerol, K. S. W. Sing, *Pure and Applied Chemistry* 2015, *87*, 1051–1069.
[19] K. Bai, J. Hao, Y. Yang, A. Qian, *Heliyon* 2020, *6*, e04436.
[20] M. M. Vadiyar, S. C. Bhise, S. K. Patil, S. S. Kolekar, A. R. Shelke, N. G. Deshpande, J. Y. Chang, K. S. Ghule, A. V. Ghule, *Chem. Commun.* 2016, *52*, 2557–2560.
[21] T. Liu, K. Wang, Y. Chen, S. Zhao, Y. Han, *Green Energy & Environment* 2019, *4*, 171–179.
[22] Y. Huang, Y. Liu, G. Zhao, J. Y. Chen, *J Mater Sci* 2017, *52*, 478–488.
[23] S. Ci, Z. Wen, Y. Qian, S. Mao, S. Cui, J. Chen, *Sci Rep* 2015, *5*, 11919.
[24] K. Nanaji, V. Upadhyayula, T. N. Rao, S. Anandan, *ACS Sustainable Chem. Eng.* 2019, *7*, 2516–2529.
[25] S. M. Jadhav, R. S. Kalubarme, N. Suzuki, C. Terashima, J. Mun, B. B. Kale, S. W. Gosavi, A. Fujishima, *ACS Omega* 2021, *6*, 5717–5729.
[26] B.A. Mei, O. Munteshari, J. Lau, B. Dunn, L. Pilon, *J. Phys. Chem. C* 2018, *122*, 194–206.
[27] A. Cymann-Sachajdak, M. Graczyk-Zajac, G. Trykowski, M. Wilamowska-Zawłocka, *Electrochimica Acta* 2021, *383*, 138356.
[28] J. Liu, J. Wang, C. Xu, H. Jiang, C. Li, L. Zhang, J. Lin, Z. X. Shen, *Adv. Sci.* 2018, *5*, 1700322.
[29] K. M. Thulasi, S. T. Manikkoth, A. Paravannoor, S. Palantavida, B. K. Vijayan, *International Journal of Materials Research* 2021, *0*, 000010151520207828.
[30] A. M., A. Paul, *ACS Omega* 2017, *2*, 8039–8050.

* (The image in figure 2.7a taken from internet sources)

Abstract

Vanadium oxides are highly regarded for their versatility, readily transitioning between multiple oxidation states and adopting various polymorphic phases. This synthesis involves a template-free, one-step hydrothermal synthesis to produce mesoporous monoclinic VO_2(B) nanosheets and its self-assembled VO_2(B)-RGO nanoflower binary hybrid. This strategic incorporation of graphene oxide during synthesis significantly enhanced the electrochemical properties of the nanosheets, elevating their potential for supercapacitor applications. When tested as a symmetric supercapacitor device with a neutral aqueous electrolyte of 0.1 M Na_2SO_4, the monoclinic VO_2(B) nanosheets exhibited an impressive specific capacitance of 232.56 F/g at a scan rate of 5 mV/s, within a potential window of 1V. Likewise the binary hybrid nanoflowers, with the same potential window and electrolytic conditions, demonstrated a remarkable specific capacitance of 469.38 F/g at 5 mV/s, along with energy density of 1.57 Wh/kg and a formidable power density of 12.94 W/kg. The elegant design of the hybrid nanoflowers exhibits exceptional stability of 50000 cycles as well. The same binary hybrid tested for asymmetric supercapacitor and ended up with a specific capacitance of 68.88 F/g at 5mV/s with a potential limit of 1.5 V. This provided an enhanced energy density of 1.96 Wh/kg and power density of 26.04 W/kg. The implications of this research are profound, as the improved electrochemical properties of the VO_2(B)-RGO nanoflowers hold immense promise for future applications in advanced energy storage systems and beyond.

Key Words: Monoclinic VO_2(B) polymorph, Nanosheets, Hydrothermal, Reduced Graphene Oxide binary hybrid, Energy storage

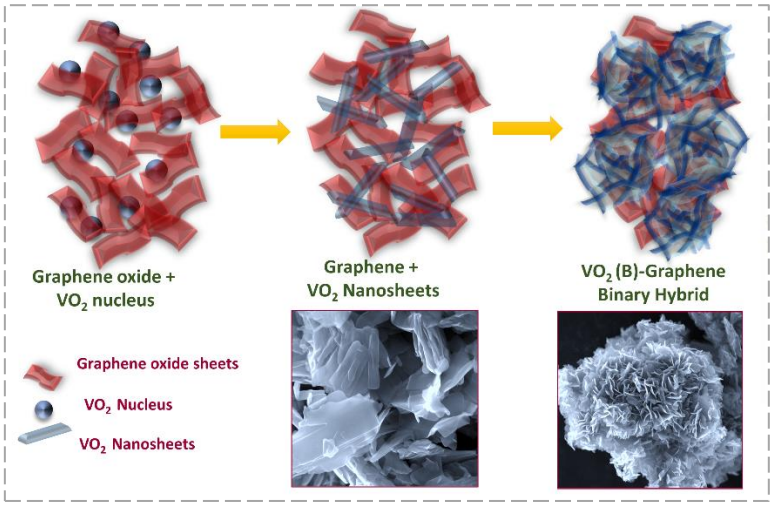

3. Temperature Tuned Phase Selective Synthesis of VO_2 (B) Nanosheet and Its Self-Assembled Flower like Binary Hybrid

Introduction

Vanadium exists as a partially filled 3d orbital in electronic configuration, which leads to different oxides such as VO, V_2O_5, V_2O_3, VO_2, V_4O_7, V_6O_{13} etc[1]. These variety of vanadium oxides are classifieds into different series like Magneli ($V_n O_{2n-1}$) and Wadsley ($V_{2n} O_{5n-2}$)[2]. The system is well studied due to its first-order reversible phase transition between the semiconductor and metallic states at its critical temperature of 68°C. This transformation alters the electronic structure as well as the optical properties of vanadium oxide. VO_2 exists in a rutile hexagonal structure above the transition temperature and below its transition temperature exist as the monoclinic system. This is where the metal-to-semiconductor conversion is taking place and is in an invertible transition state[3]. Vanadium dioxide[4], a significant binary compound, exists in five crystalline phases, rutile type VO_2(R), monoclinic VO_2(M), tetragonal VO_2(A), VO_2(B) and VO_2(C)[3]. In the view of previous literatures, the VO_2(R) and VO_2(M) exhibit fully reversible metal-semiconductor phase transitions (MST) at the critical temperature of 68 ^oC[5] by showing a clear transformation in the electrical resistivity and optical transmittance of magnitude around 10^4-10^5[6]. VO_2(A) is a meta-stable phase that possess a three-dimensional network of VO_6 octahedron. The VO_2(B) is a metallic phase consists of distorted octahedron which sharing corners and edges. Its layered structure, excellent nanoscale properties, and ability to switch between crystalline and amorphous phases under high pressure make vanadium oxide an attractive cathode material for Li-ion batteries[6] and supercapacitors[7,8]. Numerous synthesis methods, including Pulsed Laser Ablation[7], Magnetron Sputtering[8], Chemical Vapour Deposition[9], Sol-Gel[2] synthesis, Wet Chemical methods[1], Thermolysis[10], and Hydrothermal synthesis[11], are used to produce VO_2(B) polymorph. Hydrothermal synthesis is one of the better options because of its lower temperature, green reaction conditions, simplicity of operation, and low cost. Furthermore, morphology and porosity tuning can be accomplished by varying surfactants, templates, and solvents. The VO_2(B) of various nanostructures, such as 0D[12], 1D[13], nanorods[13], nanotubes and nanobelts, 2D[14,15]nanosheets and 3D[16–19] nanoflowers, is achievable with different synthesis selection and reaction circumstances.

In this study, a one-step hydrothermal method is employed for the synthesis of 2D nanosheets of the VO_2(B) phase. As a result, the VO_2(B) monoclinic polymorph was the only polymorph present without any interference from other polymorphs. To further enhance its electrochemical properties, the VO_2(B) nanosheets are ingeniously converted into a binary hybrid by incorporating graphene oxide (GO). This novel hybridization of VO_2(B) with graphene holds great promise for improving its electrochemical performance. A binary hybrid is formed by altering the concentration of graphene precursor. Supercapacitors use these hybrid compounds as electrode materials with aqueous electrolytes. The morphology tuned vanadium oxide and graphene incorporated hybrid exhibits excellent performance as a supercapacitor electrode.

3.1 Experimental

3.1.1 Materials Used

Ammonium metavanadate (NH_4VO_3) and Oxalic acid ($H_2C_2O_4$) were used for synthesis of VO_2(B). Graphite, Conc. Sulphuric acid (H_2SO_4), Potassium permanganate ($KMnO_4$) and 30% Hydrogen peroxide (H_2O_2) were used in Modified Hummers method for the synthesis of graphene oxide. All chemical reagents used for the synthesis are AR grade without further purification.

3.1.2 Synthesis

3.1.2.1 Synthesis of Monoclinic VO_2 (B) Nanosheets

This approach is intended to be a simple, easy, and convenient one-step synthesis of VO_2(B) nanosheets. In 50 mL of deionized water, combine oxalic acid and vanadium precursor in a 1:0.75 molar ratio. The reaction mixture was then moved to a 100 mL Teflon liner in a stainless-steel autoclave, followed by an 18-hr hydrothermal reaction at 160 ^oC. The final product was washed with water copiously and then extracted with ethanol to yield a blue- black precipitate. The acquired precipitate was dried for a few hours at 55 ^oC to obtain the final VO_2 powder, labelled as V160. The procedures were performed for the temperatures of 180 ^oC, 200 ^oC and samples were labelled as V180 and V200.

3.1.2.2 Synthesis of VO_2 (B)-RGO Binary Hybrid

To enhance the electrochemical performance of the VO_2(B) nanosheets, graphene oxide synthesized by modified Hummer's method is added to the reaction. The graphene oxide stock solution was prepared in 10 mg/mL. Subsequently, 1 mL and 2 mL of the graphene oxide were added to the reaction mixture to create binary hybrid denoted as VR1 and VR2, respectively. Figure 3.1 represents the process of generating VO_2(B) nanosheets and binary hybrid through

hydrothermal method.

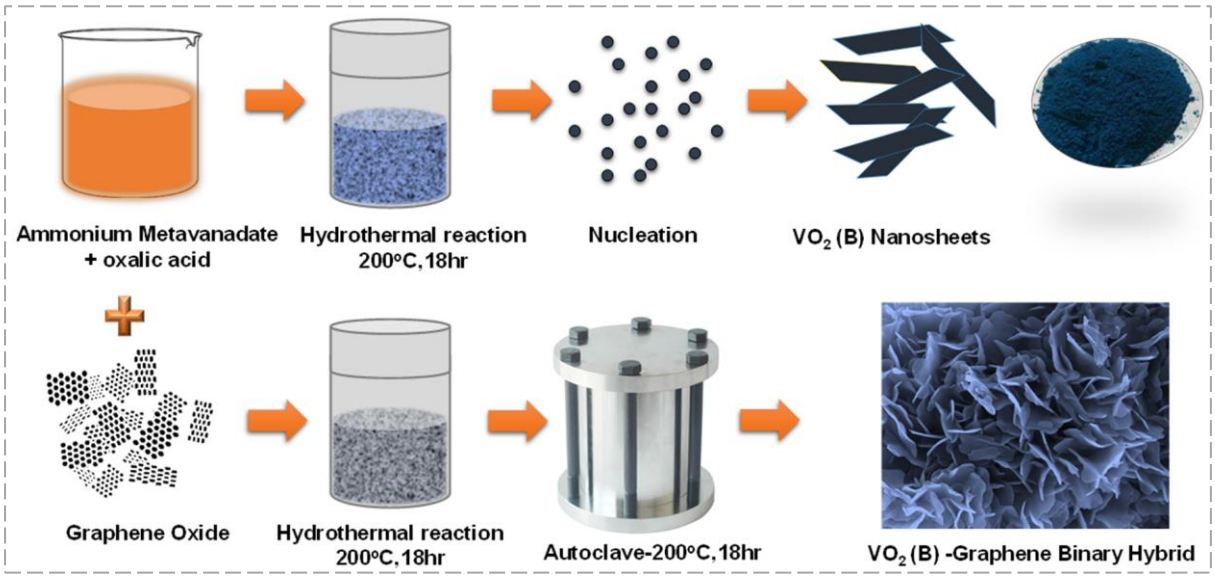

Figure 3.1 One-pot hydrothermal synthesis procedure of Vanadium oxide polymorph; monoclinic VO_2(B) nanosheets and its graphene binary hybrid nanoflower

3.1.3 Characterizations

Analyses were conducted on VO_2(B) nanosheets and their binary hybrids prepared by hydrothermal method. PANalytical-Xpert3 powder X-ray diffractometer (XRD) was used to study the crystal structure and other information. Raman analysis was performed with a 532 nm DPSS laser (Alpha 300RA, WiTec, Germany). FESEM (ZEISS-GEMINI SEM 300) was used for morphology and microstructure analysis. A BELSORP- max BET surface area analyzer was used to determine the porosity and surface area of the samples. The wettability characteristics were measured using a Kyowa drop master DMs 401 equipped with the FAMAS interface measurement and analysis system. The electrochemical studies like CV, GCD, EIS and cyclic stability were tested by Biologic SP-150 and SP-300 electrochemical workstation.

3.1.4 Formation Mechanism

A three-step process was described for the formation of VO_2(B) with ammonium metavanadate and oxalic acid. In the first step shown in equation (1), the ammonium metavanadate combines with oxalic acid to form an intermediate product and then converted into VOC_2O_4 in second stage in equation (2). On final stage, it was converted into main product, which is Vanadium (IV) oxide along with by-products CO_2 and CO as shown in equation (3) and (4)[12].

$$2NH_4VO_3 + 4C_2H_4O_4 \rightarrow (NH_4)_2[(VO_2)(C_2O_4)_3] + 2CO_2 + 4H_2O \quad (1)$$

$$(NH_4)_2[(VO)_2(C_2O_4)_3] \rightarrow 2VOC_2O_4 + 2NH_3 + CO + CO_2 + H_2O \quad (2)$$

$$VOC_2O_4 \rightarrow VO_2 + CO + CO_2 \quad (3)$$

Or simply we can represent via

$$NH_4VO_3 + 2H^+ + e^- \rightarrow VO_2 + H_2O + NH_4^+ \quad (4)$$

In hydrothermal synthesis both the time and temperature play a significant role in determining the morphology of final product. The formation of VO_2 is a staged process in which initially V^{5+} reduced to V^{4+}, and next stage the growth of VO_2 begins. Within the reaction medium, NH_4VO_3 decomposes into NH_4^+ and VO_3^- ions resulting in the formation of $(NH_4)_2$ $[(VO)_2(C_2O_4)_3]$. Further reactions lead to the formation of VOC_2O_4, eventually yielding VO_2. Pham et al examined the microstructure and luminescent properties of VO_2(B). They identified 80 °C as the onset of the higher temperature range where 2D nanosheets formation took place[12]. The development of the nanoparticles accelerates as the hydrothermal temperature approaches 200 °C. Due to a larger nucleation density in the reaction medium at this temperature, the production of 2D nanosheets is more pronounced. Compared to lower temperatures, higher hydrothermal temperatures result in highly crystalline structure. Microstructure of nanosheets or plates with a smooth surface generated under these conditions, without the use of any surfactants.

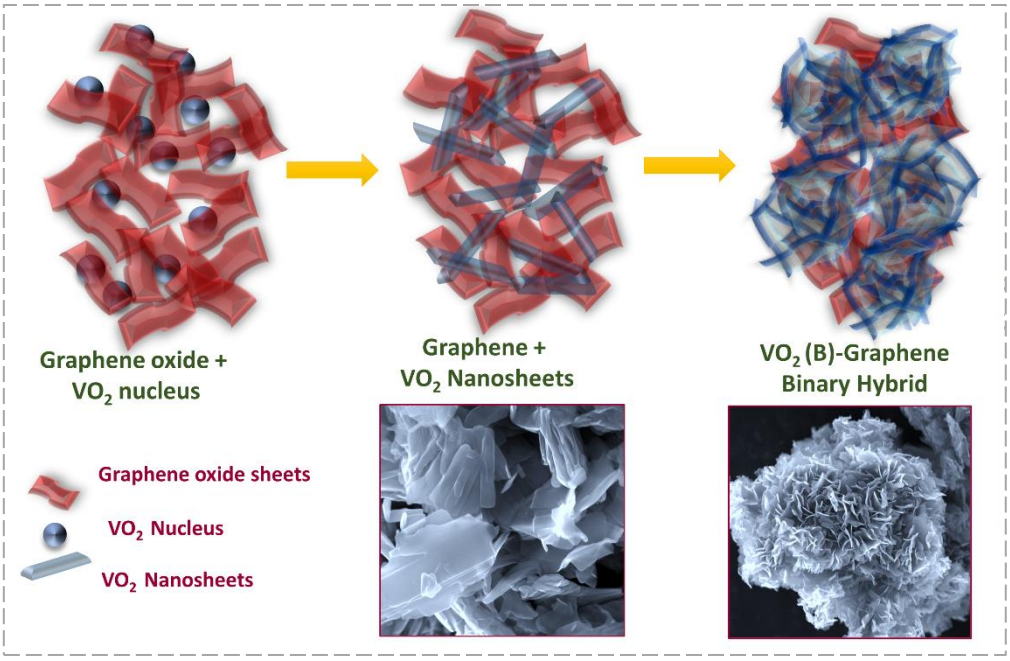

Figure 3.2 The schematics for the formation of a nanoflower monoclinic VO_2(B)-graphene binary hybrid through hydrothermal method

The VO_2(B)-RGO binary hybrid nanoflower is generated through the in-situ growth of VO_2(B) nanosheets over the graphene oxide surface. The graphene oxide undergoes reduction under hydrothermal condition of 200 °C. Initially, the VO_2 nucleus is attracted to the defect sites or flaws on the graphene oxide sheets. The VO_2 nucleus begins to expand when its radius reaches a critical threshold, and VO_2 nuclei or VO_2^+ ions start to combining, promoting core extension[16]. This process represents a unique self-assembly method of VO_2(B)-RGO binary

synthesis, where the nanoflowers are formed from nanosheets in the presence of graphene oxide sheets, shown in figure 3.2. This leads to the formation of VO_2(B)-graphene binary flower-like hybrids, along with the in-situ formation of graphene. The mechanism offers an effective electron pathway, improved electrical contacts, enhanced pseudocapacitive activity, high porosity, and high surface area and is rarely reported.

3.2 Results and Discussions

3.2.1 Structure and Phase Analysis

3.2.1.1 X-Ray Diffraction

The mesoporous monoclinicVO_2(B) nanosheets and VO_2(B)-RGO binary hybrid is synthesized by single step hydrothermal method. Figure 3.3 illustrates XRD pattern of a typical phase- pure VO_2(B) monoclinic, as validated using the JCPDS card number 81-2392.

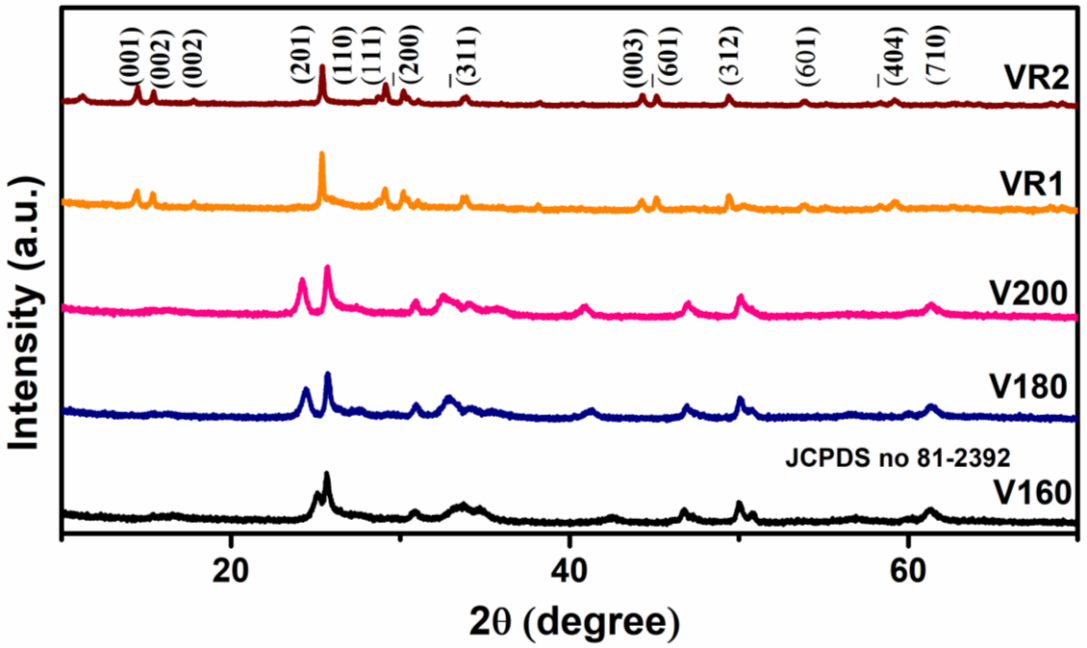

Figure 3.3 XRD pattern of the temperature tuned monoclincVO_2(B) polymorph (V160, V180, V200) and its binary hybrid of VO_2(B)-graphene (VR1, VR2)

It is possible to generate monoclinic VO_2(B) polymorphs at various reaction temperatures under the given reaction conditions. There are no additional peaks corresponding to other chemical or polymorphs are observed, and there are no impurity-related peaks present in the data. All peaks strictly fall inside the boundaries of VO_2(B) monoclinic of JCPDS card number 81-2392[18]. The structure belongs to monoclinic crystal system with space group of C2/m, lattice constant a =12.093 A^o, b = 3.702 A^o and c = 6.433 A^o and $\alpha = \gamma = 90^o$ and $\beta = 107.0^o$. The well crystalline nature of the samples demonstrated by the existence of sharp and strong

peaks[20]. The peak corresponding to the plane of (001) is sharp and indicate the perfect crystallinity. The broad peaks present at diffraction angle of 10^o-20^o represents the reduced graphene oxide formation, are completely resolved by the prolonged reaction time. These peaks are corresponded to the (002) and (100) reflections of graphitic planes, which demonstrate graphene integration and complete reduction of graphene oxide during synthesis.

3.2.1.2 Raman Analysis

Figure 3.4 shows the Raman spectra of VO_2(B)-RGO binary hybrid with five primary peaks and some subsidiary peaks. Peaks were observed at 145 cm^{-1}, 196 cm^{-1}, 286 cm^{-1}, 410 cm^{-1}, 695 cm^{-1}, 878 cm^{-1}, and 996 cm^{-1}. Vibration modes associated with monoclinic structure of VO_2(B) are represented by these peaks. 145 cm^{-1} and 196 cm^{-1} are two peaks evident in the low wavenumber region around 200 cm^{-1}. It is clear from these peaks that hydrothermally synthesized VO_2(B) has a layering structure. Observed peaks at 286 cm^{-1} and 410 cm^{-1} are caused by V=O bending vibrations. A peak at 695 cm^{-1} indicates the presence of V-O-V

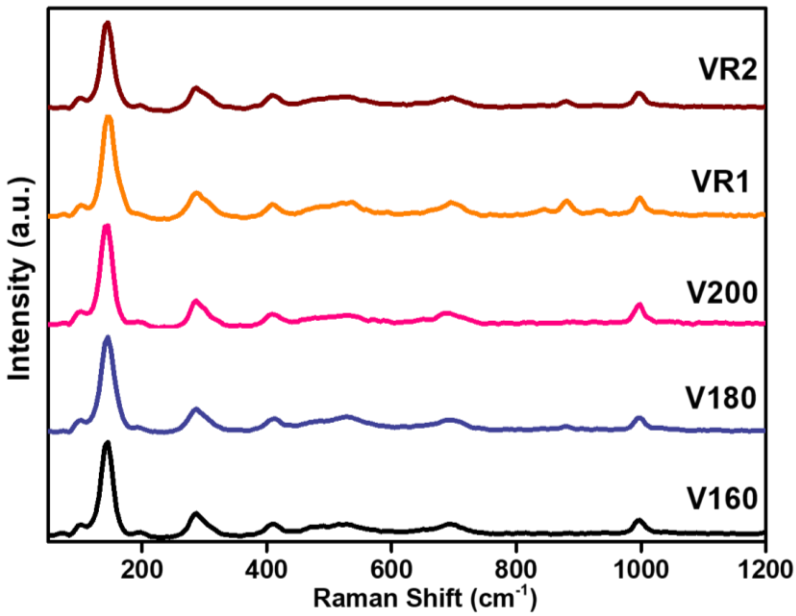

Figure 3.4 Raman spectra of the temperature tuned monoclincVO_2 (B) polymorph (V160, V180, V200) and its binary hybrid of VO_2(B)-graphene (VR1, VR2)

bending vibrations, while 996 cm^{-1} indicates the presence of terminal oxygen stretching vibrations. Raman spectra of Graphene reveal the presence of the D band at 1345 cm^{-1} and the G band at 1580 cm^{-1}[15,23].

3.2.2 Morphology Analysis

3.2.2.1 FE-SEM Analysis

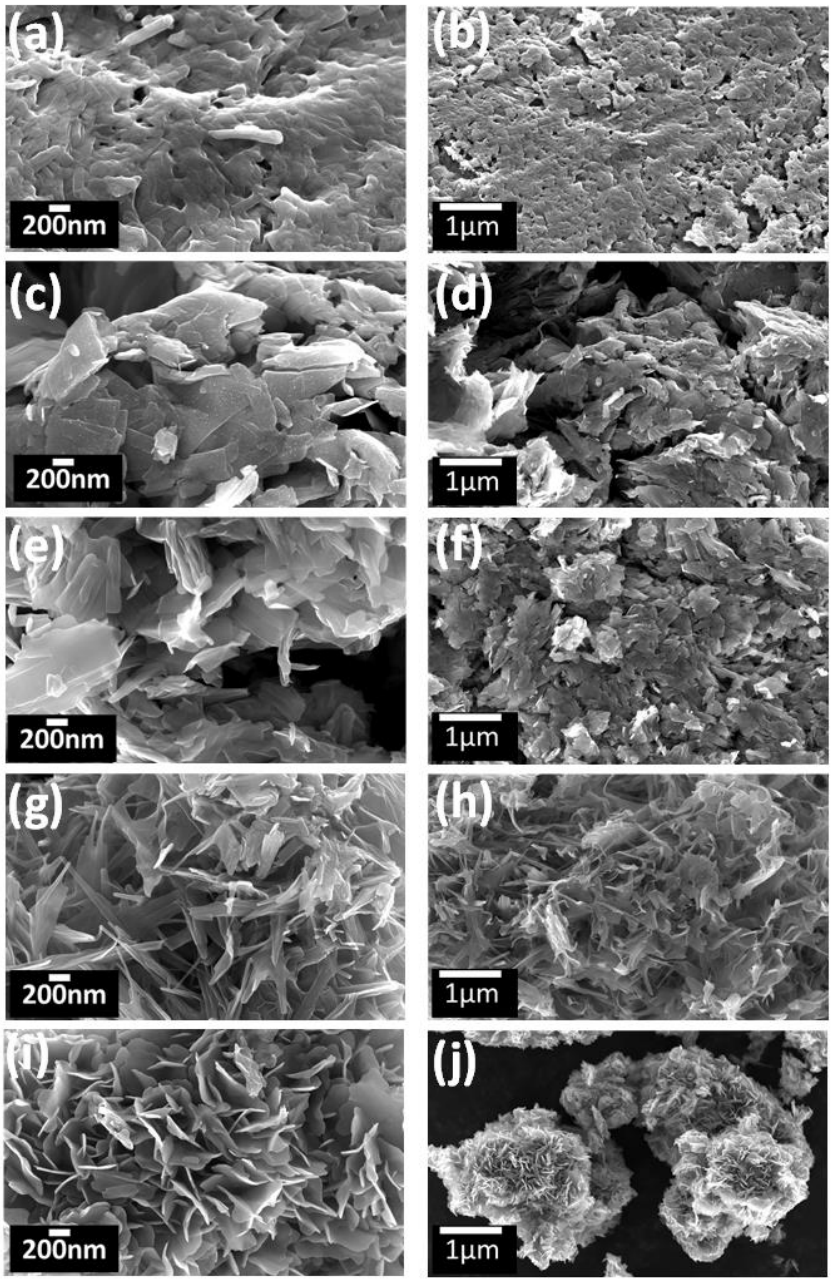

Figure 3.5 FE-SEM images of the VO_2(B) at different temperature and its binary hybrid at higher and lower magnification (a) and (b) V160, (c) and (d) V 180, (e) and (f) V200, (g) and (h) VR1 and (i) and (j) VR2

Figure 3.5a and 3.5b show how nanosheets take on a sticky and clumsy morphology during hydrothermal synthesis at 160 ^{o}C. Figure 3.5c-3.5f shows morphology changes at 180°C and 200 °C resulting in smoother, better nanosheets. Therefore, a reaction temperature of 200 °C

was chosen for further reactions. FE-SEM images (figure 3.5a, 3.5c and 3.5e) of the morphology demonstrate the tunability of nanosheet formation across three temperature ranges (160 °C, 180 °C, and 200 °C). Increasing the temperature from lower to higher speeds up the decomposition of oxalic acid. The reduction reaction is facilitated by this, resulting in the formation of nanosheets. The addition of graphene oxide to the reaction leads to the formation of nanoflowers. According to figure 3.5g - 3.5j, the nanosheets grew and developed in a petal-like arrangement, clustering together to form nanoflower-like structures.

3.2.3 Surface area and Porosity Analysis

3.2.3.1 BET Analysis

N_2 adsorption-desorption isotherms shown in figure 3.6a demonstrate the distinct porous properties of nanosheets made of VO_2 (B) and binary hybrid nanoflowers made of VO_2 (B) and graphene. The VO_2(B) nanosheets in figure 3.6a exhibit weak capillary condensation, manifested as a gradual and gentle increase in N_2 adsorption as pressure increases. Conversely, the binary hybrid nanoflower-based system exhibits a rapid and efficient uptake of N_2 molecules due to a sharp capillary condensation process at high relative pressure. In both nanosheets and binary hybrids, N_2 adsorption-desorption isotherms exhibit hysteresis of Type III and IV. According to the Type III H3 hysteresis, the material exhibits a weak interaction and is composed of non-rigid aggregates with plate-like particles or slit-shaped pores. The type IV H1 hysteresis is characterized by network of ink bottle shaped pores [24]. Overall, the presented data in figure 3.6a provide a comprehensive understanding of both the VO_2(B) nanosheet and its binary hybrid's porous nature and capillary condensation behaviour.

The BET specific surface area of the nanosheets varies with hydrothermal reaction temperature. At lower temperatures, the specific surface area is smaller. For instance, V160 shows a surface area of 9.58 m^2/g, indicating the absence of ideal nanosheets. However, at higher hydrothermal temperatures, the specific surface area increases significantly. The surface area of the V180 and V200 is 11.75 m^2/g and 22.95 m^2/g, respectively. VO_2(B) nanosheets exhibit a higher specific surface area than previously reported vanadium oxide systems with specific surface areas between 3-12 m^2/g. A binary hybrid, on the other hand, has relatively less surface area due to its morphological differences. Specifically, VR1 and VR2 yield specific surface areas of 7.87 m^2/g and 4.19 m^2/g, respectively.

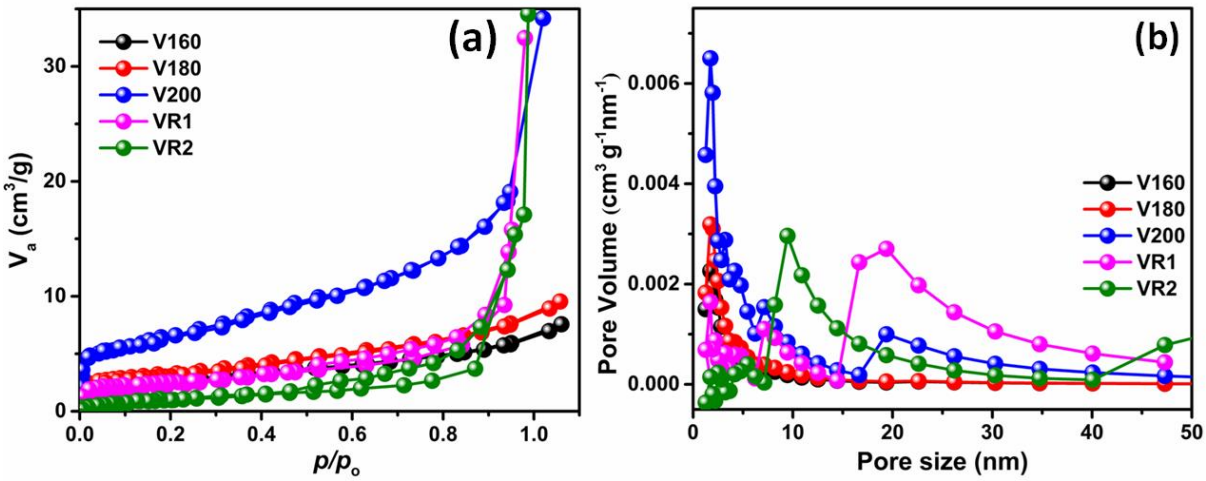

Figure 3.6 (a) N_2 adsorption-desorption isotherm and (b) BJH pore size distribution curves of VO_2 (B) nanosheets and its binary hybrid VO_2(B)-graphene hybrid

Based on the BJH analysis shown in figure 3.6b, the nanosheets have an average pore size of 4.21 to 7.57 nm, indicative of mesopores. On the other hand, the binary hybrids exhibit larger pore sizes, ranging from 25.50 nm to 50.96 nm. The total pore volume falls within the range of 0.01 cm^3/g to 0.05 cm^3/g as tabulated in Table 3.1, providing ample space for ion storage and migration. The high mesoporosity of the nanosheets and the unique flowerlike morphology of the binary hybrids make them promising candidate for energy storage. This study demonstrates the correlation between hydrothermal reaction temperature, specific surface area, and porosity during the synthesis of VO_2(B) nanosheets and binary hybrids. It is highly promising for a wide range of applications that these findings provide valuable insights for the design of nanomaterials with improved properties.

Sample	SSA^a_{BET} (m^2/gm)	TPV^b (cm^3/g)	Mean Pore Diameter^c (nm)
V160	9.58	0.01	4.21
V180	11.75	0.01	4.40
V200	22.95	0.04	7.57
VR1	7.87	0.05	25.50
VR2	4.19	0.05	50.96

Table 3.1 The total specific surface area, total pore volume and mean pore diameter of the hydrothermally synthesized VO_2 (B)-at different temperature and binary hybrids

[^{a}SSA-specific surface area obtained from BET (Brunauer-Emmet-Teller) method, ^{b}TPV-total pore volume and ^{c}Mean pore diameter-average pore size diameter from BJH (Barret-Joyner-Halenda) method]

3.2.4 Wettability Characteristics

3.2.4.1 Contact Angle Measurement

The hydrothermal temperature variation influences the material's contact angle[21], indicating fluctuations in hydrophilic properties as shown in figure 3.7a-3.7e. Higher temperatures lead to smooth nanosheets due to the complete reduction of oxalic acid. Consequently, the wettability increases, as seen by the reduced contact angle. V200 nanosheets exhibit the highest wettability of 12.3º compared to V160 at 25.5º and V180 at 13.6º. The binary hybrids like VR1 and VR2 have contact angles of 15.7º and 32.7º, respectively, surpassing those of nanosheets. The addition of graphene oxide not only alters the surface wettability but also enhancing pore diameter due to morphology change and make it more advantageous for energy storage.

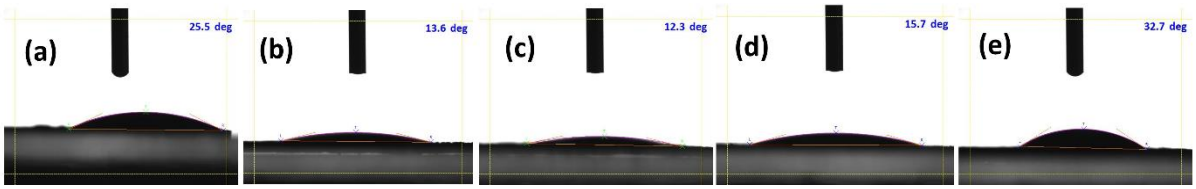

Figure 3.7 Contact angle measurement of the VO_2(B) Nanosheets (a) V160, (b) V180, (c) V200 and VO_2(B)-Graphene nanoflowers (d) VR1 and (e) VR2

3.2.5 Electrochemical Property Analysis - Supercapacitor Applications

3.2.5.1 Electrode Preparation

The working electrode is made by mixing 75% VO_2 with 15% carbon black as a conducting additive and 10% polyvinylidene fluoride as a binder. A homogeneous slurry was made with N-methyl pyrrolidone, and the substrate was coated with doctor blade technique (1x1 cm^2). The electrode material was then dried at 90 °C for a few hours. We calculated the weight of the active material by comparing the weight of the current collector before and after coating. With a two-electrode system, cyclic voltammetry is performed using sodium sulphate (Na_2SO_4) as an electrolyte. Whatman filter paper, soaked in the electrolyte for 10 hours is used as the separator. The symmetric cell is fabricated by sandwiching two coated electrodes with electrolyte.

3.2.5.2 Electrochemical Analysis- Symmetric Supercapacitor Formation

The electrochemical performance of VO_2(B) nanosheets and their binary hybrid was initially evaluated with cyclic voltammograms (CVs), galvanostatic charge discharge (GCD) and

electrochemical impedance spectroscopy (EIS). These measurements were performed in a two-electrode symmetric configuration, utilizing 0.1 M Na_2SO_4 aqueous electrolyte. The CV curves depicted in figure 3.8 a is obtained at a scan rate of 5 mV/s covering a potential range of 0 V to 1 V. The presence of redox peaks within the CV curves signifies the existence of redox couples, suggesting that energy storage is accomplished through redox reactions. Similarly, comparison of the GCD profiles at current density of 0.25 A/g is seen in figure 3.8b.The coexistence of V^{4+} and V^{5+} ions on the surface of the VO_2(B) nanosheets[19,22] facilitates the redox reactions as described in equation 5. The coexistence of these oxidation states promotes the occurrence of redox reactions, there by contributing to the excellent electrochemical performance of the material.

$$VO_2 + xNa^+ + xe^- \leftrightarrow Na_xVO_2 \qquad (5)$$

In various studies, symmetric supercapacitors operating within a voltage range of 0 V to 1.0 V were investigated with scan rates ranging from 5 mV/s to 100 mV/s. The figure 3.8c displays the CV of VR1 at different scan rate and figure 3.8d is the GCD profile at various current densities. The symmetric supercapacitor's curve shape remained consistent with increasing scan rates, indicating enhanced rate capability. The specific capacitance calculated from the CV are 106.28 F/g, 74 F/g, 232.56 F/g, 469.38 F/g and 152.76 F/g for V160, V180, V200, VR1 and VR2 at 5mV/s. The VR1 gives the energy density of 1.57 Wh/kg and power density of 12.94 W/kg at current density of 0.25 A/g. A Comparison of EIS spectra of both V200 and VR1 is given in figure 3.8e. This shows that the increased specific capacitance of VR1 attributed to its lower charge transfer resistance as indicated by the smaller semicircle. Exceptional cyclic stability of 50000 cycles is exhibited by this system as shown in figure 3.8f. Among nanosheets, V200 has the highest surface area, as well as the highest specific capacitance. The development of binary hybrids, which increased porosity and surface area, further boosted its electrochemical activity.

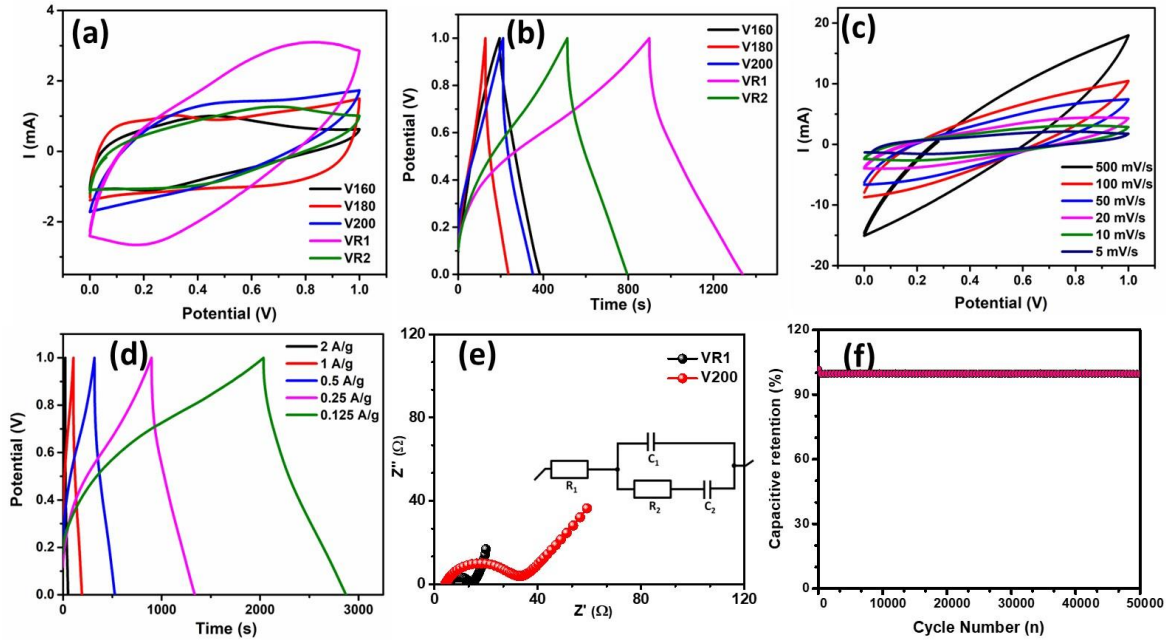

Figure 3.8 Electrochemical performance of materials (a) comparison of CV at 5.0mV/s, (b) comparison of GCD at 0.25A/g of V160, V180, V200, VR1 and VR2, (c) CV of VR1 at different scan rate, (d) GCD of VR1 at different current densities, (e) EIS spectra of V200 and VR1 and (f) cyclic stability test of VR1

3.2.5.3 Quantification of Specific Capacitance

Trassati's method was employed to quantify the contribution of storage mechanisms based on the obtained data. In this analysis, a semi-infinite diffusion condition was assumed, where ions freely diffuse to the electrode-electrolyte interface from the bulk electrolyte[18,23]. The addition of the graphene can contribute more capacitive property in VR1 than that of V200. Figure 3.9 shows the formation of a binary hybrid (VR1) exhibiting higher EDLC characteristics than V200 via its higher specific capacitance. A higher proportion of pseudocapacitive nature is found in V200 (95.05%) than in VR1 (90.33%), which indicates that VR1 contributes more EDLC than V200.

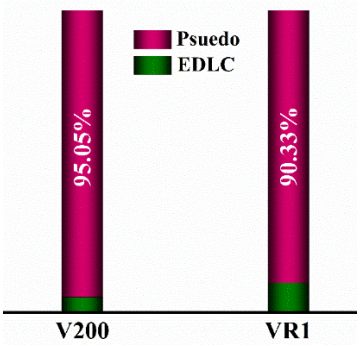

Figure 3.9 Quantification of the specific capacitance of VO_2(B) and its binary hybrid

Our newly developed hybrid material, which combines VO_2(B) with graphene, exhibits outstanding electrochemical properties. In 0.1 M Na_2SO_4 aqueous electrolyte media at 5 mV/s scan rate, it exhibits excellent electrochemical properties by showcasing a specific capacitance of 469.38 F/g. This remarkable performance can be attributed to the high conductivity of graphene, which significantly enhances electron transport and improves the electrochemical properties of the composite. Comparatively, the results surpass those achieved by previously studied nanocomposites, such as RuO_2-RGO nanocomposites[24], Fe_3O_4-carbon nanocomposites[25], and β-$Cu_2V_2O_7$-TiO_2-RGO nanocomposite[26], all of which show increased activity. Zhang et al synthesized VO_2 (B) polymorph with the carbon material to make the composite/hybrid[22]. The prepared VO_2 (B) carbon core shell composite exhibit 203 F/g in 1 M Na_2SO_4 aqueous electrolyte media at 0.2 A/g of current density with excellent energy density and power density. Similarly, Ren et al prepared edge-oriented graphene form as carbon source with VO_2 nanoparticles to form VO_2-EOGF. The electrochemical properties obtained for this combination is 119 mF/cm^2 at the scan rate of 2 mV/s and observed two-fold increase over EOGF alone[9].

3.2.5.4 Electrochemical Analysis- Asymmetric Supercapacitor (ASC) Formation

An asymmetric supercapacitor (ASC) was fabricated using activated carbon (AC) as the positive electrode and a VO_2(B)-graphene binary hybrid as the negative electrode[27]. Interestingly, the combination of these materials led to an extended potential window by achieving an increase of 1.5 V, as shown in figure 3.10a. The CV and GCD profiles of VR1//AC ASC shown in figure 3.10b and 3.10c provide specific capacitance of 68.88 F/g at 5 mV/s and 62.96 F/g at 0.125 A/g. The ASC delivers an energy density of 1.96 Wh/kg with a power density of 26.04 W/kg at 0.125 A/g. Impedance curves are obtained by fitting the appropriate equivalent circuit to the frequency range from 10 kHz to 50 mHz. Figure 3.10d displays the impedance curve of ASC. The improved charge-transfer is facilitated by a lower solution resistance, leading to faster electron transport.

The VR1//AC ASC provides continuous charge- discharge cycles, indicating its ability for long-term cyclic capacity. It can endure 3000 cycles of charging and discharging with a retention of 97%, as shown in figure 3.10e. It is clear from this retention that the supercapacitor is capable of operating in the designated potential window with stable performance. In conjunction with activated carbon, the VO_2-graphene binary hybrid offers enhanced specific surface area. This expanded surface area facilitates more efficient ion adsorption and

desorption during charge and discharge cycles. By enhancing electrolytic ion penetration into the binary hybrid structure, the asymmetric supercapacitor maintains excellent electrical conductivity.

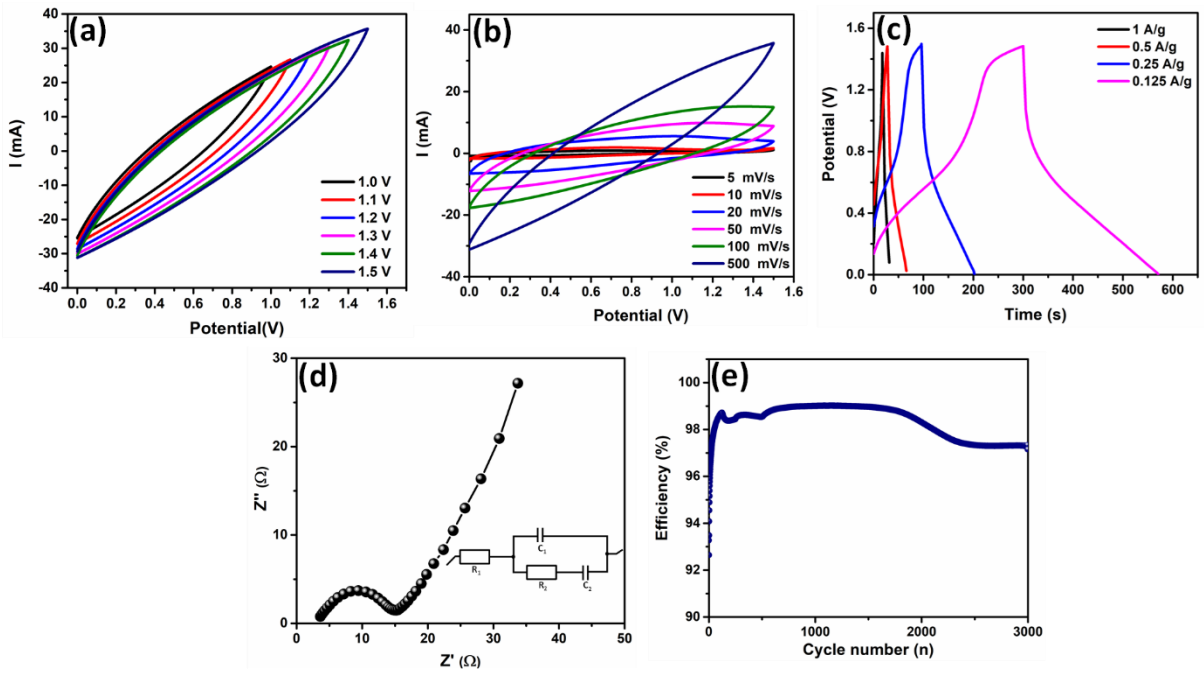

Figure 3.10 Electrochemical studies of AC// VR1 ASC (a) optimization of the voltage window limits, (b) performance of CV at various scan rates, (c) GCD studies at different current densities, (d) EIS analysis and (e) Cyclic stability measurement during 3000 charge- discharge cycles

3.3 Conclusion

In this study, monoclinic VO_2(B) nanosheets were successfully synthesized in a single stage hydrothermal approach. A symmetric supercapacitor constructed with VO_2(B) and an aqueous neutral electrolyte of 0.1 M Na_2SO_4, operated at a working potential of 1.0 V, exhibits a specific capacitance of 232.56 F/g at 5 mV/s. To enhance the capacitance activity, a binary hybrid was created by incorporating graphene oxide into VO_2(B). During the synthesis, graphene oxide was converted in situ to graphene, leading to the formation of vertically aligned nanoflowers that exhibited superior performance compared to VO_2(B) nanosheets. This VO_2(B)-graphene binary hybrid demonstrated a remarkable specific capacitance of 469.38 F/g at 5 mV/s, along with an energy density of 1.57 Wh/kg and a power density of 12.94 W/kg at a current density of 0.25 A/g. In addition to exhibiting impressive cyclic stability over 50,000 cycles of charging and discharging, this binary nanoflower hybrid demonstrated significant improvements in electrochemical storage capacity and electrical conductivity. Furthermore, an asymmetric supercapacitor AC//VO_2(B)-graphene hybrid was developed, with a stable potential window of 1.5 V and a specific capacitance of 68.88 F/g at 5 mV/s. At a current density of 0.125 A/g,

this asymmetric supercapacitor demonstrated an energy density of 1.96 Wh/kg and a power density of 26.04 W/kg. Due to the close contact between VO_2(B)-graphene hybrid and highly porous AC, the asymmetric supercapacitor was able to withstand 3,000 charge-discharge cycles without losing performance. The results of this study demonstrate the successful development of a binary nanoflower hybrid with enhanced electrochemical properties with outstanding stability and performance. These findings present exciting possibilities for the development of future high-performance energy storage systems.

*****

References

[1] P. Hu, P. Hu, T. D. Vu, M. Li, S. Wang, Y. Ke, X. Zeng, L. Mai, Y. Long, *Chem. Rev.* **2023**, *123*, 4353–4415.
[2] M. M. Seyfouri, R. Binions, *Solar Energy Materials and Solar Cells* **2017**, *159*, 52–65.
[3] X. Sun, Z. Qu, Q. Wang, Y. Yuan, *J Mater Sci: Mater Electron* **2020**, *31*, 16053–16064.
[4] R. B. Rakhi, D. H. Nagaraju, P. Beaujuge, H. N. Alshareef, *Electrochimica Acta* **2016**, *220*, 601–608.
[5] H. Qin, S. Liang, L. Chen, Y. Li, Z. Luo, S. Chen, *Sustainable Energy Fuels* **2020**, *4*, 4902–4933.
[6] N. Li, W. Huang, Q. Shi, Y. Zhang, L. Song, *Ceramics International* **2013**, *39*, 6199–6206.
[7] Z. A. Umar, R. Ahmed, H. Asghar, U. Liaqat, A. Fayyaz, M. A. Baig, *Materials Chemistry and Physics* **2022**, *290*, 126655.
[8] Y. Wang, X. Li, X. Yan, S. Dou, Y. Li, L. Wang, *Materials* **2023**, *16*, 5093.
[9] G. Ren, R. Zhang, Z. Fan, *Applied Surface Science* **2018**, *441*, 466–473.
[10] T. Zhang, Q. Li, *Journal of Solid State Chemistry* **2022**, *311*, 123117.
[11] L. Huang, L. Shi, X. Zhao, J. Xu, H. Li, J. Zhang, D. Zhang, *CrystEngComm* **2014**, *16*, 5128–5133.
[12] Vuong Hung Pham, P. Duong Hong Quan, Nguyen The Manh, Vu Thi Ngoc Minh, Cao Xuan Thang, Phuong Dinh Tam, Duong Van Thiet and Hoang Nhu Van, Hoang Nhu Van, *Special Matrices* **2019**, *7*, 1–19.
[13] M. S. Kang, S. K. Park, P. Nakhanivej, K. H. Shin, J. S. Yeon, H. S. Park, *Journal of Alloys and Compounds* **2021**, *855*, 157361.
[14] S. Chen, H. Yu, L. Chen, H. Jiang, C. Li, *Chemical Engineering Journal* **2021**, *423*, 130208.
[15] Y. Fan, D. Ouyang, B.W. Li, F. Dang, Z. Ren, *Nanoscale Res Lett* **2018**, *13*, 142.
[16] Y. Zhang, X. Jing, Y. Cheng, T. Hu, M. Changgong, *Inorg. Chem. Front.* **2018**, *5*, 2798–2810.
[17] H.C. Chen, Y.C. Lin, Y.L. Chen, C.J. Chen, *ACS Appl. Energy Mater.* **2019**, *2*, 459–467.
[18] C. Nethravathi, C. R. Rajamathi, M. Rajamathi, U. K. Gautam, X. Wang, D. Golberg, Y. Bando, *ACS Appl. Mater. Interfaces* **2013**, *5*, 2708–2714.
[19] H. Wang, H. Yi, X. Chen, X. Wang, *J. Mater. Chem. A* **2014**, *2*, 1165–1173.
[20] Q. Kang, Y. Zhang, S. Bao, G. Zhang, *R. Soc. open sci.* **2019**, *6*, 181116.
[21] M. M. Vadiyar, S. C. Bhise, S. K. Patil, S. S. Kolekar, A. R. Shelke, N. G. Deshpande, J. Y. Chang, K. S. Ghule, A. V. Ghule, *Chem. Commun.* **2016**, *52*, 2557–2560.
[22] J. Zhang, L. Chen, Y. Wang, S. Cai, H. Yang, H. Yu, F. Ding, C. Huang, X. Liu, *Nanomaterials* **2018**, *8*, 1020.
[23] A. Cymann Sachajdak, M. Graczyk Zajac, G. Trykowski, M. Wilamowska Zawłocka, *Electrochimica Acta* **2021**, *383*, 138356.
[24] M. Ates, M. Yildirim, O. Kuzgun, H. Ozkan, *Journal of Alloys and Compounds* **2019**, *787*, 851–864.
[25] S. Kaipannan, K. Govindarajan, S. Sundaramoorthy, S. Marappan, *ACS Omega* **2019**, *4*, 15798–15805.
[26] S. Shuang, L. Girardi, G. Rizzi, A. Sartorel, C. Marega, Z. Zhang, G. Granozzi, *Nanomaterials* **2018**, *8*, 544.
[27] X. J. Ma, W. B. Zhang, L. B. Kong, Y. C. Luo, L. Kang, *RSC Adv.* **2015**, *5*, 97239–97247.

Abstract

This work involves the synthesis of highly conducting, ultra-thin, mesoporous manganese dioxide, nanotubes and nanowires, using a sol-gel technique. This is a template-free method for preparing mesoporous (3.3 to 5.4 nm) nanotubes and nanowires of 10-15 nm radius with surface area (221.19 m^2/g-102.09 m^2/g). In the MnO_2 lattice, oxygen and cationic vacancies are tailored by changing the reducing agent for improved energy storage. X-ray photoelectron spectroscopic studies are conducted to quantify the oxygen and cationic vacancies. The tailored one-dimensional δ-MnO_2 is used as an electrode material for symmetric and asymmetric supercapacitor designs. A non-toxic, less volatile aqueous neutral electrolyte is used for the supercapacitive measurement, giving a specific capacitance of 460.75 F/g at 2 mV/s with symmetric mode at 1V. With activated carbon, this material can also produce asymmetric supercapacitors with a specific capacitance of 107.38 F/g at 10 mV/s at 1.7 V.

Key Words: Conducting δ-MnO_2; mesoporous metal oxides, ultra-thin one-dimensional nanostructure, energy storage

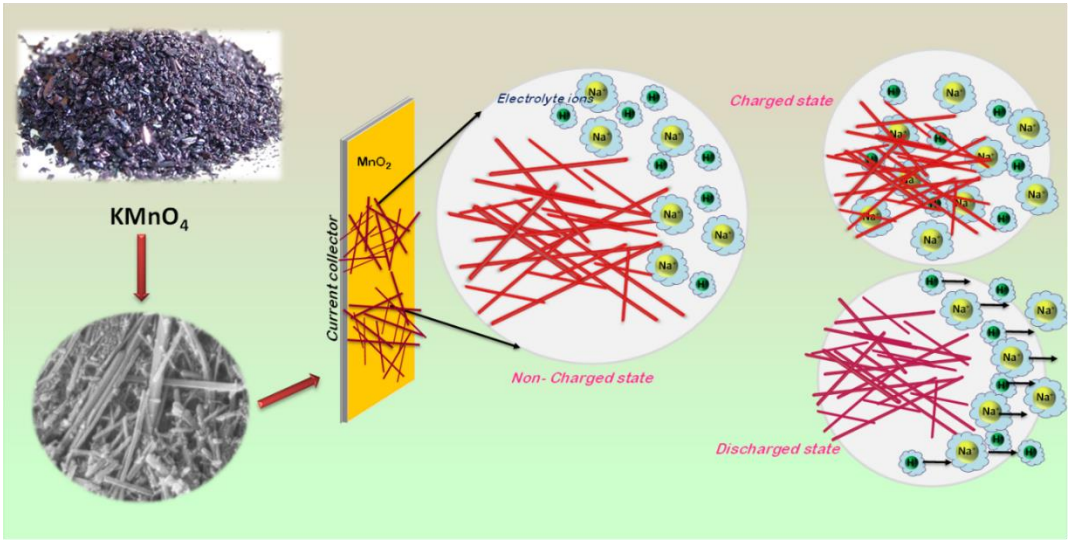

4. Porosity and Defect Tuned δ-MnO_2 Polymorph with Enhanced Electrochemical Activity

Introduction

Metal oxides are important materials due to their semiconducting nature, different optoelectronic properties, and morphologies. In addition to its low cost and environmental friendliness, manganese oxide (MnO_2) tunable physical and chemical properties [1]. MnO_2 is an interconnected MnO_6 octahedron with the Mn atom placed at the centre and the oxygen atoms at the vertices. In MnO_6, layered, tunnelled and other forms with a monoclinic crystal system are possible due to the varying structures and stoichiometries of MnO_2 [2]. MnO_2 is one of the most promising transition metal oxide materials due to its straightforward, mild preparation processes using easily accessible and reasonably priced materials.

MnO_2 is regarded as a viable candidate for electrode material in electrochemical capacitors due to its low cost, non-toxicity, abundance, easy synthesis, environmental friendliness and strong theoretical specific capacitance (1100 F/g to 1300 F/g) [3,4]. The crystalline MnO_2 exists in a variety of crystal structures (α,β,γ and δ) based on their preparation methods and its specific capacitance varies somewhat based on the phase in which it is formed [5,6]. By considering a few results of MnO_2, in an aqueous neutral electrolyte solution α-MnO_2 shows specific capacitance ranging from 265 F/g to 320 F/g [7]. The δ-MnO_2 has also a higher capacitive nature due to its layered structure, which is similar to graphene [8]. One of the most important elements in determining the specific capacitance of a synthesized material is its morphology. For MnO_2, different morphologies, such as nanosheets [9], nanoflowers [10], nanowires [11], nanobelts [12], nanoneedles [13], nanorods [14] and nanospheres [4] are possible. Its unique surface area, which is between 20 m^2/g and 150 m^2/g, also influences the performance. The large specific surface area increases the active sites and hence the specific capacitance improved [15,16]. Another method to increase MnO_2 performance is to make some vacancies. Oxide systems are more active when there are vacancies or defects in them. Chen *et al*. note this improvement in α-MnO_2, which after chemical preparation shows a high capacitance of 736.60 F/g and a specific surface area of 119.50 m^2/g [17]. Yang *et al*. chemically prepared doped MnO_2 with various cations, such as Cu^{2+}, Co^{2+} and Ni^{2+} ions [18]. Doping with metal ions alters the intrinsic conductivity of crystalline systems due to the induced defect. In comparison to the other two metal cations, Ni^{2+} doped MnO_2 measured with a high specific capacitance of 234 F/g at 8 A/g. In δ-MnO_2 prepared via electrostatic self-assembly, Gao et al. introduce surface Frenkel defects

that result in porous nanosheets with specific surface area of 150 m^2/g and specific capacitances of 306 F/g at 0.2 A/g [19]. The defect-induced MnO_2 materials are used for optical and catalytic studies [20,21], batteries [6,22] and ion exchange [23,24] systems in addition to supercapacitor [25] research.

A simple and easy procedure is described here for creating mesoporous and ultrathin one-dimensional nanowire/nanotubes with oxygen and cation vacancies in layered δ-MnO_2 comes under the category of the point defects, resulting in high conductivity and specific capacitance. This type of layered structure is also known as birnessite MnO_2, it contains mixtures of Mn (III)/Mn (IV) or Mn (II)/Mn (IV) redox couples. It takes long periods of time and many steps to synthesize birnessite phases through a phase selected approach. The high conductivity of MnO_2 in this study results in a higher supercapacitive activity. By using symmetric capacitor design and an operating potential window of about 1.0 V, 460.75 F/g of specific capacitance can be achieved at 2 mV/s. Further, an asymmetric capacitor made of MnO_2 and activated carbon was able to achieve a wider potential window of 1.7 V with a specific capacitance of 107.38 F/g at 10 mV/s. The purpose of this study is to determine these electrochemical parameters of MnO_2 by using a simple template free method at a low cost.

4.1 Experiment

4.1.1 Materials Used

All chemicals used were of analytical quality and were utilized exactly as obtained, with no additional purification. DI water is utilized as the reaction media throughout the studies. For the synthesis and electrode preparation the following chemicals were used: potassium permanganate ($KMnO_4$), citric acid ($C_6H_8O_7$-Sigma Aldrich) and ammonium oxalate ($(NH_4)_2C_2O_4$), carbon black, poly vinylidene fluoride (PVDF-Alfa Aesar), N-methyl pyrrolidone (NMP-Sigma Aldrich) and sodium sulphate (Na_2SO_4 - Sigma Aldrich).

4.1.2 Synthesis

4.1.2.1 Synthesis of the oxygen vacancy tailored δ-MnO_2 by sol-gel citrate method

For the synthesis of oxygen vacancy-tailored δ-MnO_2, 0.1 M $KMnO_4$ is dissolved in DI water and then 0.05 M citric acid prepared in DI water is added in equal aliquots. The entire reaction mixture is kept under constant stirring for an hour at 60 ^oC. After standing at room temperature for about 20 hours, the dark blackish-brown sol-gel was centrifuged. After being washed several times with DI water and once in methanol, the precipitate was thoroughly crushed and further calcined at 300 °C under different rate of heating and ambience. To obtain sample MnA, and MnB the powder samples were heated at a rate of 10 ^oC/min and 2 ^oC/min respectively for

1 hour. The sample MnC was obtained by heating at 300 °C under N_2 flow inside a tubular furnace at a heating rate of 2 °C/min for 1 hour. The calcined samples are powdered thoroughly and stored at room temperature in an airtight container for further analysis. Figure 4.1 a, shown below explains the preparation of δ-MnO_2 by a cost-effective sol-gel citrate method.

4.1.2.2 The δ-MnO_2 tailored with the cationic vacancy by oxalate reduction method

This method involves addition of another reducing agent, such as ammonium oxalate, to the 0.1 M $KMnO_4$. The Mn precursor is dissolved in DI water and added to an Erlenmeyer flask. 50 mL of 0.1 M ammonium oxalate is then slowly added while being stirred continuously. The entire reaction setup was kept at a temperature of 90 °C in a water bath for 10 hours. The final product was centrifuged, washed several times with DI water, then with methanol, dried at 100 °C for further research and given the name as MnD. Figure 4.1b shows oxalate reduction method using ammonium oxalate as a reducing agent for $KMnO_4$. The reaction is also conducted by taking lower concentration (0.5 M) of ammonium oxalate (sample code: MnD 05). Then further annealing of both MnD and MnD 05 at 300 °C gives MnD05S and MnDS. Theses samples are not performing well in electrochemical studies. So further studies are focussed on sample MnD. The characterisation details of samples MnD05, MnD05S and MnDS are given in Appendix I, see figure S1 and S2)

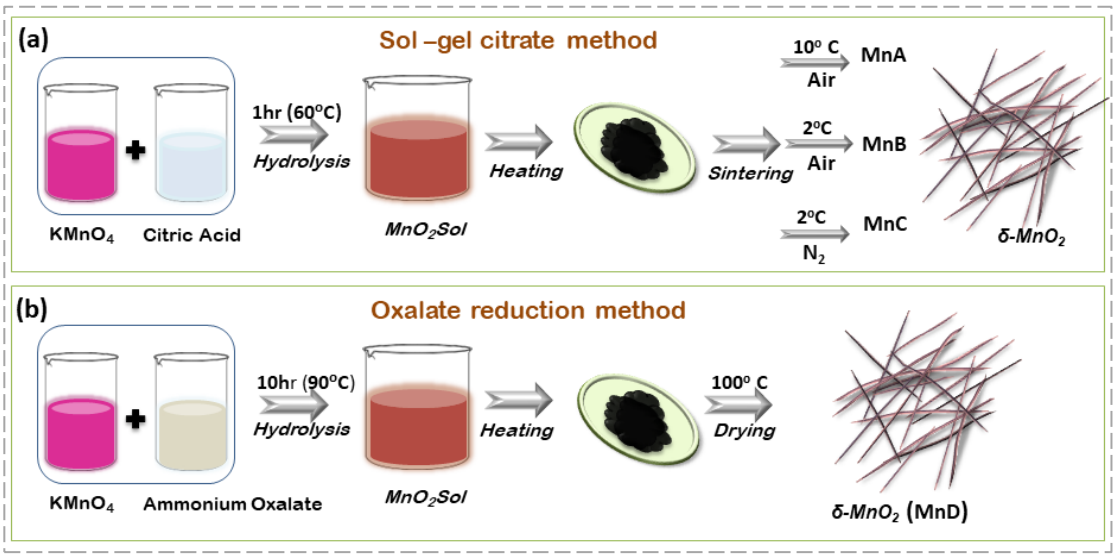

Figure 4.1 Schematic showing an easy, cost-effective and template free synthesis of one-dimensional δ-MnO_2 via two different approaches (a) Sol-gel citrate method and (b) Oxalate reduction method

4.1.3 Characterizations

The MnO_2 powders prepared via sol-gel citrate and oxalate reduction approaches were subjected to a series of analyses. FESEM (ZEISS-GEMINI SEM 300) was used for morphology and microstructure analysis. PANalytical-Xpert3 powder x-ray diffractometer

(XRD) was used to study the crystal structure, planes, crystallinity, phase purity etc. Raman analysis was performed with a 532 nm DPSS laser (Alpha 300RA, WiTec, Germany). The PerkinElmer Spectrum Two was used for FTIR analysis. The vacancies and defects were investigated using Thermo Scientific ESCALAB Xi+ and x-ray photoelectron spectroscopy (XPS) from 0 eV to 1300 eV. A BELSORP- max BET surface area analyzer was used to determine the porosity of the samples. The wettability characteristics were measured using a Kyowa drop master DMs 401 equipped with the FAMAS interface measurement and analysis system.

4.2 Results and Discussions

4.2.1 Structure and Phase Analysis

4.2.1.1 X-Ray Diffraction

The structural characterization of δ-MnO_2 heated in air and nitrogen at different heating rates are analyzed using X-ray diffraction. Many broad diffraction peaks can be seen in the XRD pattern given in Figure 4.2. The diffraction peaks at 12.6°, 36.0° and 65.0° can be attributed to typical δ-MnO_2 (JCPDS 18-0802) [26]. The weak crystalline properties of the as-prepared δ-MnO_2 are shown by the low intensity diffraction peaks.

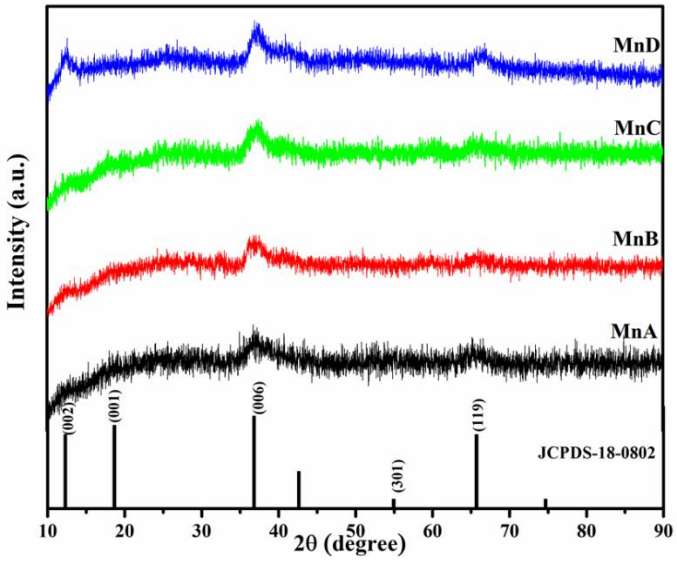

Figure 4.2 XRD pattern of the δ-MnO_2 prepared at different heating conditions

The diffraction peaks due to (002), (001), (006), (301) and (119) plane are well match with the reported literature [22,26–28]. The lattice parameters a=5.82 A^o, b=5.82 A^o and c=14.62 A^o with the basal spacing of 0.25 nm, are in accordance with the hexagonal crystal phase. Absence of any impurity or additional peaks reveals the phase pure nature of the synthesized samples. The crystallinity of material depends upon different parameters like reaction condition,

concentration, temperature etc. However, low crystalline and amorphous nanomaterial exhibits better electrochemical property than crystalline material due to its disordered structure. Which is also beneficial to rapid ion diffusion and that facilitates fast charge transfer kinetics in a super capacitor structure[29]. The obtained results confirm a complete reduction of $KMnO_4$ by both citric acid and ammonium oxalate.

4.2.1.2 Raman Analysis

The δ-MnO_2 has low Raman activity, it will be difficult to determine the stretching and bending vibrations by Raman analysis. The presence of Mn^{+3} in the Mn sites of the octahedral structure is explained by the Raman mode of vibration close to 630 cm^{-1} in Figure 4.3. This peak is the stretching mode of vibration that corresponds to the Mn-O bonds present in the MnO_6 octahedral layers [30,31]. The presence of this bands indicates that the prepared material is completely converted into layered manganese oxide in the δ-phase. The peak shift in Raman analysis is due to the vacancies and defects present in the synthesized material. The structural modification to the lattice may causes the shift in the peak. The different heat treatments and

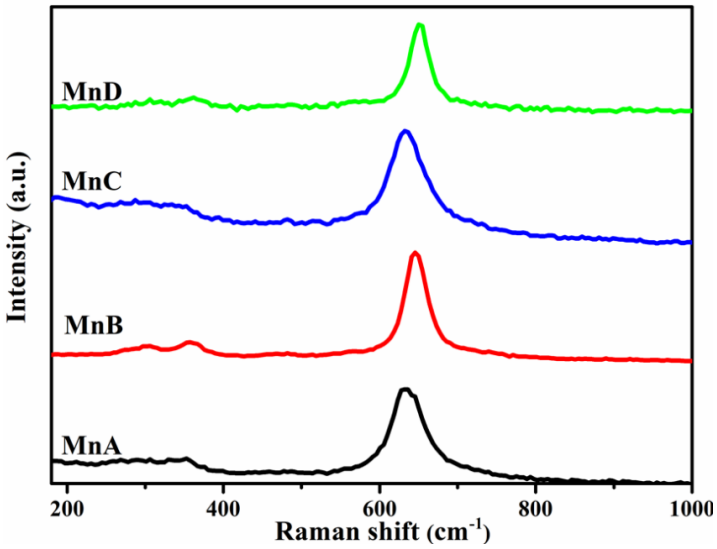

Figure 4.3 Raman spectra of the δ-MnO_2 prepared at different heating conditions

reducing agents can create vacancies, lattice defects or disorder in MnO_2 crystal, leading to the shift in Raman spectra [32–34]. The broad peak appearance in this analysis also supports the formation of less crystalline material [30,35–37]. Again, the Raman results and XRD characteristics cohere with the formation of weakly crystalline δ-MnO_2.

4.2.1.3 XPS Analysis

The XPS analysis has been conducted to quantify the presence of vacancies and oxidation state of the Mn ion in MnO_2. The XPS survey spectrum (Figure S3 in Appendix I) ensures the presence of manganese and oxygen in it. The deconvoluted XPS profile of O 1s is shown in

Figure 4.4 (the corresponding oxygen peaks are given in Table S1) and that of Mn 2p is shown in Figure 4.5. The spin-splitting separation (ΔE) obtained for MnA, MnB, MnC and MnD are respectively 11.66 eV, 11.70 eV, 11.61 eV, and 11.61 eV and this information is used to determine the oxidation state of Mn. The introduction of oxygen vacancies is indicated by the high values of adsorbed oxygen to the lattice oxygen (O_{ads}/O_{latt}) ratio as detailed in Table 4.1 and the values are 0.33, 0.24, 0.67 and 0.12 for MnA, MnB, MnC, and MnD respectively. Among the four samples MnC possess high oxygen vacancies.

The O 1s peaks observed at 529.65 eV for MnA and 529.53 eV for MnC correspond to the lattice oxygen content (O_2^{2-}) in the MnO_2 system [38–40]. The peaks at 531.18 eV and 529.85 eV indicate the presence of oxygen defects or other oxygen species like hydroxides (OH^-) in manganese oxide. These oxygen defects cause a reduction in lattice oxygen (O_2^-) content and an increase in oxygen deficiency.

From Figure 4.4, it is evident that the lattice oxygen content decreased from 72.43 % to 47.32 % when transitioning from MnA to MnC. Simultaneously, the atomic concentration of adsorbed oxygen increased from 24.07 % in MnA to 32.06 % in MnC. This decrease in lattice oxygen and increase in adsorbed oxygen confirm the successful conversion of the oxygen-deficient MnC after the heat treatment.

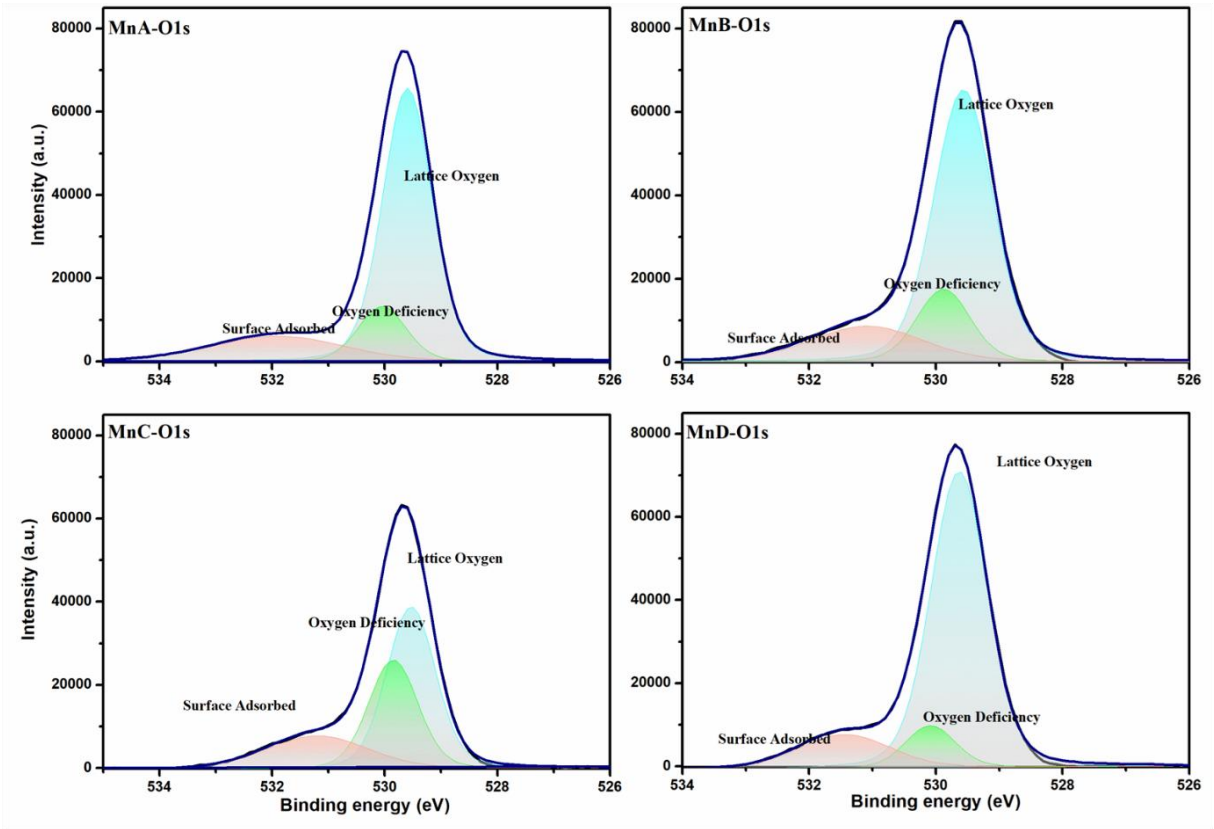

Figure 4.4 XPS deconvoluted O1s spectra of citrate synthesized samples MnA, MnB and MnC at different heating rates and oxalate reduced MnD

Sample	Mn^{3+}/ Mn^{4+}	O_{ads} (%)	O_{latt} (%)
MnA	2.71	24.07	72.43
MnB	1.45	16.16	67.20
MnC	2.84	32.06	47.32
MnD	2.33	9.72	75.94

Table 4.1 Mn^{3+}/ Mn^{4+} ratios and oxygen contents in δ-MnO_2 samples from XPS analysis

Figure 4.5, shows the XPS spectra of Mn2p profile of various manganese dioxide samples, MnA, MnB, MnC and MnD. Each spin state is deconvoluted into two peaks (the corresponding manganese peaks are given in Table S2). The Mn^{3+}/ Mn^{4+} ratio is detailed in Table 4.1. The two deconvoluted peaks of the Mn 2p spectrum corresponds to Mn $2p_{1/2}$ and Mn $2p_{3/2}$ (Figure 4.5). For sample MnA, the Mn^{3+}/ Mn^{4+} ratio is 2.71, this ratio is decreased in sample MnB and MnD as 1.45 and 2.33. This implies that the Mn^{3+} content decreased with increasing manganese vacancy. For sample MnC the Mn^{3+}/ Mn^{4+} ratio is 2.84, this value is higher than the other three samples indicating relatively less manganese vacancy. Due to parallel spin coupling, all samples exhibit double peaks. A comparison among the four samples reveals higher oxygen defects in MnC, and higher Mn vacancies in MnB and MnD, that estimated from the integrated area under the defects peaks [34]. In MnB and MnD, the occurrence of Mn vacancies induces a shift in the binding energy of O 1s compared to MnA. This Mn vacancy induced shift in binding energy is accompanied by a decrease in cluster density at neighbouring O-sites, leading to a reduction in oxygen-binding energy. Consequently, the Mn^{3+}/Mn^{4+} ratios in MnB and MnD dropped significantly than MnA, highlighting the higher chemical valence of Manganese and occurrence of Mn vacancies. The introduction of vacancies not only enhance the active sites the but also improves the charge transfer capability of MnO_2. This dual improvement in active sites due to oxygen vacancy and the charge transfer capability helps MnO_2 as a promising candidate for energy storage applications[42,43].

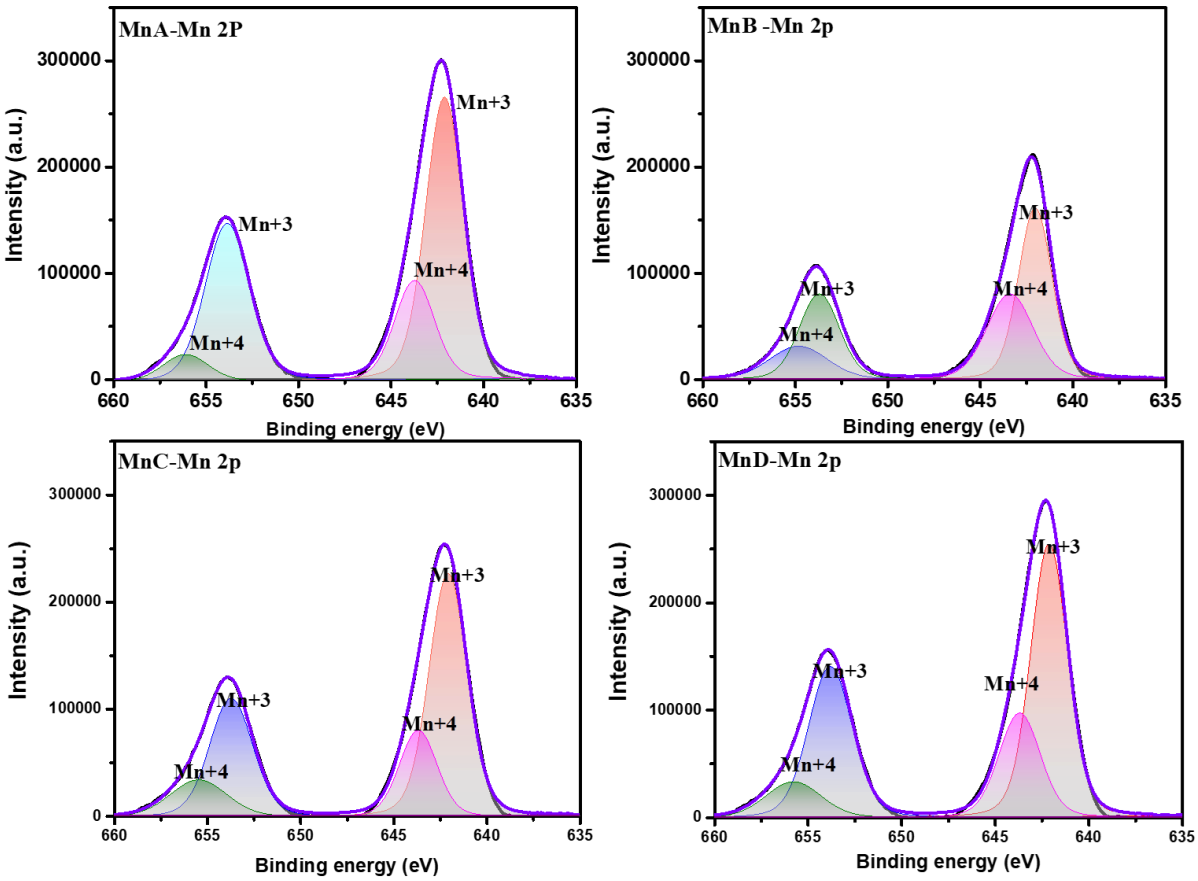

Figure 4.5 Mn2p-deconvoluted spectra of citrate synthesized MnA, MnB, and MnC at a different heating rate, and ammonium oxalate reduced MnD analyzed by X-ray photoelectron spectroscopy

4.2.2 Morphology Analysis

4.2.2.1 FE-SEM Analysis

Figure 4.6 shows SEM images of MnA, MnB, MnC and MnD. Figure 4.6a shows the δ-MnO_2 nanotube formed by citrate method followed by annealing at a temperature of 300 ^oC with a heating rate of 10 ^oC/min for 1 hour in air. By changing the heating rate to 2 ^oC/min, a thin nanowire is formed with a diameter of 10-15 nm (Figure 4.6b).

The un-sintered sample shows an irregular faceted morphology as shown in Figure S4 in the supporting information (Appendix I). This method makes single-stage morphology conversion possible by keeping the same phase, which is extremely rare. In MnC, the formation of nanowire morphology with shorter length (Figure 4.6c) is seen by changing the annealing rate and heating environment (2 ^oC/min at N_2 atmosphere). Thermal treatment changes grain size, which reduces the pore volume and facilitates densification. Thermal treatment eliminates smaller grains and forms larger grains at the expense of smaller grains. These variations are evident in the BET analysis, that discussed in the following section. Alterations in annealing rate contribute to a decrease in surface area due to pore removal. Similar observations occur

when the heating atmosphere changed to nitrogen [43–46]. In the case of MnD, ammonium oxalate is used as reducing agent to form nanowires with diameter of 10-50 nm (see Figure 4.6d) [1,2,22].

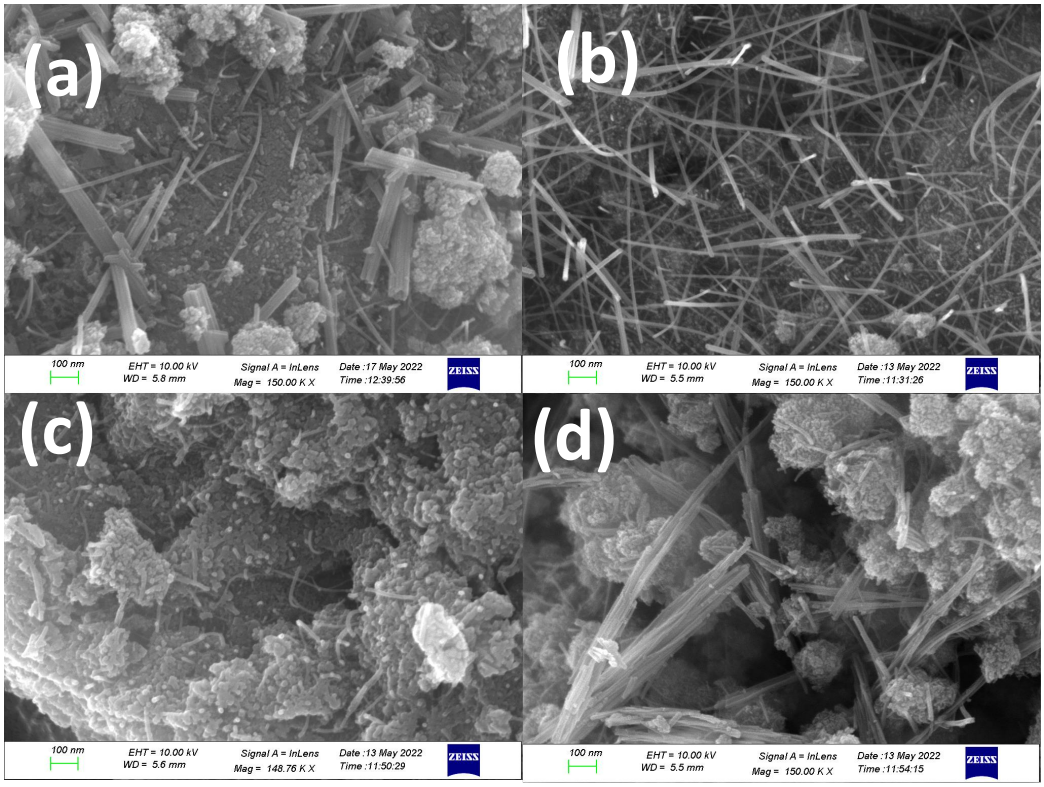

Figure 4.6 Structure and morphology of δ-MnO_2 at citrate synthesis and annealed at 300 °C (a) MnA with a heating rate of 10 °C in air, (b) MnB with a heating rate of 2 °C in air, (c) MnC with a heating rate of 2 °C in N_2 and (d) MnD by oxalate reduction method

4.2.3 Surface area and Porosity Analysis

4.2.3.1 BET Analysis

Figure 4.7 illustrates the N_2 adsorption-desorption curves for samples with mesoporous nature as determined by the BET analysis, BJH analysis for the porosity determination. The volume of the gas adsorption increased and formed a nearly sigmoid curve with type IV hysteresis [47,48]. It is believed that capillary condensation causes mesopores, which have a filling and emptying process, that appear between relative pressure values of 0.4 and 0.9. The formation of secondary pores by aggregation of uniform-sized pores results in an increased N_2 adsorption volume above 0.9 relative pressure. The pore size distribution curves give a pore value of 5.2 nm, 3.3 nm, 4.6 nm, and 5.5 nm respectively for MnA, MnB, MnC, and MnD. The specific surface area, pore volume and pore size of these samples are tabulated in Table 4.2.

The type IV H3 hysteresis observed in the MnA (Figure 4.7a) is caused by the accumulation of flakes-like nanoparticles or non-rigid aggregates. There is a type IV H2 (b) hysteresis in MnB, MnC and MnD (Figure 4.7b to 4.7d). Pore blocking caused by different annealing conditions creates this intricate pore system. An ink bottle-shaped pore network results from this process. The surface area observed for the samples MnA, MnB, MnC and MnD are respectively 221.2 m^2/g, 181.2 m^2/g, 102.0 m^2/g, and 141.2 m^2/g. Based on FE-SEM images that have previously been discussed, the morphology of the samples changes from tubular to wire as the annealing environment changes.

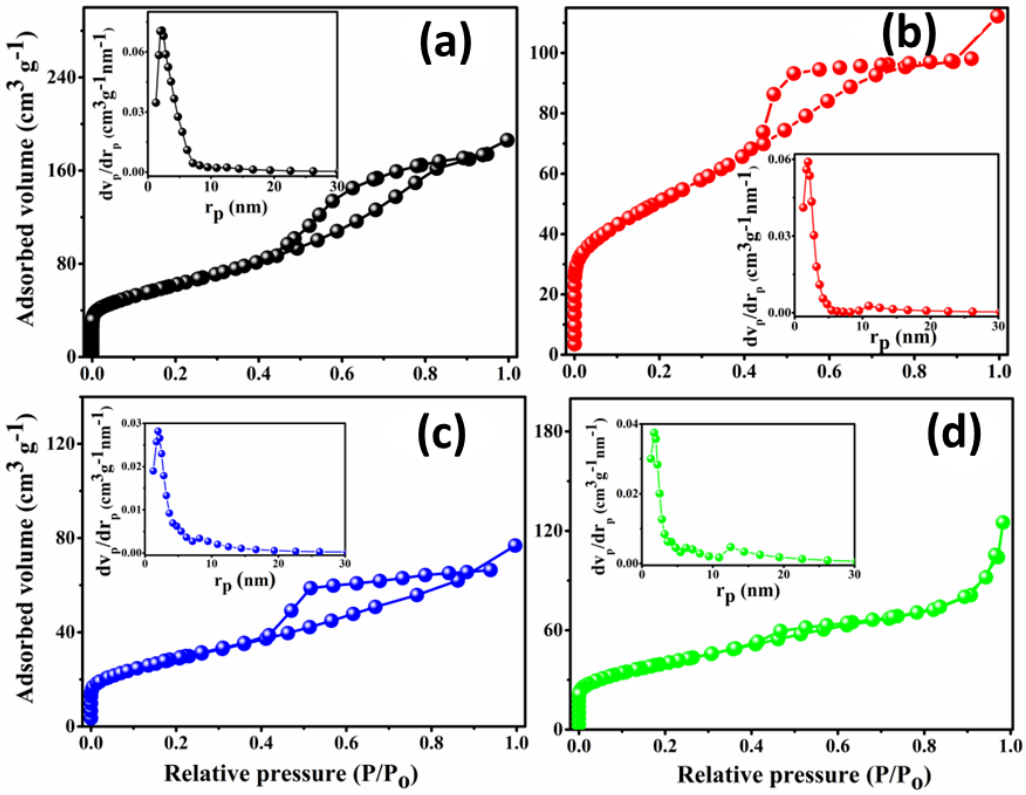

Figure 4.7 Surface physical characterization of δ-MnO_2: N_2 adsorption-desorption isotherms of (a) MnA, (b) MnB, (c) MnC and (d) oxalate reduced MnD

Sample Code	Specific Surface Area (m^2g^{-1})	Total Pore Volume (cm^3g^{-1})	Mean Pore Diameter (nm)
MnA	221.19	0.2859	5.16
MnB	181.15	0.1723	3.30
MnC	102.01	0.1177	4.61
MnD	141.22	0.1935	5.48

Table 4.2 The specific surface area, total pore volume and mean pore diameter of MnA, MnB, MnC and MnD

4.2.4 Wettability Characteristics

4.2.4.1 Contact Angle Measurement

Contact angle measurement of the material with water is conducted to determine its hydrophilicity or hydrophobicity. The change in contact angle regulates the wettability or the attachment of water with the material. This property facilitates the diffusion of ions at the electrode -electrolyte interface [49,50] and that affect the material's electrochemical properties. The wetting characteristics of the samples are shown in Figure 4.8 [47–49]. For MnA, MnB, MnC, and MnD, the contact angles measured with 0.1 M Na_2SO_4 electrolyte are 123.8°, 77.9°, 103° and 94.5°, respectively. As shown in the obtained images, the synthesis conditions have a significant impact on the surface characteristics of the material. Comparing MnC and MnD, MnD is showing better electrolyte contact and anticipate improved electrochemical performance.

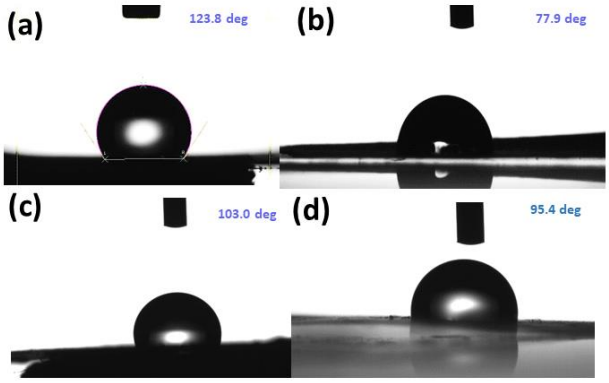

Figure 4.8 The images of contact angle measurement of citrate synthesized samples (a) MnA, (b) MnB, (c) MnC and (d) ammonium oxalate reduced MnD

4.2.5 Electrochemical Property Analysis - Supercapacitor Applications

4.2.5.1 Electrode Preparation

The working electrode is made by mixing 75% MnO_2 with 15% carbon black (conducting additive-characterization details are provided in the SI as Figure S5 in Appendix I) and 10% polyvinylidene fluoride (binder). A homogeneous slurry was made with N-methyl pyrrolidone, and the stainless-steel substrate was coated with doctor blade technique (1x1 cm^2). The electrode material was then dried at 90 °C for few hours. The weight of the active material was fixed to 2 mg by comparing the weight of the current collector before and after coating. With a two-electrode system, cyclic voltammetry was performed using 0.1 M Na_2SO_4 as an electrolyte. Whatman filter paper, soaked in the electrolyte for 10 hours is used as the separator. The symmetric cell is fabricated by sandwiching two coated electrodes with electrolyte

4.2.5.2 Electrochemical Analysis- Symmetric Supercapacitor Formation

The energy storage properties of δ-MnO_2 are studied by CV, GCD, EIS and cyclic stability tests. The electrochemical properties are studied with 0.1 M Na_2SO_4. The Biologic SP-150 and SP-300 electrochemical workstations are used to conduct all electrochemical studies. Figure S6 shows the CV curves of all four samples at a voltage window of 0 V to 1 V at a scan rate of 20 mV/s. The two samples with anionic and cationic vacancies, MnC and MnD, are performing better than MnA and MnB. So, MnC and MnD are taken for further electrochemical studies. The specific capacitance obtained is 325 F/g at 2 mV/s and 78.1 F/g at 100 mV/s for MnC (Figure 4.9a). Figure 4.9b shows the CV curves of MnD at different scan rates and the specific capacitance obtained is 460.75 F/g at 2 mV/s, 216 F/g at 5mV/s and 75.34 F/g at 100 mV/s. Sagar et al studied about MnO_2 nanoflakes that gives 145 F/g at 5mV/s [36]. Shang et al studied flower like MnO_2 structure with a specific capacitance of 197 F/g at 2 mV/s [37]. Similarly electrochemical properties of the agglomerated MnO_2 nanoparticles were studied by Prabhat et al that gives specific capacitance of 200 F/g at 5 mV/s [38]. Justin raj et al studied flower like MnO_2 showing the electrochemical activity of 160 F/g [39]. The present studies on δ-MnO_2 gives a specific capacitance of 460.75 F/g at 2 mV/s with symmetric supercapacitor mode at 1V and produce asymmetric supercapacitors with a specific capacitance of 107.38 F/g at 10 mV/s at 1.7 V. As the scan rate of the MnO_2 increases, its specific capacitance decreases due to the reduced contact time of the electrolyte at the electrode-electrolyte interface. With a lower scan rate, the electrolyte is in contact with the electrode for a longer period, allowing the ions to interact with both the outer and inner surfaces of the MnO_2 [48,51]. The CV of the synthesized δ-MnO_2 is perfectly rectangular in shape and exhibits good capacitive behavior. The equations (1) and (2) correspond to the redox reactions causing the pseudo-capacitive nature and equation (3) corresponds to the surface reactions leading to double-layer capacitive contribution.

$$MnO_2 + Na^+ + e^- \leftrightarrow MnOONa \quad (1)$$

$$MnO_2 + H^+ + e^- \leftrightarrow MnOOH \quad (2)$$

$$(MnO_2)_{surface} + Na^+ + e^- \leftrightarrow (MnO_2^- Na^+)_{surface} \quad (3)$$

Crystalline defects play an important role in electrochemical aspects such as increasing electrolyte affinity, increasing specific capacitance, and improving charge-discharge characteristics. The tailored oxygen vacancies in the metal oxide lattice make larger interlayer spacing. This initiates faster kinetics and better insertion and removal of the Na^+ ions. Likely the cation vacancies act as ion channels for the electrolytic ions. Which allows the ions easily

penetrable into the MnO_2's internal surfaces. So, both vacancies are making improvements in the storage property compared to the other two samples (MnA and MnB). There is good symmetry in the GCD analysis curves (Figures 4.9c-4.9d), which indicates that the electrode had good storage properties. The better performance exhibited by MnD with ultra-thin nanowire structure having high mesoporous nature possess an energy density of 4.098 Wh/kg and power density of 0.125 W/kg at 0.125 A/g as calculated from the GCD measurements (Figure 4.9c-4.9d).

The EIS analysis of MnC and MnD demonstrates that the specific capacitive performance is enhanced by the lower charge transfer and diffusion resistance (Figure 4.9e) than MnA and MnB. The better semi-infinite ion diffusions turn the electrodes into good storage capacity. The series resistance (R_s) obtained from the EIS spectra are 4.03, 3.85, 0.95 and 0.41 Ω for samples MnA, MnB, MnC and MnD respectively. The resistance was calculated by using Z-fit in the EC lab software of Bio-logic. Error values obtained are ± 0.33, ± 0.28, ± 0.21 and ± 0.09, respectively for the above-mentioned series resistance. The magnitude of charge transfer resistance (Rct) measured are 33.54, 38.09, 17.03 and 4.30 Ω respectively for MnA, MnB, MnC and MnD. Among the four samples MnD shows lower internal resistance and shows better electrochemical performance. The stability of the MnD samples was studied by continuous charging and discharging measurement and it is stable for around 10000 GCD cycles with a retention of 97% (Figure 4.9f).

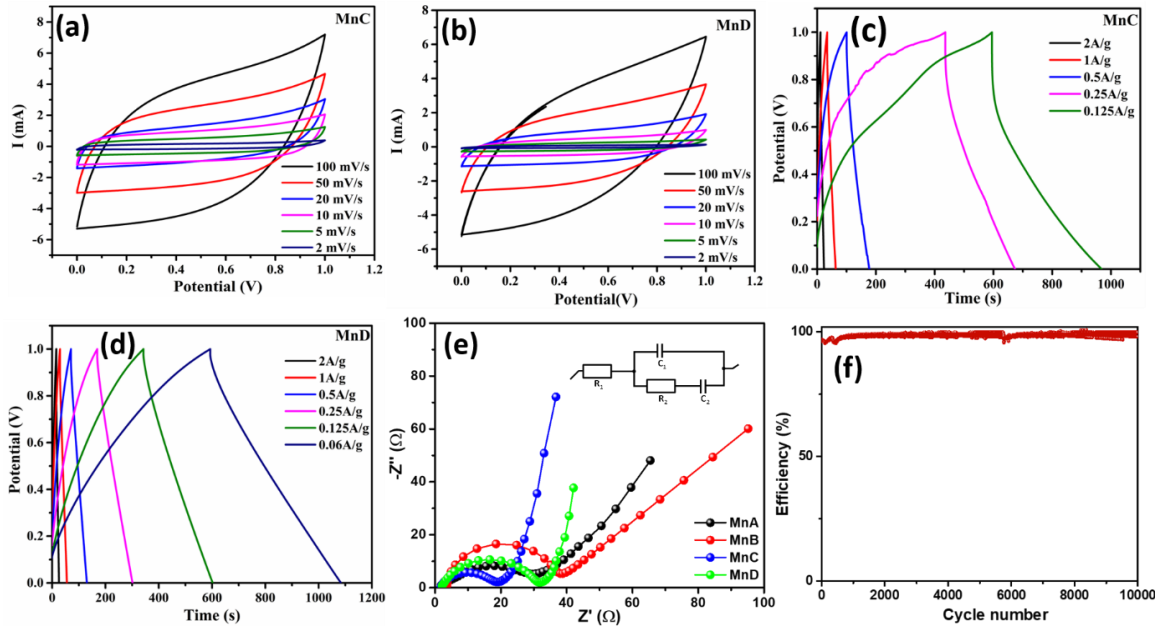

Figure 4.9 Electrochemical studies of δ-MnO_2 in neutral aqueous 0.1 M Na_2SO_4 electrolyte at room temperature. CV curves of δ-MnO_2 at different scan rates from 2 mV/s – 100 mV/s (a) MnC and (b) MnD. GCD curve at different current densities (c) MnC and (d) MnD, (e) Impedance analysis, and (f) cyclic stability in terms of the efficiency Vs cycle number at the GCD measurement of MnD

4.2.5.3 Quantification of Specific Capacitance

The figure 4.10 shows capacitive contributions of MnC and MnD. The presence of defects contributes more specific capacitance in MnD than that of MnC. Calculating contribution of each mechanism by applying equations (7)-(10) mentioned in chapter 2.

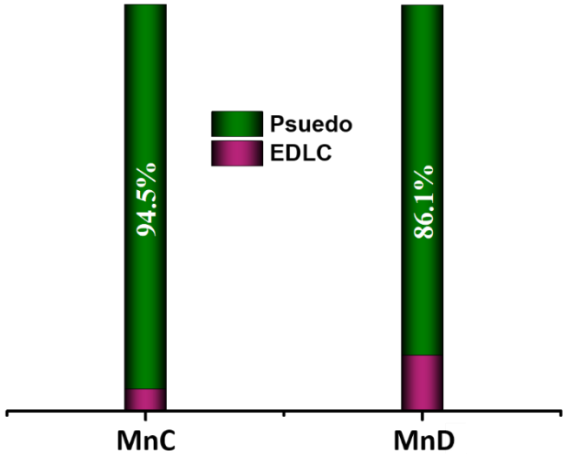

Figure 4.10 Capacitance contributions obtained from MnC and MnD

The figure 4.10 shows the percentage of pseudo capacitance contribution, 94.5% and 86.1% in MnC and MnD respectively. The remaining percentage is contributed by EDLC and is high in MnD, causes its better performance than MnC.[52]

4.2.5.4 Electrochemical Analysis- Asymmetric supercapacitor Formation

To explore the further potential application of δ-MnO_2, the manganese oxide is taken as the positive electrode, and the activated carbon (AC) as the negative electrode for the fabrication of the asymmetric supercapacitor (ASC) studies. The mass ratio of manganese oxide to activated carbon was adjusted using the equation (4) below [53,54].

$$\frac{m_+}{m_-} = \frac{Cm^- \Delta V^-}{Cm^+ \Delta V^+} \qquad (4)$$

Where m_+ and m_- are the individual masses of the positive and negative electrodes. Cm^+ and Cm^- are the individual capacitance of positive and negative materials. Similarly, ΔV^+ and ΔV^- are the individual potential window of the positive and negative electrodes.

Optimization of the voltage window for the asymmetric super capacitor (δ-MnO_2 // AC) was done by running the CV between 0 to 1.0 V, 1.3 V, 1.5 V and 1.7 V as shown in Figure 4.11a. As the potential window is expanded, the area under the CV curve expands up to 1.7 V. Figure 4.11b shows the CV curves of δ-MnO_2 // AC capacitor with a potential window of 0 to 1.7 V at different scan rate and the estimated maximum specific capacitance is 107.38 F/g at 10 mV/s. The specific capacitance obtained from the GCD analysis (Figure 4.11c) is 22.98 F/g at 0.125

A/g, which is comparable with the previous reports [55,56]. The energy density is 4.31 Wh/kg and the power density is 57.04 W/kg for the δ-MnO_2 // AC super capacitor. The cell's stability was tested with 3000 galvanostatic charge-discharge cycles at a high scan rate and is shown in Figure 4.11d. The fabricated cell has better stability, with a retention of 92 %. Figure 4.11e represents the Nyquist plot, in which the smaller semicircle indicates the better storage property. The Nyquist plot (Figure 4.11e) shows a lower interfacial charge transfer resistance with a smaller intercept relative to the real axis. The sheet resistance is 6.05 Ω and the charge transfer resistance is 6.08 Ω. This indicates that the electrode-electrolyte charge transfer is easier and leads to better energy storage due to the easy and fast to and fro movement of electrolytic ions within the mesoporous material [6,35,48,54]. According to these findings, this material may be used in upcoming energy-based research and is highly beneficial for its intended use.

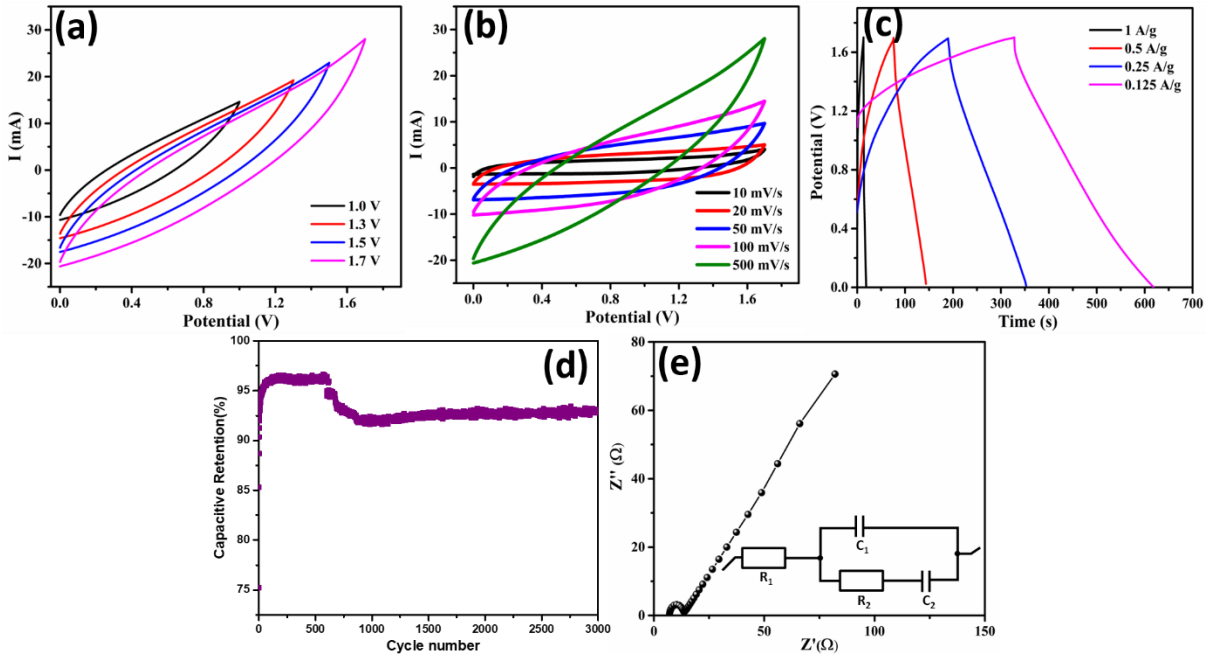

Figure 4.11 Cyclic voltammograms of δ-MnO_2 // AC ASC (a) Optimization of potential window (b) different scan rate from 10 mV/s –500 mV/s, (c) Galvanostatic charge-discharge at different A/g, (d) Long-term cyclic stability studies by charge-discharge measurement and (e) Electrochemical impedance spectra data plot of δ-MnO_2 // AC ASC with Randle's equivalent circuit

The potential window observed for symmetric (1 V) and asymmetric (1.7 V) supercapacitors are different (Table 4.3), this is one of the reasons why it shows performance variations. The formation of asymmetric supercapacitor enhanced the power density without altering the energy density compared to symmetric supercapacitor.

MnD	Cm (F/g)	De (Wh/Kg)	Dp (W/Kg)	Voltage (V)
Symmetric	460.75 -2mV/s	4.09	0.12	1
Asymmetric	107.38-10 mV/s	4.31	57.04	1.7

Table 4.3 Electrochemical parameters of MnD sample obtained for symmetric and Asymmetric super capacitor

4.3 Conclusion

In the work summary, we describe a straightforward, low-cost method for producing highly mesoporous 1D δ-MnO_2, with anionic and cationic vacancies and improved electrochemical properties. The samples are made using the sol-gel citrate and oxalate reduction techniques. The formation of one-dimensional tubular, as well as nanowire structures, results from the first method, which is then followed by controlled heat treatment to create oxygen vacancy. The cationic vacancy is produced in the second method without further heat treatment. The symmetric supercapacitor gives a specific capacitance of 460.75 F/g at 2 mV/s with a potential window of 1V and a cyclic stability of 10000. Asymmetric supercapacitor design was fabricated by means of δ-MnO_2 and activated carbon using 0.1 M Na_2SO_4 electrolyte with a potential window of 1.7 V. The electrochemical properties of δ-MnO_2 // AC gives a specific capacitance of 107.38 F/g at 10 mV/s with a cyclic stability of 3000 with 92 % retention efficiency. The energy density calculated is 4.31 Wh/kg and the power density obtained is 57.04 W/kg. As a result of this research, we now have a better understanding of how oxygen and cation vacancy concentration affect the electrochemical performance of MnO_2.

*****

Appendix I

Supporting Information

Characterization Details of MnD05, MnD05S and MnDS

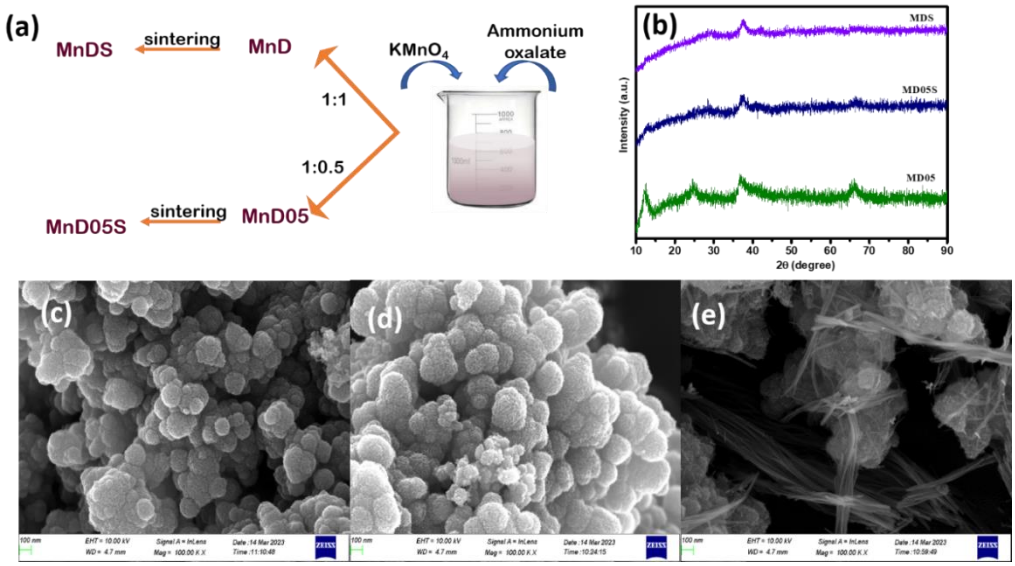

Figure S1. (a) Synthesis (b) XRD analysis (c), (d) and (e) are FE-SEM images of MnD05, MnD05S and MnDS respectively

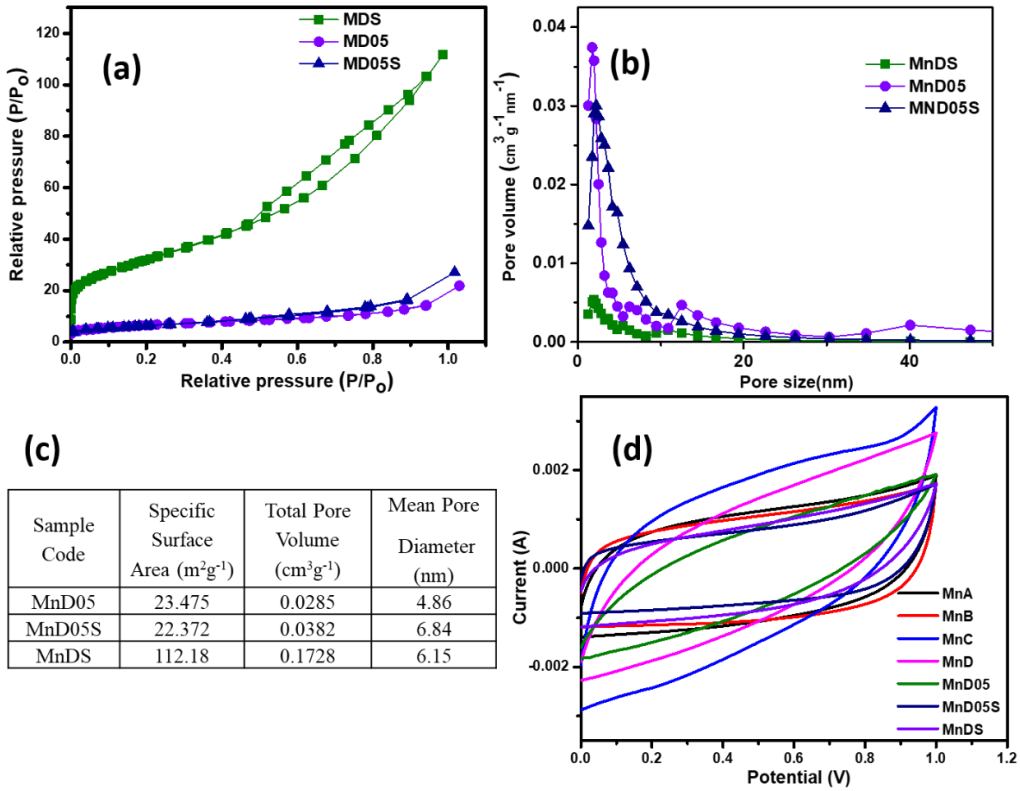

(c)

Sample Code	Specific Surface Area (m^2g^{-1})	Total Pore Volume (cm^3g^{-1})	Mean Pore Diameter (nm)
MnD05	23.475	0.0285	4.86
MnD05S	22.372	0.0382	6.84
MnDS	112.18	0.1728	6.15

Figure S2. (a) BET analysis (b) BJH analysis (c), specific surface area, total pore volume and mean pore diameter of MnD05, MnD05S and MnDS respectively and (d) Electrochemical analysis of all samples

XPS analysis

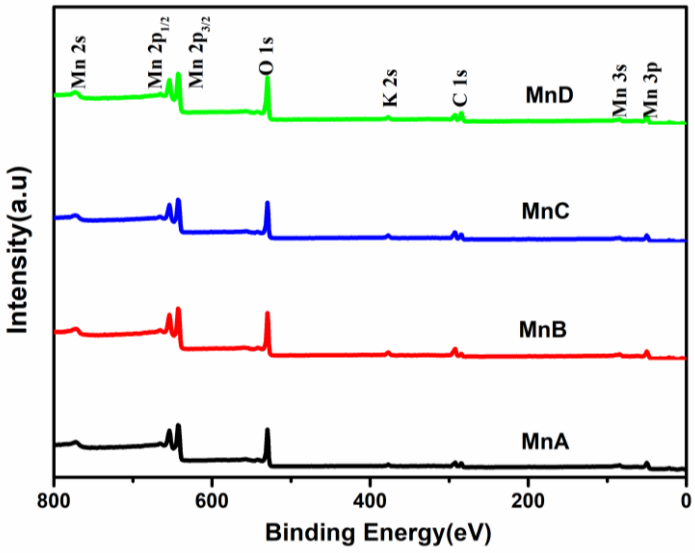

Figure S3. XPS survey spectra of MnA, MnB, MnC, and MnD

Peak Positions (binding energy)	Lattice Oxygen (eV)	Oxygen Deficiency (eV)	Surface Adsorbed (eV)	O_{ads}/O_{lat}
MnA	529.65	531.18	532.99	33.23
MnB	529.57	529.88	531.09	24.04
MnC	529.53	529.85	531.19	67.75
MnD	529.63	530.09	531.44	12.79

Table S1. Peak positions of Oxygen contents obtained from XPS analysis

Peak position	$2p_{3/2}$		$2p_{1/2}$	
	Mn^{+3} (eV)	Mn^{+4} (eV)	Mn^{+3} (eV)	Mn^{+4} (eV)
MnA	642.19	643.73	653.85	656.12
MnB	642.04	643.40	653.71	654.84
MnC	642.09	643.70	653.74	655.49
MnD	642.12	643.70	653.82	655.79

Table S2. Peak positions of Manganese contents obtained from XPS analysis

FE-SEM

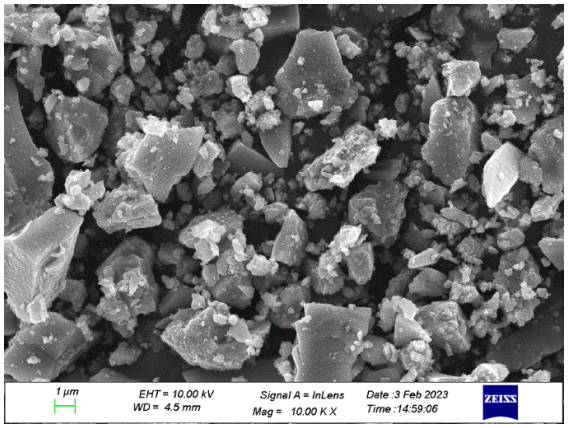

Figure S4. FE-SEM images of the MnO_2 sample before sintering

Supercapacitor application

Characterization of Carbon black used for electrode preparation

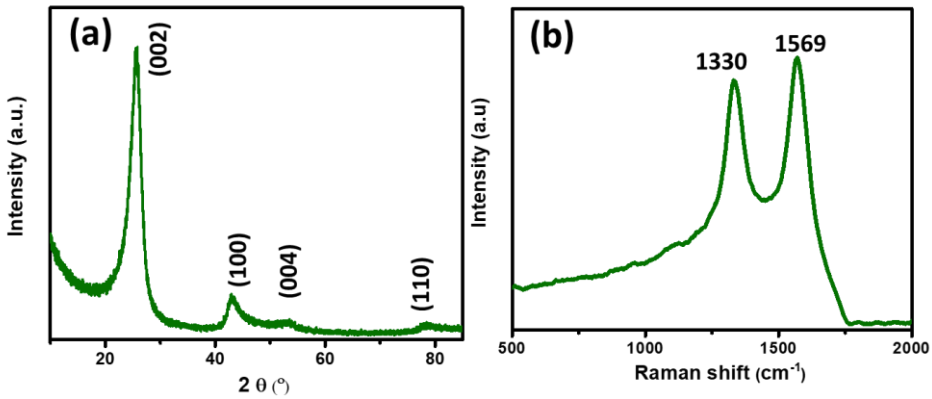

Figure S5. (a) XRD pattern of carbon and (b) Raman analysis

Symmetric supercapacitor application

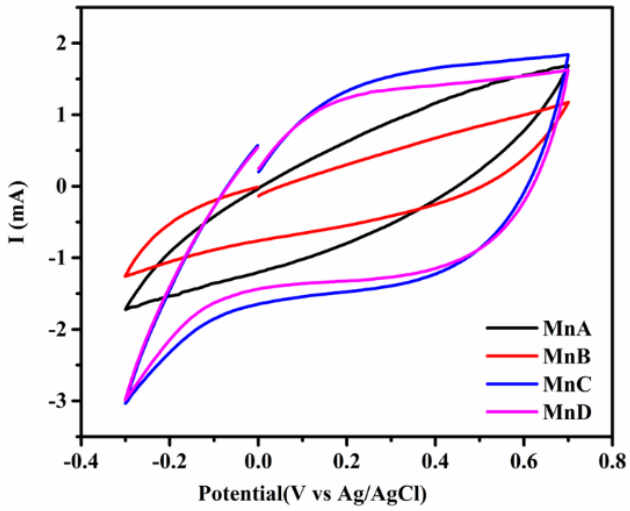

Figure S6. Comparing cyclic voltammograms at 20mV/s of MnA, MnB, MnC, and MnD

References

[1] A. Xia, W. Yu, J. Yi, G. Tan, H. Ren, C. Liu, *Journal of Electroanalytical Chemistry* **2019**, *839*, 25–31.
[2] X. Fu, W. Huo, X. Liu, Q. Shan, Z. Guo, C. Jing, F. Dong, H. C. Yao, Y. Zhang, K. Chen, *CrystEngComm* **2019**, *21*, 4593–4598.
[3] H. Peng, H. Fan, J. Sui, C. Wang, W. Zhang, W. Wang, *ChemistrySelect* **2020**, *5*, 869–874.
[4] M. Huang, F. Li, F. Dong, Y. X. Zhang, L. L. Zhang, *Journal of Materials Chemistry A* **2015**, *3*, 21380–21423.
[5] N. Shimamura, R. Kanda, Y. Matsukubo, Y. Hirai, H. Abe, Y. Hirai, T. Yoshida, H. Yabu, A. Masuhara, *ACS Omega* **2019**, *4*, 3827–3831.
[6] J. Shin, J. K. Seo, R. Yaylian, A. Huang, Y. S. Meng, *International Materials Reviews* **2020**, *65*, 356–387.
[7] C. C. Hu, T. W. Tsou, *Electrochimica Acta* **2002**, *47*, 3523–3532.
[8] S. Devaraj, N. Munichandraiah, *Journal of Physical Chemistry C* **2008**, *112*, 4406–4417.
[9] X. Zhang, J. Liu, Q. Chu, Y. Su, S. Tang, *Materials Research Express* **2020**, *6*, 126002.
[10] G. S. Gudavalli, J. N. Turner, T. P. Dhakal, *Nanotechnology* **2019**, *30*, 455701.
[11] W. Yuan, S. P. Jiang, *ECS Transactions* **2013**, *58*, 63–69.
[12] A. Shahani, J. Wu, L. Wu, Q. Wang, X.-D. Zhou, *ECS Transactions* **2011**, *33*, 185–193.
[13] X. Chang, X. Zhai, S. Sun, D. Gu, L. Dong, Y. Yin, Y. Zhu, *Nanotechnology* **2017**, *28*, 135705.
[14] A. A. Hlaing, P. P. Win, *Advances in Natural Sciences: Nanoscience and Nanotechnology* **2012**, *3*, 025001.
[15] L. Zhang, L. Kang, H. Lv, Z. Su, K. Ooi, Z.-H. Liu, *Journal of Materials Research* **2008**, *23*, 780–789.
[16] M.-S. Wu, *Applied Physics Letters* **2005**, *87*, 153102.
[17] Y. Chen, C. Zhou, G. Liu, C. Kang, L. Ma, Q. Liu, *Journal of Materials Chemistry A* **2021**, *9*, 2872–2887.
[18] K. Rajendra Prasad, N. Miura, *Electrochemistry Communications* **2004**, *6*, 1004–1008.
[19] P. Gao, P. Metz, T. Hey, Y. Gong, D. Liu, D. D. Edwards, J. Y. Howe, R. Huang, S. T. Misture, *Nature Communications* **2017**, *8*, 14559.
[20] R. E. John, A. Chandran, M. Thomas, J. Jose, K. C. George, *Applied Surface Science* **2016**, *367*, 43–51.
[21] D. A. Tompsett, S. C. Parker, M. S. Islam, *Journal of the American Chemical Society* **2014**, *136*, 1418–1426.
[22] D. S. Liu, Y. Mai, S. Chen, S. Liu, E. H. Ang, M. Ye, Y. Yang, Y. Zhang, H. Geng, C. C. Li, *Electrochimica Acta* **2021**, *370*, 137740.
[23] J. Luo, W. Hu, Z. Suo, Y. Wang, Y. Zhang, *Journal of Hazardous Materials* **2021**, *418*, 126275.
[24] O. Giraldo, S. L. Brock, W. S. Willis, M. Marquez, S. L. Suib, S. Ching, *Journal of the American Chemical Society* **2000**, *122*, 9330–9331.
[25] D. L. Fang, B. C. Wu, A. Q. Mao, Y. Yan, C. H. Zheng, *Journal of Alloys and Compounds* **2010**, *507*, 526–530.
[26] Y. Kumar, S. Chopra, A. Gupta, Y. Kumar, S. J. Uke, S. P. Mardikar, *Materials Science for Energy Technologies* **2020**, *3*, 566–574.
[27] W. Di, X. Zhang, W. Qin, *Applied Surface Science* **2017**, *400*, 200–205.
[28] Z. Y. Leong, H. Y. Yang, *ACS Applied Materials & Interfaces* **2019**, *11*, 13176–13184.
[29] X. Fu, X. Wang, Y. Chen, W. Huo, X. Liu, K. Chen, F. Dong, H. Yao, Y. Zhang, *Journal of Colloid and Interface Science* **2019**, *557*, 168–173.
[30] J. E. Post, D. A. McKeown, P. J. Heaney, *American Mineralogist* **2021**, *106*, 351–366.
[31] H. R. Barai, A. N. Banerjee, S. W. Joo, *Journal of Industrial and Engineering Chemistry* **2017**, *56*, 212–224.
[32] V. K. Veerapandiyan, S. Khosravi H, G. Canu, A. Feteira, V. Buscaglia, K. Reichmann, M. Deluca, *Journal of the European Ceramic Society* **2020**, *40*, 4684–4688.
[33] S. A. Ait Abdelkader, O. Boutahir, M. Boutahir, B. Fakrach, M. Bentaleb, A. Rahmani, H. Chadli, A. Rahmani, *J. Phys.: Conf. Ser.* **2019**, *1292*, 012019.
[34] S. A. Acharya, V. M. Gaikwad, V. Sathe, S. K. Kulkarni, *Applied Physics Letters* **2014**, *104*, 113508.
[35] P. Wu, S. Cheng, L. Yang, Z. Lin, X. Gui, X. Ou, J. Zhou, M. Yao, M. Wang, Y. Zhu, M. Liu, *ACS Applied Materials & Interfaces* **2016**, *8*, 23721–23728.
[36] L. Yang, S. Cheng, J. Wang, X. Ji, Y. Jiang, M. Yao, P. Wu, M. Wang, J. Zhou, M. Liu, *Nano Energy* **2016**, *30*, 293–302.
[37] J. Mondal, S. K. Srivastava, *ACS Applied Nano Materials* **2020**, *3*, 11048–11059.
[38] Z. W. J. Ang, T. Xiong, W. S. V. Lee, J. Xue, *ChemNanoMat* **2020**, *6*, 1357–1364.
[39] L. Niu, L. Yan, Z. Lu, Y. Gong, T. Chen, C. Li, X. Liu, S. Xu, *Journal of Energy Chemistry* **2021**, *56*, 245–258.
[40] A. Zhang, R. Gao, L. Hu, X. Zang, R. Yang, S. Wang, S. Yao, Z. Yang, H. Hao, Y.-M. Yan, *Chemical Engineering Journal* **2021**, *417*, 129186.

[41] L. Yan, C. Shen, L. Niu, M. Liu, J. Lin, T. Chen, Y. Gong, C. Li, X. Liu, S. Xu, *ChemSusChem* **2019**, *12*, 3571–3581.
[42] L. Niu, L. Yan, Z. Lu, Y. Gong, T. Chen, C. Li, X. Liu, S. Xu, *Journal of Energy Chemistry* **2021**, *56*, 245–258.
[43] J. Wang, J. Li, C. Jiang, P. Zhou, P. Zhang, J. Yu, *Applied Catalysis B: Environmental* **2017**, *204*, 147–155.
[44] Md. Harun-Or-Rashid, M. N. Islam, M. Arifuzzaman, A. K. M. A. Hossain, *J Mater Sci: Mater Electron* **2021**, *32*, 2505–2523.
[45] P. K. Pagare, K. G. Kanade, A. P. Torane, *Mater. Res. Express* **2017**, *4*, 105011.
[46] C. Yao, M. Ismail, A. Hao, S. K. Thatikonda, W. Huang, N. Qin, D. Bao, *RSC Adv.* **2019**, *9*, 12615–12625.
[47] G. Zhang, L. Ren, Z. Yan, L. Kang, Z. Lei, H. Xu, F. Shi, Z. H. Liu, *Journal of Materials Chemistry A* **2015**, *3*, 14567–14572.
[48] S. Bag, C. R. Raj, *Journal of Materials Chemistry A* **2016**, *4*, 8384–8394.
[49] M. M. Vadiyar, S. C. Bhise, S. K. Patil, S. S. Kolekar, A. R. Shelke, N. G. Deshpande, J. Y. Chang, K. S. Ghule, A. V. Ghule, *Chem. Commun.* **2016**, *52*, 2557–2560.
[50] A. Ramakrishnan, S. Swaminathan, J. Mayandi, *ChemistrySelect* **2023**, *8*, e202303098.
[51] N. Kaabi, B. Chouchene, W. Mabrouk, F. Matoussi, E. Selmane B.H. Hmida, *Solid State Ionics* **2018**, *325*, 74–79.
[52] A. M., A. Paul, *ACS Omega* **2017**, *2*, 8039–8050.
[53] T. Liu, K. Wang, Y. Chen, S. Zhao, Y. Han, *Green Energy & Environment* **2019**, *4*, 171–179.
[54] H. Shen, X. Kong, P. Zhang, X. Song, H. Wang, Y. Zhang, *Journal of Alloys and Compounds* **2021**, *853*, 157357.
[55] S. N. N. Mohd Yusof, N. K. Mohd Zain, I. I. Misnon, R. Jose, *MATEC Web of Conferences* **2018**, *150*, 02006.
[56] G. S. Gund, D. P. Dubal, N. R. Chodankar, J. Y. Cho, P. Gomez-Romero, C. Park, C. D. Lokhande, *Sci Rep* **2015**, *5*, 12454.

Abstract

A zincospiroffite-reduced graphene oxide ($Zn_2Te_3O_8$-RGO) hybrid material was synthesized using a straightforward, cost-efficient method for the preparation of an efficient electrode material for supercapacitor application. In ambient conditions, a one-step solvothermal synthesis produces a black glittering composite of $Zn_2Te_3O_8$-RGO. The structure and morphology of the material was analysed by using FE-SEM, Fourier Transform Infrared spectroscopy (FTIR), X-ray diffraction (XRD), and Raman scattering. The electrode material was designed to be highly conductive and wettable. A symmetric supercapacitor made of hybrid electrode material exhibits a high specific capacitance of 600 F/g at 1 A/g with energy and power densities of 83.33 Wh/kg and 0.99 kW/kg, respectively. A specific capacitance of 513.51 F/g at 10 mV/s with 99 % retention has also been measured after 5000 charge-discharge cycles. The hybrid material combines well with an aqueous electrolyte, such as 0.1 M KNO_3, to form a symmetric supercapacitor with higher power and energy density. For energy storage applications, this material can be an excellent alternative to conventional electrodes.

Keywords: Zincospiroffite-RGO hybrid, One-pot synthesis, Supercapacitor

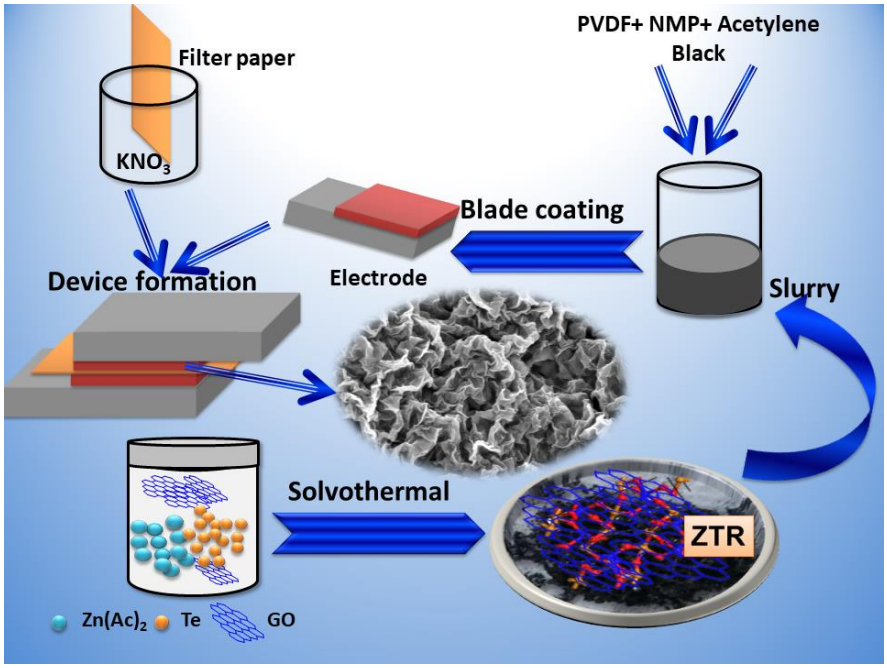

5. Solvothermal Synthesis of Ternary Mesoporous Zincospiroffite ($Zn_2Te_3O_8$) -RGO Hybrid

Introduction

The increasing usage of portable electronic devices, and electrical transportation systems requires more development and demands higher output in the electrochemical energy storage systems (EES)[1–3]. The supercapacitor and batteries are the efficient electrochemical energy storage systems nowadays[4,5]. Supercapacitors, also known as ultracapacitors or electrochemical capacitors, are very appealing because they have a significantly higher power density, longer cyclic stability, and charge-discharging qualities than batteries, as well as a far higher energy density than regular capacitors. Because of these factors, the supercapacitor serves as an alternate energy storage device. Generally, supercapacitor materials are broadly classified into two, like electrical double-layered materials and pseudocapacitive materials. Among the carbon-based materials activated carbon, graphene, carbon nanotube, amorphous carbon, etc contribute via non-faradic charge storage mechanism by charge absorption on the surface of the electrode. The high conductivity and high surface area contribute purely to electrostatic energy storage. While the pseudocapacitor material like transition metal oxide and conducting polymer materials, impart reversible faradic mechanism for charge storage. This fast faraday reaction between electrode and electrolyte will generate pseudocapacitive energy storage. Metal oxides like RuO_2[6],NiO[7], MnO_2[8], SnO_2[9], V_2O_5[10], Co_3O_4[11], ZnO[12,13], and so forth show pseudocapacitive behaviour, and initiates high specific capacitance. Among these RuO_2 shows better theoretical performance of above 1000 F/g, but the lack of material, toxic effect, and high material cost will limit its use in commercial applications. Due to the relatively lower capacitive behaviour of these materials makes hybrid with carbon-based material gives better performance. This will induce both the faradic and non-faradic processes together. These synergistic effects improve the capacitive performance as well as other electrochemical properties.

Nowadays Tellurium[14] based materials are used as the supercapacitor material due to their good charge storage properties. The physical properties and good structural chemistry make them an important role in material science and solid-state chemistry. Because of their semiconductor property, capable of forming alloys used to improve the electrical, thermal, and optical properties of devices in different fields[15]. The reaction of transition metals with tellurium forms metal tellurides like CdTe[15], PbTe[16], ZnTe[17], and Sb_2Te_3[18].The metal-

telluride systems have application in thermoelectric systems also. Other than transition metals it can form poly tellurides or poly chalcogenides with rare earth materials like lanthanum tellurides show thermos-electric properties due to its high thermal stability[19]. Different methods are adopted for the synthesis of the telluride nanomaterials based on their physical and chemical approaches like chemical vapour deposition, hydrothermal-solvothermal, wet chemical synthesis, and biomolecule-assisted methods[18–20]etc. Tsai et al reported that tellurium nanowire synthesis by electrochemical method for the supercapacitor application gives 25 F/g with retention of 46%[21]. Tellurium nanoparticle synthesis by wet chemical method gives 586 F/g at 2 mA/cm^2 by Manikandan et al with 1000 cyclic stability and 100% retention[20]. Cao et al synthesized core-shell nanomaterials on carbon fiber by Te-Au-MnO_2 gives specific capacity of 930 F/g with 97% retention[22]. Liu et al synthesized the Lithium Telluride battery material with Te-C shows 87% capacity[23]. Considering II-IV group semiconductors, Zinc oxide has eminent properties like semiconducting, pyroelectric, and piezoelectric. The Zinc-based systems are also used in different application due to its excellent optical and electrical properties. It can be used in solar cell, LED application, gas sensors, actuators, and optoelectronic systems. Zhang et al synthesized a graphene-ZnO electrode and make an electrode with the spray pyrolysis technique gives 11.3 F/g[12]. ZnO-carbon aerogel synthesis by Kalpana et al gives 500 F/g in 6 M KOH electrolyte[24]. The synthesis of ZnO-CNT composite electrode exhibit a specific capacitance of 126.3 F/g with solid state gel polymeric electrolyte of poly vinyl alcohol (PVA) with poly phosphor molybdic acid (PMA)[12].

According to prior literature reviews, a solvothermal technique was used to synthesize novel hybrid electrode material containing zinc-tellurium oxide and graphene. Here, our team attempt to study and explore the electrochemical parameters of the zincospiroffite-RGO nanosized material with a neutral electrolyte. The synthesis of this hybrid material was a direct one-step solvothermal approach, under mild conditions. According to Diana *et al.,* solvothermal setup is an easy, affordable, and scalable process compared to other synthesis techniques by maintaining lower temperature scales[25]. In this method, simultaneous reduction of the metal precursors like Zn and Te is followed by the incorporation of graphene by the addition of graphene oxide during the synthesis. The performance of this material as a hybrid electrode in a symmetric supercapacitor structure gives an energy density of 83.33 Wh/kg and a power density of 0.99 kW/kg at a constant current density of 1 A/g with an aqueous neutral 0.1 M KNO_3 electrolyte. This material also shows very good cyclic stability indicating a promising candidate for energy storage applications. It has not yet been investigated as a supercapacitor

electrode, to the best of our knowledge. Various tellurium-based systems, including La_3Te_2[26], $SmTe_3$[27] and CoTe[28] etc have been studied. In comparison to these materials, zincospirofite-RGO demonstrates significantly improved electrochemical storage properties. This enhanced performance of zincospirofite-RGO make it as a promising material for various energy storage applications.

5.1 Experimental

5.1.1 Materials required

The Zincospiroffite/RGO nanocomposite material is obtained by using graphene oxide, zinc acetate dihydrate ($Zn(CH_3COOH)_2.2H_2O$), (MW;183.48 g/mol), tellurium powder (MW;127.6 g/mol) and ethylenediamine (MW;60.1 g/mol). Whereas graphene oxide is synthesized using a Hummer's method based on previous literature[29], and all of the reagents used in this method are analytical grade and used without further purification.

5.1.2 Synthesis

5.1.2.1 Synthesis of Zincospiroffite

Zincospiroffite-RGO nanocomposite material and zinc telluride are synthesized solvothermally using zinc acetate as a precursor and ethylene diamine as a solvent in our laboratory. Due to its properties like polarity, solubility, and strong chelation, ethylene diamine is particularly useful during synthesis. As ethylene diamine and tellurium attack each other under reaction conditions, telluride forms. The synthesis consists of dissolving 20 mg of graphene oxide (prepared by Hummer's method) in 2 ml of water and ultrasonically treating it for 1 hour. This solution was then diluted in 20 ml of ethylenediamine with 0.1317 g (0.03 M) zinc acetate dihydrate and 0.0766 g (0.03 M) tellurium powder.

The suspension was transferred in to a 100 ml Teflon-lined autoclave, and the autoclave was sealed and maintained at 200 ^oC for six hours vibrations[30]. The formed precipitate was washed several times with methanol after six hours until the solvent had disappeared and allowed to dry at room temperature. A shining black nanocomposite denoted ZTR2 was obtained after complete washing. ZTR1 and ZTR3 are prepared by adding 1ml and 3ml graphene oxide respectively in the above reaction condition. In the absence of graphene oxide, pure Zinc Tellurium Oxide (ZTO) nanomaterial was prepared by following the aforementioned procedure. Similarly, zinc acetate dihydrate and tellurium powder were not added when pure ARGO (Autoclaved-RGO) was prepared under the same reaction conditions. As shown in figure 5.1, the Zincospiroffite hybrid is prepared using this method in a one-step process.

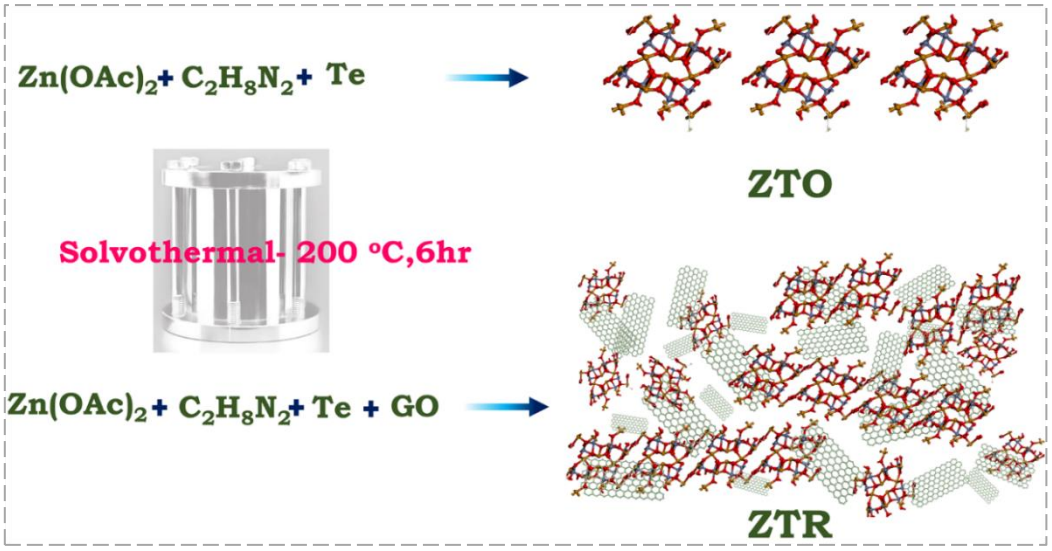

Figure 5.1 A schematic of the procedure followed for the preparation of hybrid ZTR by one-pot solvothermal method

5.1.3 Characterizations

The X-ray Diffraction (XRD) was performed on a Rigaku-Miniplex X-ray diffractometer using Cu-Kα radiation with a wavelength of 1.5406 A^{o}. X-plora plus Raman Spectrophotometer used for Raman analysis. Using a Zeiss Gemini 300 Scanning Electron Microscope (SEM) morphology studies were conducted. The Belsorp Max was used to measure surface area (BET), and the Kyowa Dropmaster DMs series was used to measure contact angle (CA). To precisely weigh the masses of blank substrate and material-coated substrate (Shimadzu AUW220D), a five-precision electronic balance was used. The Biologic SP-150 electrochemical workstation was used for all electrochemical experiments.

5.2. Characterizations

5.2.1. Structure and phase analysis

5.2.1.1 X-Ray Diffraction

The structural analysis of the material is obtained from the X-ray diffraction spectrum The XRD pattern of ARGO, ZTO, graphene hybrids (ZTR1, ZTR2 and ZTR 3) are shown in Figure 5.2a to 5.2c. The X-ray diffraction pattern of ZTO matches with JCPDS Card no. 72-1283, corresponding to the planes of monoclinic $Zn_2Te_3O_8$ in the space group C_2/c. Notably, there are no signature peaks representing RGO are present in the ZTR samples due to the very low diffraction intensity of reduced graphene oxide compared to the crystalline ZTO. Furthermore, the XRD analysis of both ZTO and ZTR hybrids shows no additional peaks, indicating the absence of any other crystalline impurity[31,32]. The XRD data of GO is given as figure S1in supporting information (see Appendix II).

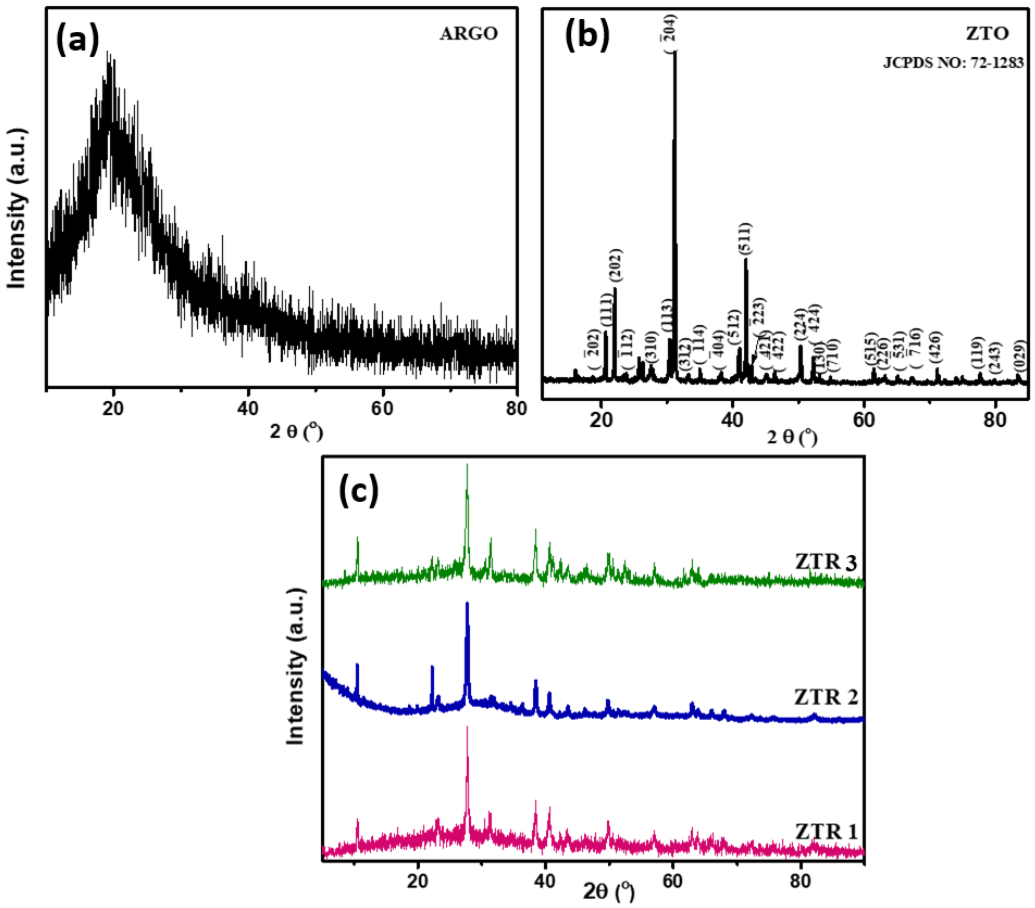

Figure 5.2. X-ray diffractograms of hydrothermally synthesized ARGO, ZTO and ZTR1, ZTR2 and ZTR3

5.2.1.2 Raman analysis

Figure 5.3 (a) to (c) shows the Raman spectra of ARGO, ZTO and hybrids (ZTR1, ZTR2, and ZTR3) respectively. The D and G bands are observed at ~1308 cm^{-1} and~ 1585 cm^{-1} respectively for ZTR and ARGO. The intensity of the D band in ZTR2 and ZTR3 is increased compared with ARGO, which corresponds to the presence of more sp^2 domains during graphene oxide reduction[33]. The structural disorder is determined by calculating the intensity ratio between D and G bands. The I_D/I_G ratio of ZTR nanocomposite is 1.21, which is much higher than that observed for graphene oxide as shown in figure S2 in SI (Appendix II), indicating the removal of oxygen functionalities and a partially ordered crystal structure of reduced graphene oxide sheets[34]. Raman results confirm the hydrothermal reduction of graphene oxide (See figure S2 in Appendix II). The zincospiroffite nanoparticles are successfully deposited onto the reduced graphene oxide sheets in the solvothermal treatment at 200 ^oC in ZTR1, ZTR2, and ZTR3. However, the ZTO sample shows no D or G bands, instead an intense peak corresponds to Te-O vibrations[30] is seen.

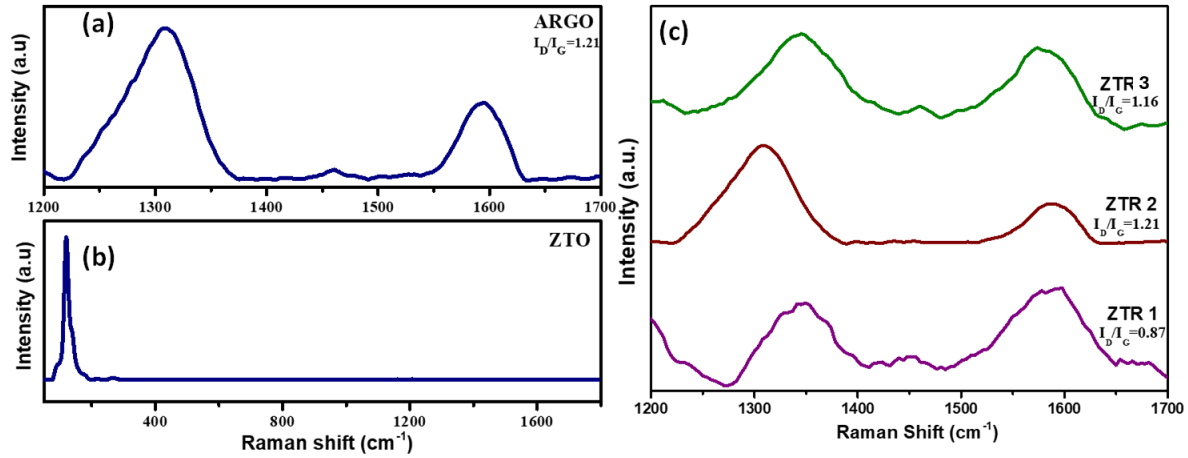

Figure 5.3 Raman spectra of (a) ARGO (I_D/I_G=1.06), (b) ZTO and (c) ZTR1(I_D/I_G=0.87), ZTR2 (I_D/I_G=1.21) and ZTR3 (I_D/I_G=1.16)

5.2.2 Morphology analysis

5.2.2.1 FE-SEM analysis

The morphological studies of ARGO, ZTO, and ZTR hybrids are shown in figure 5.4. The surface morphology of the three samples is different with respect to each other. Figure 5.4a depicts ARGO's folded surface, which has a layer structure with irregular, and ultrathin paper-like morphology similar to graphene sheets.

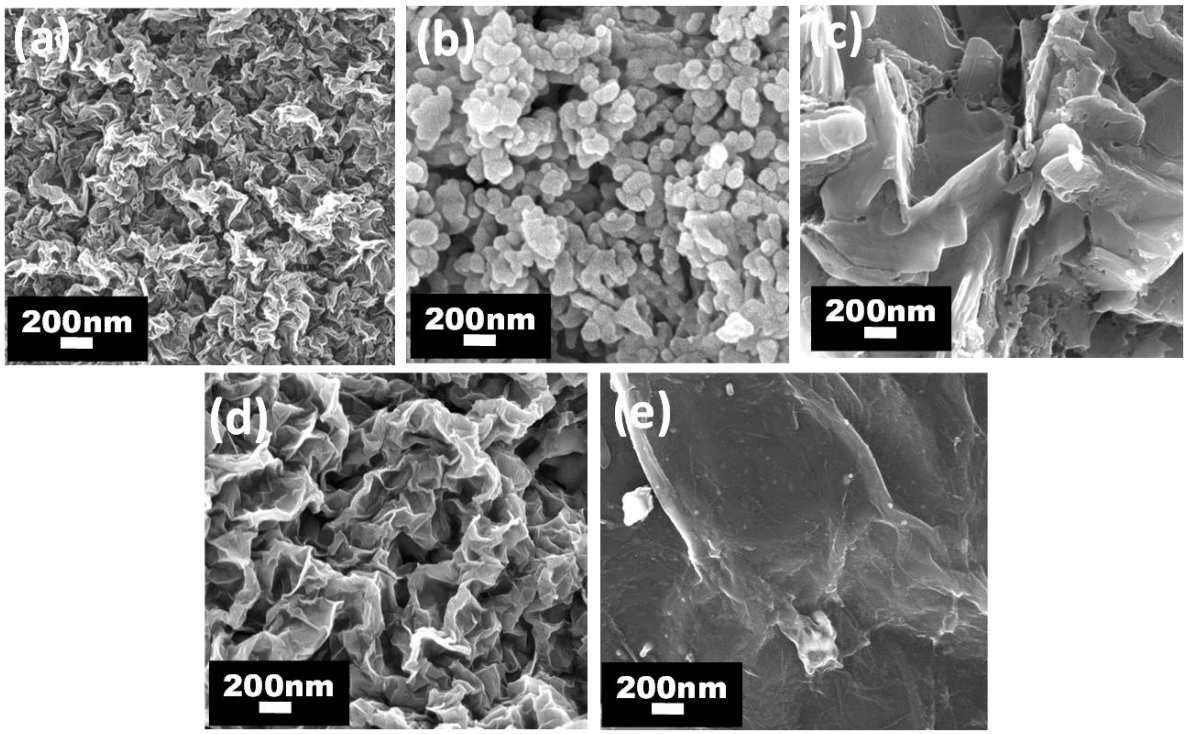

Figure 5.4 SEM micrographs of (a) ARGO, (b) ZTO, (c) ZTR1, (c) ZTR2, and (c) ZTR3 processed by solvothermal one-step synthesis method

This indicates that the hydrothermal method[35] is successful in reducing GO (figure S3 in SI-

Appendix II.) to RGO. As a result of the folded layers and overlapped structure, the ARGO sample has a large surface area. The SEM image of the ZTO in figure 5.4b shows an irregularly shaped sphere-like structure that is uniformly distributed. In the case of ZTR2, the particles are uniformly distributed across the surface during the one-pot solvothermal technique, as shown in Figure 5.4c. Furthermore, when compared to the ZTO system, an overlapped layer-like formation is visible during ZTR2 synthesis and is also observed in ZTR1 and ZTR3 (figure 5.4c and 5.4e). The addition of graphene oxide during the synthesis improves the sheet-like formation of the ZTR2, making it more porous than ZTO. Because of the larger surface area of the ARGO doubles the surface area of the ZTR2. This sample is more electrochemically active than the other two.

5.2.3 Surface area and porosity

5.2.3.1 BET analysis

The BET measurement is used for analyzing the porous nature of the synthesized material. Figure 5.5a shows the N_2 adsorption–desorption results of the sample ZTO, ZTR, and ARGO. The analysis reveals it as a type IV hysteresis nature[36], which indicates the mesoporous behaviour. The specific surface area of ZTO, ARGO, and ZTR are respectively 6.17 $m^2 g^{-1}$, 242.57 $m^2 g^{-1}$, and 15.09 $m^2 g^{-1}$. As a result of the hybrid synthesis process, ZTR has twice the surface area of ZTO. The zincospiroffite was distributed over the graphene sheets while using GO to increase the surface area and give rise to the doubled porosity. The hybrid material ZTR's high specific surface area will help to improve the electron transfer and mass transport during the electrochemical process. This is a good criterion for the material, which has a higher performance-specific capacitance. The BJH (Barrett-Joyner-Halenda) pore size distribution curve (figure 5.5b) with a pore diameter of ZTR2 as 4.29 nm and ZTO as 5.25 nm, which corresponds to mesopore characteristics. The p/p_o values of ZTO, ZTR, and RGO are 0.0161 $cm^3 g^{-1}$, 0.0081 $cm^3 g^{-1}$ and 0.2281 $cm^3 g^{-1}$ respectively. The details of specific surface area, total pore volume and pore diameter are tabulated in Table 5.1.

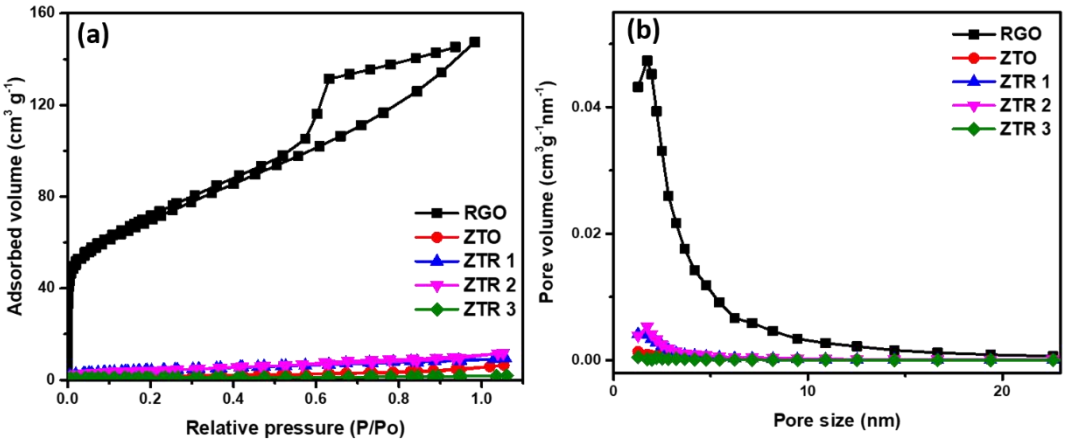

Figure 5.5 (a) BET N_2 adsorption–desorption and (b) BJH plot details of ARGO, ZTO, ZTR1, ZTR2 and ZTR3

Sample Name	$SSA_{BET}(m^2/gm)$	TPV (cm^3/g)	Pore diameter (nm)
ARGO	242.57	0.228	3.76
ZTO	6.17	0.008	5.25
ZTR1	15.20	0.013	3.56
ZTR2	15.09	0.016	4.29
ZTR3	3.64	0.002	2.88

Table 5.1. Specific surface area (SSA), total pore volume (TPV), and pore diameter of ZTO, ARGO, and ZTR hybrids

5.2.4 Wettability Measurement

5.2.4.1 Contact Angle Measurement

Measurement of the contact angle is one of the useful techniques to know how the electrode surface interacts with the electrolyte as well as the chemical nature of the surface. In the supercapacitor application, surface wettability is a primary evaluation technique. The surface science of the prepared material is critical to its storage application and efficiency[37]. The shape of the liquid droplets on the surface of the material as a result of the pressure difference created between the air and liquid interface is analyzed. Supercapacitance performance is improved due to the improved surface wettability of the liquid electrolyte.

According to the preliminary evaluation of the electrode surface that was subjected to CA measurement, the electrode-electrolyte interaction was good, and improved supercapacitor performance is anticipated[37]. Figure 5.6a to 5.6e shows the results of the contact angle measurement of the composite samples, ARGO, ZTO, ZTR1, ZTR2 and ZTR3. The obtained contact angle values for ARGO, ZTO, and ZTR2 are respectively 44.3°, 33.6° and 28.6°. There

is a lower contact angle in ZTR2 than in the other two samples, ensuring that it is highly wettable. Generally, a hydrophilic surface has a contact angle less than 90^o, and a hydrophobic surface has a contact angle greater than 90^o. This indicates that all of our prepared samples' ARGO (44.3°), ZTO (33.6^o), ZTR1 (35.2°), ZTR2 (28.6°) and ZTR3 (42.1^o) are hydrophilic and better for the electrode-electrolyte interaction[38].

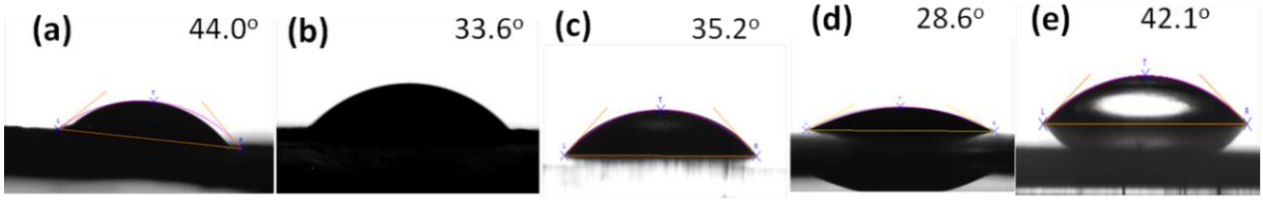

Figure 5.6 Contact angle measurement of (a) ARGO, (b) ZTO, (c) ZTR1, (d) ZTR2, and (e) ZTR3 to check the wettability characteristics

5.2.5 Electrochemical property analysis - Supercapacitor Applications

5.2.5.1 Electrode preparation

The working electrode is made by mixing 75% zincospiroffite with 15% carbon black as a conducting additive and 10% polyvinylidene fluoride as a binder. A homogeneous slurry was made with N-methyl pyrrolidone, and the substrate was coated with doctor blade technique (1x1 cm^2). The electrode material was then dried at 90 °C for a few hours. We calculated the weight of the active material by comparing the weight of the current collector before and after coating. With a two-electrode system, cyclic voltammetry is performed using potassium nitrate (KNO_3) as an electrolyte. Whatman filter paper, soaked in the electrolyte for 10 hours. is used as the separator. The symmetric cell is fabricated by sandwiching two coated electrodes with electrolyte.

5.2.5.2 Electrochemical Analysis-Symmetric Supercapacitor formation

To evaluate the electrochemical and capacitive performance of the obtained hybrid materials CV (Cyclic Voltammetry) and GCD (Galvanostatic Charge Discharge) tests were carried out at different scan rates and current densities. The CV curve in figure 5.7a ARGO shows double-layer capacitance, while 5.7b ZTO and 5.7(c-d) ZTR hybrids show pseudocapacitive behaviour with excellent charge diffusion at the electrode-electrolyte interface. As the scan rate increased from lower to higher, the curve shape was well maintained without any deviation, showing good performance from the supercapacitors. Increasing scan rates from 10 mV/s to 500 mV/s shifts the cathodic and anodic peak potentials in opposite directions. Comparing the CV (figure 5.7c) of ZTR1, ZTR2, and ZTR3, the ZTR2 shows better storage and is taken for further

analysis. The specific capacitance values of ZTR2 is 513.51 F/g for 10 mV/s, which is excellent for the telluride material compared to other metal chalcogenides like CoS (41.36 F/g)[4] and CoS_2 (348 F/g)[39]. Evaluating the CV at 10 mV/s, ZTR1 gives 106.8 F/g, ZTR2 gives 513.51 F/g and ZTR3 gives 298.0 F/g. The specific capacitance obtained for ZTR2 at scan rates 20 mV/s, 50 mV/s, 100 mV/s and 500 mV/s are respectively 304.88 F/g, 117.71 F/g, 70.28 F/g and 19.66 F/g for a potential window of -1V to 1V. ZTO-specific capacitance ranges between 42.29 F/g and 2.42 F/g, with a potential window of -1.2 V to 0.7 V, with a scan rate ranging from 10 to 500 mV/s. The specific capacitance obtained for ARGO is between 183.24 F/g for 10 mV/s and 14.70 F/g for 500 mV/s over a potential window of 0.8 V to -1.3 V. According to the improved specific capacitance of ZTR2, the in-situ incorporation of RGO in ZTO provides a synergetic effect between the two compounds. ZTR2 hybrid is capable of working in a wide range of scan rates ranging from 10 mV/s to 500 mV/s (figure 5.7d).

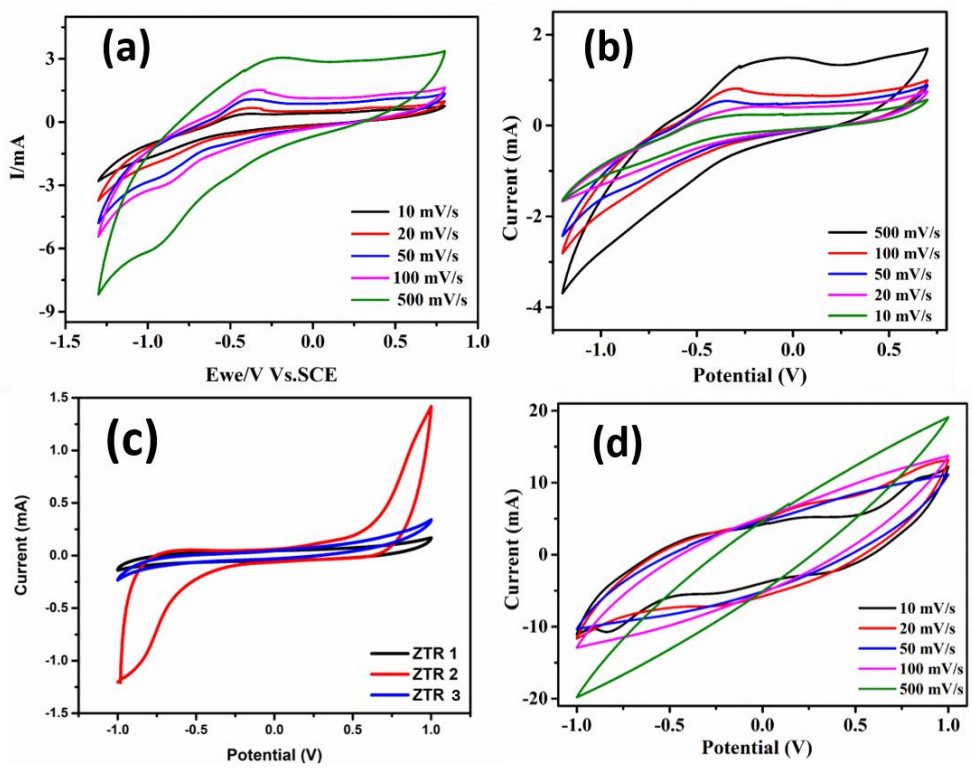

Figure 5.7 CV plot details of (a) ARGO (b) ZTO with different scan rates from 10 mV/s-500 mV/s and (c) comparison of ZTR1, ZTR2 and ZTR3 hybrids in and (d) ZTR2 with various with different scan rates from 10 mV/s-500 mV/s in 0.1 M KNO_3 electrolyte

The more efficient storage property is due to the excellent oxidation and reduction reaction and good rate performance during the lower scan rate to the higher scan rate. As a result of the effective utilization of the higher surface area during intercalation-deintercalation, a high specific capacitance can be achieved while lowering the scan rate. A decrease in specific capacitance during a higher scan rate indicates the good rate capability of the synthesized

material[36]. The redox process of hybrid in KNO_3 takes place via intercalation-deintercalation of K^+ ions in the electrolytic medium[19]. The following equations describe the expected mechanism (1)-(2),

$$Zn_2Te_3O_8 + K^+ \leftrightarrow (Zn_2Te_3O_8K)_{surface} + e^- \quad (1)$$

$$(Zn_2Te_3O_8K)_{surface} + e^- \overset{Charge/discharge}{\longleftrightarrow} Zn_2Te_3O_8\,K^+ \quad (2)$$

The specific capacitance was gradually decreased with an increase in scan rate. The nanocomposite ZTR2 integrates the advantages of each component in the material or the synergic effect of both faradaic and non-faradaic components helps to increase the specific capacitance. Figure 5.8a shows the charge-discharge curve of ZTR2 hybrid material over various current densities like 1 A/g to 10 A/g. The initial dip in the plot conveys some restricted electron transfer due to electron series resistance. The linear variation deals with the double-layer capacitance and slope part generated from the pseudocapacitive behaviour of the material. The lower scan rate provides higher specific capacitance due to better electrode-electrolyte contact.

Electrochemical impedance spectroscopy is one of the perfect tools used to analyze charge transfer resistance, phase angle, surface of the material, and electrode-electrolyte interface[19]. The higher frequency region in figure 5.8b shows a smaller semi-circle compared to others, indicating less hindrance during the migration to the surface of the material and that imparts better specific capacitance for ZTR2[40]. Considering all the parameters, ZTR2 shows a better performance due to enough electrode-electrolyte contact and better to-and-fro migration of K^+ ions than other two compounds. The energy density and power density obtained for ZTR is 83.33 Wh/kg and 0.99 kW/kg. The continuous cycling experiment (up to 5000 cycles) under constant current of 10 A/g establishes the long-term cyclic stability of the hybrid ZTR electrode. Figure 5.8c shows high-capacity retention of 99% up to 5000 cycles and Table 5.2 compares the specific capacitance and cyclic stability of other reported compounds with that of the ZTR electrode.

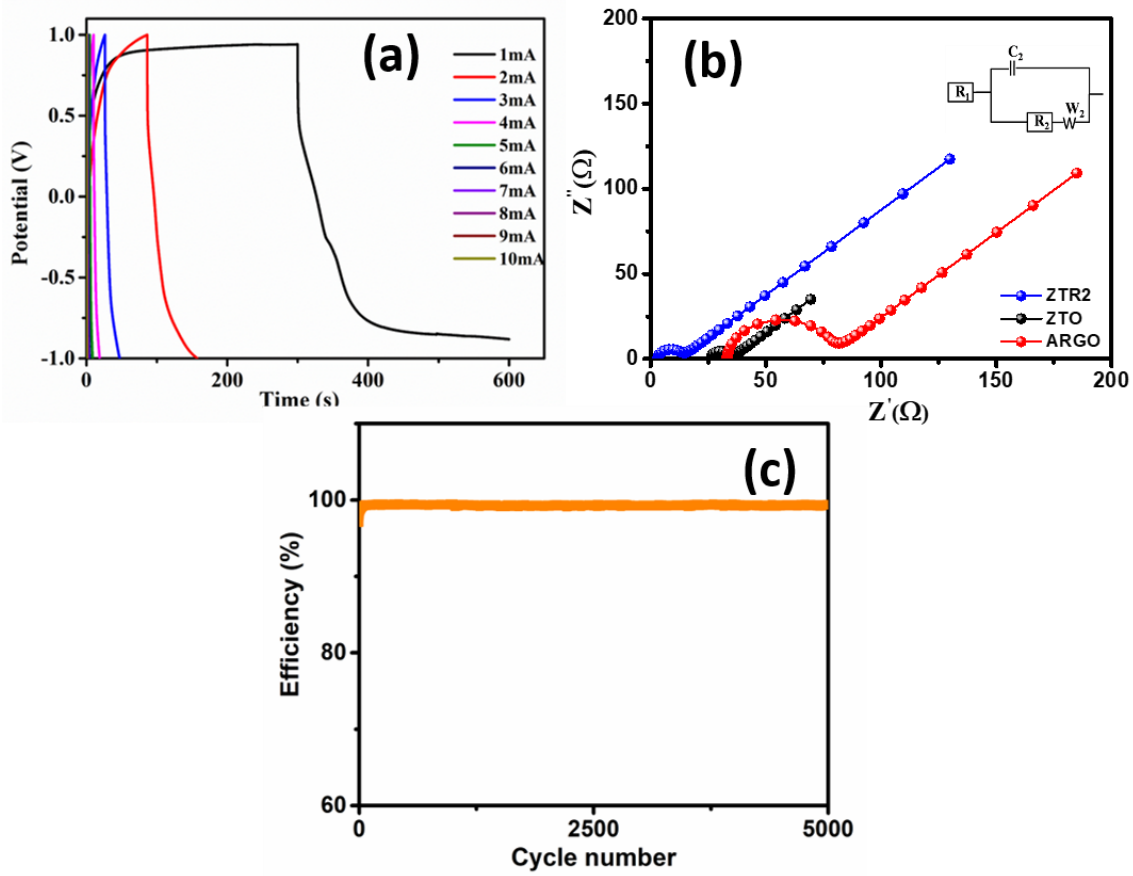

Figure 5.8 (a) Galvanostatic charge-discharge of ZTR2 at different current densities (b) EIS data plots with fitted circuit for ARGO, ZTO, and ZTR2 and (c)Variation of the efficiency as a function of cycle number for ZTR2

Material	Specific capacitance	Cyclic stability	References
La_2Te_3	469 F/g	74% at 1000 cycles	[19]
NiTe	618 F/g	75% at 5000 cycles	[40]
CoTe	183 F/g	85% at 10000 cycles	[36]
$SmTe_3$	144 F/g	69.3% at 1000 cycles	[41]
ZTR2	600 F/g	99% at 5000 cycles	**This work**

Table 5.2 Compares the specific capacitance, cyclic stability, and retention of the other metal telluride-based electrode material

5.3 Conclusion

Zincospiroffite-graphene hybrid ($Zn_2Te_3O_8$/ RGO) material was prepared by a simple one-pot solvothermal method. The addition of graphene oxide during the synthesis increases the porosity. This makes considerable improvement in specific capacitance and other electrochemical properties. The synthesized zincospiroffite-RGO electrode material shows a

higher specific capacitance of 600 F/g at 1 A/g in a symmetric electrode arrangement with 0.1 M KNO_3 aqueous electrolytic medium and is higher than that of other compounds. ZTR2 exhibits an energy density of 83.33 Wh/kg and a power density of 0.99 kW/kg. To the best of our knowledge, Zn-based metal chalcogenide-carbon hybrid has not been reported as a supercapacitor electrode. It is relevant for future applications.

*****

Appendix II

Supporting Information

XRD analysis

A strong peak can be seen at 2θ =10.89^{o} with a stacking in the (0 0 2) direction seen in figure S1. This is the graphene oxide diffraction peak. The interlayer spacing, or d spacing, is 0.816 nm. The presence of oxygen-containing functional groups causes the larger d spacing. This diffraction peak changes with changes in interlayer spacing depending on the concentration of $KMnO_4$. The extent of oxidation and the number of water molecules intercalated into the interlayer spacing determine the d spacing of graphene oxide in the 0.6 nm to 1.0 nm range. The crystalline size, D, was calculated using Scherrer's equation and was found to be 5.1 nm. The graphene oxide XRD results show that the graphite powder has been successfully oxidised.

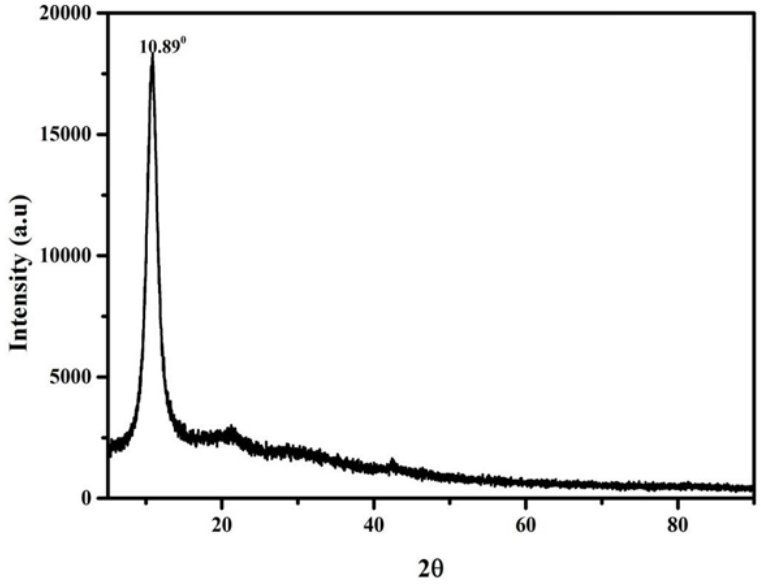

Figure S1. XRD pattern of the graphene oxide

Raman analysis

The Raman spectrum reveals two distinct peaks: D-defects and G-graphite. The D band at 1347 cm^{-1} indicates that the size of the in-plane sp^2 domains is reduced during oxidation. The intensity of the D peak indicates the degree of disorder, which is the defect in its structure. This band was created as a result of the breathing mode of a six-membered ring. The G band at 1599 cm^{-1} corresponds to graphene oxide in phase vibration. The obtained I_D/I_G ratio is 0.47 shown in figure S2. The lower the I_D/I_G value, the higher the level of oxidation.

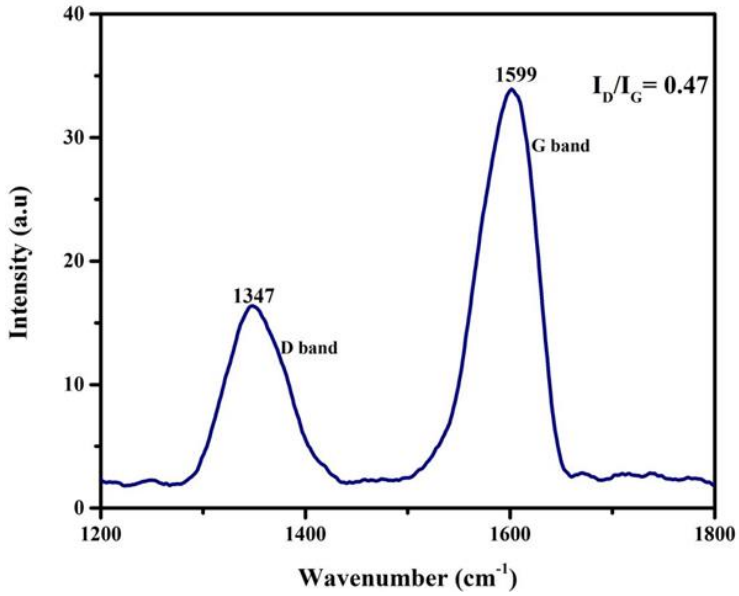

Figure S2. Raman spectra of graphene oxide (I_D/I_G = 0.47)

SEM analysis

According to SEM micrographs, the structure of graphene oxide is look like two-dimensional sheet in figure S3a. (a) and (b). In addition, the SEM images shows that graphene oxide has a crumbled and rippled structure as a result of deformation during the stacking process.

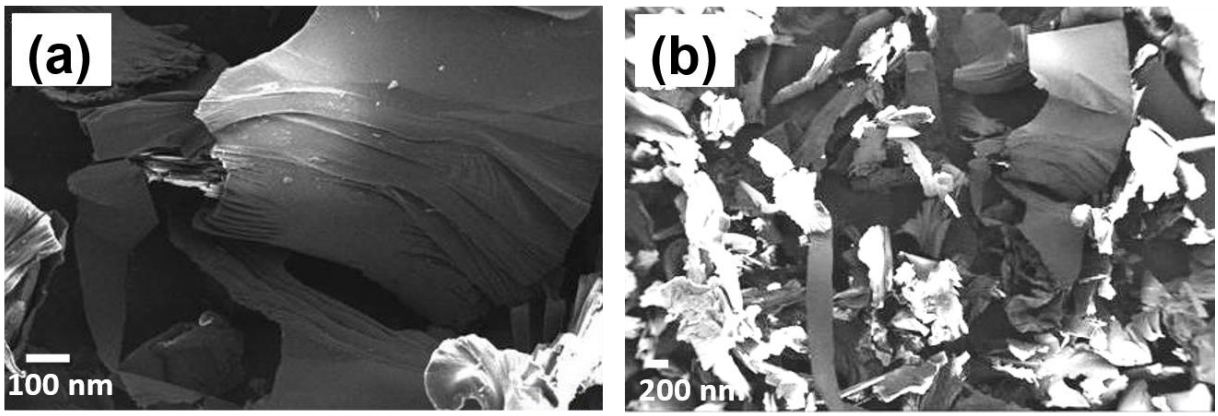

Figure S3. Different magnification of FE-SEM images of graphene oxide (a) 100 nm and (b) 200nm

Reference

[1] J. M. Lim, Y. S. Jang, H. Van T. Nguyen, J. S. Kim, Y. Yoon, B. J. Park, D. H. Seo, K.-K. Lee, Z. Han, K. Ostrikov, S. G. Doo, *Nanoscale Adv.* **2023**, *5*, 615–626.

[2] H. Fang, D. Li, M. Zhao, Y. Zhang, J. Yang, K. Wang, *Energy Sources, Part A: Recovery, Utilization, and Environmental Effects* **2022**, 1–18.

[3] S. Karthikeyan, B. Narenthiran, A. Sivanantham, L. D. Bhatlu, T. Maridurai, *Materials Today: Proceedings* **2021**, *46*, 3984–3988.

[4] Y. Anil Kumar, S. Srinivasa Rao, D. Punnoose, C. Venkata Tulasivarma, C. V. V. M. Gopi, K. Prabakar, H. J. Kim, *Royal Society Open Science* **2017**, *4*, 170427.

[5] M. I. A. Abdel Maksoud, R. A. Fahim, A. E. Shalan, M. Abd Elkodous, S. O. Olojede, A. I. Osman, C. Farrell, A. H. Al-Muhtaseb, A. S. Awed, A. H. Ashour, D. W. Rooney, *Environmental Chemistry Letters* **2021**, *19*, 375–439.

[6] T. Nguyen, M. de F. Montemor, *Advanced Science* **2019**, *6*, 1801797.

[7] B. Vidhyadharan, N. K. M. Zain, I. I. Misnon, R. A. Aziz, J. Ismail, M. M. Yusoff, R. Jose, *Journal of Alloys and Compounds* **2014**, *610*, 143–150.

[8] L. Feng, Z. Xuan, H. Zhao, Y. Bai, J. Guo, C. Su, X. Chen, *Nanoscale Research Letters* **2014**, *9*, 290.

[9] F. Shi, L. Li, X. Wang, C. Gu, J. Tu, *RSC Adv.* **2014**, *4*, 41910–41921.

[10] X. Liu, J. Zeng, H. Yang, K. Zhou, D. Pan, *RSC Advances* **2018**, *8*, 4014–4031.

[11] S. Raj, S. K. Srivastava, P. Kar, P. Roy, *Electrochimica Acta* **2019**, *302*, 327–337.

[12] Y. Zhang, H. Li, L. Pan, T. Lu, Z. Sun, *Journal of Electroanalytical Chemistry* **2009**, *634*, 68–71.

[13] T. Kavitha, S. Kumar, *Materials Research Express* **2021**, *8*, 115504.

[14] M. Manikandan, S. Dhanuskodi, N. Maheswari, G. Muralidharan, C. Revathi, R. T. Rajendra Kumar, G. Mohan Rao, *Sensing and Bio-Sensing Research* **2017**, *13*, 40–48.

[15] M. S. Khan, M. N. Ashiq, M. F. Ehsan, T. He, S. Ijaz, *Applied Catalysis A: General* **2014**, *487*, 202–209.

[16] D. James, X. Lu, A. C. Nguyen, D. Morelli, S. L. Brock, *The Journal of Physical Chemistry C* **2015**, *119*, 4635–4644.

[17] S. F. Wang, Y. F. Hsu, Y. R. Wang, C. C. Sung, *Journal of the American Ceramic Society* **2011**, *94*, 812–816.

[18] D. Jamwal, S. K. Mehta, *ChemistrySelect* **2019**, *4*, 1943–1963.

[19] S. J. Patil, B. H. Patil, R. N. Bulakhe, C. D. Lokhande, *RSC Advances* **2014**, *4*, 56332–56341.

[20] M. Manikandan, S. Dhanuskodi, N. Maheswari, G. Muralidharan, C. Revathi, R. T. Rajendra Kumar, G. Mohan Rao, *Sensing and Bio-Sensing Research* **2017**, *13*, 40–48.

[21] H.-W. Tsai, A. Yaghoubi, T.-C. Chan, C.-C. Wang, W.-T. Liu, C.-N. Liao, S.-Y. Lu, L.-J. Chen, Y.-L. Chueh, *Nanoscale* **2015**, *7*, 7535–7539.

[22] J. Cao, M. Safdar, Z. Wang, J. He, *J. Mater. Chem. A* **2013**, *1*, 10024–10029.

[23] Y. Liu, J. Wang, Y. Xu, Y. Zhu, D. Bigio, C. Wang, *J. Mater. Chem. A* **2014**, *2*, 12201–12207.

[24] D. Kalpana, K. S. Omkumar, S. S. Kumar, N. G. Renganathan, *Electrochimica Acta* **2006**, *52*, 1309–1315.

[25] D. Teixeira, R. Quesada-Cabrera, M. J. Powell, G. K. L. Goh, G. Sankar, I. P. Parkin, R. G. Palgrave, *New Journal of Chemistry* **2017**, *41*, 9216–9222.

[26] S. J. Patil, B. H. Patil, R. N. Bulakhe, C. D. Lokhande, *RSC Adv.* **2014**, *4*, 56332–56341.

[27] V. S. Kumbhar, A. C. Lokhande, N. S. Gaikwad, C. D. Lokhande, *Materials Science in Semiconductor Processing* **2016**, *46*, 29–34.

[28] M. Manikandan, K. Subramani, M. Sathish, S. Dhanuskodi, *RSC Adv.* **2020**, *10*, 13632–13641.

[29] Y. Gu, J. Wu, X. Wang, W. Liu, S. Yan, *ACS Omega* **2020**, *5*, 18975–18986.

[30] B. Ninnora Meethal, A. F. Panichikkal, J. F. Manamkeri Jafferali, D. M. Vidyadharan, S. Swaminathan, *Materials and Design* **2019**, *165*, 107600.

[31] K. Chakraborty, T. Pal, S. Ghosh, *ACS Applied Nano Materials* **2018**, *1*, 3137–3144.

[32] K. Chakraborty, S. Ghosh, T. Pal, *ChemistrySelect* **2018**, *3*, 8637–8643.

[33] H.X. Wang, R. Wu, S.H. Wei, L.R. Yu, J. K. Jian, J. Hou, J. Wang, H. Y. Zhang, Y. F. Sun, *Chinese Chemical Letters* **2016**, *27*, 1572–1576.

[34] X. Li, Z. Wang, Y. Qiu, Q. Pan, P. Hu, *Journal of Alloys and Compounds* **2015**, *620*, 31–37.
[35] M. Saranya, R. Ramachandran, F. Wang, *Journal of Science: Advanced Materials and Devices* **2016**, *1*, 454–460.
[36] M. Manikandan, K. Subramani, M. Sathish, S. Dhanuskodi, *RSC Advances* **2020**, *10*, 13632–13641.
[37] T. Liu, K. Wang, Y. Chen, S. Zhao, Y. Han, *Green Energy & Environment* **2019**, *4*, 171–179.
[38] Y. Huang, Y. Liu, G. Zhao, J. Y. Chen, *Journal of Materials Science* **2017**, *52*, 478–488.
[39] K. A. Kumar, A. Pandurangan, S. Arumugam, M. Sathiskumar, *Scientific Reports* **2019**, 1–16.
[40] M. Manikandan, K. Subramani, M. Sathish, S. Dhanuskodi, *ChemistrySelect* **2018**, *3*, 9034–9040.
[41] V. S. Kumbhar, A. C. Lokhande, N. S. Gaikwad, C. D. Lokhande, *Materials Science in Semiconductor Processing* **2016**, *46*, 29–34.

Abstract

1. Poly Acrylonitrile Derived Porous Electrospun Carbon Nanofibers

Polyacrylonitrile-based carbon nanofibers (CNFs) are prepared by cost-effective electrospinning followed by high carbonization at different temperature. The electrospun CNFs exhibit excellent mesoporous surface characteristics at high carbonization temperatures. By tuning the carbonization temperature, variations in specific surface area and pore volume are achieved. The specific surface area and pore volume range from 8.62 to 616.12 m^2/g and 0 to 2.27 nm. Compared with other samples, CNF 900 obtained at an optimum temperature of 900 ^oC exhibits highest specific capacitance of 119 F/g at 5 mV/s. The use of the redox additive electrolyte 0.1 M Na_2SO_4 + 0.03 M KI enhances storage properties compared to bare 0.1 M Na_2SO_4. The improved electrochemical parameters like specific capacitance and cyclic stability of 30,000 cycles with improved energy density and power density are observed. The carbon nanofibers, activated through high carbonization temperatures, serve as high-performance electrode materials for both current and future supercapacitor applications.

Keywords: Polyacrylonitrile; Electrospinning; Carbon Nanofibers; Redox additive electrolyte; Supercapacitor

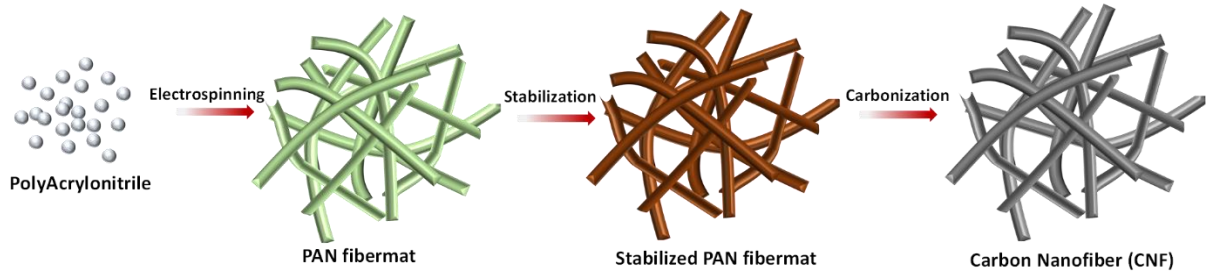

2. Saw Dust (*Ailanthus Triphysa*) Derived Hierarchical Porous Carbon

Three-dimensional hierarchical hexagonal porous carbon was synthesized from *Ailanthus Triphysa* sawdust for the first time. A two-step carbonization process results in etching of the carbon structure caused by $ZnCl_2$ activation and tailoring pores over the carbon structure caused by gasification. The $ZnCl_2$ acts as an activating agent, a template and a facilitator of the activation process, and its concentration regulates the porosity as well as specific surface area of the carbon nanostructures. There are two distinct types of pores in the prepared carbon i.e.mesopores and micropores. The highest specific surface area of 1757.80 m^2/g was obtained when the ratio of $ZnCl_2$ is four times higher than that of the sample. The resulting carbon is

used as an electrode in an electrochemical supercapacitor which gives a specific capacitance of 92.24 F/g at 5 mV/s and a cyclic stability of 3000 with a retention of 98%. The highly porous activated carbon exhibits excellent electrochemical storage properties in an aqueous neutral electrolyte of 0.1 M Na_2SO_4. A redox-enhanced electrolyte like 0.1 M Na_2SO_4 with 0.03 M KI combination improvise the specific capacitance and cyclic stability. The specific capacitance of the redox-enhanced electrolyte combination increases to 104 F/g at 5 mV/s and cyclic stability of 50000 with a retention of 95% during continuous charge-discharge cycles. This work brings forth a simple and green approach to transforming biomass waste into a scalable and economic high-performance supercapacitor.

Keywords: Biomass; hexagonal hierarchical nanostructure; micro-meso porous carbon; supercapacitor

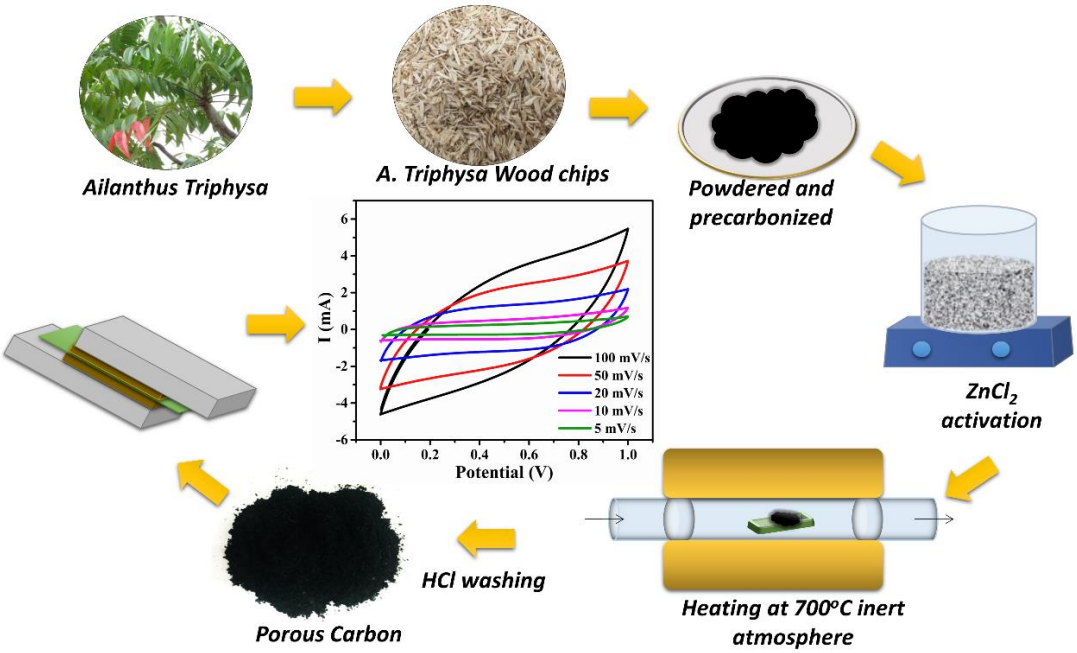

3. Leaf Derived Microporous Carbon from Palmyra Palm Leaves

Carbon materials derived from palmyra palm leaves and chemically activated with $ZnCl_2$ exhibit remarkable energy storage characteristics. Carbon derived from leaves has a specific surface area of 1300 m^2/g and provides extensive electrochemical interfaces. The leaf-derived carbon initially displays a specific capacitance of 75.60 F/g at 5 mV/s in 0.1 M Na_2SO_4 electrolyte. Specific capacitance is significantly improved by introducing a redox additive into the parent electrolyte. In a potential window of 1V, the combination of 0.1 M Na_2SO_4 and 0.03

M KI yields a specific capacitance of 173.04 F/g at 5 mV/s. The findings highlight the exceptional performance and higher stability of leaf-derived activated carbon.

Keywords; Carbon materials, Energy storage and conversion, Porous materials, Supercapacitor

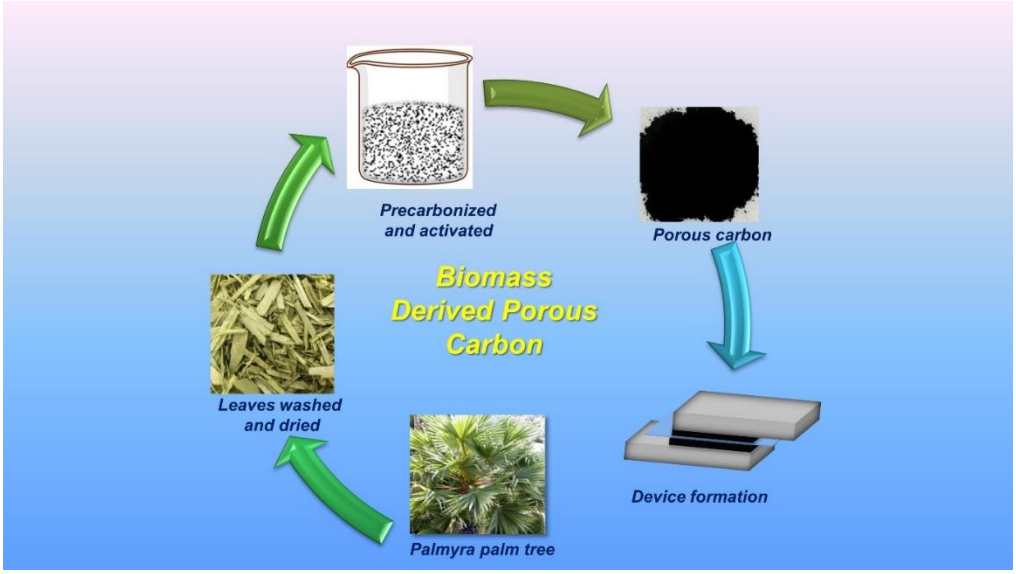

6. Synthetic and Biomass Derived Porous Carbon with Redox Additive Electrolyte for Supercapacitor Application

Introduction

Carbon is an unavoidable element in human life due to its ease of bonding with other elements[1]. It also plays an important role in living systems due to the presence of various allotropes. Carbon materials exist in a variety of shapes and sizes, including carbon nanofiber[2], carbon spheres[3], carbon nano-onions[4], carbon hydrogel[5], carbon nanotubes[6], graphene[6], activated carbons[7], and highly porous carbon. Among these, porous carbon has properties such as high specific surface area, conductivity, tunable porosity, chemical stability, and long shelf life, which attracts it to use as an electrode material in supercapacitors and other energy storage systems. Because of the distribution of pore size in different modes such as micro, meso, and macropores, porous carbon has received more attention in this field. The ordered distribution of the pores provides the shortest ion pathways for effective ion diffusion, as well as abundance in active sites, molecular retention, interfacial reaction, and other factors will improve supercapacitor performance and cyclic stability. Because of this, the electric double-layer materials in supercapacitors make greater use of porous carbon in action. There are various sources available from which activated carbon can be produced using a variety of techniques[8–11].

In this unit we discuss synthesizing of porous carbon material with varying specific surface area and morphology. Based on the selected synthesis methods and resources, changes in various properties like surface area, porosity, morphology are observed. Initially the studies are based on a synthetic source like poly acrylonitrile (PAN). Carbon nanofibers are prepared from PAN by electrospinning technique and followed by carbonization. Further studies are based on biomass (versatile sources for carbon) derived carbons. Highly porous carons are prepared from saw dust (*Ailanthus Triphysa or A.Triphysa*) and leaf (*Palmyra palm or wine palm*). The specific surface area variations were studied with BET technique. The electrochemical studies are done and improvisations made with addition of redox additive electrolyte. Redox electrolytes have received a lot of interest in recent years due to their improved storage qualities. The redox active species consists of simple or complex systems such as halide ions, transition metal ions, phenyl amide, and hydroquinones, which can enhance redox reactions on material surfaces. Adding redox additive species to an existing electrolyte improves its

electrochemical characteristics and enhances the specific capacitance, cell voltage, and energy density, without directly modifying the electrode materials. Various redox additives have been developed for energy storage. These are generally classified as inorganic and organic, depending on their chemical compositions. Further classifications are based on the pH values and the number of redox species.[12,13]

6.1 Saw Dust (*Ailanthus Triphysa*) Derived Hierarchical Porous Carbon

Introduction

Over the past decades, Biomass Derived Carbon (BDC) has gained importance due to the naturally occurring biowaste, availability, low cost, unique structure, renewability, large-scale application well as environmentally safe materials. The BDC has a higher surface area greater than 1500 m^2/g and these are more sustainable than its counterparts that use fossil fuels. This has been used in research and development for Li-S batteries,[29] supercapacitors,[30] Li-ion batteries,[31] and microbial fuel cells.[4] Supercapacitors are widely used in wearable electronic devices, solar devices, grid storage, memory backups, energy recovery, and other applications. The biomass-derived sources are encouraged due to their appealing qualities and the waste-to-wealth concept. For the preparation of such highly porous carbon materials, various sources have been introduced to date. Porous carbon has been produced using inexpensive materials like corn stalks,[32,33] pistachio shells,[34] peanut shells,[35] cotton waste,[36] orange peels,[37] bamboo fiber,[38] straw,[39] etc[32,40–43] that are used in supercapacitor applications.[41] By using a chemical activation process, Yan et al. created activated carbon from a waste lotus stem with a high specific surface area of 1322 m^2/g.[44] Phiri et al. used a chemical activation process to synthesize carbon from field stock waste, such as willow wood. This carbon has coexisting mesopores and micropores with a specific surface area and pore volume of 2800 m^2/g and 1.45 cm^3/g, respectively.[45] By chemically activating eucalyptus leaves, Jain et al. produced activated charcoal with a specific surface area of 2639 m^2/g.[46] Similarly, Zequine et al attempted to use jute thread as a bio-waste source for energy storage applications. The resulting carbon has an average pore diameter of 2.9 nm, a maximum pore diameter of 1.7 nm, and a specific surface area of 1769 m^2/g. [47] According to the studies and reports mentioned above, this kind of biomass is one of the most effective and environmentally friendly sources for creating highly efficient supercapacitor electrodes. As a result, there is still a need to investigate newer resources that are easily controllable, structurally ordered, sustainable, and low in cost.

The distinctive feature of biomass resources is their varying structures with the sources under consideration. The structure and morphology also vary depending on the synthesis methods and reaction conditions applied. While using chemical activation methods, the porosity and pore size change with the porosity-controlling agents.[48] The porosity-enhancing agents (PEA), which fall into the categories of acid, base, and neutral, are effective in chemical activation. A few of them are KOH, H_3PO_4, and $ZnCl_2$ which allow the raw material to be penetrated, subjected to additional thermal processing, and produce the material's high specific surface area. The porosity will aid in the rapid passage of electrolyte ions into the pores. In general, $ZnCl_2$ activation causes matrices to swell, lateral bonds to break, and the inter and intra-micelle voids to expand, resulting in a high specific surface area. Optimizing the PEA's impregnation ratio is crucial for preventing the collapse of the metric's orderly structure. $ZnCl_2$ produces a better graphitic structure by increasing the carbon content through aromatization. It is a dehydrating agent that causes hydrolysis, which in turn triggers processes like intermolecular exchange and molecular migration. Weight loss results from the removal of organic matter by breaking aromatic and aliphatic bonds. The low melting point of $ZnCl_2$ allows for better impregnation with the carbon surface even at lower activation temperatures of 500 ^oC. Because of the smaller ionic radius of zinc ion (74 pm), it serves as a template for the formation of microporous materials.[48,49]

In this section, we propose *Ailanthus Triphysa* (*A.triphysa*), also known as Ailanthus Malabaricus, from the Simaroubaceae family as a novel source of high porosity activated carbon with improved electrochemical properties. It is a medium-sized evergreen tree with a straight and cylindrical structure that stands 30 meters tall and has a diameter of 1.2 meters. The wood is brittle and soft, and it is useful for making charcoal as well as timber and plywood. The plant contains resins that are used to make incense and also contains some organic compounds like alkaloids, quassinoids, and beta-carbolines. It is also used medicinally for diseases such as bronchitis, ophthalmia, dyspepsia, and snake bites. To the best of our knowledge, these plant's saw dust has never been used as a supercapacitor electrode material source before. Different plant sources are used as these studies earlier, even though this study shows the potential of using *A.triphysa* saw dust as an alternative green energy material source for high-performance supercapacitor electrode.

6.2.1 Experimental

6.2.1.1 Materials

For the material synthesis procedures, *A.triphysa* saw dust, hydrochloric acid, zinc chloride,

and DI water were used. Carbon black, Poly Vinylidene Fluoride (PVDF-Alfa Aesar), and N-methyl pyrrolidone (NMP-Sigma Aldrich) were used to make the electrode, and sodium sulfate (Na_2SO_4 - Sigma Aldrich) was used for further electrochemical analysis.

6.2.1.2 Synthesis

6.2.1.2.1 Synthesis of Sawdust-Derived Hierarchical Porous Carbon (AC)

The sawdust was washed well with water to remove the dirt and dust. The powder was then sun-dried for a few hours to remove all moisture content. The sample was then treated with 1N HCl for 5 days and stirred well to remove organic matter. After soaking in HCl, it was rinsed with DI water until the pH was neutralized. The sawdust was then thoroughly dried in an oven prior to pre-carbonization. To keep the carbon structure from collapsing, these were pre-carbonized for 2 hrs at a temperature of 300 ^oC with a constant ramping of 5 ^oC/min. The next step involves treating well-powdered, pre-carbonized samples with anhydrous $ZnCl_2$ in the following ratios: 1:0, 1:2, 1:4, and 1:6. The sample containing $ZnCl_2$ was then heated for an additional hour to ensure complete impregnation into the carbon skeleton. The $ZnCl_2$ activated mixture was then allowed to dry overnight at 110 ^oC to produce dried char. All of these then undergo a second carbonization step called pyrolysis, in which samples were heated to 700 ^oC in an inert atmosphere (N_2-99.999%) to create highly porous samples that ramp up at a constant rate of 5 ^oC/min. The samples were cleaned with hot water and HCl after pyrolysis to get rid of any unreacted species and any byproducts that may have developed. The finally obtained highly porous carbon was named as AC 1:0, AC 1:2, AC 1:4, and AC 1:6.

6.2.1.3 Characterizations

Field emission scanning electron microscopy (ZEISS- GEMINISEM 300) was used to examine the surface topography, morphology, and microstructure development over the adsorbents. The crystal structure and crystalline nature were assessed using a PANalytical-Xpert3 powder X-Ray diffractometer. A 532 nm DPSS laser, the Alpha 300RA from WiTec in Germany, was used to conduct the Raman analysis. The Fourier transform infrared spectroscopy (FTIR) was recorded with Perkin Elmer spectrum two FTIR spectrophotometer using the KBr pellet method. After degassing at 200 ^oC for 18 hours, the specific surface area (SSA) was measured using N_2 and the Brunner-Emmet-Teller (BET) method was used to analyze the adsorption-desorption isotherm. Using the Barrett- Joyner-Halenda (BJH) and *t*-plot methods, the porosity was assessed. The Kyowa drop master DMs 401 was used to test the wettability characteristics. Biologic SP-150 and SP-300 were used for the electrochemical analysis.

6.2.1.4 Formation mechanism

Two-step synthesis procedure was adopted for the preparation of activated carbon using zinc chloride as activating agent. (Figure 6.9). Zinc chloride ($ZnCl_2$) is generally known as a dehydrant in nature and belongs to a low melting point material (in the range of 283-293 ^oC). Over 500 ^oC, $ZnCl_2$ enables better contact with the carbon surface, despite the fact that the chemical activation mechanism is still not completely understood. There are primarily three methods for creating pores with carbon surfaces. The raw material contains a lot of zinc chloride, which when combined with water produces a higher concentration of hydroxy dichloro zincic acid and H [$ZnCl_2$ (OH)] as mentioned in equation (5).

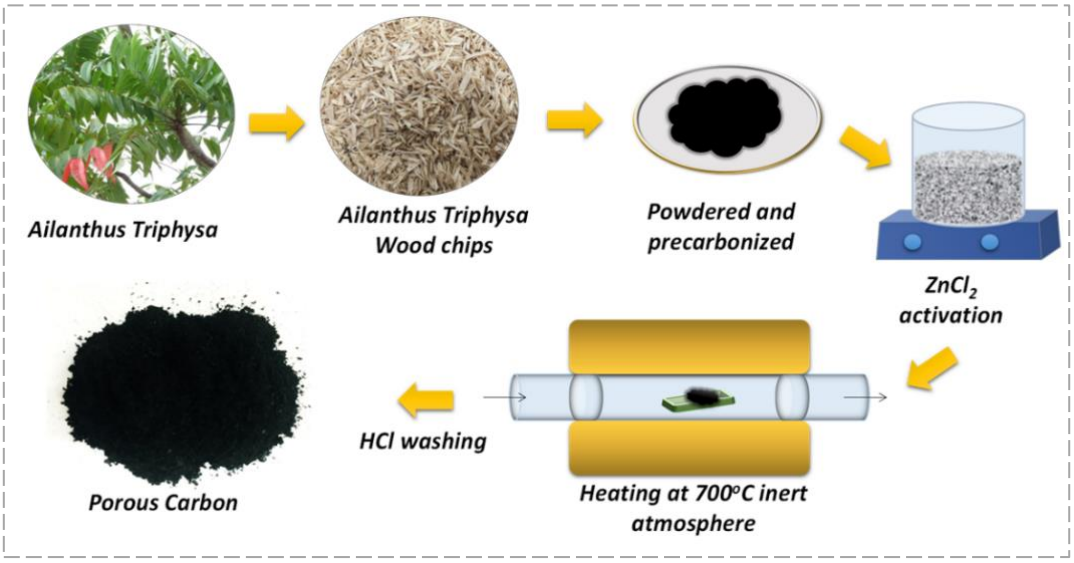

Figure 6.9. Schematics of the two-step synthesis of the highly porous carbon by chemical activation followed by pyrolysis at high temperature in an inert atmosphere

Thus, the corrosive effect of the formed acid causes an etching on the walls of the carbon surface, which introduces a range of porosity with the creation of the channeled structure. Equation (6) describes how the interaction of water and $ZnCl_2$, that is present in the material's pores during pyrolysis at 700 °C, results in the formation of ZnO (figure 6.10). During pyrolysis, this $ZnCl_2$ activation led to poor tar content. Additionally, that raises the carbon content and reduces the development of organic matter and hydrocarbon. The microporous structure throughout the system is modeled after this PEA activation. The additional porosity is created by the removal of ZnO or $ZnCl_2$ from the internal structure using acid washing. The aromatized carbon framework with the coexistence of more than one porosity range could make it multifunctional.

$$ZnCl_2 + H_2O \rightarrow H[ZnCl_2(OH)] \quad (5)$$

$$ZnCl_2 + -OH \rightarrow ZnO + HCl \quad (6)$$

The cellulose counterparts inside the resource are degrade by the activating agent. The rate of formation of the highly porous structure after pyrolysis depends on the extent of the activating agent's impregnation[50].

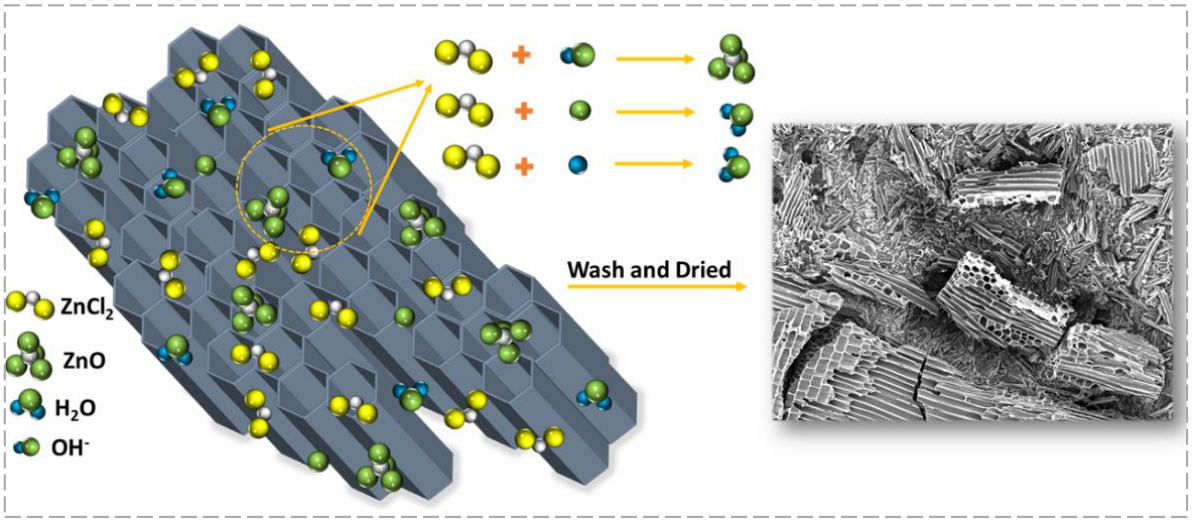

Figure 6.10 Representations of the reaction during the chemical activation process followed by pyrolysis at 700 ºC generates different porous carbon

6.2.2 Results and discussions

6.2.2.1 Structure, Phase and Chemical Analysis

6.2.2.1.1 X-Ray Diffraction

Figure 6.11 shows the XRD diffraction patterns of four activated carbon samples. Crystallinity and phases are confirmed by XRD analysis.

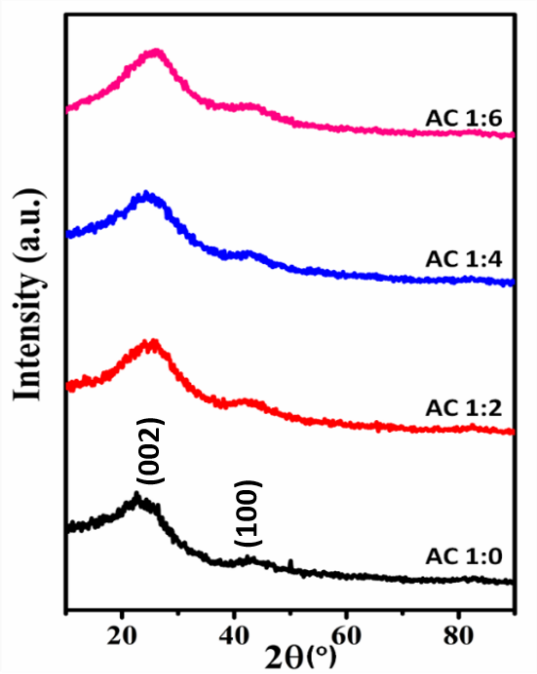

Figure 6.11 XRD pattern of the porous carbon formed by the $ZnCl_2$ activation of *A.triphysa* followed by pyrolysis at high temperature

Two distinctive peaks can be seen at 24.5° and 43°, indicating partial re-stacking and aggregation. It shows the well-defined stacking of the graphitic carbon responsible for the plane of (002) by a peak at 24.5°. The broad peak also indicates the amorphous nature of the so-formed activated carbon. The second weak peak at 43° corresponds to the (100) plane, and this plane is responsible for a higher degree of carbon condensation in the interlayer. According to these results, pre-arranged graphene sheets exist in this structure in the form of small domains. [15,27,28] The presence of graphene domains is expected to increase the material's conductivity and charge storage capacity

6.2.2.1.2 Raman analysis

Raman analysis is used for a precise understanding of the incorporation of $ZnCl_2$ in different amounts in the raw material. Raman analysis is a robust technique used for studying the structure of carbon and graphitized samples. Graphitization and crystalline structure can be determined from these studies. The two peaks appeared at 1300 cm^{-1} and 1550 cm^{-1} in figure 6.12, are assigned to the D and G bands, which stand for the sp^2 hybridized disordered carbon and graphitized carbon respectively.

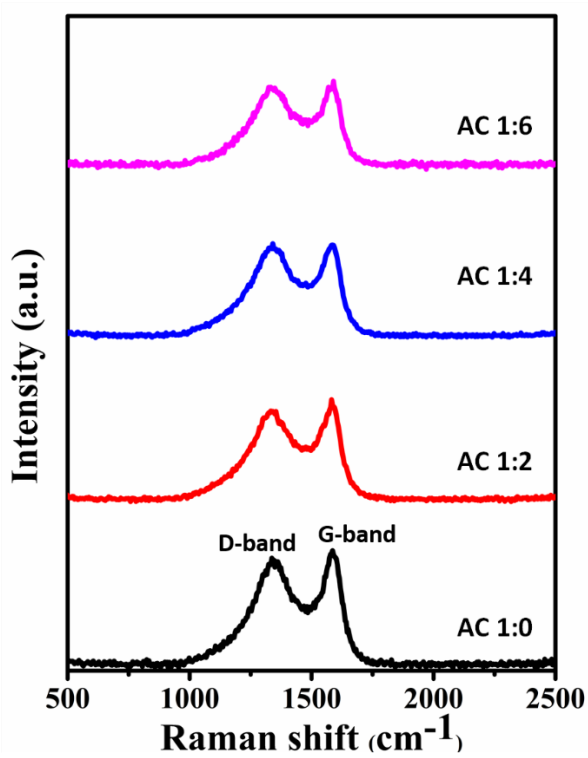

Figure 6.12 Raman spectra of the porous carbon formed by the $ZnCl_2$ activation of *A.triphysa* followed by pyrolysis at high temperature, AC 1:0 (I_D/I_G = 0.96), AC 1:2 (I_D/I_G = 0.94), AC 1:4 (I_D/I_G = 1.03) and AC 1:6 (I_D/I_G = 0.92)

The first broad peak describes the defect-induced or disorder-activated breathing mode of six-membered carbon rings. The second peak corresponds to the E_{2g} phonons at the Brillouin zone center. The intensity ratio of the D and G

bands, I_D/I_G , obtained for the four samples are 0.96, 0.94, 1.03, and 0.92 are respectively for AC1:0 to AC 1:6. This manifests a gradual gain in the degree of graphitization with a higher dosage of $ZnCl_2$, which improves the carbon's conductivity. It can be inferred from the estimated values of I_D/I_G ratio, sample AC1:4 has a higher degree of graphitization and this is responsible for the high conductivity of the AC 1:4.[8,51] Additionally, it states that as the dosage of the activating agent is increased, chemical activation and pyrolysis gradually improve graphitization. which combines mecha nical stability and robustness with improved electronic conductivity. This analysis is consistent with the earlier XRD pattern analysis.

6.2.2.1.3 FT-IR analysis

It is already known that activated carbon contains a wide range of surface functionalized groups. These groups play an important role in determining the properties of activated carbon. FTIR spectroscopy was used for the study of the functional groups. The formation of surface functionalized groups depends on the method of chemical activation used during synthesis. The

FTIR spectra of raw *A.triphysa*, AC 1: 0, AC 1: 2, AC 1: 4, and AC 1: 6 are shown in figure 6.13. The spectra of activated carbons occupied with identical functional groups, because they are synthesized from the same raw sample. Despite varying the concentration of the dehydrating agent, the obtained spectra showed no significant change. Such findings were made by Yorgun et al, who used phosphoric acid activation to create activated carbon from Paulownia wood.[52] Anisuzzaman et al. produced highly porous carbon from Typha orientalis leaf through chemical activation, which exhibits similar behaviour.[1] The broad and wider region band located around ~3135 cm^{-1} is attributed to the hydroxyl groups, due to adsorbed water species, phenol, or the presence of aliphatic alcoholic groups. The peaks around ~1566 cm^{-1} corresponds to the C=O groups. The vibrational stretching of the C=O groups is found in the alcohol, ketone, lactone, and carboxylic groups. The peak around 1381 cm^{-1} is due to C-H bond stretching vibrations. The C-O group is typically represented by a peak near 1200 cm^{-1}. The R-OH groups are distinguished by the appearance of a shoulder peak below 1000 cm^{-1}. Similarly, the presence of the aromatic skeleton structure in the synthesized activated carbon generates weak peaks between 700 to 400 cm^{-1}. The presence of various hydrophilic groups such as C-O, R-OH, C=O, C-H, O-H, and others may improve the wettability characteristic of the activated carbon derived from the *A.triphysa* sawdust via $ZnCl_2$ chemical activation.[1,52] As a result of the improved interface of the electrolyte-activated carbon, the aqueous electrolyte performs better in electrochemical studies.

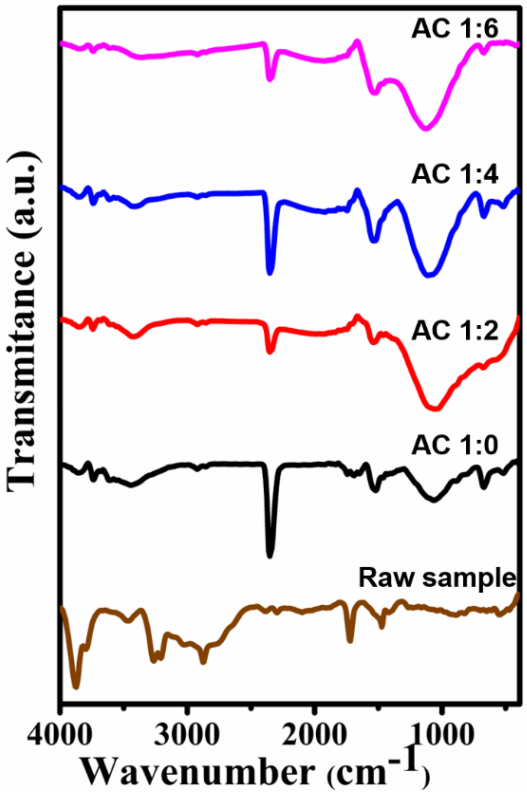

Figure 6.13. FT-IR pattern of the porous carbon formed by the $ZnCl_2$ activation of *A.triphysa*

6.2.2.2. Morphology analysis

6.2.2.2.1 FE-SEM analysis

Figure 6.14a to 6.14h shows the FE-SEM images of the porous carbon samples. The surface morphology influences surface porosity, which determines adsorption capacity. The effectiveness of the material's contact with the electrolyte is vital. The FE-SEM images of chemically activated sawdust reveal that it contains several interconnected pores that form a honeycomb-like structure. Such channelled and interconnected structures facilitate and promote shortest ion paths during electrochemical analysis. The development of porous carbon is affected by the changes in $ZnCl_2$ dosage and reaction conditions. The removal of pre-occupied $ZnCl_2$ molecules results in the expansion of carbon's layered structure. Here, the porous layered structure is formed by the release of some gaseous products as a result of pyrolysis. The step-by-step interconnected micron-sized pores are benevolently taking part in adsorption due to the effectively accessible inner/outer surfaces. This property will enable this material to perform well in a supercapacitor design. The grooves appeared as both vertical and horizontal streaks across the precursor surface look like 3D structure. Figure 6.14 shows a honeycomb-like pattern that is well-ordered and connected. Here we can see the high degree of interconnection, hierarchy, and the hollow tube-like 3D structure. The surface morphology is subjected to change depending on the source, PEA nature and $ZnCl_2$ concentration. Due to the removal of organic volatiles such as oxygen and hydrogen atoms, porosity is generated during the carbonization step. In this process, the nearest carbon atoms combine with each other to form a stable structure. The sample without activation agent contains only a few pores (figure 6.14a), but when $ZnCl_2$ is added as an activating agent, the pores form on the walls of the horizontal and vertical grooves as seen in figure 6.14b. Figure 6.14c and 6.14d shows the role of concentration of activation agent on the density of pores formed on the groove walls of carbon structure.

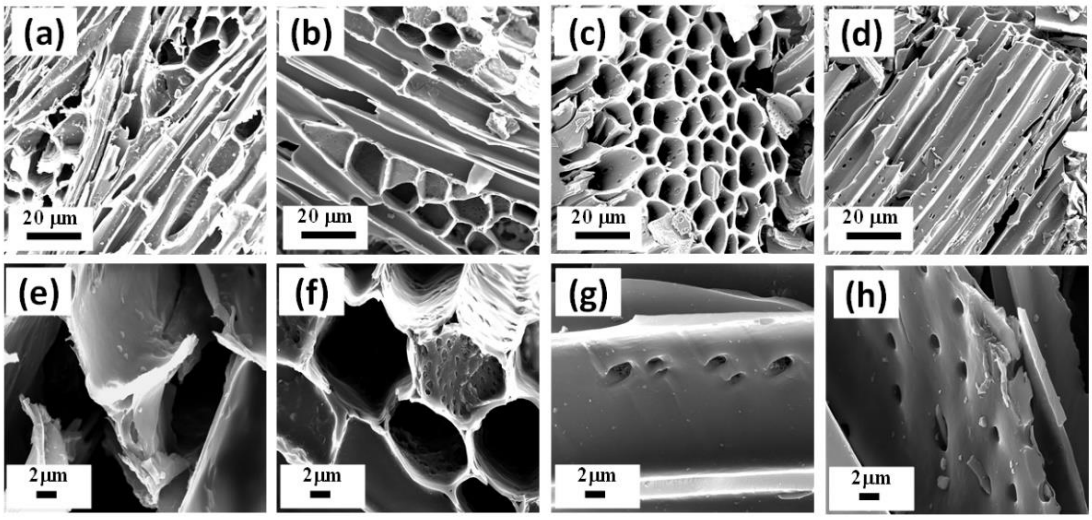

Figure 6.14 SEM images of the *A.triphysa* derived porous carbons by the activation of $ZnCl_2$ at different concentrations at 20µm scale of (a) AC 1:0, (b) AC 1:2, (c) AC 1:4 and (d) AC 1:6. Figure 6.14 e-6.14 h are the magnified images of the samples AC 1:0, AC 1:2, AC 1:4 and AC 1:6 respectively

6.2.2.3 Surface area and Porosity Analysis

6.2.2.3.1 BET analysis

The textural characteristics of the activated porous carbon, has been investigated using N_2 adsorption-desorption studies and the respective graphs are shown in figure 6.15a. Nature of the adsorption-desorption curves reveals type I hysteresis with micropore-dominating characteristics. The sharper adsorption knees (figure 6.15a) are associated with the presence of micropores in carbon. Figure 6.15b shows the pore size distribution curves (PSD), which also dominate microporous characteristics. Based on the strength of the activation process the specific surface area changed and it ranged from 657.77 m^2/g to -1757.80 m^2/g, indicating a moderately high value. Similarly, the total pore volume changes from 0.25 cm^3/g to 0.82 cm^3/g. The *A.triphysa*-derived carbon has a higher specific surface area than palm leaves-derived carbon prepared by Tear *et al* which has a specific surface area within the range of 216 m^2/g - 1218 m^2/g.[53] Rajesh *et al* reported activated pine cone-derived carbon which shows a specific surface area of 853.66 m^2/g – 1169 m^2/g controlling KOH activation.[54] Figure 6.15c depicts the variation of specific surface area with $ZnCl_2$ concentration in the current study. As expected, the sample with the smallest surface area was obtained for AC 1:0 (657.77 m^2/g) which does not undergo any activation. Then up to AC1:4 surface area increased and then decreased due to the breaking or merging of pores structure. The distribution of micro-pores and meso-pores in activated carbon is shown in figure 6.15d. Mesopores may be generated when micropores are superimposed at relatively high concentrations of $ZnCl_2$.

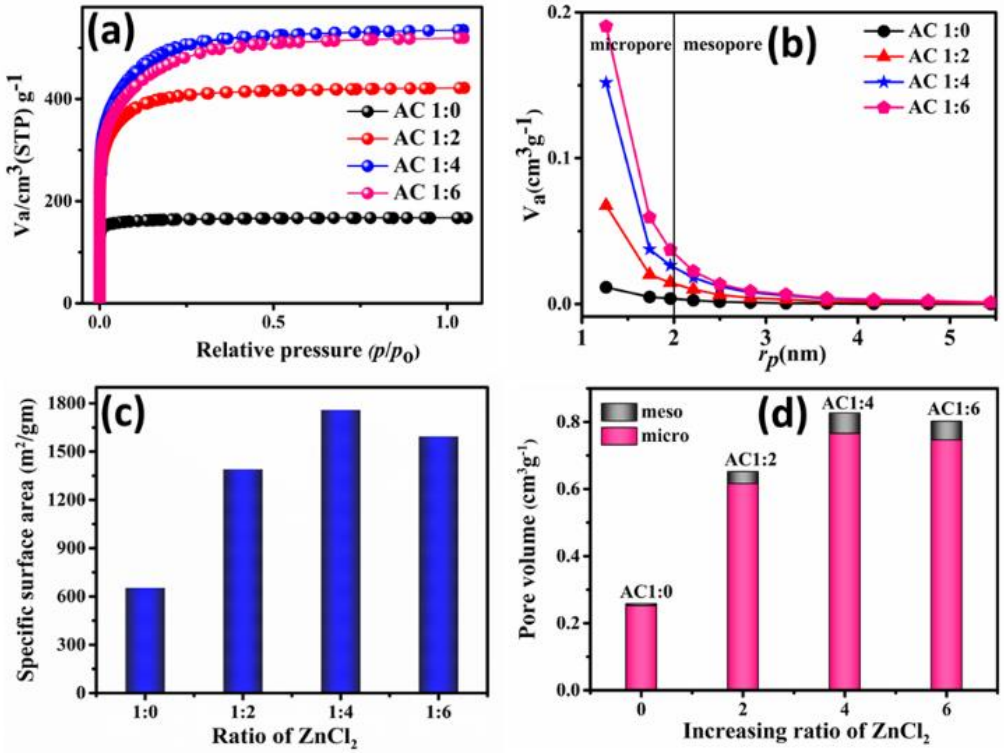

Figure 6.15 (a) N_2 adsorption-desorption isotherm of the *A.triphysa* derived porous carbon (b) BJH curves showing pore size vs pore volume (c) the effect of $ZnCl_2$ concentration versus surface area of the porous carbon structure and (d) the distribution of the mesopores and micropores with respect to the concentration of $ZnCl_2$

Sample Code	SSA[a] [m^2/g]	TPV[b] [cm^3/g]	$SA^{[c]}_{micro}$ [m^2/g]	$SA^{[d]}_{meso}$ [m^2/g]	$PV^{[e]}_{micro}$ [cm^3/g]	$PV^{[f]}_{meso}$ [cm^3/g]	$PD^{[g]}_{micro}$ [nm]	$D^{[h]}_{ave}$ [nm]
AC 1:0	651.77	0.2583	564.96	86.80	0.2523	0.0060	0.5578	1.5852
AC 1:2	1390.30	0.6517	1238.13	103.16	0.6168	0.0349	0.7793	1.8751
AC 1:4	1757.80	0.8267	1545.25	212.54	0.7832	0.0435	0.8775	1.9358
AC 1:6	1593.30	0.8027	1412.54	150.75	0.7465	0.0562	0.9075	2.0152

Table 6.2 Specific surface area and pore volume analysis of the $ZnCl_2$-activated porous carbon

[a]SSA-specific surface area obtained from BET (Brunnet-Emmet-Teller) method, [b] S_{micro}-micropore surface area obtained from the *t*-plot method, [c] TPV-total pore volume, [d] SA_{meso}- mesopore surface area obtained from the *t*-plot method, [e] PV_{meso}- *t*-plot micropore volume, [f] PV_{micro}- *t*-plot micropore volume, [g] PD_{micro}- micropore pore diameter, [h] D_{ave}- average pore size distribution from BJH (Barret-Joyner-Halenda) method]

The *t*-plot method's calculation is used to analyze microporosity contribution with respect to the total specific surface area. It is one of the well-known methods that enables the differentiation of micro or mesoporous volume and particular surface area with a reference compound. This technique validates the hierarchical mesoporous or microporous nature [55] as shown in Figure 6.16a to 6.16d.

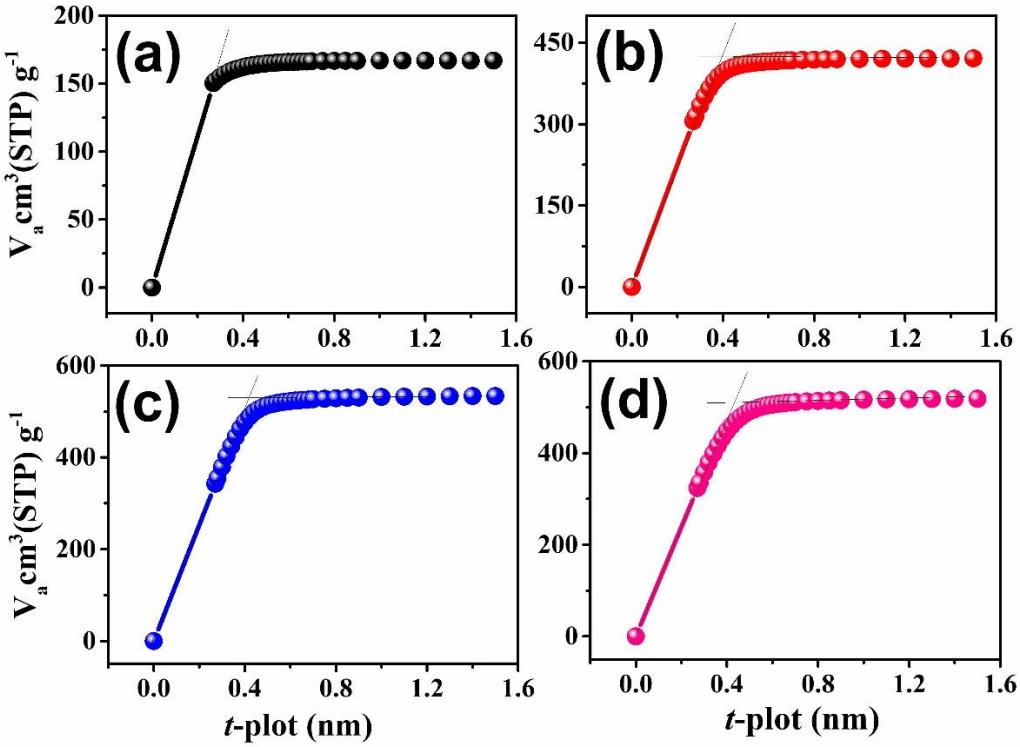

Figure 6.16 *t*- plot for nitrogen adsorbed porous carbon structures (at 77K) prepared by chemical activation method (a) AC 1:0 (b) AC 1:2 (c) AC 1:4 and (d) AC 1:6

The surface properties shown by these carbon structures are well suited for electrochemical double layer capacitor application. Surface area, porosity, nature of the pores, wettability of the surfaces etc are the factors that controls the intercalation and de-intercalation of ions in a supercapacitor structure. The quantification of these parameters has been done and the details are tabulated in Table 6.2. The specific surface area obtained for AC 1:0, AC 1:2, AC 1:4 and AC 1:6 are 651.77 m^2/g, 1390.30 m^2/g, 1757.80 m^2/g, and 1593.30 m^2/g, respectively. The data shows that up to AC 1:4 ratio the surface area increases and shows a slight dip for AC 1:6. Here, the increase in $ZnCl_2$ concentration increases surface area and porosity up to AC 1:4, further increase in activation agent results a slight dip in surface area and porosity. It is anticipated that the superimposition or merging of micropores to mesopores may happen at AC1:6 composition and that may destroy the carbon structure. *t*-plot data shown in Table 6.2 support this assumption. The contribution of microporous surface area and mesoporous surface area is further evaluated from the *t*-plot data.[11,53] Based on the surface properties shown, this material can be considered as a good candidate for energy storage applications, where the ion transport kinetics improves and enhances the storage efficiency.

6.2.2.4. Wettability characteristics

6.2.2.4.1 Contact angle measurements

The wettability characteristics of these porous carbon structures are important for them to use

as electrode materials for supercapacitor application. The contact angle measurement shows that the hydrophilicity increases with increase in porosity. Among the four samples AC 1:0 with no activating agent shows highly hydrophobic behaviour with a contact angle of 132.0^{o} (figure 6.17a), its surface area is also relatively low. The contact angle observed for AC 1:2 is 109.7^{o} and that for AC 1:4 is 108.7^{o}. Here, an increase in $ZnCl_2$ dosage shows a gradual increase in hydrophilicity due to the co-existence of micro and mesoporous surfaces (Figure 6.17b and 6.17c). Figure 6.17d shows the contact angle of AC 1:6 (119.2^{o}) , which is slightly higher than that of AC 1:4, indicting less hydrophilic surface.[56] Lowering the contact angle with $ZnCl_2$ activation will improves electrochemical performance due to better electrode-electrolyte interface.

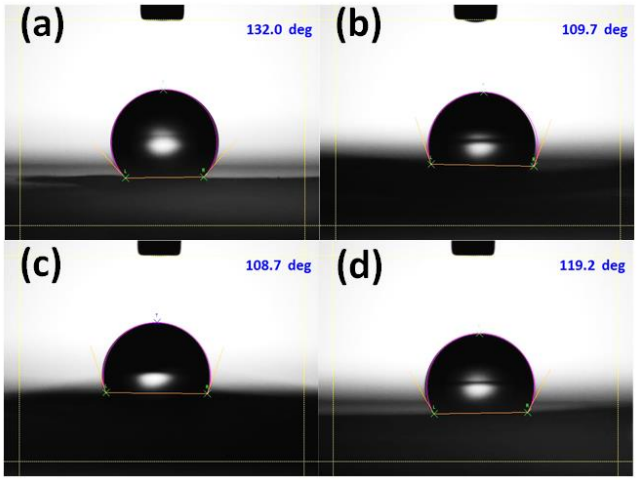

Figure 6.17 Contact angle measurement of the porous carbon (a) without activation AC 1:0, (b) AC 1:2, (c) AC 1:4 and (d) AC 1:6. Samples with $ZnCl_2$ activation at various concentration ratios with pyrolysis at 700 ^{o}C

6.2.2.5 Electrochemical Analysis- Supercapacitor Applications

6.2.2.5.1 Electrode preparation

Electrodes were prepared by mixing active material, carbon black (as a conducting additive), and a polymeric binder (PVDF) in a ratio of 75:10:15. An appropriate solvent, such as N-Methyl Pyrrolidone, was used to mix them. Over the pre-weighed stainless-steel substrate, the prepared slurry was coated. In this well-dried electrode, a mass loading of 2 mg is applied to a surface area of 1x1 cm^2. Sandwiching electrodes with separators result in symmetric cell configurations. Separator was (Whatman filter paper no:1) previously immersed in 0.1 M Na_2SO_4 aqueous electrolyte.

6.2.2.5.2 Electrochemical analysis- Symmetric Supercapacitor formation

The electrochemical performance of the porous carbon electrodes was assessed using cyclic voltammetry (CV). The charge-discharge kinetics was determined by galvanostatic charge-

discharge (GCD) technique. Electrochemical Impedance Spectroscopy (EIS) was used to conduct the internal resistance studies. Two electrode configuration was used to assess the electrochemical performance of the synthesized activated carbon. The symmetric device created by sandwiching two identical electrodes and adding 0.1 M Na_2SO_4 as an electrolyte in between.

Figure 6.18 depicts the electrochemical analysis of the samples prepared. Figure 6.18a shows the sweeping rates of AC 1:0, AC 1:2, AC 1:4, and AC 1:6 at 50 mV/s. The sample that is not activated (AC 1:0) performs very poorly in comparison to other samples because it has a smaller surface area than the activated samples. Additionally, the average pore diameter is 1.58 nm, which is significantly smaller than other values as shown in Table 6.2. The lower surface area allows for less penetration of the guest species into the pores, thus inhibiting ion transfer from the electrolyte. When compared to other activated samples such as AC 1:2, AC 1:4, and AC 1:6, the squareness of the voltammogram is larger for AC 1:4, which has a larger surface area and high pore volume (figure 6.18a). High surface area and pore volume offers many more active sites than the other, which greatly improves the penetration of the electrolyte ions. As a result, it will behave more capacitively and have a higher storage capacity than the other samples. The enclosed CV curves areas increase with $ZnCl_2$ dosage and when the dosage increased beyond 1:4, the carbon skeleton starts degrading and lose the surface area. Further the electrochemical performance of AC1:4 at different sweep rates, 5 mV/s to 100 mV/s, is performed and the corresponding graphs are shown in Figure 6.18b. The specific capacitance is enhancement from a higher to lower scan rate, due to the longer sustaining time of the electrolyte ions with the electrode surface. The specific capacitance varied from 92.24 F/g (specific capacity of 25.78 mAh/g) at 5 mV/s to 39.68 F/g (11.02 mAh/g) at 100 mV/s. The inclusion of pseudocapacitive nature caused by the presence of oxygen functionalities has resulted in the loss of perfect squareness in the CV.[51,57] To improve the performance of the activated carbon, introduce more redox couples into the electrolyte to produce effective charge transfer ions. Figure 6.18c shows the GCD measurements that analyzed from 2 A/g to 0.06 A/g and the capacitance values change from 13.33 F/g (3.70 mAh/g) to 53.86 F/g (14.96 mAh/g).

The impedance analysis was done to study the interfacial characteristics of the synthesized electrode materials. The impedance spectra of the fabricated two-electrode supercapacitor were measured in the frequency range of 100 kHz - 10 mHz with OCP of 5mV at room temperature shown in figure 6.18e. The obtained spectra behave differently with different frequency ranges. The presence of nearly vertical lines in the lower frequency region demonstrates the capacitive

nature. At higher frequencies, a semicircle is obtained and it indicates the porous nature of electrodes and the resistance aroused at the electrode-electrolyte interface.[58,59] The size of the semicircle determines whether the capacitive or resistance nature is dominant. The smallest semicircle dominates capacitive behaviour, while the largest one dominates resistive behaviour. It shows an electrical resistance of 5.32 Ω, charge transfer resistance of (R_{ct}) 50.8 Ω with a Warburg inclination greater than 45°. The impedance generated at the electrode-electrolyte interface during charge transfer affects the total specific capacitance and inhibits ion movement, which affects the specific capacitance value. The Warburg impedance is the tail slope at a low frequency that attributes to the rate of ionic diffusion in the electrolyte. The cyclic stability of 3000 charge-discharge cycles shown in figure 6.18f and is capable for long term charging and discharging

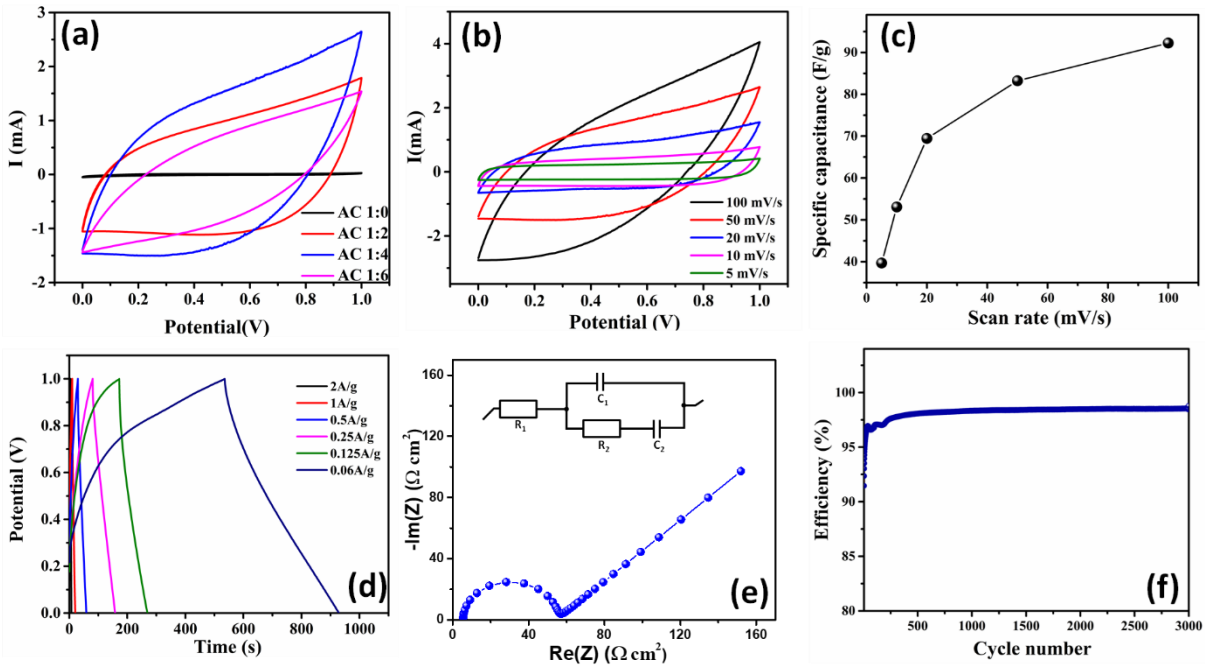

Figure 6.18 Electrochemical performance of activated carbon prepared from *Ailanthus Triphysa* (a) Cyclic voltammetric analysis at 50 mV/s, (b) different scan rate variation of AC 1:4 from 5mV/s to 100 mV/s, (c) Scan rate Vs Specific capacitance of AC 1:4 from CV, (d) GCD analysis of AC 1:4 from 0.06 A/g to 2 A/g, (e) EIS analysis of AC 1:4 with fitted Randle's circuit and (f) Galvanostatic cyclic charge discharging for 3000 cycles

6.2.2.5.3 Electrochemical Analysis-Redox Additive Enhanced Electrolyte Measurement

Electroactive materials like redox additive species are used to improve the properties such as specific capacitance, cell voltage as well as energy density. Instead of improving the electrode materials themselves, the redox additive enhancement improves the electrochemical property and increases the specific capacitance. The modification of the reversible redox reaction at the electrode-electrolyte interface can increase the specific capacitance. The addition of redox additives like KBr, KI, and Hydroquinone into the parent electrolyte, improves the performance

of Na_2SO_4. Among the three additives mentioned, KI, Na_2SO_4 combination (0.1 M Na_2SO_4 + 0.03 M KI) shows better performance (figure 6.19a). The use of KI is more advantageous due to its environmentally friendly nature, exceptionally low toxic, and other important characteristics such as the formation of a spectrum of redox electroactive species. While applying the suitable reduction potential, a series of redox couples such as $3I^-/I_3^-$, $2I^-/I_2$, $2I_3^-/3I_2$, and $I_2/2IO_3$ are formed along with the formation of poly iodide ions. Anionic species such as iodide, bromide, and hydroquinone have been used as active species for redox electrolytes in supercapacitors.

The solvated iodine species, like poly iodide species, intercalated into the highly porous carbon electrode and accumulated inside the pore. Due to the larger pore size than the iodide species, the polyiodide species diffuses easily into the pores because its size is around 1.8 nm. As a result of the suitable potential generated, iodine/iodide is formed at the electrode-electrolyte interface. The high-efficiency charge storage process is based on the adsorption and stable reactions of polyiodide ions (I_n^-), which have various oxidation states. In this system, iodide not only plays an important role in the faradic reactions, but it also serves as a high ionic conductivity medium. The redox capacity is caused by the following redox reactions (represented in equations 7-10), in addition to the Na^+ and SO_4^{2-} ions already present in the electrolyte.

$$3I^{-1} \rightarrow I_3^{-1} + 2e^- \quad (7)$$

$$2I^{-1} \rightarrow I_2 + 2e^- \quad (8)$$

$$2I_3^- \rightarrow 3I_2 + 2e^- \quad (9)$$

$$I_2 + 6H_2O \leftrightarrow 2IO_3^- + 12H^+ + 10e^- \quad (10)$$

In this poly iodide, both the I_n^- and I^- are negatively charged. This iodide can contribute not only to the redox active source for increased charge capacity, but it can also act as an EDLC by being electrostatically adsorbed on the electrode surface. As the concentration of KI increases, a number of I-based redox reactions will occur at the positive electrode-electrolyte interfaces, fading the specific capacitance. [60,61]

The addition of KI and KI-generated redox reactions generate extra redox peaks on the CV curves. The change in the shape of the CV is due to the pseudocapacitive type energy storage, due to the presence of KI, and the electrical double layer contribution from the highly porous carbon derived from *A.triphysa*. The ionic species and redox couples had enough time to insert into the pores of the electrode during the cyclic voltammetric analysis, which was performed at scan rates ranging from 100 mV/s to 5 mV/s (figure 6.19b). Therefore, at 5 mV/s, the slowest

scan rate offers a higher specific capacitance than the fastest scan rate. KI + Na_2SO_4 on a porous carbon electrode produces a specific capacitance of 109.12 F/g (30.11 mAh/g). The galvanostatic charge-discharge curve similarly exhibits the same behaviour (figure 6.19c). A specific capacitance of 41.62 F/g (11.56 mAh/g) is obtained from GCD measurements at 0.06 A/g.

The impedance measurement is shown in figure 6.19d, where the values R_1 = 3.1 Ω and R_2 = 4 Ω are the internal resistances developed during the addition of KI + Na_2SO_4. The cyclic stability of the activated porous carbon with redox-enhanced electrolyte is significantly greater than that of the electrolyte lacking any redox species. Up to 50000 cycles of continuous charging and discharging with 95% retention, the system remains stable (figure 6.19e). Initially, the system has a lower efficiency of ~80%, which increases as the number of cycles increases. The presence of larger iodine ions slows the reaction of the electrolyte during the cyclic test and that causes ~25000 cycles to reach high efficiency. With a current density of 1A/g, galvanostatic charge discharging cycles were performed. The redox additive electrolyte requires less time to interact with the electrode material during the initial cycles. The energy density and power density are found to be 8.26 Wh/kg and 97.20 W/kg at 0.06A/g. The main contribution of capacitance comes from the ions generated by Na_2SO_4, and as the number of cycles increases, the contribution of the redox couples in the 0.1 M Na_2SO_4 + 0.03 M KI increases. The lower internal resistance of the activated porous carbon with the redox additive electrolyte enhances its specific capacitance. Furthermore, the capacitance last up to 50000 cycles without losing its storage property as shown in figure 6.19e.

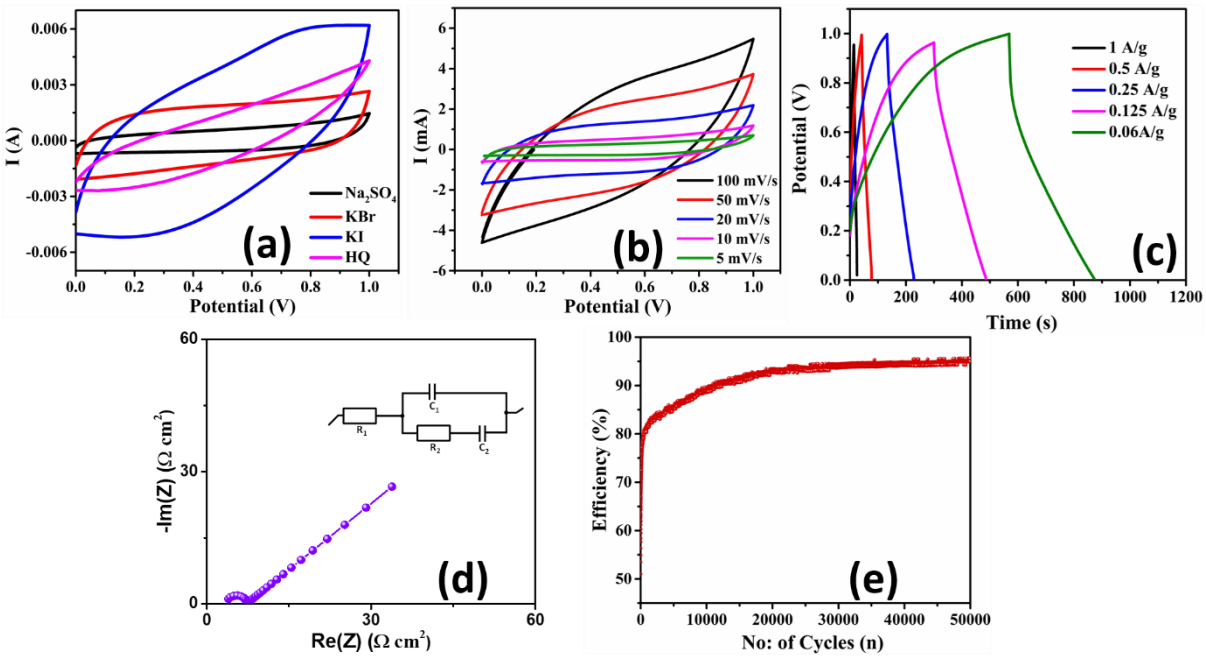

Figure 6.19 Electrochemical analysis of redox additive enhanced studies (a) performance of material with different redox additives along with Na_2SO_4, (b) CV of KI enhanced electrolyte over the activated carbon AC 1:4, (c) GCD of KI enhanced electrolyte over AC 1:4 (d) Impedance analysis with KI + Na_2SO_4 electrolyte and (e) cyclic charge discharging study with redox enhanced electrolyte over AC 1:4.

Carbon source	SSA (m^2/g)	Capacitance (F/g)	Electrolyte	Cyclic Stability	Ref.
AC(Commercial)	1370	55.95 F/g at 5mV/s	KOH	--	[9]
Banana fiber	1097	74 F/g at 5 mV/s	1M Na_2SO_4	500	[62]
Corn stalk	2349	140 F/g at 5mV/s	3M KOH	10000	[63]
Rice husk	1493	112 F/g at 5mV/s	1M Na_2SO_4	--	[64]
Cotton pulp	--	90 F/g at 5mV/s	5M KCl	2000	[65]
Saw dust	1757	92.84 F/g at 5mV/s	0.1M Na_2SO_4	3000	**This work**
Saw dust	1757	109.12 F/g at 5mV/s	0.1M Na_2SO_4 + 0.03 M KI	50000	**This work**

Table 6.3 Comparison of the synthesized material's electrochemical properties with the other activated carbon materials

Therefore, the addition of redox couples to the neutral aqueous electrolyte boosts not only the specific capacitance but also the longer shelf life than that of the non-redox electrolyte. Table 6.3 compares the electrochemical properties of the synthesized material to those reported in other activated carbon materials. [5,16,53-55]

6.2.3 Conclusion

In summary, for the first time, hierarchically porous carbon was synthesized from an *A.triphysa* source using a two-step carbonization method with $ZnCl_2$ activation in an inert atmosphere. Activated carbon has a hierarchically porous hexagonal nanostructure as well as a high surface area and porosity. By controlling the activating agent's concentration, both surface area and porosity are improved. Surface area and porosity enhancement improves the energy storage capacity of the material by showing a specific capacitance of 92.24 F/g (25.78 mAh/g) at 5mV/s with an electrolyte of 0.1 M Na_2SO_4. The specific capacitance and shelf life are further improved by addition of redox additives, like KI, to the 0.1 M Na_2SO_4 electrolyte. The prepared symmetric device has a specific capacitance of 109.12 F/g (30.11 mAh/g) at 5 mV/s, is capable of running for up to 50000 cycles, and has a 95 % retention rate. The energy density and power density found to be 8.26 Wh/kg and 97.20 W/kg at 0.06A/g. Based on this systematic study,

we conclude that *A.triphysa* saw dust derived porous carbon is a very good alternative green energy material source for high-performance supercapacitor electrodes.

6.3 Leaf Derived Microporous Carbon from Palmyra Palm Leaves

Introduction

Energy production has been greatly influenced by renewable and green energy resources. Supercapacitors and batteries have become increasingly important due to the crucial problem of energy production and storage. Materials that contain carbon as well as their derivatives are appropriate for use in supercapacitors[66]. Conductivity, large specific surface area, and high porosity make it an ideal electrode material. Materials derived from carbon, such as carbon nanotubes [67], carbon nanofibers [68], graphene [69,70], activated carbon [71], and graphite [72] are used to store energy. Activated carbon (AC) is commonly used for supercapacitor applications [71] and is typically made by burning petroleum coke, coal, and pitch. A shortage of such

resources has led to the use of alternative biomass sources such as agricultural wastes[73], domestic wastes, and plant wastes[73] for the synthesis of activated carbon. Besides its high specific surface area, high conductivity, special structures, and cost-effectiveness, it is also environmentally friendly. A high specific capacitance is favoured by better charge accumulation at the electrode-electrolyte interface[74]. In recent years, the lack of conventional carbon resources has led to alternative sources such as biomass, agricultural wastes, and domestic wastes. These materials are suitable for the synthesis of activated carbon [10]. Diverse biomass sources offer a wide range of research opportunities. The majority of plant and animal leftovers are burned, resulting in significant pollution [11,12]. The emission of gases also contributes to environmental pollution. Biomass sources are converted into carbon materials through controlled reactions. Carbon of this type is low in toxicity, environmentally benign, highly porous, and has a high specific surface area and conductivity. It is possible to produce activated carbon from various biomass sources, such as plant tissue[75], leaf [76], fruit[77], bark[78] or stem[79], root[80], spores[81], wood[82] etc. Resources play a major role in determining the specific surface area and porosity of the activated carbon.

Palmyra palm leaves, a plant widely grown in Asia, is used as a precursor for biomass carbon synthesis. In addition to being inexpensive and abundant, these leaves are rich in lignin, cellulose, and hemicellulose. By using a simple step-by-step process, we created honeycomb-like hierarchically graphitized porous carbon structures. Carbonization produces a hierarchical structure with a high specific surface area and porosity after removing inorganic components. As an energy storage material, it is used in conjunction with redox additive electrolytes.

This study aims to evaluate the feasibility of producing highly porous carbon from palmyra palm leaf waste as a cost-effective method. The carbonization at high temperature is evaluated by varying the impregnation ratio of $ZnCl_2$ as an activating agent. Based on the variation in $ZnCl_2$ ratios, the total specific surface areas of the prepared samples are compared. Electrolytes containing potassium iodide (KI) and sodium sulphate (Na_2SO_4) are being used to study the electrochemical properties of prepared carbon. An assessment of electrochemical properties using palmyra palm leaves, a regional and possibly underutilized resource, represents a novel approach in this context.

6.3.1 Experimental

6.3.1.1 Materials used

For the material synthesis procedures, Palm (Palmyra palm) leaves are harvested, and dried leaves are powdered well. Carbon black, Poly Vinylidene Fluoride (PVDF-Alfa Aesar), and N-methyl pyrrolidone (NMP-Sigma Aldrich) were used to make the electrode, and sodium sulfate (Na_2SO_4 - Sigma Aldrich) was used for further electrochemical analysis

6.3.1.2 Synthesis

6.3.1.2.1 Synthesis of Leaf-Derived Hierarchical Porous Carbon (LC)

The palmyra palm leaf was washed well with water to remove the dirt and dust. The powder was then sun-dried for a few hours to remove all moisture content. The leaf powder was then thoroughly powdered before pre-carbonization. To keep the carbon structure from collapsing and removing water content, these were pre-carbonized for 2 hrs at a temperature of 300 °C with a constant ramping of 5 °C/min. The next step involved treating finely powdered, pre-carbonized samples with anhydrous $ZnCl_2$ in various mass ratios: 1:0, 1:2, 1:4, and 1:6. Subsequently, the mixture was heated for an additional 1 hour to ensure complete impregnation into the carbon skeleton. The $ZnCl_2$-activated mixture is then allowed to dry overnight at 110 °C. Then go for pyrolysis where the samples are heated to 600 °C for 1 hr in an inert N_2 atmosphere (99.999 %) at a constant rate of 5 °C/min and beyond this temperature yield was very poor. The carbonization temperature was fixed based on the thermogravimetric analysis of the sample (See figure S1 in the SI in Appendix III). Then the samples were cleaned using hot water and HCl to eliminate any unreacted species and byproducts. Ultimately, the resulting product is a set of highly porous carbons referred to as LC 1:0, LC 1:2, LC 1:4, and LC 1:6. Figure 6.20 represents the $ZnCl_2$ activation process of palm leaf followed by pyrolysis.

Figure 6.20. Schematic illustration of $ZnCl_2$ activated highly porous carbon formation from palm leaf by pyrolysis at 600 ^oC

6.3.1.3 Characterizations

Each activated carbon material was subjected to a series of analyses. FESEM ZEISS-GEMINISEM 300 was used for morphology and microstructure analysis. PANalytical-Xpert3 powder X-ray diffractometer (XRD) was used to study the crystal structure. Raman analysis was performed with a 532 nm DPSS laser, Alpha 300RA, WiTec, Germany. The Fourier transform infrared spectroscopy (FTIR) was recorded with Perkin Elmer spectrum two FTIR spectrophotometer using the KBr pellet method. A BELSORP- max BET surface area analyzer was used to determine the porosity of samples. The wettability characteristics were measured using a Kyowa drop master DMs 401 equipped with the FAMAS interface measurement and analysis system.

6.3.2 Results and Discussion

6.3.2.1 Structure, Phase and Chemical Analysis

6.3.2.1.1 X-Ray Diffraction

The primary objective of XRD analysis is to examine the structure and crystallinity of the samples. The XRD pattern shows two broad peaks at 25^o and 43^o , that correspond to turbostatic carbon and graphitic carbon, respectively (figure 6.21).

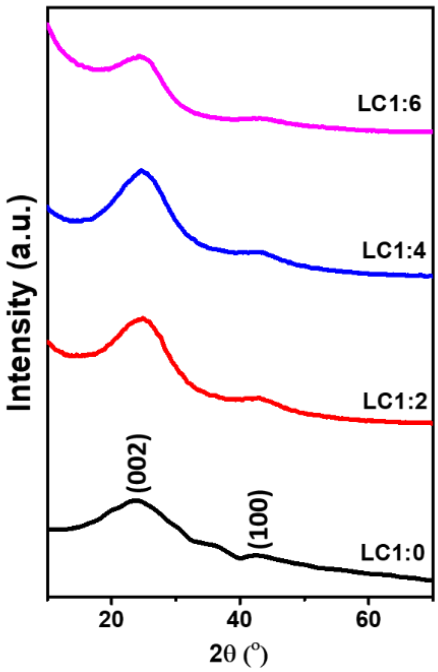

Figure 6.21 XRD diffraction pattern of leaf derived highly porous carbon

It appears that graphitic carbon is responsible for the peak at 25° in the diffraction from (002) plane and (001) plane. The shift in diffraction direction around the 25° peak indicates a low degree of graphitization [83].

6.3.2.1.2 Raman Analysis

In figure 6.22, the Raman peak at around 1350 cm^{-1} and 1600 cm^{-1} is attributed to the D and G bands respectively.

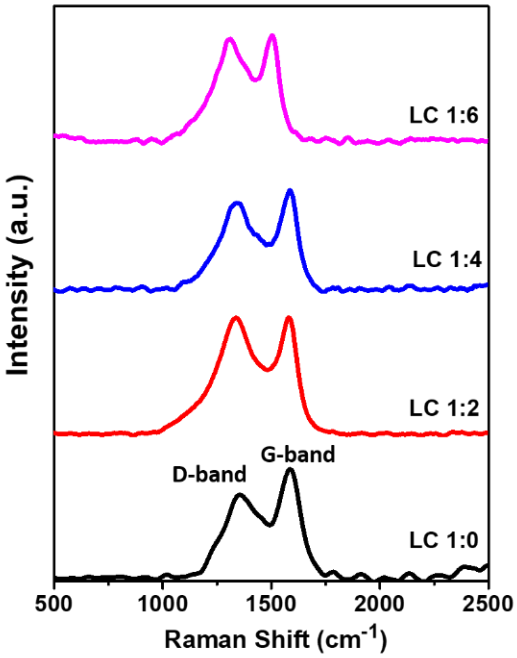

Figure 6.22 Raman analysis of leaf derived carbons by $ZnCl_2$ activation followed by pyrolysis

The G band is caused by in-plane stretching between sp^2 carbon atoms. Structure defects, edge effects, and dangling sp^2 carbon bonds cause the D band [84]. The I_D/I_G ratios obtained are 0.80, 0.92, 1.04, and 0.98 respectively for samples LC 1:0, LC 1:2, LC 1:4, and LC 1:6. As the concentration of the activating agent increases, more defects are formed. The sample LC 1:4 has a higher degree of graphitization leading to better conductivity. Moreover, increasing $ZnCl_2$ dosage increases I_D/I_G values to some extent, indicating the disordered nature of the carbon samples. As the carbonization process proceeds, heat emissions may result in enhanced graphitization.

6.3.2.1.3 FTIR analysis

It is well known that activated carbon has a wide range of surface functional groups. These groups influence the characteristics of activated carbon. FTIR spectroscopy was utilized to examine the functional groups. Surface functionalized groups are formed according to the chemical activation used during synthesis. Figure 6.23 shows the FTIR spectra of samples, raw sample (RL), LC 1: 0, LC 1: 2, LC 1: 4, and LC 1: 6. The spectra of activated carbons occupied with identical functional groups, because they are synthesized from the same raw sample. Despite changing the concentration of the dehydrating agent, the resulting spectra indicated no significant change.

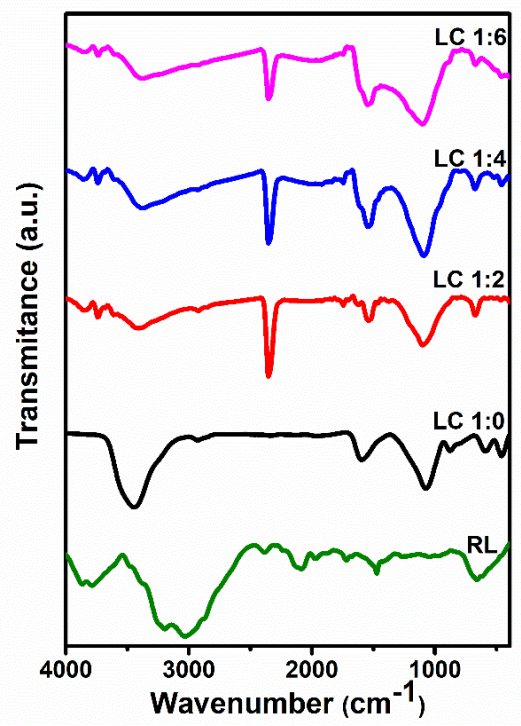

Figure 6.23 FT-IR analysis of leaf derived carbons by ZnCl2 activation followed by pyrolysis

The broad and larger band located around ~3128 cm^{-1} is attributed to the hydroxyl groups, due

to adsorbed water species, or the presence of aliphatic alcoholic groups[85]. The peaks correspond to ~1604 cm^{-1} represent the C=O groups. The vibrational stretching of the C=O groups is indicated by the presence of carboxyl, lactone, ketone, and alcoholic groups. The peak around 1375 cm^{-1} is due to C-H bond stretching vibrations. The C-O group is typically represented by a peak near 1092 cm^{-1}. Similarly, the presence of an aromatic skeleton structure in the synthesized carbon generates weak peaks[86] between 700 to 400 cm^{-1}. The existence of various hydrophilic groups such as C- H, C-O, C=O, O-H, R-OH, and others may enhance the performance of activated carbon derived from *palmyra palm* leaves.

6.3.2.1.4 XPS analysis

Figure 6.24 shows the XPS spectra of LC 1:0 and LC 1:4 samples. The survey spectra show three peaks, C1s, O1s, and N1s for LC 1:0 and LC 1:4 (figure 6.24a). The C1s profiles are deconvoluted into three peaks (figure 6.24b and 6.24e). The three distinct peaks indicate the existence of sp^2-C (284.58 eV), sp^3-C (285.78 eV), and C=O (287.86 eV). The deconvoluted O1s spectra (figure 6.24c and 6.24f) show three peaks associated with carbonyl groups (C=O), phenyl or ether-type groups (C-O), and adsorbed oxygen. It is found that the oxygen content increased from 10.57 % to 11.88 % for LC 1:0 and LC 1:4 respectively. The increased content of oxygen may enhance the electrochemical performance. The high-resolution N1s spectra of LC 1:0 and LC 1:4 is shown in figure 6.24d and 6.24g. The N content is 1.5 % and 1.84 % respectively for LC 1:0 and LC 1:4, indicating that LC 1:4 retained the N content after $ZnCl_2$ activation. The presence of oxygen and nitrogen enhances the electrochemical performance of the carbon[87–89].

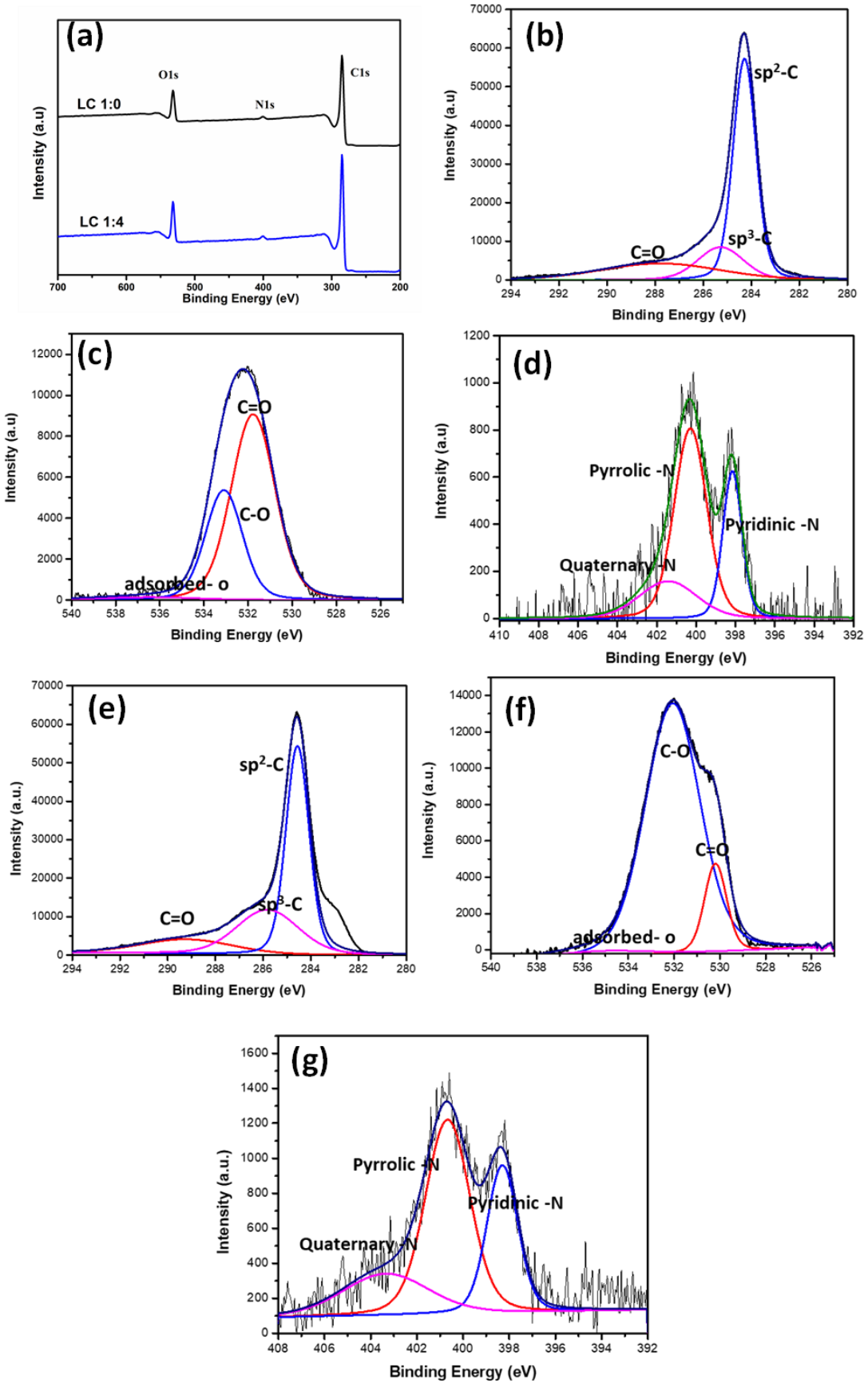

Figure. 6.24 The XPS profile of LC 1:0 and 1:4. (a) survey spectrum, (b) C1s, (c) O1s and (d) N1s profile of LC 1:0; (e) C1s, (f) O1s and (g) N1s profile of LC 1:4

6.3.2.2 Morphology analysis

6.3.2.2.1 FE-SEM analysis

Figure 6.25 (a-h) illustrates FE-SEM micrographs of activated carbon samples produced with varying $ZnCl_2$ ratios and heated at 600 ºC. As the impregnation ratio increases from 0 to 6, pore diameters increase, and new pores emerge. This results in an increase in the specific surface area of the activated carbon. Analysis of the SEM micrographs reveals that the pores exhibit a tunnel-like structure, with interconnected pores forming a distinctive honeycomb-like structure.

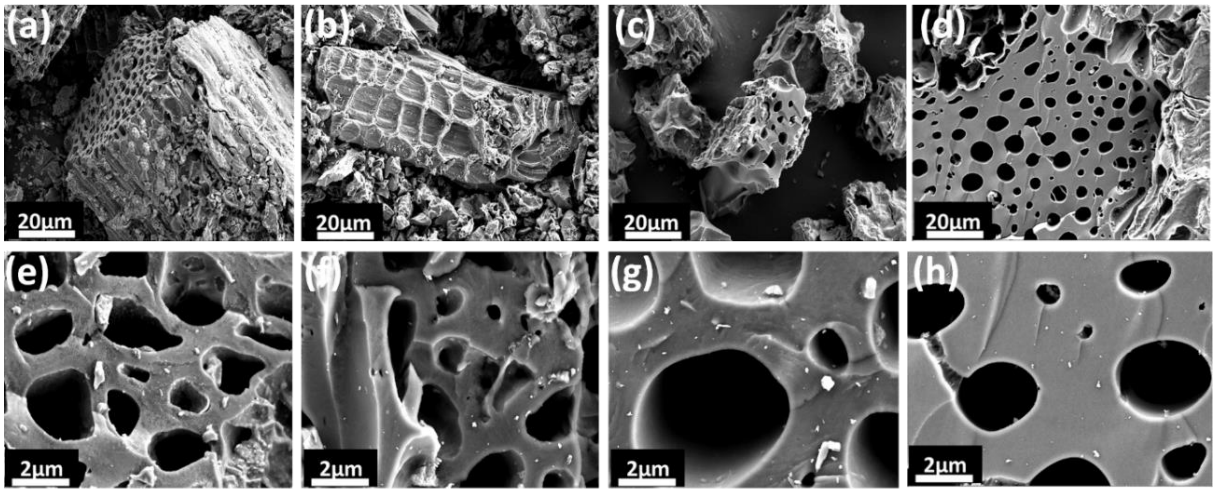

Figure 6.25 FE-SEM images of the leaf derived $ZnCl_2$ activated LC 1:0 (a and e), LC 1:2 (b and f), LC 1:4 (c and g) and (d and h)

6.3.2.3 Surface area Porosity analysis

6.3.2.3.1 BET analysis

The porosity details are shown in figures 6.26i and 6.26j, which depict the N_2 adsorption and desorption of biomass-derived carbon, and all samples have a type-I isotherm[90]. Because the adsorption and desorption curves overlap, absorption at lower pressure indicates the presence of micropores in the materials[84]. When compared to the nonactivated sample, the adsorption isotherm increases with increased concentration. The pore sizes ranging from 1.86 nm to 3.09 nm, show micropores to mesopores characteristics. The specific surface area obtained are 408.25 m^2/gm, 1209.20 m^2/gm, 1234.10 m^2/gm, and 1347.10 m^2/gm respectively for LC 1:0, LC 1:2, LC 1:4, and LC 1:6. The quantification of the parameters related surface area are tabulated in Table 1. The large specific surface area accelerates charge storage at the electrode-electrolyte interface.

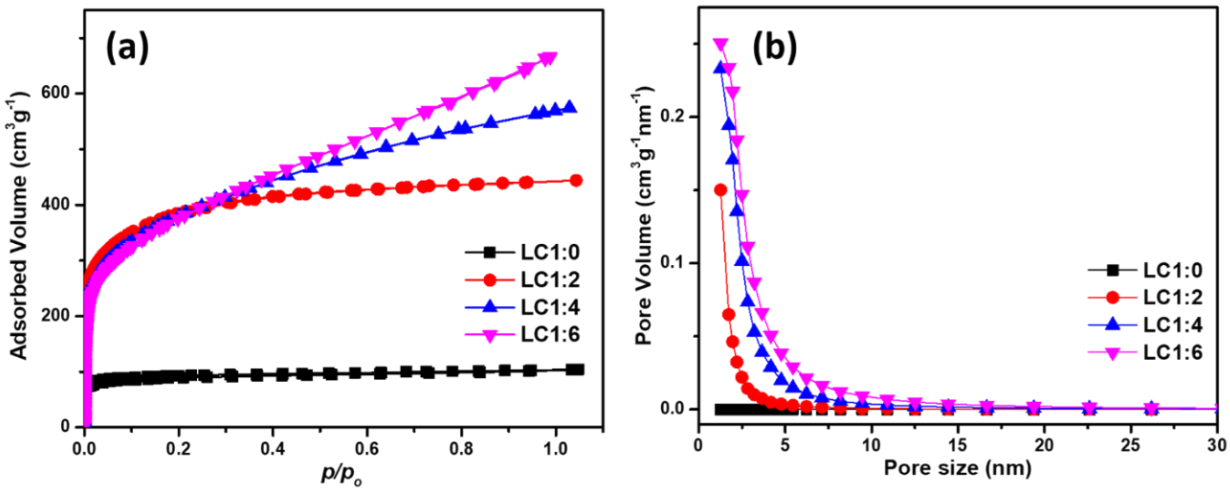

Figure 6.26 (a) N_2 adsorption-desorption isotherm of the palm leaf derived porous carbon (b) BJH curves showing pore size vs pore volume of the same samples

Sample	SSA[a] (m^2/g)	TPV[b] (cm^3/g)	SA^c_{micro} (m^2/g)	SA^d_{meso} (m^2/g)	D^e_{ave} (nm)
LC 1:0	408.25	0.1585	389.26	19.04	1.86
LC 1:2	1209.20	0.6387	1135.13	74.50	2.00
LC 1:4	1234.10	0.8785	1117.10	117.00	2.69
LC 1:6	1347.10	1.0297	1156.11	191.00	3.09

Table 6.4. Specific surface area and pore volume analysis of the $ZnCl_2$-activated porous carbon [[a]SSA-specific surface area obtained from BET (Brunnet-Emmet-Teller) method, [b]S_{micro}-micropore surface area obtained from the *t*-plot method, [c]TPV-total pore volume, [d]SA_{meso}- mesopore surface area obtained from the *t*-plot method, [e]D_{ave}- average pore size distribution from BJH (Barret-Joyner-Halenda) method]

6.3.2.4. Wettability characteristics

6.3.2.4.1 Contact angle measurement

The sample LC 1:0 with no activation shows114.8^o (figure 6.27a) and its surface area is also relatively lower. The contact angle for the samples LC 1:2 (113.8^o), LC 1:4 (110.4^o) and LC 1:6 (113.2^o) is not showing a large shift in contact angle. The contact angle maintaining almost same values.

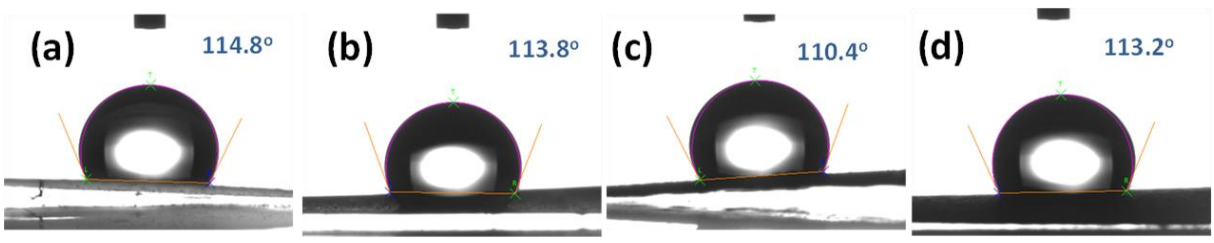

Figure 6.27. Wettability characteristics of LC (a) 1:0, (b) 1: 2, (c) 1:4 and (d) 1:6

6.3.2.5 Electrochemical Characterization of Leaf Derived Carbon

6.3.2.5.1 Electrode Preparation

The electrodes were prepared by mixing the above three at the ratio of 80:10:10 in NMP. Then coated onto a pre-weighed stainless-steel substrate with a mass loading of ~2 mg over an area of 1*1 cm^2. To assemble the symmetric cell configurations, the electrodes were sandwiched with a separator (Whatman filter paper no:1 pre-immersed in an aqueous electrolyte of 0.1 M Na_2SO_4).

6.3.2.5.2 Symmetric Capacitor Formation

Figure 6.28 depicts the electrochemical profile of the synthesized samples. The specific capacitance of different carbon materials follows the order of LC 1:4 > LC 1:6 > LC 1:2 > LC 1:0 by comparing at a constant sweep rate of 10 mV/s. The highest specific capacitance is observed for LC 1:4 with 0.1 M Na_2SO_4 electrolyte, as shown in Figure 6.28a. Increasing concentration of $ZnCl_2$ gradually forms a highly porous structure, resulting in LC 1:4 with a specific capacitance of 75.60 F/g at 5 mV/s. This porous structure is advantageous as it enhances the transmission of electrolyte ions and offers multiple adsorption sites. However, if the concentration becomes too high, the carbon matrix starts to collapse, preventing further increase in porosity.

Considering four samples, LC 1:4 had the maximum curve area and excellent capacity, which is consistent with the galvanostatic profiles in Figure 6.28b. Due to the excellent electrochemical capacity, LC 1:4 was selected for the subsequent electrochemical tests. The CV curves of LC 1:4 was generated at different sweep rates of 5 mV/s to 500 mV/s, as seen in Figure 6.28c. At a high scan rate of 500 mV/s, the CV curves maintain a quasi-rectangular shape indicating excellent specific capacitive behaviour of the electrode material. The EDLC nature of the material enables the intercalation-deintercalation process. This to-and-fro movement of Na^+ ions in the electrolyte is responsible for energy storage.

Figure 6.28d depicts LC 1:4 at different current densities, 0.06 A/g to 2 A/g. As the current density goes up, the discharge time gets shorter. This is due to the less time for electrolyte ions to enter the pores of the activated carbon. The LC 1:4 impedance curve in Figure 6.28e shows some resistance in the electrode-electrolyte interface, contributing to the relatively lower specific capacitance values. However, it can be capable of continuous charge-discharge cycles up to 10000 and has better stability as shown in Figure 6.28f.

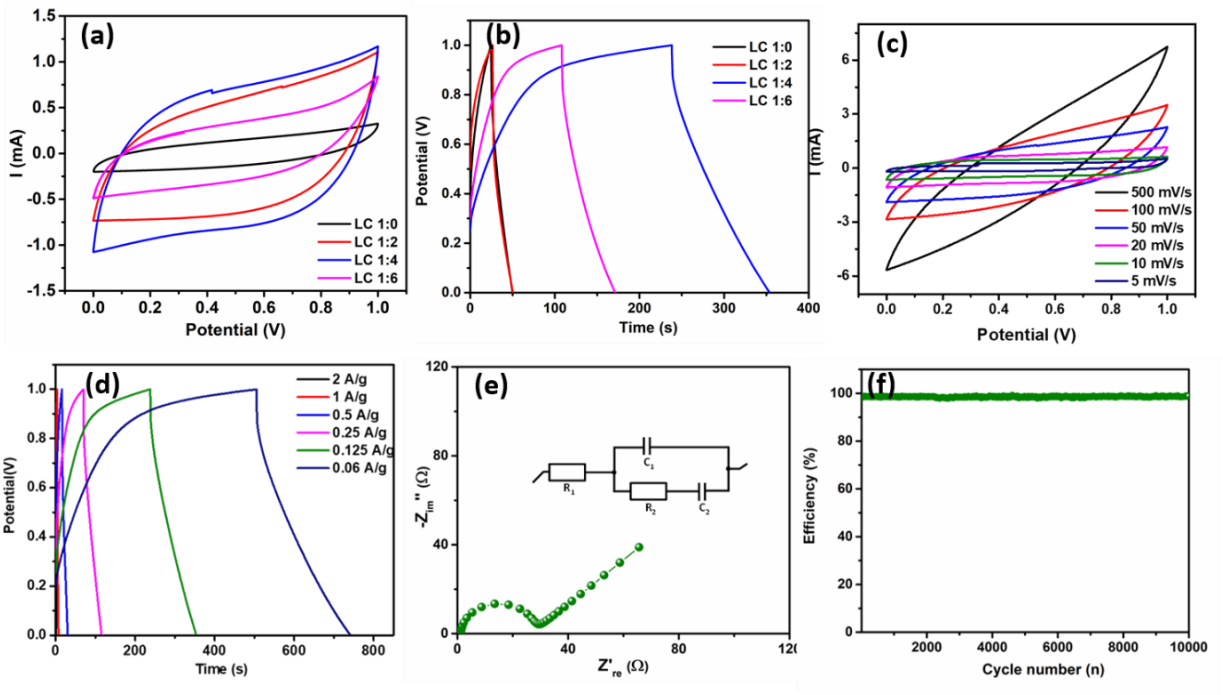

Figure 6.28 Electrochemical performances of *Palm leave* derived carbon (a) Cyclic voltammetric analysis at 10 mV/s, (b) GCD profile of samples at 0.5 A/g (c) Different scan rate variation of LC 1:4 from 5 mV/s to 500 mV/s, (d) GCD profile of LC 1:4 from 0.06 A/g to 2 A/g, (e) EIS analysis and (f) Galvanostatic cyclic charge-discharging for 10000 cycles

6.3.2.5.3 Redox additive enhancement in supercapacitor performance

The addition of a redox species (KI) significantly enhances the capacitive behaviour[91] of the supercapacitor as seen in figure 6.29a. By comparing both CV curves, it is clear that the redox additive electrolyte (LC 1:4 and 0.1 M Na_2SO_4 + 0.03 M KI) performs better than the bare electrolyte. Figure 6.29b shows the CV at different scan rates and its GCD profiles are given in figure 6.29c.

The shift in CV curve shape is caused by how redox reactions take place between pairs like I_2/IO_3^-, $2I^-/I_2$, $2I_3^-/3I_2$, and $3I^-/IO_3^-$. The presence of solvated iodine species, such as polyiodide species, are intercalated into the highly porous carbon electrode and accumulate inside the pore. The larger pore size allows the polyiodide species (with a size of around 1.8 nm) to diffuse easily into the pores compared to the iodide species. This diffusion, combined with a suitable potential, leads to the formation of iodine/iodide at the electrode-electrolyte interface. The high-efficiency charge storage process relies on the adsorption and stable reactions of polyiodide ions (I_n^-), which exist in various oxidation states. Iodide not only plays a crucial role in the faradic reactions but also acts as a high ionic conductivity medium. The redox capacity arises from the redox reactions (represented in equations 11-14), in addition to the Na^+ and SO_4^{2-} ions already present in the electrolyte.

$$3I^{-1} \rightarrow I_3^{-1} + 2e^- \quad (11)$$

$$2I^{-1} \rightarrow I_2 + 2e^- \quad (12)$$

$$2I_3^- \rightarrow 3I_2 + 2e^- \quad (13)$$

$$I_2 + 6H_2O \leftrightarrow 2IO_3^- + 12H^+ + 10e^- \quad (14)$$

At a scan rate of 5 mV/s, the performance improves to 173.04 F/g and 100.61 F/g at 0.06 A/g. This results in an energy density of 3.15 Wh/kg and a power density of 0.03 kW/kg. The semicircle observed in Figure 6.29d at high frequency indicates the charge transfer resistance at the electrode-electrolyte interface. Although larger ions slightly increase this resistance, it doesn't significantly affect the performance. Another benefit of the LC 1:4 with redox electrolyte is its impressive cyclic stability, allowing for 30,000 cycles (Figure 6.29e). This highlights the better performance and superior stability of biomass-derived activated carbon.

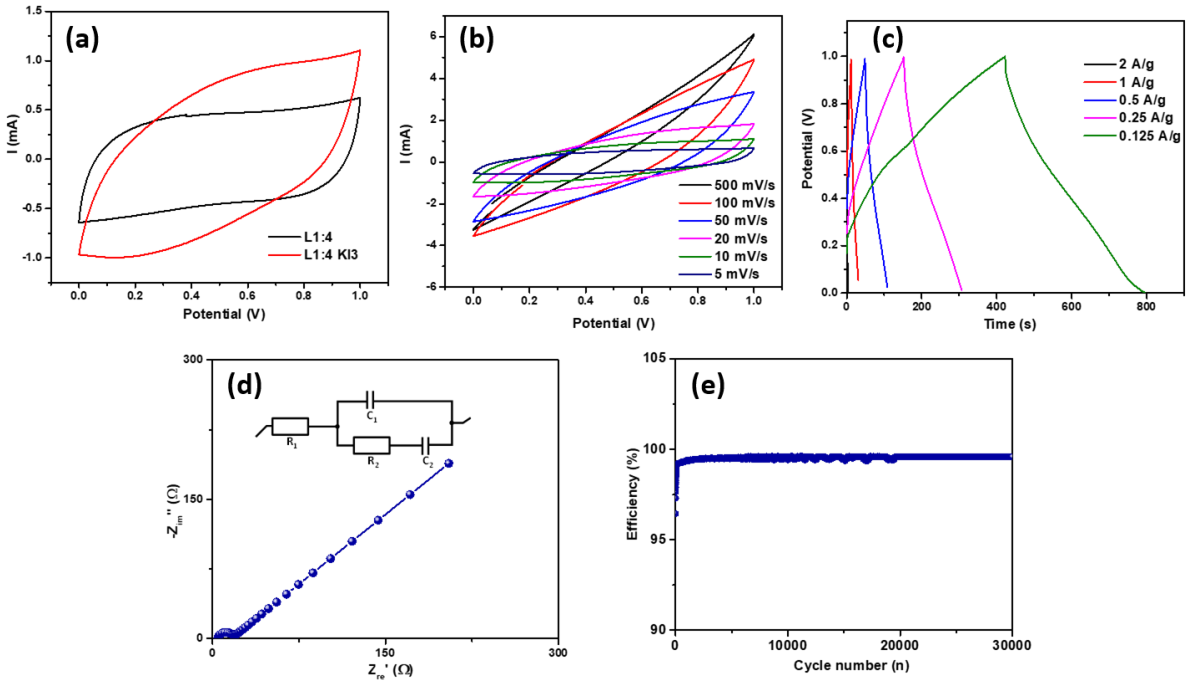

Figure. 6.29 Electrochemical analysis of redox additive enhanced studies (a) performance of the material, (b) CV of KI enhanced electrolyte over the activated carbon LC 1:4, (c) GCD of KI enhanced electrolyte over LC 1:4 (d) Impedance analysis and (e) Cyclic charge discharging study with redox enhanced electrolyte over LC 1:4

6.3.3 Conclusion

In conclusion, porous carbon derived from palmyra palm leaves exhibits remarkable characteristics for energy storage applications when chemically activated with $ZnCl_2$. This material has a specific surface area of 1300 m^2/g, providing a wide range of interfaces for electrochemical reactions. An electrolyte containing 0.1 M Na_2SO_4 demonstrates a specific

capacitance of 75.60 F/g for activated leaf-derived carbon. Further, introducing a redox additive into the electrolyte improves specific capacitance significantly. By combining 0.1 M Na_2SO_4 with 0.03 M KI, a specific capacitance of 173.04 F/g in 1V at a scan rate of 5 mV/s is achieved. With a current density of 0.12 A/g, the galvanostatic charge-discharge specific capacitance measured is 100.61 F/g. The material has a power density of 0.03 kW/kg and an energy density of 3.15 Wh/kg. The impressive capability to endure 30,000 cycles is one of the most noteworthy achievements. Based on these results, it can be concluded that activated carbon derived from palmyra palm leaves performs exceptionally well and is exceptionally stable.

*****

Appendix II

Thermogravimetric Analysis (TGA)

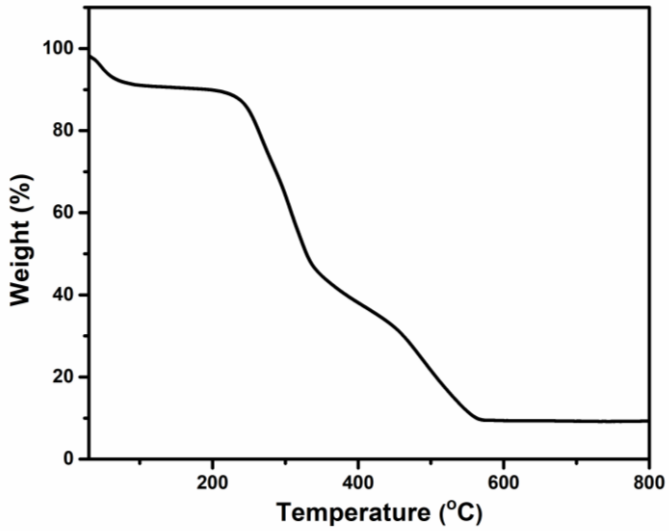

Figure S1. Thermogravimetric analysis of palmyra palm leaf

References

[1] S. M. Anisuzzaman, C. G. Joseph, W. M. A. B. W. Daud, D. Krishnaiah, H. S. Yee, *International Journal of Industrial Chemistry* **2015**, *6*, 9–21.
[2] J. Sodtipinta, T. Amornsakchai, P. Pakawatpanurut, *Advances in Natural Sciences: Nanoscience and Nanotechnology* **2017**, *8*, 035017.
[3] A. G. Pandolfo, A. F. Hollenkamp, *Journal of Power Sources* **2006**, *157*, 11–27.
[4] M. A. Yahya, M. H. Mansor, W. A. A. W. Zolkarnaini, N. S. Rusli, A. Aminuddin, K. Mohamad, F. A. M. Sabhan, A. A. A. Atik, L. N. Ozair, in *AIP Conference Proceedings*, **2018**, p. 030023.
[5] H. Yang, S. Ye, J. Zhou, T. Liang, *Frontiers in Chemistry* **2019**, *7*, 1–17.
[6] C. Wang, H. Li, J. Zhao, Y. Zhu, W. Z. Yuan, Y. Zhang, *International Journal of Hydrogen Energy* **2013**, *38*, 13230–13237.
[7] Z. Liu, X. Zhou, F. Wu, Z. Liu, *ACS Omega* **2020**, *5*, 10106–10114.
[8] Z. Zhu, H. Jiang, S. Guo, Q. Cheng, Y. Hu, C. Li, *Scientific Reports* **2015**, *5*, 15936.
[9] D. Qu, H. Shi, *Journal of Power Sources* **1998**, *74*, 99–107.
[10] J. L. Goldfarb, G. Dou, M. Salari, M. W. Grinstaff, *ACS Sustainable Chemistry & Engineering* **2017**, *5*, 3046–3054.
[11] B. Liu, L. Liu, Y. Yu, Y. Zhang, A. Chen, *New Journal of Chemistry* **2020**, *44*, 1036–1044.
[12] M. R. Singh, C. Xiang, N. S. Lewis, *Sustainable Energy Fuels* **2017**, *1*, 458–466.
[13] R. Kushwaha, S. Haldar, P. Shekhar, A. Krishnan, J. Saha, P. Hui, C. P. Vinod, C. Subramaniam, R. Vaidhyanathan, *Advanced Energy Materials* **2021**, *11*, 2003626.
[14] A. A. Ogale, M. Zhang, J. Jin, *J of Applied Polymer Sci* **2016**, *133*, app.43794.
[15] M. Inagaki, Y. Yang, F. Kang, *Advanced Materials* **2012**, *24*, 2547–2566.
[16] A. Ramakrishnan, S. Swaminathan, J. Mayandi, *ChemistrySelect* **2023**, *8*, e202303098.
[17] R. Aswini, C. V. Niveditha, S. Swaminathan, *Materials Today: Proceedings* **2022**, *56*, 587–593.
[18] Y.J. Heo, H. I. Lee, J. W. Lee, M. Park, K. Y. Rhee, S. J. Park, *Composites Part B: Engineering* **2019**, *161*, 10–17.
[19] M. Kopeć, M. Lamson, R. Yuan, C. Tang, M. Kruk, M. Zhong, K. Matyjaszewski, T. Kowalewski, *Progress in Polymer Science* **2019**, *92*, 89–134.
[20] D. Y. Kim, S. Radhakrishnan, S. Yu, B. S. Kim, *Mater. Adv.* **2023**, *4*, 3215–3223.
[21] R. Awad, A. Haghighat Mamaghani, Y. Boluk, Z. Hashisho, *Chemical Engineering Journal* **2021**, *410*, 128412.
[22] T. Wang, Z. Chen, W. Gong, F. Xu, X. Song, X. He, M. Fan, *ACS Omega* **2023**, *8*, 22316–22330.
[23] Y. Liu, J. Ma, T. Lu, L. Pan, *Sci Rep* **2016**, *6*, 32784.
[24] S. A. Jadhav, S. B. Dhavale, A. H. Patil, P. S. Patil, *Mat Design & Process Comms* **2019**, *1*, DOI 10.1002/mdp2.83.
[25] X. Y. Li, Y. Yan, B. Zhang, T. J. Bai, Z. Z. Wang, T. S. He, *J Mater Sci* **2021**, *56*, 10745–10781.
[26] D. Y. Kim, S. Radhakrishnan, S. Yu, B. S. Kim, *Mater. Adv.* **2023**, *4*, 3215–3223.
[27] I. Alarifi, A. Alharbi, W. Khan, A. Swindle, R. Asmatulu, *Materials* **2015**, *8*, 7017–7031.
[28] N. C. Abeykoon, J. S. Bonso, J. P. Ferraris, *RSC Adv.* **2015**, *5*, 19865–19873.
[29] R. L. McCreery, *Chemical Reviews* **2008**, *108*, 2646–2687.
[30] J. Wang, X. Zhang, Z. Li, Y. Ma, L. Ma, *Journal of Power Sources* **2020**, *451*, 227794.
[31] C. Liedel, *ChemSusChem* **2020**, *13*, 2110–2141.
[32] Z. Peng, Y. Xu, W. Luo, C. Wang, L. Ma, *ChemistrySelect* **2020**, *5*, 11221–11228.
[33] L. Wang, G. Mu, C. Tian, L. Sun, W. Zhou, P. Yu, J. Yin, H. Fu, *ChemSusChem* **2013**, *6*, 880–889.
[34] M. Muhyuddin, N. Zocche, R. Lorenzi, C. Ferrara, F. Poli, F. Soavi, C. Santoro, *Mater Renew Sustain Energy* **2022**, *11*, 131–141.
[35] M. F. Wu, C. H. Hsiao, C. Y. Lee, N. H. Tai, *ACS Omega* **2020**, *5*, 14417–14426.
[36] J. Tian, T. Zhang, D. Talifu, A. Abulizi, Y. Ji, *Materials Research Bulletin* **2021**, *143*, 111457.
[37] T. Miah, P. Demoro, I. Nduka, F. De Luca, S. Abate, R. Arrigo, *ChemPhysChem* **2023**, *24*, e202200589.
[38] J. Gelfond, T. Meng, S. Li, T. Li, L. Hu, *Sustainable Materials and Technologies* **2023**, *35*, e00573.
[39] Z. Chen, X. Wang, B. Xue, Q. Wei, L. Hu, Z. Wang, X. Yang, J. Qiu, *ChemSusChem* **2019**, *12*, 1390–1400.
[40] J. J. Zhang, Y. Sun, L. K. Guo, X. N. Sun, N. B. Huang, *ChemistrySelect* **2021**, *6*, 6019–6028.
[41] M. L. Divya, S. Natarajan, Y. Lee, V. Aravindan, *ChemSusChem* **2019**, *12*, 4353–4382.
[42] Y. Zhu, T. Fang, J. Hua, S. Qiu, H. Chu, Y. Zou, C. Xiang, P. Huang, K. Zhang, X. Lin, E. Yan, H. Zhang, F. Xu, L. Sun, J. Zeng, *ChemistrySelect* **2019**, *4*, 7358–7365.
[43] Z. Liu, Z. Zhu, J. Dai, Y. Yan, *ChemistrySelect* **2018**, *3*, 5726–5732.
[44] S. Yan, J. Lin, P. Liu, Z. Zhao, J. Lian, W. Chang, L. Yao, Y. Liu, H. Lin, S. Han, *RSC Advances* **2018**, *8*, 6806–6813.
[45] J. Phiri, J. Dou, T. Vuorinen, P. A. C. Gane, T. C. Maloney, *ACS Omega* **2019**, *4*, 18108–18117.

[46] D. Jain, J. Kanungo, S. K. Tripathi, *Journal of Alloys and Compounds* **2020**, *832*, 154956.
[47] C. Zequine, C. K. Ranaweera, Z. Wang, P. R. Dvornic, P. K. Kahol, S. Singh, P. Tripathi, O. N. Srivastava, S. Singh, B. K. Gupta, G. Gupta, R. K. Gupta, *Scientific Reports* **2017**, *7*, 1174.
[48] P. Feng, J. Li, H. Wang, Z. Xu, *ACS Omega* **2020**, *5*, 24064–24072.
[49] C. Ding, T. Liu, X. Yan, L. Huang, S. Ryu, J. Lan, Y. Yu, W. H. Zhong, X. Yang, *Nano-Micro Letters* **2020**, *12*, 63.
[50] B. Li, J. Hu, H. Xiong, Y. Xiao, *ACS Omega* **2020**, *5*, 9398–9407.
[51] Y. Zhao, J. Yang, X. Y. Wang, X. C. Zheng, *Journal of Materials Science: Materials in Electronics* **2021**, *32*, 3498–3511.
[52] S. Yorgun, D. Yıldız, *Journal of the Taiwan Institute of Chemical Engineers* **2015**, *53*, 122–131.
[53] E. Taer, A. Apriwandi, R. Taslim, A. Agutino, D. A. Yusra, *Journal of Materials Research and Technology* **2020**, *9*, 13332–13340.
[54] M. Rajesh, R. Manikandan, S. Park, B. C. Kim, W. Cho, K. H. Yu, C. J. Raj, *International Journal of Energy Research* **2020**, *44*, 8591–8605.
[55] A. Galarneau, F. Villemot, J. Rodriguez, F. Fajula, B. Coasne, *Langmuir* **2014**, *30*, 13266–13274.
[56] Y. Huang, Y. Liu, G. Zhao, J. Y. Chen, *Journal of Materials Science* **2017**, *52*, 478–488.
[57] P. De, J. Halder, C. C. Gowda, S. Kansal, S. Priya, S. Anshu, A. Chowdhury, D. Mandal, S. Biswas, B. K. Dubey, A. Chandra, *Electrochemical Science Advances* **2022**, 1–15.
[58] B. A. Mei, O. Munteshari, J. Lau, B. Dunn, L. Pilon, *The Journal of Physical Chemistry C* **2018**, *122*, 194–206.
[59] N. O. Laschuk, E. B. Easton, O. V. Zenkina, *RSC Advances* **2021**, *11*, 27925–27936.
[60] D. Jain, J. Kanungo, S. K. Tripathi, *Applied Physics A* **2018**, *124*, 397.
[61] R. Kushwaha, S. Haldar, P. Shekhar, A. Krishnan, J. Saha, P. Hui, C. P. Vinod, C. Subramaniam, R. Vaidhyanathan, *Advanced Energy Materials* **2021**, *11*, 1–14.
[62] V. Subramanian, C. Luo, A. M. Stephan, K. S. Nahm, S. Thomas, B. Wei, *The Journal of Physical Chemistry C* **2007**, *111*, 7527–7531.
[63] K. Yu, H. Zhu, H. Qi, C. Liang, *Diamond and Related Materials* **2018**, *88*, 18–22.
[64] A. Ganesan, R. Mukherjee, J. Raj, M. M. Shaijumon, *Journal of Porous Materials* **2014**, *21*, 839–847.
[65] L. Jiang, G. W. Nelson, S. O. Han, H. Kim, I. N. Sim, J. S. Foord, *Electrochimica Acta* **2016**, *192*, 251–258.
[66] C. Lu, W. Wu, L. Wang, R. Tian, F. Du, *Next Materials* **2024**, *4*, 100170.
[67] W. Gong, B. Fugetsu, Z. Wang, I. Sakata, L. Su, X. Zhang, H. Ogata, M. Li, C. Wang, J. Li, J. Ortiz-Medina, M. Terrones, M. Endo, *Commun Chem* **2018**, *1*, 16.
[68] Y. J. Heo, H. I. Lee, J. W. Lee, M. Park, K. Y. Rhee, S. J. Park, *Composites Part B: Engineering* **2019**, *161*, 10–17.
[69] V. Skrypnychuk, N. Boulanger, A. Nordenström, A. Talyzin, *J. Phys. Chem. Lett.* **2020**, *11*, 3032–3038.
[70] R. Aswini, C. V. Niveditha, S. Swaminathan, *Materials Today: Proceedings* **2022**, *56*, 587–593.
[71] L. Miao, Z. Song, D. Zhu, L. Li, L. Gan, M. Liu, *Mater. Adv.* **2020**, *1*, 945–966.
[72] F. Zeng, Z. Meng, Z. Xu, J. Xu, W. Shi, H. Wang, X. Hu, H. Tian, *Ceramics International* **2023**, *49*, 15377–15386.
[73] J. Phiri, J. Dou, T. Vuorinen, P. A. C. Gane, T. C. Maloney, *ACS Omega* **2019**, *4*, 18108–18117.
[74] J. Wang, X. Zhang, Z. Li, Y. Ma, L. Ma, *Journal of Power Sources* **2020**, *451*, 227794.
[75] J. Li, Y. Gao, K. Han, J. Qi, M. Li, Z. Teng, *Sci Rep* **2019**, *9*, 17270.
[76] S. Yaglikci, Y. Gokce, E. Yagmur, Z. Aktas, *Environmental Technology* **2020**, *41*, 36–48.
[77] J. Sodtipinta, T. Amornsakchai, P. Pakawatpanurut, *Adv. Nat. Sci: Nanosci. Nanotechnol.* **2017**, *8*, 035017.
[78] Y. Li, S. Liu, Y. Liang, Y. Xiao, H. Dong, M. Zheng, H. Hu, Y. Liu, *ACS Sustainable Chem. Eng.* **2019**, *7*, 13827–13835.
[79] D. He, W. Zhao, P. Li, Z. Liu, H. Wu, L. Liu, K. Han, L. Liu, Q. Wan, F. K. Butt, X. Qu, *Applied Surface Science* **2019**, *465*, 303–312.
[80] G. Zhong, S. Xu, J. Chao, X. Fu, W. Liao, Y. Xu, Z. Liu, Y. Cao, *Ind. Eng. Chem. Res.* **2020**, *59*, 21756–21767.
[81] Y. Li, Z. Liu, Z. Li, Q. Wang, *Journal of Colloid and Interface Science* **2022**, *606*, 1311–1321.
[82] A. Ramakrishnan, S. Swaminathan, J. Mayandi, *ChemistrySelect* **2023**, *8*, e202303098.
[83] J. Wang, Q. Zhang, M. Deng, *ACS Omega* **2022**, *7*, 22689–22697.
[84] C. Ding, T. Liu, X. Yan, L. Huang, S. Ryu, J. Lan, Y. Yu, W.-H. Zhong, X. Yang, *Nano-Micro Lett.* **2020**, *12*, 63.
[85] S. M. Anisuzzaman, C. G. Joseph, W. M. A. B. W. Daud, D. Krishnaiah, H. S. Yee, *Int J Ind Chem* **2015**, *6*, 9–21.
[86] S. Yorgun, D. Yıldız, *Journal of the Taiwan Institute of Chemical Engineers* **2015**, *53*, 122–131.

[87] Y. Sun, J. Xue, S. Dong, Y. Zhang, Y. An, B. Ding, T. Zhang, H. Dou, X. Zhang, *J Mater Sci* **2020**, *55*, 5166–5176.
[88] Z. Zhu, H. Jiang, S. Guo, Q. Cheng, Y. Hu, C. Li, *Sci Rep* **2015**, *5*, 15936.
[89] M. Zhu, J. Lan, X. Zhang, G. Sui, X. Yang, *New J. Chem.* **2017**, *41*, 4281–4285.
[90] A. Altwala, R. Mokaya, *Energy Environ. Sci.* **2020**, *13*, 2967–2978.
[91] D. Jain, J. Kanungo, S. K. Tripathi, *Appl. Phys. A* **2018**, *124*, 397.

7. Conclusion and Scope of Future Work

The performance of energy storage devices is primarily depended on the electrode materials used and their inherent electrochemical properties influenced by factors such as crystal structure, morphology, size, surface area, and porosity. This thesis examines a variety of electrode materials, such as binary and ternary metal oxides, carbon nanostructures, and combinations of them, in order to gain a better understanding of how they affect supercapacitor performance efficiency.

The initial section of this thesis comprehensively addresses the significance of supercapacitors in contemporary energy storage applications. A detailed and in-depth examination of the constituent elements of supercapacitors is presented, as well as a look at the mechanisms that govern energy storage within them and outlines the specific goals and objectives driving this research. The following chapters explore methodologies and operational principles that underlie the diverse characterizations employed throughout the study.

Chapter three explores a binary metal oxide VO_2 (B) polymorph system, has 2D crystal structure. Through hydrothermal treatment, the manipulation of temperature (specifically on 160 °C, 180 °C, and 200 °C) is employed to modulate porosity and morphology. Notably, the elevated temperature of 200 °C demonstrates superior nanosheet morphology. To augment electrochemical performance, the introduction of graphene oxide during synthesis is pursued. This strategic inclusion leads to a transformative shift in the 2D nanosheets of VO_2 (B), culminating in an elegant flower-like morphology. This is achieved through the creation of a VO_2 (B)-graphene binary hybrid. The synergy achieved in this binary hybrid structure significantly enhances electrochemical activity. Additionally, an investigation is conducted into its asymmetrical fabrication with a highly porous activated carbon. The result is a comprehensive understanding of the enhanced electrochemical characteristics originating from the judicious combination of VO_2 (B)-graphene binary hybrid and highly porous activated carbon.

The fourth chapter intricately details the synthesis of the δ-MnO_2 polymorph, utilizing a straightforward sol-gel method and yielding a unique one-dimensional morphology. Employing a low-temperature approach, two distinct reducing agents, namely citric acid and ammonium oxalate, were systematically employed. Subsequently, an in-depth exploration of

the impact of sintering temperature, heating rate, and annealing atmosphere on inducing intrinsic vacancies was pursued to amplify the material's properties. This synthesis process yields ultrathin one-dimensional nanostructures, exhibiting an exceptional thickness ranging from 10 nm to 15 nm. The material's pronounced mesoporous characteristics were explained extensively, drawing upon comprehensive electrochemical studies. Similarly, Asymmetric supercapacitors with highly porous carbon elevates the electrochemical performances.

Chapter five provides a comprehensive exploration of the novel ternary metal oxide $Zn_2Te_3O_8$, also known as zincospirrofite. The solvothermal method, utilizing ethylenediamine as the solvent, was employed at a temperature of 200 °C for a duration of 6 hours. Which results in the formation of spherical particles characterized by their distinctive morphology. To further enhance the electrochemical properties of the material and facilitate its integration, a graphene hybrid composite was carried out. The electrochemical analysis, conducted in a 0.1 M KNO_3 electrolyte, revealed a remarkably elevated electrochemical performance, showcasing an extended potential window of 2 V.

In the sixth chapter, a comprehensive exploration into EDLC materials, particularly carbon-based materials, is undertaken. This thorough investigation searches into the details of utilizing biomass sources such as sawdust and leaves to create porous carbon structures. The process involves an activation with $ZnCl_2$, succeeded by a controlled pyrolysis procedure. The resulting biomass-derived porous carbon exhibits a remarkable porous nature, showcasing a harmonious blend of both mesoporous and microporous characteristics. In addition to that, elucidating the formation of carbon nanofibers through the innovative technique of electrospinning PAN (polyacrylonitrile), succeeded by high-temperature carbonization. This temperature manipulation at varying degrees like 500 °C, 700 °C, and 900 °C yields carbon nanofibers having diverse diameters ranging from 354 nm to 100 nm, accompanied by a specific surface area ranging from 3 m^2/gm - 616 m^2/gm. Furthermore, the study of redox additives within the electrolyte was done to enhance the supercapacitor performance. The additives contribute to enhancing the overall electrochemical performance of the EDLC materials.

Below is a summary of the materials used in this thesis with their synthesis method, morphology, specific capacitance, etc. (Table 7.1)

Type		Sample	C_s (F/g) from CV	Scan rate (mV/s)	Electrolyte	Total Pot. Window (V)	Surface Area (m^2/g)	Synthesis	Morphology
Pseudo (Symmetric)	1	VO_2	232.56	5	Na_2SO_4	1	22.95	Hydrothermal	Nanosheet
	2	MnO_2	295.12	5	Na_2SO_4	1	221.19	Sol-Gel Chemical	Nanotube & Nanowire
	3	ZTO	42.29	10	KNO_3	1.9	6.00	Solvothermal	Nanoparticles
EDLC (Symmetric)	1	WC	91.58	5	Na_2SO_4	1	1757.80	Carbonization	Honeycomb like
		WC +KI	109.12	5	Na_2SO_4+ KI	1		Redox Additive Electrolyte Study	
	2	LC	75.60	5	Na_2SO_4	1	1363.60	Carbonization	Tunnel like
		LC +KI	173.04	5	Na_2SO_4+ KI	1		Redox Additive Electrolyte Study	
	3	CNF	28.20	5	Na_2SO_4	1	616.00	E-spin	Nanofiber
		CNF + KI	119	5	Na_2SO_4+ KI	1.2		Redox Additive Electrolyte Study	
Hybrid (Symmetric-EDLC+ Pseudo)	1	ZTR	513	10	KNO_3	2	15.00	Solvothermal	Nanosheet
	2	VR	469.38	5	Na_2SO_4	1	7.87	Hydrothermal	Nanoflower
Asymmetric (Pseudo//EDLC)	1	MnO_2//AC	107.38	10	Na_2SO_4	1.5		Hydrothermal and carbonization	Nanowire + Honey comb like carbon
	2	VR_1//AC	84.97 F/g	10	Na_2SO_4	1.7		Hydrothermal and carbonization	Nanoflower + Honey comb like carbon

Table 7.1 Summary of the thesis work

It is concluded that the electrode and electrolyte materials utilized for studying energy storage applications possess beneficial properties. Current study focuses mainly on electrode materials than electrolyte. Most of the cases we have used Na_2SO_4 as electrolyte. Performance of these electrode materials in presence of other electrolytes like a gel electrolyte, organic liquid electrolyte, or ionic liquid electrolyte can further enhance their performance. Incorporating other active materials, introducing additional functionalities, electrolytes could significantly improve their storage efficiency. The developed materials also hold potential for battery applications, highlighting their versatility and utility for the future. Also, the materials are capable for integrating with other devices and applications as shown in figure 7.2.

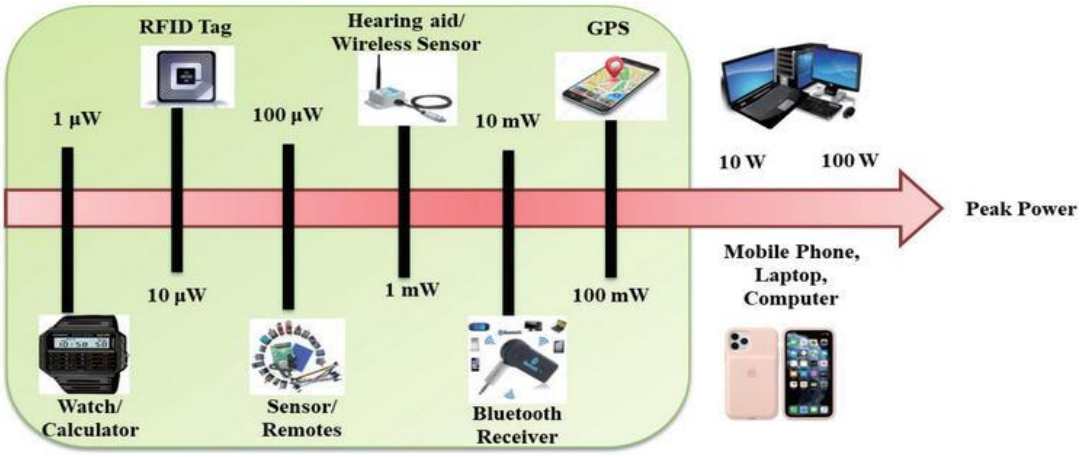

Figure 7.1 Applications of supercapacitor